Optical Modulators Based on Microfabricated Tilting Flaps Operating at low Actuation Voltages

THÈSE N^{O} 5317 (2012)

PRÉSENTÉE LE 27 AVRIL 2012
À LA FACULTÉ DES SCIENCES ET TECHNIQUES DE L'INGÉNIEUR
LABORATOIRE DE CAPTEURS, ACTUATEURS ET MICROSYSTÈMES
PROGRAMME DOCTORAL EN MICROSYSTÈMES ET MICROÉLECTRONIQUE

ÉCOLE POLYTECHNIQUE FÉDÉRALE DE LAUSANNE

POUR L'OBTENTION DU GRADE DE DOCTEUR ÈS SCIENCES

PAR

Fabio JUTZI

acceptée sur proposition du jury:

Prof. H. Shea, président du jury
Prof. N. de Rooij, Dr W. Noell, directeurs de thèse
F. Gueissaz, rapporteur
Prof. H. P. Herzig, rapporteur
Dr A. Hoogerwerf, rapporteur

ÉCOLE POLYTECHNIQUE
FÉDÉRALE DE LAUSANNE
Suisse
2012

Abstract

In this thesis the concept, modelling, design, fabrication process and characterization of novel optical modulators are presented. The devices consist of flaps exhibiting a large tilt with electrostatic actuation at low voltages. The applications comprise, but are not limited to, a monochromatic reflective display, a transmissive shutter array and switchable diffraction-gratings.

Nowadays the LCD-technology for reflective displays which is the most widely used technology exhibits a low contrast and reflectivity. Different technologies have been developed or commercialised, but still do not reach the quality of printed paper. It is demonstrated that the technology developed in this thesis is very competitive. If it is applied as reflective display it could reach an overall reflectivity of 45% in the white state, a contrast ratio of 50, a 100dpi resolution, a fast switching time of 0.5ms and an actuation voltage below 40V; leading to low power consumption. When the device is employed as a transmissive shutter array a 40% fill-factor of the modulated area is obtained.

The modulators consist of flaps with $250\mu m$ width and $50\mu m$ height. Theyh are in vertical position at rest and in particular after fabrication. The flaps in array-configuration are suspended by a torsion beam and are electrostatically tilted to almost horizontal position. For applications as a reflective display, light gets absorbed on an underlying black-layer as the flaps are in vertical rest state, giving a black pixel. At tilted position incoming irradiation is reflected and the pixel is perceived as white. In the application as transmissive shutter array light passes through as the flaps are in rest-state and light is blocked in the actuated-state.

A model of the device is presented which permits us to properly design the dimensions, knowing the scaling laws.

A novel bulk microfabrication process was developed that employs micro-moulding for obtaining flaps and torsion beams made out of poly-silicon. Thin high aspect-ratio trenches are refilled by poly-silicon followed by dry etching of the surrounding material. With this process a large variety of flap shapes are fabricated, such as a wave-, lens- , comb- and grid-form.

For electromechanical and optical characterization special setups and methodologies were conceived. Typically 60° tilt angles for 60V actuation voltages were measured. Depending on the geometry there was a hysteresis in the actuation trajectory and some flaps exhibited tilt angles close to 90 °. The actuation voltage ranged from 35 to 85V. The resonance frequency was at 700Hz in the rest state and at 2.3kHz in the actuated state. The poly-silicon flap surface had a reflectivity of 37% and an absorbance of 85 to 96%, depending on the wavelength. When the configuration was used as a reflective display a maximal contras ratio of 145, with typical values between 30 and 40, was measured on the active modulation area.

The use of a blazed-grating shaped flap as switchable diffraction-grating was also demonstrated.

Besides the concept of vertical flaps, a study is presented for the design of surface micromachined horizontal flaps actuated electrostatically to vertical position towards a transparent electrode.

Keywords: optical modulator, microfabrication, large tilt angle, micromirror, low voltage electrostatic actuation, reflective display, shutter array, high contrast ratio

Zusammenfassung

In dieser Thesis werden das Konzept, die Modellierung, der Aufbau, der Fabrikationsprozess und die Charakterisierung von neuartigen optischen Modulatoren vorgestellt. Die Anordnung besteht aus Drehklappen die mit tiefen Betätigungsspannungen elektrostatisch eine grosse Winkelauslenkung erreichen. Die Anwendungen umfassen unter anderem monochromatische Reflektionsdisplays, transmissive Shuttermatrizen und schaltbare Beugungsgitter.

Die heutzutage grösstenteils genutzte LCD-Technologie für Reflektionsdisplays bietet ein Grau-in-Grau-Bild mit schlechtem Kontrastverhältnis und Reflektionsgrad. Verschiedene andere in der Literatur erwähnte Technologien sind in der Entwicklungs- oder Kommerzialisierungsphase, erreichen aber noch nicht die Qualität von gedrucktem Papier. Es kann gezeigt werden, dass die in dieser Thesis entwickelte Technologie sehr konkurrenzfähig ist. In der Anwendung als Reflektionsdisplay hat sie das Potential eines Reflektionsgrads im Weisszustand von 45%, eines Kontrastverhältnisses von 50, einer Auflösung von 100dpi und schnellen Umschaltzeiten von 0.5ms. Mit einer Betätigungsspannung unter 40V wird zudem ein tiefer Leistungsverbrauch erreicht. In der Anwendung als transmissive Shuttermatrix wird ein Füllungsgrad der aktiv modulierenden Fläche von 40% erzielt.

Die Modulatoren bestehen aus einer Matrix von $250\mu m$ breiten und $50\mu m$ hohen Klappen, die von Torsionsbalken getragen werden. Die Klappen sind im Ruhezustand und direkt nach der Herstellung in vertikaler Lage. Elektrostatisch können sie in beinahe horizontale Lage gebracht werden. In der Anwendung als Reflektionsdisplay wird eingehendes Licht in vertikaler Lage der Klappen in einer darunterliegenden Schicht absorbiert, so dass man ein schwarzes Pixel erhält. In horizontaler Lage der Klappe wird das Licht reflektiert und das Pixel als Weiss wahrgenommen. In der Anwendung als tranmissive Shuttermatrix wird das Licht in der Ruheposition ungehindert durchgelassen und in der gekippten Lage blockiert.

Ein Model wird vorgestellt mit welchem die richtigen Dimensionen ausgelegt werden können.

Ein neuartiger Mikrofabrikationsprozess wurde entwickelt, der auf Mikroabformung der Polysilizium-Klappen und Drehbalken basiert. Dünne Rinnen von hohem Aspektverhältnis werden mit Polysilizium aufgefüllt. Nachfolgend wird in einem Trockenätzverfahren das umliegende Material entfernt. Mit diesem Prozess können eine grosse Vielfalt von Klappenprofielen fabriziert werden, wie Wellen-, Linsen-, Kamm-, Rastergitter- oder Beugungsgitterformen.

Für die elektromechanische und optische Charakterisierung wurden spezielle Aufbauten und Messmethoden konzipiert. Typische Neigungswinkel von 60° wurden für einen Betätigungsspannung von 60V gemessen. Je nach Konfiguration erhielt man eine Hysteresis der Betätigungskurve, Betätigungsspannungen von 35 bis 85V und Neigungswinkel von fast 90°.

Die Resonanzfrequenz lag im Ruhezustand bei 700Hz und im betätigten Zustand bei 2.3kHz. Die Polysiliziumklappen hatten einen Reflektionsgrad von 37% und einen Absorptionsgrad von 85 bis 95%, abhängig von der Wellenlänge. In der Konfiguration als Reflektionsdisplay wurde auf der aktiven modulierenden Fläche ein maximales Kontrastverhältnis von 145 gemessen mit typischen Werten zwischen 30 und 40.

Es wurde zudem der Einsatz eines Blazegitters als schaltbares Beugungsgitter gezeigt.

Neben dem Konzept der vertikalen Klappen wird eine Studie von Klappen präsentiert, die im Ruhezustand horizontal sind und gegen eine transparente Elektrode elektrostatisch in vertikale Position betätigt werden.

Stichwörter: optische Modulatoren, Mikrofabrikation, grosse Neigugswinkel, Mikrospiegel, Elektrostatik, tiefe Betätigungspannungen, Reflektionsdisplay, Shuttermatrize, hohes Kontrastverhältnis

Résumé

Dans cette thèse, le concept, la modélisation, la conception, la fabrication et la caractérisation de nouveaux modulateurs optiques sont présentés. Le dispositif est constitué de volets pivotants qui atteignent des grands angles d'inclinaison par actionnement électrostatique à bas voltage. Les applications comprennent, entre autres, un affichage réflectif monochromatique, des matrices d'obturateurs transmissifs, et des réseaux de diffraction commutables.

Aujourd'hui, la technologie LCD la plus largement utilisée pour les systèmes d'affichage réflectifs présente une image grise-grise avec un bas rapport de contraste et une basse réflectivité. D'après une revue de littérature, les technologies en phase de développement ou de commercialisation n'atteignent pas le contraste du papier imprimé. La technologie développée au sein de cette thèse est très compétitive. Comme affichage réflectif elle peut atteindre une réflectivité dans l'état blanc de 45%, avec un rapport de contraste de 50, un temps de commutation de 0.5ms et une résolution de 100 dpi. De plus, sa consommation énergétique est faible grâce à sa tension d'actionnement inférieure à 40V. Sous la forme de matrice d'obturateur transmissif un taux de remplissage de la surface modulée de 40% peut être obtenu.

Les modulateurs sont formés d'une matrice de volets ayant une largeur de $250\mu m$ et une hauteur de $50\mu m$ suspendus par des barres de torsion. Après fabrication, c'est-à-dire dans la position de repos, les volets sont en position verticale. Par l'application d'une force électrostatique les volets peuvent atteindre une position horizontale. En mode d'affichage réflectif, la lumière arrivant sur un volet en position vertical est absorbée dans une couche sous-jacente, de manière à obtenir un pixel noir. Lorsque le volet est en position horizontale, la lumière est réfléchie produisant un pixel blanc. En mode d'obturateurs transmissifs, la lumière traverse librement la matrice lorsque le volet est en position verticale et est bloquée lorsque le volet est en position horizontale.

Le dimensionnement du système a été accompli à l'aide d'un modèle basé sur les lois d'échelle et spécialement conçu pour ce dispositif.

Un nouveau procédé de fabrication basé sur le micro-moulage des volets et des barres de torsions en poly-silicium a été développé. Des tranchées ayant un rapport d'aspect élevé ont été remplies de poly-silicium, puis le matériel les entourant a été enlevé par gravure sèche. Ce procédé a permis de fabriquer des volets ayant une grande variété de profils, tels que des formes d'ondes, de lentille, de peigne ainsi qu'un réseau de diffraction commutable.

Selon le design une tension d'actuation variant de 35 à 85V a pu être mesurée, de plus pour certaines configurations un angle d'inclinaison de 90° a été atteint et une courbe d'hystérèse a été observée. La fréquence de résonance du volet à l'état de repos était à 700Hz et à 2.3kHz à l'état actionné. La caractérisation optique, a permis de mesurer pour les volets une réflectivité de 37% et un degré d'absorption de 85 à 95% selon la longueur d'onde. En affichage réflectif, un contraste maximum de 145 et un contraste moyen de 30 à 40 ont été obtenus pour la surface de modulation active.

En plus des volets verticaux, une étude sur des volets en position horizontale au repos et actionnés par une force électrostatique générée par une électrode transparente est présentée.

Mots clés : modulateurs optiques, microfabrication, grand déplacement angulaire, micromirror, actionnement électrostatique à basse tension, affichage réflectif, matrice d'obturateurs, rapport de contraste haut

Contents

1 Introduction

Paper is the most versatile medium for transfer of information. It has low weight, is pliable, consumes no power and gives a good image quality at all illumination conditions. White paper exhibits a reflectance of 80% and contrast ratio of 15 (with a good laser-printer). Unfortunately it lacks the ability of changing the image or text displayed. On the other hand we have electronic display systems which are able to show moving images. The nowadays most widely used LCD-technology has only a good image quality with back-illumination, which accounts for more than 60% of the power consumption [1]. In addition we have a poor readability at bright sun-light, where we get the best images with a printed paper.

Different new technologies are being developed for obtaining an electronic paper-like display having high reflectivity and contrast and being able to show moving images at low power consumption. This thesis investigates an approach based on micro- electro mechanical systems (MEMS). Novel microfabricated optical modulators are developed for this purpose. The modulators are based on arrays of flaps tilting by an angle close to 90° from horizontal to vertical position. Light is reflected back up and blocked from transmission as the flap is perpendicular to its direction of propagation. As the flap is parallel to the direction of propagation the light is not obstructed and passes through the modulator. A schematic is shown in figure 1.1.

In the field of optical MEMS a large variety of modulators have been reported. Electrostatic actuation is frequently used. It has a low power consumption, since it does not involve large electric currents. Close to 90° tilting flaps have only been presented by a few groups [2–6]. But, all devices require rather large actuation voltage above 100V or have large dimensions.

This thesis will aim to:

- Develop electrostatic optical modulators based on tilting flaps operating at low actuation voltages.
- Implement the optical modulators in the application of a reflective display exhibiting better performance than nowadays available technologies.

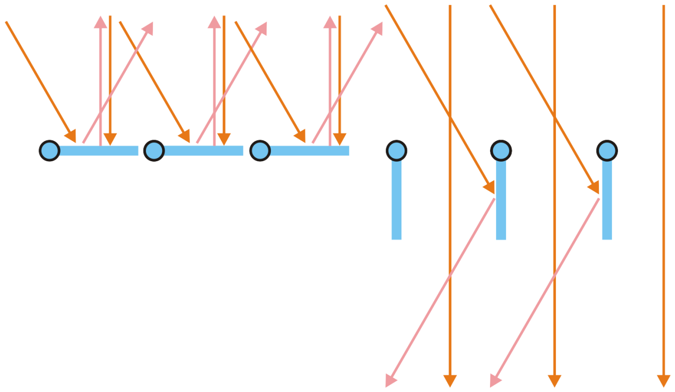

Figure 1.1: *Schematic of optical modulator. On the left the flaps block incoming light or reflect it back up since they are in perpendicular position. On the right side the flaps are parallel to the optical light path and light passes through.*

- Explore the devices ability to be used also in other applications such as a transmissive shutter array.
- Develop a novel fabrication process for the optical modulators and investigate its possibilities and limits.

The thesis will first give in chapter 2 an overview of reflective display technologies reported in literature. It will also look at the different reported microfabricated shutters exhibiting large tilt. After the introduction to some fundamentals, chapter 3 will present the concept of the tilting flaps optical modulators, with the requirements of the system in the application as reflective display or transmissive shutter array. Further the system will be modelled electromechanically permitting to design the modulators shape. In chapter 4 a design study of surface micromachined horizontal flaps will be presented, with its fabrication process including a transparent electrode which actuates the flap to vertical tilted position. A concept of flaps which are in vertical position at rest state and after fabrication will be presented in chapter 5. The systems architecture will be designed with the flaps of different shape being actuated electrostatically to horizontal position. A novel fabrication process will be described which is based on bulk microfabrication. The fabricated devices will be characterized electromechanically and optically in chapter 6. In chapter 7 will be discussed the suitability of the developed optical modulators for use in different applications including a reflective display, by comparing it to existing technologies. An outlook will outline the direction of further developments, aspects to be improved and other possible applications. Finally in the last chapter a conclusion of the whole work will be draw.

2 Fundamentals

In this chapter are presented some fundamentals required for the explanations in the thesis. First an overview of the state of the art in reflective displays, transmissive shutters, micromirrors exhibiting a large tilt-angle and microfabrication technology will be given. Next are exhibited some basic theoretical expressions required for calculating the properties of an electromechanical and optical system.

2.1 State of the art

The past and actual developments in technologies of reflective displays and electrostatically tilting flaps will be treated in the following sections. The here presented technologies will be compared with the technology developed in the frame of this thesis in chapter 7.

2.1.1 Reflective Displays

Reflective displays work only with ambient light. There is no back-light illumination. Light arriving at the display is either reflected or absorbed, giving a white or a black pixel. When different wavelengths are selectively reflected or a colour filter is placed on top of the pixels a coloured display can be obtained.

2.1.1.1 Liquid crystal displays

Most of nowadays used reflective displays are based on liquid crystal technology. The most basic liquid crystal technology is a twisted-nematic (TN)-cell [7, 8]. It consists of a liquid crystal placed between two crossed polarisers and a reflective layer at the backside. A schematic of a normally black 90° TN-cell is shown in figure 2.1. In coming light is polarised in one direction by the first polariser. At the OFF-state the liquid crystal rotates the polarisation of the traversing light by 90°. Therefore it can cross the second also 90° rotated polariser and is reflected on a mirror on the backside. On the way back the light passes again through both polarisers and exist the pixel, it is perceived as bright. When the liquid crystal is switched ON, the polarisation of the incoming light in not rotated anymore and it is blocked on the second polariser. No light is reflected and the pixel is perceived as dark.

Since in the configuration of a TN-cell light requires to pass four times through a polariser we can obtain only a low total reflectance. Other configurations using only one polariser or being normally black have also been developed. But, all these architectures exhibit a reflectance of about maximal 40% [8]. The contrast ratio depends on the viewing angle and is in the range of 20. Required actuation voltages are about 5V [8].

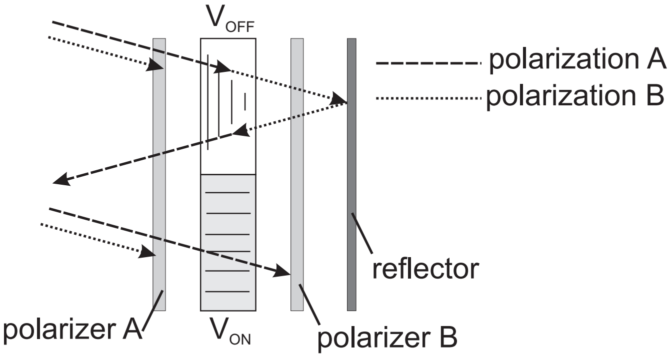

Figure 2.1: *Working principle of a reflective display based on a twisted nematic cell with two crossed polarisers. Unpolarised light (i.e. light with both polarisations A and B) arrives first on polariser A. Only light of polarisation A passes through. In the OFF-state the twisted liquid crystal rotates the polarisation by 90°, so it can also cross the second polariser and be reflected on the back-reflector. In the ON-state the polarisation of the light traversing the liquid crystal is not rotated and it is blocked by the second polariser B. Redrawn from [8].*

Based on liquid crystal technology a wide range of other concepts have been developed such as in-plane switching (IPS) technology [1, 9] or liquid crystal on silicon (LCoS) [9] employed in projectors. These technologies have better optical properties than the TN-cell. The LCoS exhibits a contrast ratio of up to 5000 [10], which is however limited to a small viewing cone of about 10° [9]. Fundamentally the maximal reflectivity which can be obtained with polariser based liquid crystal technology is 50%, since a polariser always filters out half of the unpolarised ambient light.

An other liquid crystal based approach is employed by the company Kent Displays [11–16]. It is based on cholesteric liquid crystals which reflect light by Bragg-reflections in one state and let light pass trough in their other state. 45V actuation voltage is required to change from one state to the other. A contrast ratio of up to 40 and a reflectivity of 40% are reported [17]. The response time is rather slow. A 128x32 pixels *Reflex Graphic Display Module* of *Kent Display* has an update time of 1.5s [18].

2.1.1.2 Electrophoretic displays

Electrophoretic displays use coloured charged particles which are suspended in an electrophoretic dispersion [19–22]. Black particles are charged positively and white particles are charged negatively. When applying a voltage bias to a transparent electrode at the front and the electrode at the backside, accordingly either the black or the white particles are moved to surface, making the pixel appear in the according colour. The microparticles are packaged into a microcapsule by polycondensation. This encapsulation permits to obtain a long life time, avoiding particle clustering and lateral migration. The microcapsules are placed on top of a TFT-backplane, which permits to use common LCD-display addressing technology [21]. Switching times are at about 250 ms [20]. After switching the pixel is reported to stay stable for several months. A reflectivity of the white state of 35% [19] to 50% [21] is shown with contrast-ratios around 8. This display technology is currently commercialized by the company E-ink and already employed in different E-book tablet readers. E-Ink reports their display to have a contrast ratio of 10 with minimum reflectivity or 40%, 16 grey-scale levels, $+/-$ 15 V actuation voltage and 200 dpi resolution [23].

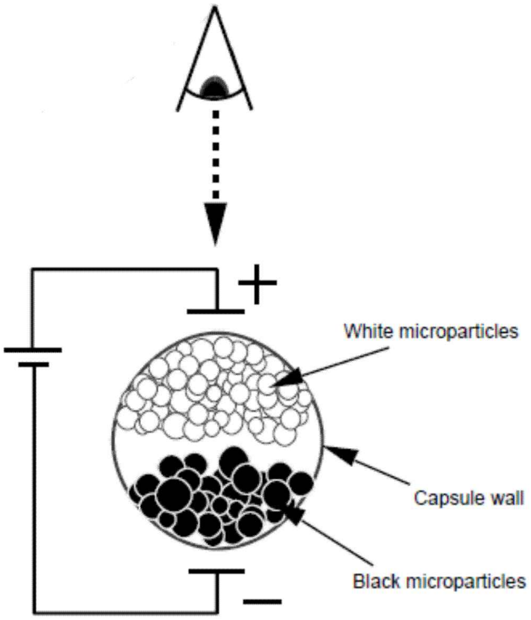

Figure 2.2: *Working principle of electrophoretic displays. White and black opposite charged microparticles in a electrophoretic dispersion are encapsulated in microcapsules of 30-300µm diameter. By applying a voltage difference between a transparent electrode on the top and on the bottom, either the white or black particles migrate to the surface. [19]*

2.1.1.3 Interference based displays

In interference based displays each pixel consists of an adaptive interference cavity, which is created by having a reflective membrane at the bottom and a semitransparent thin film stack at the top, as depicted in figure 2.3. Incoming light reflects back up only at the a wavelength for which we have constructive interference in the Fabry-Perot-cavity, so the pixel is perceived at a certain colour. The width of the cavity can be changed by applying a voltage between the reflective membrane and an electrode on top. The reflective membrane is actuated electrostatically to the top, leading to a cavity with constructive interference at a different wavelength, which does not lay anymore in the visible spectrum. The pixel is now perceived as black. There is a hysteresis in the actuation curve of the reflective movable membrane. A lower voltage is required to hold the membrane at the collapsed state than to switch it from bottom to top. This voltage difference can be used for line-column addressing [24].

This technology is currently in development at the company Qualcomm which is commercialising it with the brand Mirasol [24, 25]. A bi-chrome black-green display which is already employed in some portable products is reported to have a contrast ratio of 7, a reflectivity at green state of 45%, a refresh-rate of 15 frames per seconds for 128x96 pixels, a resolution of 130dpi and a supply voltage of 3V [26].

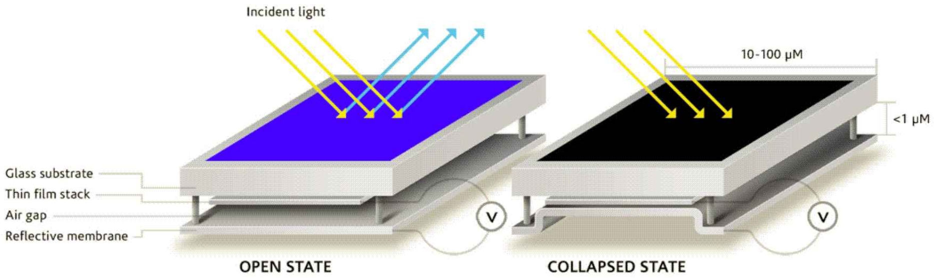

Figure 2.3: *Working principle of interference based display. Light arrives onto a Farby-Perot cavity defined by a thin film-stack and a reflective membrane. Only one wavelength is reflected by the cavity for which constructive interference occurs. When applying a voltage difference between the bottom membrane and a top electrode, the cavity collapses. We have now constructive interference at a different wavelength, which is not in the visible spectrum. The pixel appears black. [24]*

Another group [27] has also reported a interference based display system. The device works with back-illumination. In a roll-to-roll process flexible foils with semitransparent reflectors are processed to an adaptive cavity, which is collapsed by application of 20V actuation voltage. A transmittance of 50% is reported.

2.1.1.4 Electrowetting based displays

Electrowetting denotes the change of the wetting characteristics of a surface by application of a voltage. The electrostatic energy is added to the surface energy balance, causing a initially hydrophobic surface to become hydrophilic. A reflective display is proposed using a coloured oil in water on top of a hydrophobic layer with an electrode below [28]. Figure 2.4 shows the working principle. In the rest state the oil covers a hydrophobic surface. From the top the area is perceived in the colour of the oil. As a voltage is applied between the electrode and the water, the oil is pushed aside. An underlying white substrate is now seen from the top, so the pixel is white. Response times of 40ms are reported for switching from dark to white state at an actuation voltage of 22.5V [29]. The corresponding change in capacitance at switching is $16pF/mm^2$.

The company Liquavista is currently developing this technology. The company reports a contrast ratio between coloured and white state of 15 and a reflectivity of 40% at an actuation voltage of 22V. The switching time of a pixel of 240x240μm^2 is 10ms [30]. Also a transmissive device has been presented [31].

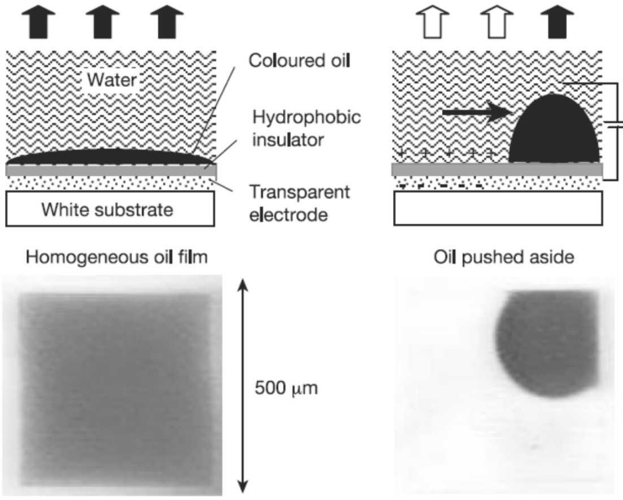

Figure 2.4: Working principle of an electrowetting based display. A coloured oil droplet in water is placed on top of an electrode. In equilibrium state the oil lays between the water and a hydrophobic coating on top of the electrode, as shown on the left. From the top a coloured film is seen. As a voltage is applied between the electrode and the water, the oil droplet is pushed aside due to a change in surface energy. An underlying white substrate is now perceived from the top.

2.1.1.5 Shutter based displays

In the beginning of the 1980ies in the Centre Electronique Horloger in Neuchâtel a reflective display was developed based on tilting flaps. The concept is depicted in figure 2.5. The aluminium flaps reflect light as they are in the horizontal rest state. When applying a voltage between the reflecting elements and a transparent electrode placed at a certain distance on top, the flaps tilt by about 90°. They are now vertical to the substrate and light is absorbed on an underlying black layer. An actuation voltage of 10V is reported [6] for 50nm thick aluminium flaps of 80x480μm^2 surface area suspended by 100μm long and 5μm wide torsion beams on both sides. 200nm thick devices of same size are actuated with 70V [32]. The devices have a switching time of 1ms and a contrast ratio of more than 20. A number of patents exist for this

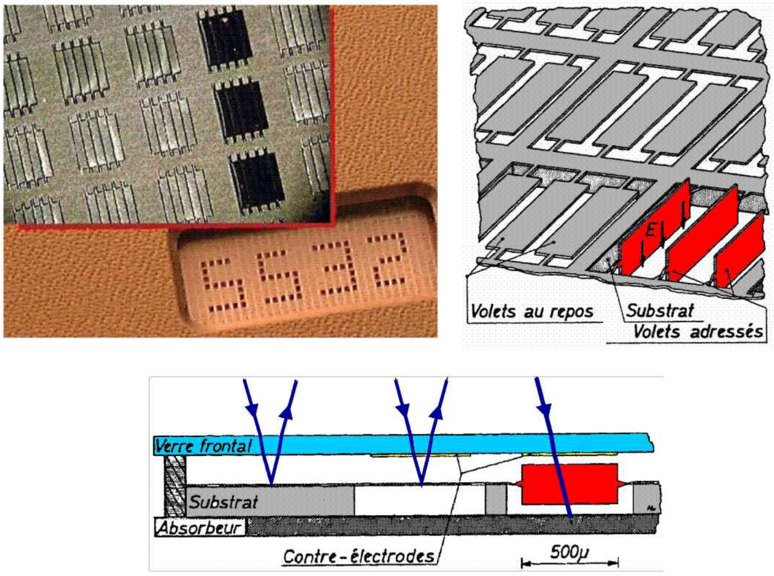

Figure 2.5: *Reflective display device based on aluminium flaps tilting electrostatically by 90°. A group of five flaps forms one pixel reflecting light at horizontal rest state. At vertical position of the flaps light is absorbed on an underlying black layer. On the top left is shown a photograph of a device displaying four digits. [6, 37]*

system [33–36]. The flaps are fabricated by patterning lithographically an Al-film evaporated on a plastic sheet. The structures are released in oxygen plasma.

A similar display concept based on flaps is presented in [38], with the difference that they are in rest state vertical to the substrate. The flaps are actuated to horizontal position electrostatically.

A shutter based display for use in transmission mode is presented by [39]. A curled thin-film is stretched by zipping-actuation on top of an electrode. Low voltage actuation and less than 1ms switching time for a contrast ratio in transmission of 20 is reported.

Different groups showed single transmissive shutters which are displaced laterally on a substrate. Zigzag shaped actuators displace a shutter above a opening hole by $18\mu m$ at 38V actuation voltage [40]. A system working at 70V actuation voltage was presented by [41, 42].

The company Pixtronix is developing a transmissive display based as well on lateral displacing shutters. The shutters are by-stable and displaced laterally by approximately $10\mu m$ with an actuation voltage of 20V [43, 44] .

2.1.1.6 Other working principles of displays

Different concepts for displays have been proposed in literature, based on other working principles than presented above. Most of them are still in exploratory state.

A ionic liquid packaged by Parylene-on-liquid deposition is presented in [45]. Here a pHindicator in the liquid changes its colour when applying a current to a pixel.

A photonic crystal fabricated of self-assembled silica spheres is reported in [46]. The lattice constant of the crystal is changed by swelling leading to a change in reflected wavelength .

Microsoft research presented a transmissive display with a fill-factor of 78% using telescopic pixels [47]. A suspended membrane is utilized as optical modulator actuated electrostatically at 120V and leading to a contrast ratio of 20.

2.1.2 Micromirrors and shutters exhibiting large tilt

In the area of optical MEMS a large number of tilting micromirrors have been developed. The most famous example is probably the digital micromirror array of Texas Instrument, which is nowadays employed in many projection systems [48]. Nevertheless of the large number of activities in this area, most of the devices reported to date have a rather small tilt angle. Only few groups presented micromirrors or shutters tilting by angles close to 90° which are electrostatically actuated. A difficulty is the large gap between movable device and electrode giving rise to a high actuation voltage. For the reflective display presented in section 2.1.1.5 an actuation voltage of 10V was reported, by employing hinges of very low compliance. Here will be presented next different other devices exhibiting large tilt.

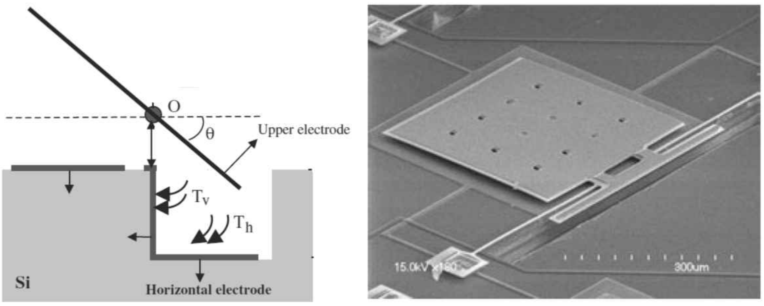

Figure 2.6: *This micromirror can tilt by an angle of 90° from horizontal to vertical state. The device consist of a large surface on one side of the torsion beam used for optical modulation and a small surface on the on the other side of the beam employed for actuation. The small surface is electrostatically attracted down to an electrode laying in a trench beneath, tilting simultaneously the large surface upwards. [4]*

Samsung presented a micromirror tilting from horizontal to vertical state for optical switching applications as shown in figure 2.6. The device has a large mirror surface on one side of the torsion beam suspension and a smaller surface on the other side for actuation purpose. This small surface is tilted down towards an electrode placed in a cavity beneath by electrostatic actuation. At the same time as the small surface tilts down the large surface tilts upwards, modulating an optical beam [4]. The mirror of 450x400μm^2 is actuated with 47V and has a switching time of about 10ms. For the same application of optical beam switching in telecommunication other devices are reported. One is actuated with voltages of about 300

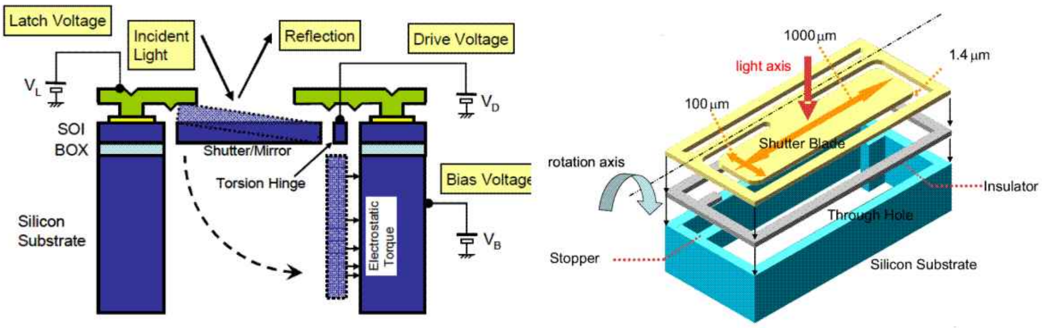

Figure 2.7: *This shutter array is developed for the application of multi-object spectroscopy in astronomy. It employs flaps suspended by a torsion beam, which are electrostatically attracted to the electrode on the walls of the cavity beneath. A top electroplated layer serves as optical mask for the non-active areas and for addressing purposes. [3, 51]*

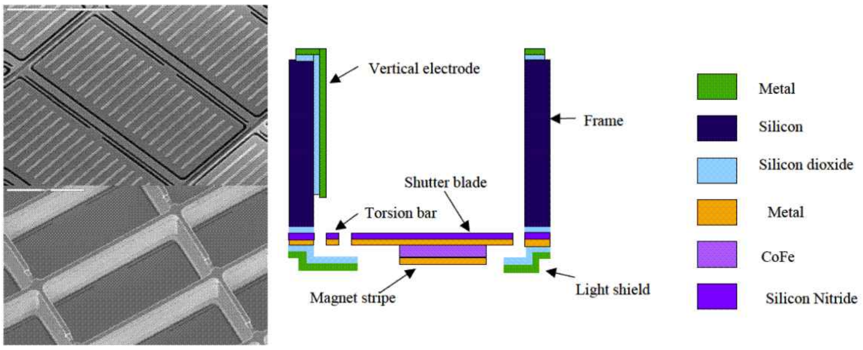

Figure 2.8: *The shutters with a coating of a magnetic material (CoFe) are tilted down by a magnetic force of an external magnet which is swept across the array. The single flaps are kept at vertical tilted position by an electrostatic force. Line-column addressing is used with voltages of* $+/-20V$*. [2] [52]*

V [5]. The other 300 x 600 μm^2 large shutters work at 100 to 150V [49]. The modelling and control of a similar torsional flap was presented in [50].

A group of the university of Tokyo presented a shutter array for the application in multi-object spectroscopy in astronomy [3]. Figure 2.7 depicts the device. 100 by 1000 μm large shutters suspended by a torsion beam are electrostatically actuated from horizontal rest state to vertical position towards an electrode placed in a cavity beneath. Actuation voltages in the range of 200V are required [51]. An electroplated layer serves as light shield of the gap between the shutter and the surrounding structure. This layer can also be used for addressing purposes.

The NASA has presented a shutter array for the James-Webb telescope (JWST) [50]. The device consists of an array of 100 x 200μm^2 large flaps suspended by a torsion flexure. A schematic is shown in figure 2.8. All shutters are in horizontal position at rest state. They are coated with a magnetic material. By means of an external magnet, which is swept across the substrate the shutters are tilted by 90° to vertical position. The shutters are kept at vertical state by an electrostatic force of a vertical electrode. Each shutter can be addressed by line-column addressing with voltages of +/− 20V. The units to which no voltage is applied return back to horizontal position after the magnet has passed. [2, 52]

2.1.3 Light modulation with switching diffraction gratings

Different groups have presented switching reflective diffraction gratings for light modulation in projector applications, among other things. In one reported device ribbons are suspended on top of periodic support structures on a silicon substrate. The ribbons can be electrostatically switched down towards the substrate. In this state a grating structure is produced. In the non-switched state there is specular reflection of light on the surface of the ribbons. In the pulled-down state light is diffracted and the light intensity is shifted from the reflected beam (0th order) to the 1st and 2nd diffraction orders [53–55]. The working principle is illustrated in figure 2.9.

The same light modulation principle has also already been presented by [56, 57]. Here the grating structure is formed by switching alternately one ribbon to down-position and leaving one ribbon at up-position. This technology is currently being commercialised by the company Silicon Light Machines [58].

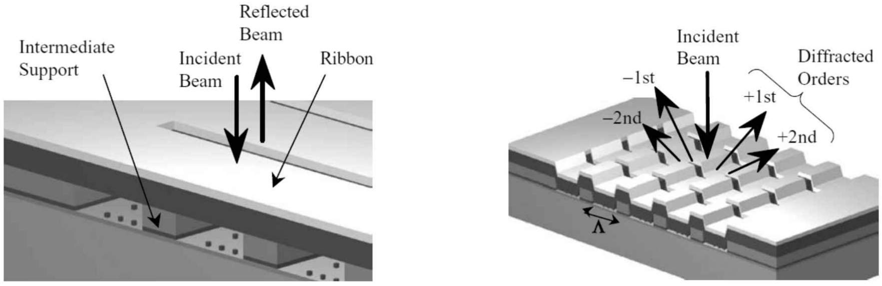

Figure 2.9: *Ribbons on top of a periodic structure can be electrostatically pulled down onto the substrate, producing a grating structure. In the OFF-state light is reflected on the ribbon surface in the ON-state the light intensity is shifted to the 1st and 2nd diffraction orders. [53]*

2.1.4 Microfabrication technology

Microfabrication is the technology employed for fabrication of a large range of devices including micro electromechanical systems (MEMS). It permits to produce devices with features of less than $1\mu m$. The structures pattern are transmitted onto the substrate by a photolithographic method. A photoresist is employed which is exposed through a mask. This resist serves as mask in a subsequent etching or deposition process. The underling layer can be etched in a wet etchant which comprise for example KOH which attacks Si or HF which attacks SiO_2. Another possibility is to use a dry-etching process in which is employed most commonly a fluorinated or chlorinated gas. The gases are used generally in a plasma which accelerates the ions towards the substrate combining this way physical and chemical etching. A large variety of microfabrication processes involving etching or also deposition of thin-films exist, but will not be introduced here. For more details please refer to literature [59].

The only process on which a short introduction will be given is the etching of deep trenches into a silicon substrate by deep reactive ion etching (DRIE). Here an ionized gas in a plasma is accelerated towards the silicon substrate as illustrated in figure 2.10. It etches the material at the locations not covered by a mask. In a next step a passivation layer is deposited which covers the whole etched area. This passivation layer protects the side-walls of being etched in a next etching-step with the ionised gas. Several times the etching and passivation steps are iteratively repeated to obtain this way a deep trench. It can be noticed that such deep trenches have a scalloping structure at its side walls, which originates from the process of alternating etching and passivation. More details about deep reactive ion etching can be found in [60, 61]

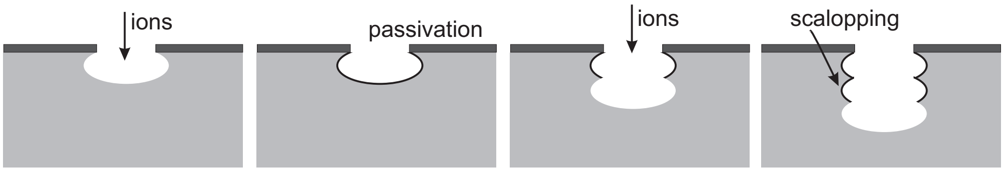

Figure 2.10: *Etching technique employed for obtaining deep trenches of high aspect ratio. The substrate is etched first at the location not protected by a mask by ion-bombardment (combined with chemical etching). Subsequently a passivation layer is deposited. In the next etching step the side walls are protected by the passivation layer. With several iterations of etching and passivation a deep trench is obtained, which has a scalloping at its side-walls.*

2.2 Basic physical dimensions

We will introduce now some basic equations which will be employed in calculations throughout the following thesis chapters.

2.2.1 Electrostatic force and torque

The electrostatic energy between two objects having between each-other a capacitance C and a potential difference of V can be expressed as:

$$E = \frac{1}{2} C \cdot V^2 \tag{2.1}$$

The electrostatic force between the two objects can be calculated out of the change in energy when the objects are moved in the direction the force is exerted. A force in direction of x can be expressed as:

$$F_x = \frac{1}{2} \frac{dC}{dx} \cdot V^2 \tag{2.2}$$

Equally the torque when turned in angular direction of θ can be written as:

$$T_\theta = \frac{1}{2}\frac{dC}{d\theta} \cdot V^2 \tag{2.3}$$

2.2.2 Mechanical torsion bar

We want to treat here the analytical formulas for the description of the deformation of a straight torsion beam fixed at both ends as schematically shown in figure 2.11. The beam has a length of $2l_{beam}$, a width of w_{beam} and a thickness of t_{beam}. It is fixed on all degrees of freedom at both ends. The forces and torques are applied to its centre. All formulas introduced in this section are from [62]. We will give the spring constants as displacement per applied force or torque.

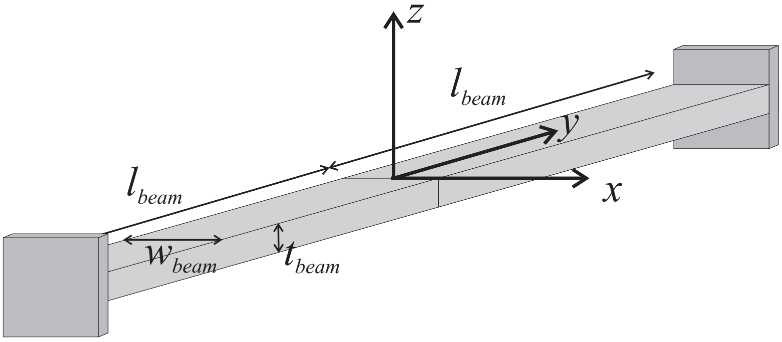

Figure 2.11: *Schematic of a torsion beam of length $2l_{beam}$ width w_{beam} and thickness t_{beam}. The beam is fixed at both ends on all degrees of freedom. A force or torque is applied to the centre of the beam.*

The area moment of inertia I for the cross-section of the beam perpendicular to the y-axis can be written as:

$$I = \frac{t_{beam}^3 \cdot w_{beam}}{12} \tag{2.4}$$

The polar moment of inertia J_p for the cross-section of the beam perpendicular to the y-axis can be written as:

$$J_p = \frac{w_{beam} \cdot t_{beam}^3}{3}(1 - 192 * \frac{t_{beam}}{\pi^5 * w_{beam}} \tanh(\pi \frac{w_{beam}}{2t_{beam}})) \tag{2.5}$$

For $w_{beam} \gg t_{beam}$ (2.5) can be simplified to:

$$J_p \approx \frac{w_{beam} \cdot t_{beam}^3}{3} \tag{2.6}$$

The spring constant for rotation of the beam around the y-axis can be written as:

$$k_\theta = \frac{2G \cdot J_p}{l_{beam}} \tag{2.7}$$

,with the shear modulus G obtained from the Young's modulus E and the Poisson's ratio μ of the material as:

$$G = \frac{E}{2(1+\mu)} \tag{2.8}$$

The spring constant for bending in z-direction can be expressed as:

$$k_z = 192\frac{E \cdot I}{l_{beam}^3} = \frac{192}{12}\frac{E \cdot t_{beam}^3 w_{beam}}{l_{beam}^3} \tag{2.9}$$

The spring constant for a rotation or twist around the x-axis can be written as:

$$k_\gamma = 16\frac{E \cdot I}{2l_{beam}} = \frac{16}{12}\frac{E t_{beam}^3 w_{beam}}{2l_{beam}} \tag{2.10}$$

2.2.3 Resonance frequency

We will now give analytical expressions for the resonance frequencies of different modes of the following system: A rigid flap of height h_{flap}, width w_{flap}, thickness t_{flap} and material density ρ is attached at its top centre to a torsion beam. The torsion beam is depicted in figure 2.11. The system is schematically depicted in figure 2.12. The analytical expressions given next can all be found in classical mechanics literature as [63, 64].

The resonance frequency of the system rotating around the y-axis can be expressed as:

$$f_\theta = \frac{1}{2\pi}\sqrt{\frac{k_\theta}{I_\theta}} \tag{2.11}$$

with I_θ the mass moment of inertia of the flap when turning around the beam.

$$I_\theta = \frac{1}{3}h_{flap}^3 \cdot t_{flap} \cdot w_{flap} \cdot \rho \tag{2.12}$$

The resonance frequency of the system bending in z-direction is given by:

$$f_z = \frac{1}{2\pi}\sqrt{\frac{k_z}{m_{flap}}} \tag{2.13}$$

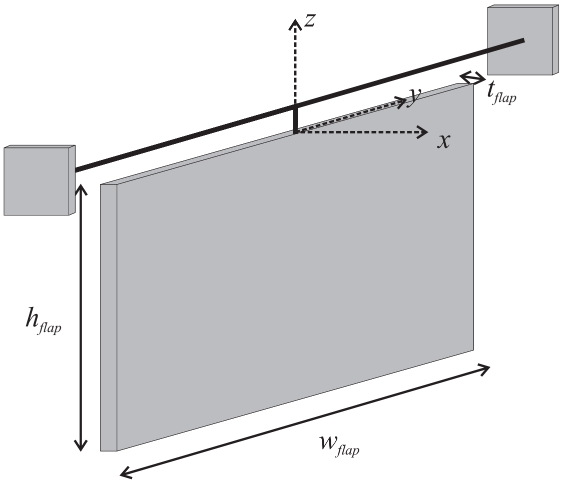

Figure 2.12: *A rigid flap is suspended by a torsion beam (as depicted in figure 2.11) at it central most top point. The flap has a height of* h_{flap}*, width of* w_{flap}*, thickness of* t_{flap} *and material density of* ρ*.*

with m the mass of the flap:

$$m = h_{flap} \cdot t_{flap} \cdot w_{flap} \cdot \rho \tag{2.14}$$

The resonance frequency of the flap twisting around the x-axis can be written as:

$$f_\gamma = \frac{1}{2\pi}\sqrt{\frac{k_\gamma}{I_\gamma}} \tag{2.15}$$

with I_γ the moment of inertia of the flap when turning around the x-axis:

$$I_\gamma = m(\frac{h_{flap}^2}{3} + \frac{w_{flap}^2}{12}) \tag{2.16}$$

2.2.4 Optical contrast

We want also to give a basic optical definition used for characterising displays. For the contrast different definition are used in literature. Therefore we define the contrast ratio CR as ratio between the measured light intensity originating from a surface at bright-state I_{white} and at dark-state I_{black}. It can also be expressed in other words as the ratio between the reflectance at white R_{white} and dark state R_{black}:

$$CR = \frac{I_{white}}{I_{black}} = \frac{R_{white}}{R_{black}} \tag{2.17}$$

3 Modelling of tilting flap

In this chapter will be introduced the concept and a model for the tilting flaps optical modulators. We will first present the concept in application as reflective display and transmissive shutter. Next the device will be modelled electromechanically. We will analyse the scaling laws for actuation voltage and resonance frequency with analytical formulas. A reduced order simulation model will give the actuation-trajectory of displacement and tilt for some chosen dimensions. By combining the analytical model of scaling and the results of simulations we will design the optimal dimensions of the system.

3.1 Concept of tilting flap as optical modulator

The system consists of arrays of flaps which can tilt by about 90°, modulating this way incoming light. As the flaps are in horizontal state towards the underlying substrate, this means they are perpendicular to the propagation direction of incoming light. In this state light gets either reflected or absorbed on the flap surface. At vertical state, when it is parallel to the direction of irradiation, the flap will not interact with incoming light. Light passes through the device. Light is modulated when switching between horizontal and vertical state.

We will now present the concept of the tilting flaps optical modulators in application as reflective display and transmissive shutter array. Next the actuation and addressing principle will be introduced.

3.1.1 Concept as reflective display

3.1.1.1 Requirements for a reflective display

We want to develop a monochrome reflective display. This is a display device which works only with ambient light. Light arriving on the display gets either reflected or absorbed. Each pixel requires thus to be changed from absorbing, dark or black state to reflecting, bright or white state.

The best nowadays available reflective display, even though it is static, is printed paper. We will have to benchmark the device we design with it. We want to look at the following requirements:

- Overall reflectivity: For obtaining a high brightness the reflectivity has to be high. The reflectivity should be comparable to other surrounding objects, such that the image displayed is perceived at the same or higher brightness as the surroundings. Paper has a reflectivity of about 80%.
- High optical contrast ratio between black and white state: It should be as high as possible for obtaining a good image quality. Printed paper has values around 10.
- Angular response: The device should have a large viewing angle. Values of more than 45° are desirable.
- Diffusivity: Since the display is working with ambient light, which may only be coming from one point-like single source, the surface of the display should be diffusive. This way the pixel can be perceived with the same brightness from all observation directions. Another possibility is to have a transparent diffusive layer included in the light path.
- Resolution: We want to aim a 100 dpi resolution with pixel sizes of 250 x 250 μm^2.
- Low power consumption: Specially in portable applications a low power consumption is required. Therefore an actuation principle with low power consumption has to be chosen.
- Actuation voltage: The device should be actuated at as low voltages as possible. In portable applications usually only voltages below 10V are available. Higher actuation voltages require a voltage up-converter, which is power consuming.
- Insensitivity to environmental vibrations: The resonance frequency of all modes requires to be higher than environmental vibrations which are generally below 1kHz.

Regarding the above requirements for a reflective display system we can set now the resulting properties the device should have:

- Fill-factor: The active area modulating light should be much larger than the passive area used for interconnections or structural purposes.
- The reflectivity of the flap material should be very high.
- Actuation principle: Electrostatic actuation will be chosen since no large currents are required here. Only the capacitance between flap and electrode is charged and discharged.

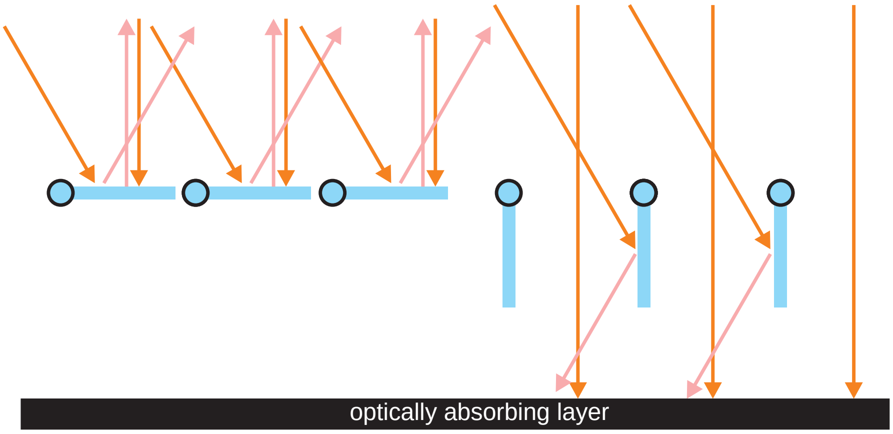

Figure 3.1: *The working principle of a reflective display using tilting flaps: When the flaps are in horizontal position (left), light is reflected back up, we obtain a bright, white pixel. When the flaps are in vertical state (right) incoming light passes through the modulator and gets absorbed on an underlying black layer, we have a black pixel.*

3.1.1.2 Working principle of reflective display with tilting flaps

We want to employ the above described optical modulator based on tilting flaps in the application as reflective display. The main feature is to place an optically absorptive layer below the tilting flaps. Each tilting flap (or a group thereof) forms one pixel. Hence, a whole array of flaps makes a display. When the flaps are in vertical position allowing light to pass, the irradiation gets absorbed on this black layer and we have a black pixel. A schematic is shown in figure 3.1. As the flaps are in horizontal position incoming light gets reflected on its surface. We have here now a bright area or white pixel.

Based on the above requirements we will have to place the flaps as close together as possible for obtaining a high fill-factor, the flap material should possess a high reflectivity for high brightness and electrostatic actuation should be employed for low power consumption. For obtaining a high contrast ratio the light absorbing layer requires to have a minimum reflectivity.

Another important criteria is the diffusivity which is stated in the requirements list above. When having a flat mirror-like flap there will be specular reflection of the surrounding light sources. A schematic can be seen in figure 3.2a), where the display is employed in a room with only one point-like light source. Only an observer at a specific location will perceive the flap at ON-state as bright. For an observer looking at the display from another incidence angle the light from the source will not arrive at his eye. He will perceive the pixel as black even if it is in ON (white)-state. For this reason the light from a source should be somehow diffused in its light path to attain all incidence angles of observations. For meeting the diffusivity criteria there are different approaches which can be taken as schematically shown in figure 3.2:

- A rough flap surface, which diffuses incoming light into all directions

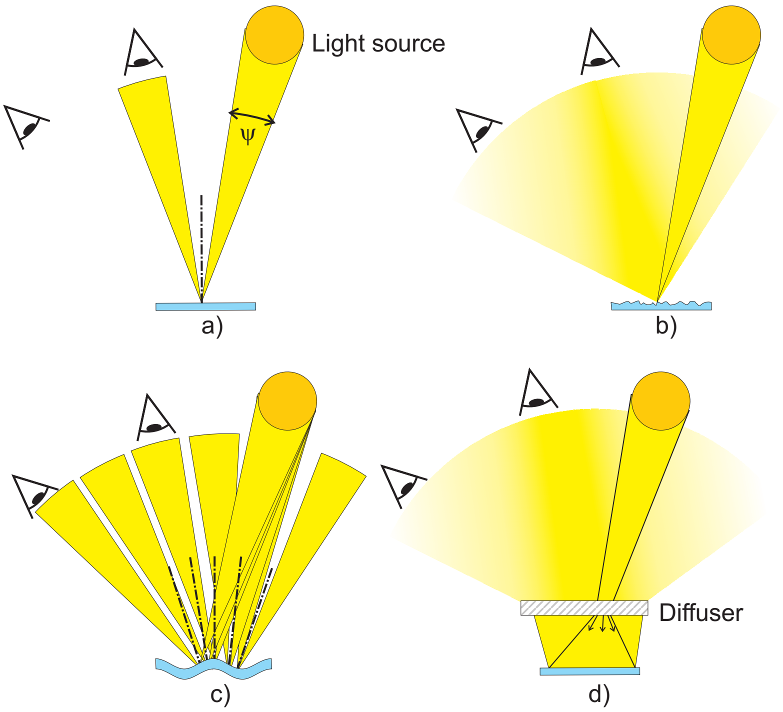

Figure 3.2: *a) When light gets reflected on a mirror only an observer at a specific location extending a solid angle of* ψ *will perceive the bright spot. Light requires to be reflected in all directions such that the light source is perceived from different positions. This can be done by: b) a rough reflector surface leading to diffusion of incoming light, c) a wave-shaped surface reflecting light into different directions depending on which location the incoming light arrives, d) a transparent diffuser which is placed along the light path.*

- A non-flat surface where each region reflects incoming light into another direction. A wave-shaped surface is an example of a reflector meeting this criteria.
- A transparent diffusive layer on top of the flaps, such that all incoming and reflected light passes through this diffuser.

3.1.2 Concept as transmissive shutter array

3.1.2.1 Requirements for a transmissive shutter array

A transmissive shutter array spatially modulates light passing through it. It either lets incoming light pass, not interacting at all (or the least possible) with the optical beam. Or it blocks irradiation of further propagation. Applications can be a back-illuminated display or spacial beam shaping where the intensity is modulated along the cross-section of the beam. The following requirements are important for such applications:

- In ON-state, where light is let pass, the transmittance should be as hight as possible. The

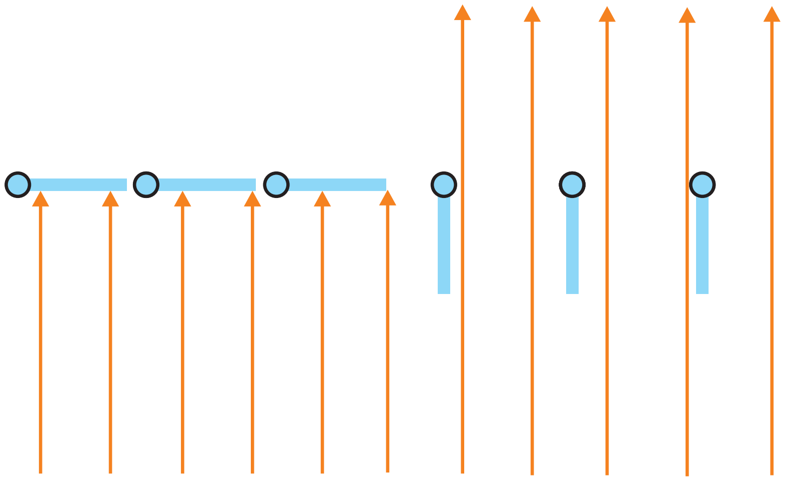

Figure 3.3: *The working principle of a transmissive shutter array using tilting flaps: When the flaps are in horizontal position (left), light is blocked from transmission, we obtain a dark area. When the flaps are in vertical state (right) incoming light passes.*

part of the beam not passing through the device due to shadowing effects or reflections has to be minimized.

- In the OFF-state, where light is blocked, the transmittance should be as low as possible. In an ideal case no light passes through the device.
- Power consumption and actuation voltage: As in the requirements for a reflective display the power consumption and actuation voltage should be as low as possible, specially if the device is used in portable application.
- Insensitivity to environmental vibrations: As in the case of a reflective display the device's resonance frequency should be higher than most of the environmental vibrations.

Regarding the above requirements we can set the properties a transmissive shutter array should have:

- The fill factor requires to be as high as possible. Thus the ratio between active area where light is modulated and passive area used for interconnection and structural purposes has to be maximized.
- A minimum light transmittance through the surface of a flap is required.
- Electrostatic actuation is desirable.

3.1.2.2 Working principle of transmissive shutter array with tilting flaps

When employing the tilting flap optical modulators as transmissive shutter array the device is placed in the light path with an opening in the backside. This way light can pass through

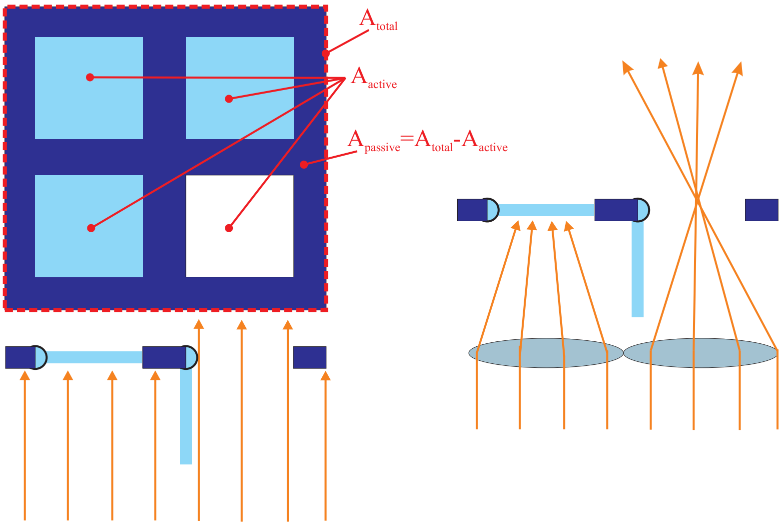

Figure 3.4: *The active area A_{active} on which light is modulated by a tilting flap is surrounded by a passive area $A_{passive} = A_{total} - A_{active}$ where any transmission is blocked. A solution for increasing the fill-ratio A_{active}/A_{total} is to place a lens in front of each flap, bundling incoming light only on A_{active}.*

as the flaps are parallel to direction of propagation. At the flaps which are at perpendicular position incoming light is blocked from transmission. The flap material has to have an as low transmittance as possible. Ideally it reflects the incoming light back or has a high absorption in the corresponding optical spectrum. A schematic of the application as transmissive shutter array is shown in figure 3.3

For obtaining a high fill-factor the flaps require to be placed the closest possible to each other. Therefore the area used for interconnections $A_{passive}$ should be minimized. Another method to increase the fill-factor consists of placing a lens in the light path bundling incoming light though the modulating area A_{active}. A schematic is shown in figure 3.4.

3.1.3 Concept of actuation

Lets look now at the concept used for actuation of the tilting flaps optical modulators. As actuation principle is chosen electrostatic actuation. The reasons are: First, it has a very low power consumption, because it dissipates power only when switching from the OFF- to ON-state due to the loading of the capacitance as will be described in section 3.2.4. Secondly, it is easy to implement since unlike electromagnetic or electrothermal actuation only a voltage requires to be applied between the moving device and an electrode. The other actuation principles require a special current path or magnetic materials which can be difficult to implement in fabrication. Thirdly, the scaling law of electrostatic actuations favours the employment in actuators of micro-metric dimensions.

An adequate hinge has to be chosen for obtaining the desired tilt by electrostatic actuation

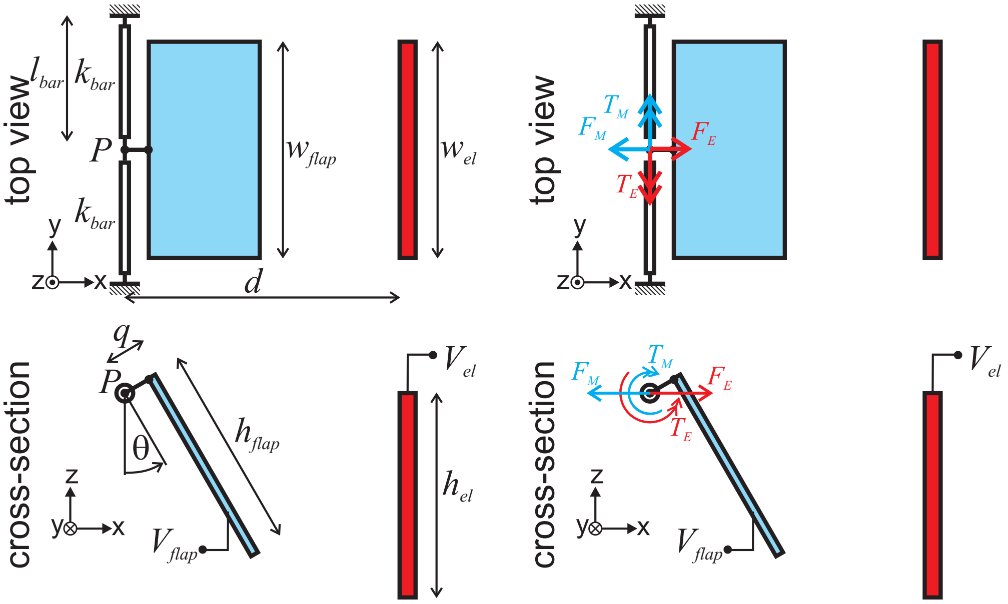

Figure 3.5: *Schematic of electromechanical system consisting of flap and electrode. The flap of width w_{flap} and height h_{flap} is suspended by a torsion beam of length l_{beam}. A rigid link of length q connects the flap to the torsion beam which is clamped at both ends. At a distance d from the torsion beam the electrode is placed.*

and a restoring torque when the voltage is switched off. It is important that the hinge moves mainly in torsion and does not bend due to forces in perpendicular direction. Therefore a serpentine-shaped beam is not adequate since it has a low compliance in bending. A straight beam clamped at both ends will be employed at whose centre the flap is attached.

The systems configuration is shown in figure 3.5. The flaps are actuated electrostatically by application of a voltage difference between them and an electrode placed at a certain distance. The devices are suspended by a torsion beam and tilt around it when being actuated, due to the electrostatic torque. The torsion beam gets deformed in titled state such that it exerts a restoring torque onto the flap. When the voltage is turned off the torque of the torsion beam brings the flap back into rest-state.

3.1.4 Addressing of flaps in an array

For addressing each flap individually in array of N by M flaps different solutions are possible:

- Individual connection: Each flap can have a separate connection. In this case all electrodes could be grounded for example and MxN connection lines go to the different flaps. In a large array this can lead to a very large number of interconnection lines what may lead to a problem of space.
- Active-matrix: In an active matrix as commonly used in LCD-displays each pixels has

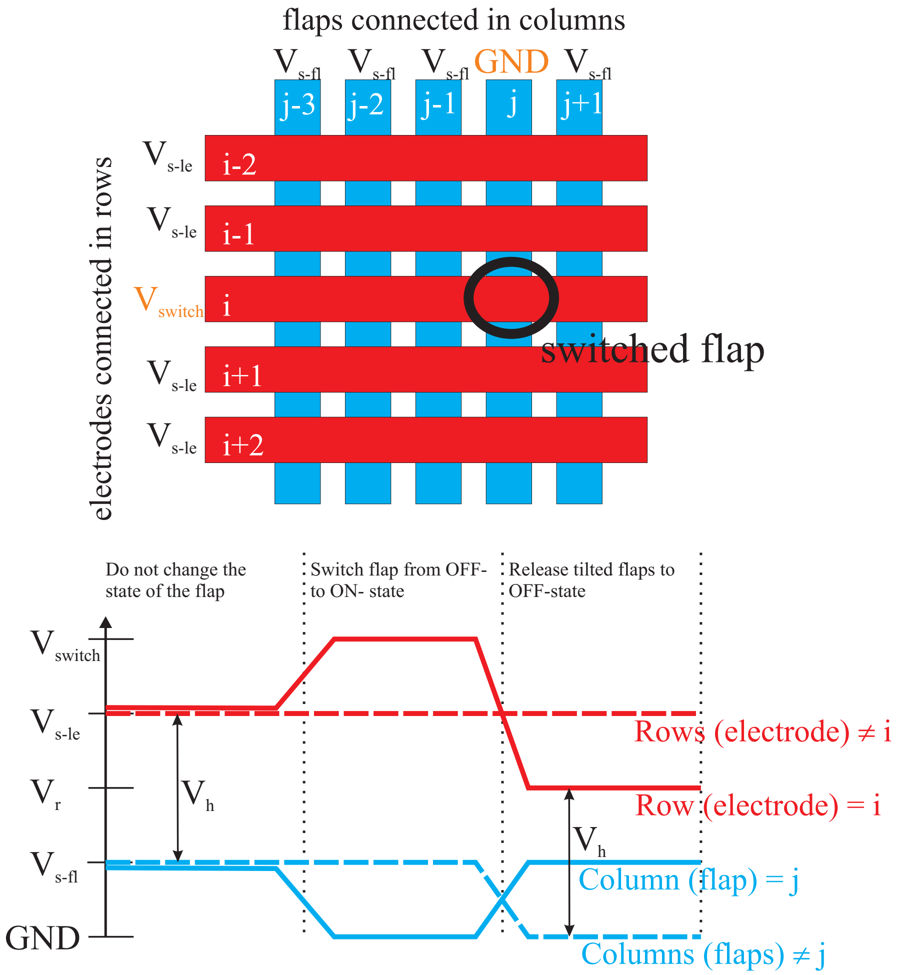

Figure 3.6: *Actuation using one electrode per flap. The flap at position (i, j) has to be actuated. The other flaps keep their state (bent or flat). The voltage required to hold a flap at bent state* V_h *is lower than the voltage required to pull a flap to vertical state* V_{pd} *due to hysteresis. A flap is released when the potential difference between flap and electrode is lower than* V_h*.*

a thin film transistor (TFT) connected to it. Each transistor can be addressed to set the voltage at its respective pixel. The transistors are connected in the lines and in the columns such that line-column addressing can be employed. We have here M+N connection lines which are required.

- Passive-matrix: Here the pixels are connected along the columns and their corresponding electrode along the rows. By setting a voltage difference on the column N and the row M the pixel at the location (M, N) can be addressed. M+N connection lines are required.

Because of its simplicity (only M+N connection lines and no transistors required) the passive matrix addressing scheme will be investigated in more details.

Passive-matrix addressing Depending on the geometrical configuration of flap and electrode the voltage required to keep the flap at tilted ON-position can be lower than the voltage required to switch the flap from OFF- to ON-state. In this case we have a hysteresis in actuation, which is due to the fact that the electrical force increases with the distance by square. Thus, the voltage exerting the force to keep the flap close to the electrode is smaller than the one required for switching. If this condition is fulfilled we can use line column-addressing in an array. This way each single flap in an N by M array is addressed with N+M connections.

A schematic of an array with line-column addressing is shown in figure 3.6. All flaps are connected here along the columns and the electrodes along the rows. Four different voltage levels are used for actuation:

- GND, ground voltage
- V_{s-fl} , standby voltage of the flaps
- V_r , release voltage
- V_{s-le} , standby voltage of the electrodes
- V_{switch}, voltage required to switch from OFF- to ON-state

The voltage levels relate to each other in the following manner: $GND < V_{s-fl} < V_r < V_{s-le} < V_{switch}$.

The potential difference between the standby voltages of flaps and electrodes V_{s-fl} and V_{s-le} corresponds to the hold voltage V_h, the voltage required to keep the flap at the vertical position.

3.2 Electromechanical modelling

We will now create a model for a flap suspended by a torsion beam which is electrostatically titled. An analytical model will give us the scaling laws for different geometrical dimensions. With finite element simulations a reduced order model will be build for analysing in more detail the behaviour of the system. The frequency response of the system will be treated as well.

3.2.1 Analytical model

In figure 3.5 a schematic is shown of the electromechanical system comprised of a flap suspended by a torsion beam clamped at both ends and an electrode. The geometrical dimensions of the system are shown for a flap at a tilt angle θ of width w_{flap} and height h_{flap}. The torsion beam consists of two sub-beams of length l_{beam}, width w_{beam} and thickness t_{beam}. The flap and beam are connected together by a rigid link of length q at point P. A voltage V_{flap} is applied onto the flap and V_{el} onto the electrode.

The electromechanical system can be treated as two linked sub-systems: A mechanical subsystem of the torsion beam and an electrostatic subsystem of the flap and electrode. The schematic of the two subsystems which are both linked at point P is shown in figure 3.7.

3.2.1.1 Torsion beam subsystem

The mechanical subsystem consists of a both side clamped beam at which the following torque T_M and force F_M in x-direction apply on point P:

$$T_M(\theta) = k_\theta \cdot \theta \tag{3.1}$$

$$F_M(\theta) = k_x(\theta) \cdot \Delta x \tag{3.2}$$

The torsional spring constant k_θ is expressed in equation (2.7). The bending spring constant in x-direction k_x changes in function of the torsion angle θ of the beam, therefore no analytical expression is given.

3.2.1.2 Electrostatic subsystem

The electrostatic subsystem consists of a flap tilting around point P and an opposing electrode. The electric field in y-direction is neglected, since the extension of the flap in y-direction is larger than in x- and z-direction. The fringing fields at both lateral ends are neglected as well. When taking the normalized capacitance per unit width of the flap as $C^*(\theta)$ the electrostatic torque T_E and force F_E at point P can be expressed for a voltage difference of $V = V_{flap} - V_{el}$

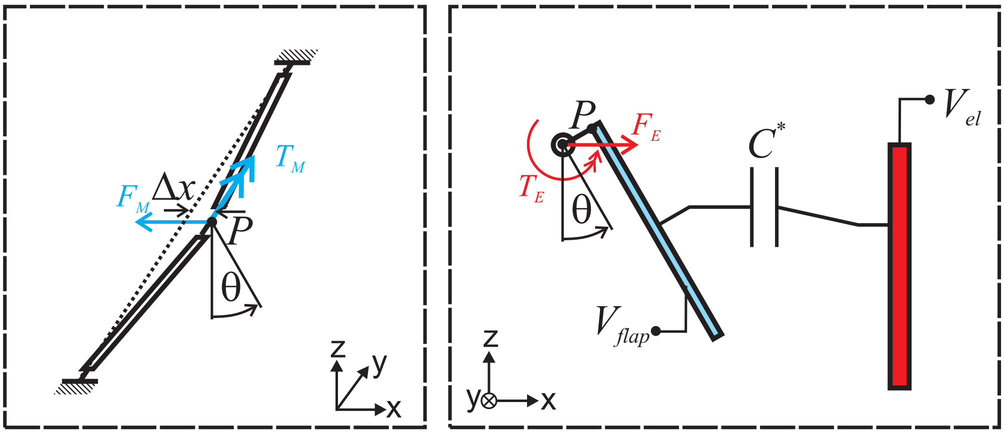

Figure 3.7: *Two subsystems linked at point P: a) 3D-mechanical subsystem consisting of a straight beam clamped at both ends. b) 2D electrostatic subsystem having capacitance C^* between electrode and a flap tilting around point P.*

with equations (2.2) and (2.3):

$$T_E(\theta) = \frac{1}{2}\frac{dC^*}{d\theta}(\theta)\cdot w_{flap}\cdot V^2 \tag{3.3}$$

$$F_E(x) = \frac{1}{2}\frac{dC^*}{dx}\cdot w_{flap}\cdot V^2 \tag{3.4}$$

3.2.1.3 Combination of both subsystems

We can now combine both subsystems, knowing that the torques and forces of both subsystems equate at point P. The following equation system can be written, which is valid for any θ and Δx:

$$T_E(\theta,\Delta x) = T_M(\theta,\Delta x) \tag{3.5}$$

$$F_E(\theta,\Delta x) = F_M(\theta,\Delta x) \tag{3.6}$$

For a simplified analytical formula describing the tilt of the flap in function of the actuation voltage only the torques T_E and T_M will be taken into account and the forces F_E and F_M will be neglected. The displacement Δx is disregarded as well. Equations (3.3) and (3.1) can be inserted into (3.5):

$$\frac{1}{2}\frac{dC^*}{d\theta}(\theta)\cdot w_{flap}\cdot V^2 = k_\theta\cdot\theta \tag{3.7}$$

When now solving the above equation for the actuation voltage V we obtain:

$$V = \sqrt{\frac{2 \cdot k_\theta \cdot \theta}{\frac{dC^*}{d\theta}(\theta) \cdot w_{flap}}} \tag{3.8}$$

Inserting the expression of the spring constant of a torsion beam stated in equation (2.7) gives:

$$V(\theta) = \sqrt{\frac{4 \cdot t_{beam}^3 \cdot w_{beam} \cdot G \cdot \theta}{3\frac{dC^*}{d\theta}(\theta) \cdot w_{flap} \cdot l_{beam}}} \tag{3.9}$$

In the rest state the capacitance per unit flap width C^* can be approximated as parallel plate capacitance with a distance d between the plates. When the flap tilts the capacitance changes with a factor $e(\theta)$. We have the following capacitance per unit flap width C^* and its corresponding differential:

$$C^*(\theta) = \epsilon_r \epsilon_0 \frac{h_{flap}}{d} e(\theta) \tag{3.10}$$

$$\frac{dC^*}{d\theta} = \epsilon_r \epsilon_0 \frac{h_{flap}}{d} \frac{de(\theta)}{d\theta} \tag{3.11}$$

The expression for the actuation voltage (3.9) can be rewritten with (3.11).

$$V(\theta) = \sqrt{\frac{4 \cdot d \cdot t_{beam}^3 \cdot w_{beam} \cdot G \cdot \theta}{3 \cdot \epsilon_r \epsilon_0 \cdot h_{flap} \cdot \frac{de(\theta)}{d\theta}(\theta) \cdot w_{flap} \cdot l_{beam}}} \tag{3.12}$$

Regarding the above equation it can be seen what geometrical dimensions lead to which scaling of the actuation voltage. For lowering the actuation voltage the largest effect is obtained by employing an as thin torsion beam as possible. A large influence is also exhibited by the width of the flaps since $l_{beam} \propto w_{flap}$. Since the flap height h_{flap} is proportional to the electrode flap distance d, the actuation voltage is invariant to the height of the flap. The actuation voltage is nevertheless depended on the ratio of $r = \frac{d}{h_{flap}}$. An overview of the scaling of the actuation voltage for different dimensions is given in table 3.1.

To obtain the exact voltage to tilt angle trajectory the term $\frac{de(\theta)}{d\theta}$ of (3.12) requires to be further analysed. For this purpose we will directly evaluate the differential of the capacitance as given in (3.3) and (3.4). As first step we have thus to evaluate the capacitance at different tilt angles. This corresponds to calculating the capacitance of a tilted plate to a second plane plate. The analytical solution of such a problem can be approximated for small θ with the equation of a

Table 3.1: *Scaling s of the actuation voltage when changing different geometrical dimensions as obtained from equation 3.12*

Dimension	Description	Scaling factor of V	Comments
w_{flap}	width of flap	$s^{-\frac{1}{2}}$	$\frac{1}{s}$ for $2l_{beam} \approx w_{flap}$
h_{flap}	height of flap	invariant	since $h_{flap} \approx d$
t_{flap}	thickness of flap	invariant	for $t_{flap} << h_{flap}$
w_{beam}	width of beam	$s^{\frac{1}{2}}$	
l_{beam}	length of half beam	$s^{-\frac{1}{2}}$	$\frac{1}{s}$ for $2l_{beam} \approx w_{flap}$
t_{beam}	thickness of beam	$s^{\frac{3}{2}}$	
G	Shear modulus of beam material	$s^{\frac{1}{2}}$	
d	electrode flap distance	$s^{\frac{1}{2}}$	
r	$\frac{d}{h_{flap}}$	$s^{\frac{1}{2}}$	

parallel plate capacitor. At larger tilt angles the problem gets more complex. The electrostatic field acts not only on the front-side of the flap but exerts also a force on the backside. A method of analytical calculation of the electrostatic field at an arbitrary configuration is conformal mapping. Since this method leads to solving numerical integrals of large complexity, we will prefer to calculate the capacitance by finite element simulations. We will do these calculations in the following section.

3.2.2 Reduced order simulations

As shown in section 3.2.1 the voltage to tilt angle relationship can be expressed with equation (3.12). In this expression $\frac{dC^*}{d\theta}$ is the only term which is not calculated analytically. But, in addition in this analytical model were only taken into account the torques. As shown in figure 3.5 there is not only a torque, but also a force towards the electrode exerting onto the flap. The torque leads to a tilting of the flap and the force to a displacement towards the electrode. The electrostatic force in x-direction will now be included in the model. Equations (3.5) and (3.6) are the governing formulas of the system. Inserting the corresponding forces and torques of (3.3) and (3.4) the following expressions have to be satisfied for obtaining the trajectory in θ and Δx.

$$\frac{1}{2}\frac{dC^*}{d\theta}(\theta,\Delta x)\cdot w_{flap}\cdot V_T^2 = T_{M,FEM}(\theta,\Delta x) \tag{3.13}$$

$$\frac{1}{2}\frac{dC^*}{dx}(\theta,\Delta x)\cdot w_{flap}\cdot V_F^2 = F_{M,FEM}(\theta,\Delta x) \tag{3.14}$$

Equations (3.13) and (3.14) can be solved for the actuation voltage V_T and V_F.

$$V_T(\theta, \Delta x) = \sqrt{\frac{2 \cdot T_{M,FEM}(\theta, \Delta x)}{\frac{dC^*}{d\theta}(\theta, \Delta x) \cdot w_{flap}}} \tag{3.15}$$

$$V_F(\theta, \Delta x) = \sqrt{\frac{2 \cdot F_{M,FEM}(\theta, \Delta x)}{\frac{dC^*}{dx}(\theta, \Delta x) \cdot w_{flap}}} \tag{3.16}$$

The trajectory of the flap $t(\theta, \Delta x)$ can obtained by calculating the points where the following expression is valid:

$$V_M(\theta, \Delta x) = V_F(\theta, \Delta x) \tag{3.17}$$

The following procedure will be used to calculate the trajectory of the flap for different geometries:

- Simulate capacitance C^* in two dimensional finite element model using Ansys 12.0 PLANE121 elements. The capacitance is calculated for different tilt angles θ, electrode-flap distances d and geometrical configurations.
- Simulate the mechanical torque $T_{M,FEM}$ and force $F_{M,FEM}$ of the torsion beam being tilted by θ and displaced by Δx.
- Insert the simulated values of C^*, $T_{M,FEM}$ and $F_{M,FEM}$ into equations 3.15 and 3.16. $C^*(\Delta x)$ is obtained from the simulated $C^*(d)$.
- Solve equation 3.17 for finding the trajectory $t(\theta, \Delta x, V)$.

The four points listed above are described in the subsequent sections in more detail.

3.2.2.1 Simulation of electrostatic capacitance

The capacitance is simulated using Ansys 12.0. The system is modelled in 2D. The obtained results correspond to a capacitance per unit flap width C^*. The model consists of a moving flap part $e1$ and a static electrode part $e2$. PLANE121 2D electrostatic elements are used and the capacitance between the conductor boundaries $e1$ and $e2$ is obtained by the COSOLVE command. The simulation area is limited to a surrounding border at a distance of at least 100 μm of the conductor elements. The simulation is performed for different tilt angles θ around P and distances d. Various configuration of flap and electrodes were modelled. Schematics of the simulation models for different flap-electrode geometries are shown in figure 3.8 and 3.9.

Table 3.2: *Geometrical parameters used for electrostatic simulations in Ansys with PLANE121 elements. The corresponding schematic of the models is shown in figure 3.8 and 3.9.*

Dimension	Model 1	Model 2	Model 3	Model 4
h_{flap}	$50\mu m$	$50\mu m$	$50\mu m$	$50\mu m$
h_{el}	$50\mu m$	$50\mu m$	$50\mu m$	$50\mu m$
t_{flap}	$1\mu m$	$1\mu m$	$1\mu m$	$1\mu m$
t_{el}	$10\mu m$	$10\mu m$	$10\mu m$	$10\mu m$
q	$15\mu m$	-	$15\mu m$	-
a	-	-	$34\mu m$	$16\mu m$
u	-	-	$10\mu m$	-
h_{el2}	-	-	$150\mu m$	-

Table 3.3: *Material properties and geometrical dimensions used in the reduced order simulations, whose results are given in figure 3.8 and 3.9. Poly-silicon is taken as beam material [65].*

Dimension	Description	Value used for calculations
0 w_{flap}	width of flap	$250\mu m$
h_{flap}	height of flap	$50\mu m$
t_{flap}	thickness of flap	$1\mu m$
w_{beam}	width of beam	$3.5\mu m$
l_{beam}	length of half beam	$140\mu m$
t_{beam}	thickness of beam	$150nm$
E_{beam}	Young modulus of beam material	160GPa
μ_{beam}	Poisson's ratio of beam material	0.22

In model 1 a flap is simulated which is fixed at an offset q from the tilting point P closer to the electrode. The electrode is placed for $\theta = 0°$ parallel to the flap at a distance d. Model 2 is similar to model 1 with the difference that the flap is directly fixed to P (q is here 0). Model 3 and 4 are of higher complexity taking into account other conductors in the system which can have an influence on the flap trajectory. Model 3 is based on model 1 with a back-boundary at the same potential as the flap and conductor walls below representing the conductive substrate on which the device is build on. This configuration is evaluated since it is very close to the configuration of a vertical flap device presented in section 5.4.2. Model 4 is based on model 2 with a second electrode added opposite at a distance $d + a$, this way can be evaluated a butterfly-flap as shown further down in section 5.4.3. The employed geometrical dimensions for the different models are given in table 3.2.

3.2.2.2 Simulation of torsion beam

For the torsion beam suspending the flap, the mechanical restoring torque $T_{M,FEM}$ and electrostatic restoring force $F_{M,FEM}$ are modelled for different tilt angles θ and beam displacements Δx. The beam is modelled as BEAM4 elements in Ansys 12.0. It consists of two sub-beams connected together at point P and fixed each at one end. The displacement and angle is applied to the centre point P and at this same point the restoring torque and force are read-out. A schematic of the model is shown in figure 3.7 and the employed geometrical dimensions and material properties are given in table 3.3.

3.2.2.3 Calculation of trajectory

Matlab numeric calculation software is used to combine the results of the electrostatic and structural simulations. For a predefined initial electrode-beam distance d it first calculates $C^*(\Delta x)$ from the simulated $C^*(d)$ as $C^*(\Delta x) = C^*(d - \Delta x)$. The simulation results C^*, $T_{M,FEM}$ and$F_{M,FEM}$ are inserted into equations (3.15) and (3.16). A flap width w_{flap} as given in table 3.3 is employed. Equation (3.17) is solved next using the *contours* function to obtain the trajectory as $t(\theta, \Delta x, V)$.

3.2.2.4 Results of simulation

The simulated trajectories of the flap as tilt angle θ and displacement towards the electrode Δx in function of the applied voltage V are plotted in figure 3.8 to 3.9. The calculations were done for four different electrostatic models whose schematic is shown next to the results. The particular geometrical dimensions and material parameters indicated in table 3.2 and 3.3 were used. By employing equation 3.12 we can scale the results, as given in table 3.1.

The following observations can be deduced from the voltage to tilt angle curves obtained:

- The required actuation voltage to reach a certain tilt angle θ increases with larger electrode-beam distance d.
- At high actuation voltage the flaps tend to a maximal achievable tilt angle. With increasing d this maximal angle decreases.
- For small d, specially for $d = 55\mu m$ in the model 1, 3 and 4 , it can be found a hysteresis in the curve. The voltage required to attain an angle θ decreases after a certain point. The trajectory curve gives the points at which the electrostatic and mechanical torques equate. This means the flap does not follow the decreasing curve, but as the voltage is further increased there is a pull-in to a larger tilt angle. When decreasing again the voltage after a pull-in, the flap remains at the large tilt angle at a lower actuation voltage than the one required for pull-in.
- The required actuation voltages for reaching a certain tilt angle are the lowest for model 1, since here the flap is at the smallest distance of the electrode compared to the other models.

The following observations can be deduced from the voltage to displacement towards the electrode Δx curve:

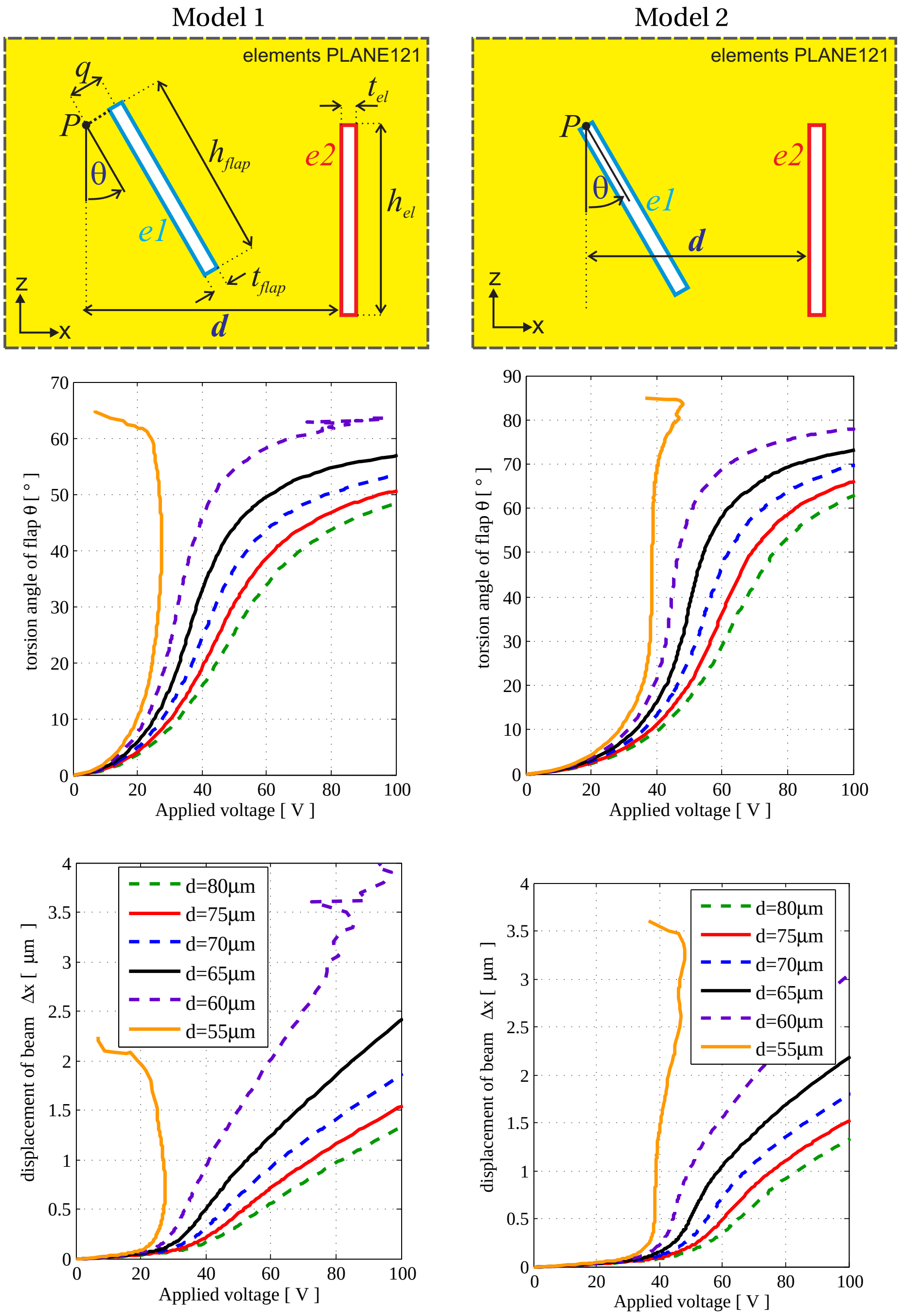

Figure 3.8: *Results of reduced order simulation. On top is shown the employed Ansys models for obtaining the capacitance* $C^*(\theta)$. *Below is plotted the corresponding flap trajectory of tilt angle* θ *and displacement* Δx *in function of the actuation voltage. At small beam-electrode distance* d *the required actuation voltage for reaching large* θ *is lower. When* d *is increased the maximal reachable* θ *is smaller. For* $d = 55\mu m$ *a hysteresis effect can be found in both models. In model 1 the flap will be displaced by* Δx *such to touch the electrode at* $d = 55\mu m$.

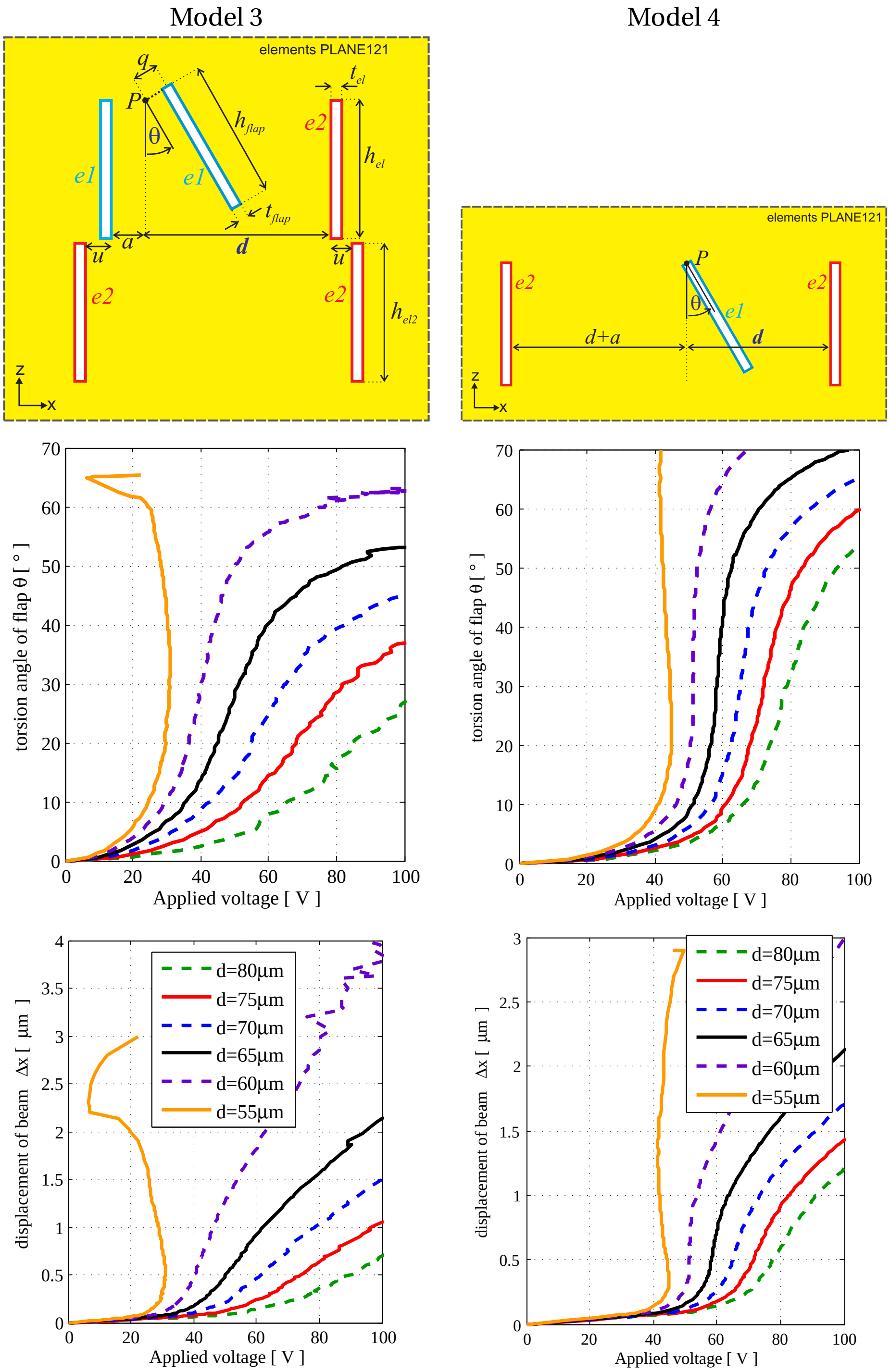

Figure 3.9: *Results of reduced order simulation. More complex electrostatic models were employed here. The back substrate and back electrode were taken into account. The influence of the additional electrodes leads to different trajectories and higher actuation voltages.*

- The displacement towards the electrode Δx decreases with larger d.

- For small d, specially for $d = 55\mu m$ in model 1 and 3, there is a hysteresis in the curve which leads at a certain voltage to a pull-in towards the electrode. The flap may be contacting the electrode. Therefore, a d of $55\mu m$ or smaller should be avoided in the final design.

- Typical displacement values are below $3\mu m$, except for d around $55\mu m$ or smaller.

3.2.3 Resonance

As given in the requirements stated in section 3.1.1.1, the resonance frequencies should lay at as high values as possible. There are two main reasons: First, the device should have an as fast switching time as possible. A higher first resonance mode can be interpreted as high velocity of the device. Second, the device should be as much as possible invariant to environmental vibrations which generally lay below 1kHz.

We will analyse separately the resonance at rest- and at actuated-state.

3.2.3.1 Resonance at rest state

For calculating the resonance frequency we model the system as rigid flap of mass m suspended by a torsion beam. The model is the same as used for analytical calculations depicted in figure 3.5. The different possible modes are given in figure 3.10, as obtained by COMSOL 4.2 finite-element simulations. We have a mode with a bending of the beam in z-direction, a mode at which the beam twists in around the x-axis and a torsional mode where the flap tilts around the beam (around the y-axis).

For a second order system the resonance frequency of the first mode can be expressed as square-root of the spring constant divided by the mass or moment of inertia.

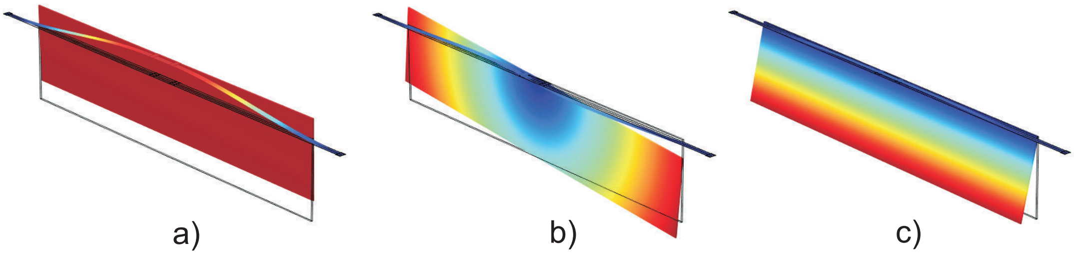

Figure 3.10: *Possible resonance modes as obtained by COMSOL finite element simulation of a flap suspended by torsion beam with the dimension given in table 3.3. Red areas make a large displacement and blue areas no displacement. a) is a bending mode, b) a twisting mode and c) a tilting mode.*

Table 3.4: *Calculation of resonance frequencies of different modes using analytical formulas of section 3.2.3.1 and COMSOL finite-element simulations with geometrical dimensions given in table 3.3. A material density of* $\rho = 2300 kg/m^3$ *is used for poly-silicon.*

Mode	Description	Analytical calculation	FEM-simulation
f_θ	torsional mode	1.94 kHz	1.95 kHz
f_z	bending mode	1.10 kHz	1.08 kHz
f_γ	twist mode	1.14 kHz	1.26 kHz

The resonance frequency of the torsional mode f_θ can be written for the torsional spring constant k_θ given in (2.7) and torsional moment of inertia I_θ expressed in (2.12):

$$f_\theta = \frac{1}{2\pi}\sqrt{\frac{k_\theta}{I_\theta}} = \frac{1}{2\pi}\sqrt{\frac{2 \cdot G \cdot w_{beam} \cdot t_{beam}^3}{l_{beam} \cdot h_{flap}^3 \cdot t_{flap} \cdot w_{flap} \cdot \rho}} \tag{3.18}$$

The resonance frequency of the bending mode f_z can be written for the torsional spring constant k_z expressed in (2.9) and mass m calculated in (2.14).

$$f_z = \frac{1}{2\pi}\sqrt{\frac{k_z}{m}} = \frac{1}{2\pi}\sqrt{\frac{2 \cdot E \cdot t_{beam}^3 \cdot w_{beam}^3}{l_{beam}^3 \cdot h_{flap} \cdot t_{flap} \cdot w_{flap} \cdot \rho}} \tag{3.19}$$

The resonance frequency of the twist mode f_γ can be written for the twist spring constant k_γ of (2.10) and moment of inertia in twist direction I_γ expressed in (2.16):

$$f_\gamma = \frac{1}{2\pi}\sqrt{\frac{k_\gamma}{I_\gamma}} = \frac{1}{2\pi}\sqrt{\frac{2 \cdot E \cdot t_{beam}^3 \cdot w_{beam}}{l_{beam} \cdot h_{flap} \cdot t_{flap} \cdot w_{flap} \cdot (h_{flap}^2 + w_{flap}^2/4)}} \tag{3.20}$$

The resonance frequency of the three modes are calculated for the dimensions given in table 3.3 and listed together with the results of COMSOL finite-element simulations in table 3.4.

3.2.3.2 Resonance at actuated state

When actuating the flap the electrostatic force or torque changes in function of the tilt angle. The system has thus an additional electrostatic spring constant. Also k_z and k_γ change in function of θ. Due to all these components the resonance frequency changes in function of the actuation voltage and tilt angle.

We will now evaluate the change in resonance frequency due to electrostatic stiffening. A similar approach will be taken as reported in [66]. We describe the system with Newton's second law of motion for a torsional movement where the sum of all torques is equal to the angular acceleration times the torsional moment of inertia I_θ.

$$I_\theta \frac{d^2\theta}{d^2 t}(\theta, V) = T_E(\theta, V) - T_M(\theta) \tag{3.21}$$

Equation is dependent on the tilt angle θ and the actuation voltage V, with T_E and T_M given in (3.3) and (3.1).

In the case of a vibrational movement when the flap is actuated with a voltage V_0 to a tilt angle θ_0 the voltage and tilt angle of (3.21) can be expressed as $V = V_0 + v_{ac}$ and $\theta = \theta_0 + \theta_{ac}$ with v_{ac} and θ_{ac} being the oscillating components.

We take now the first order Taylor approximation of T_{el} around V_0 and θ_0, modifying equation (3.3) with $C = C^* \cdot w_{flap}$:

$$T_{el}(V_0,\theta_0, v_{ac},\theta_{ac}) \approx T_{el}(V_0,\theta_0) + \frac{\partial T_{el}}{\partial V}(V_0,\theta_0) \cdot v_{ac} + \frac{\partial T_{el}}{\partial \theta} \cdot \theta_{ac} \tag{3.22}$$

$$T_{el}(V_0,\theta_0) \approx \frac{1}{2}\frac{dC}{d\theta}(\theta_0) \cdot V_0^2 + \frac{dC}{d\theta}(\theta_0) \cdot V_0 \cdot v_{ac} + \frac{1}{2}\frac{d^2C}{d^2\theta}(\theta_0) \cdot V_0^2\theta_{ac} \tag{3.23}$$

When inserting now the above result in (3.21) we obtain:

$$\frac{1}{2}\frac{dC}{d\theta}(\theta_0)\cdot V_0^2 + \frac{dC}{d\theta}(\theta_0)\cdot V_0 \cdot v_{ac} + \frac{1}{2}\frac{d^2C}{d^2\theta}(\theta_0)\cdot V_0^2 \cdot \theta_{ac} - k_\theta \cdot (\theta_0 + \theta_{ac}) = I_\theta \cdot \frac{d[\theta_0 + \theta_{ac}]}{d^2 t} \tag{3.24}$$

The above expression can be simplified by taking into account that the sum of the DC-terms is zero as expressed in equation (3.5).

$$I_\theta \frac{d\theta_{ac}^2}{dt^2} + [k_\theta \cdot - \frac{1}{2}\frac{d^2C}{d^2\theta}(\theta_0) \cdot V_0^2] \cdot \theta_{ac} = \frac{dC}{d\theta}(\theta_0) \cdot V_0 \cdot v_{ac} \tag{3.25}$$

We have here a second order system for which the resonance frequency can be written as:

$$f_{res} = \frac{1}{2\pi}\sqrt{\frac{k_\theta + k_{el}}{I_\theta}} \tag{3.26}$$

with the electrostatic stiffening k_{el} given as:

$$k_{el} = \frac{1}{2}\frac{d^2C}{d^2\theta}(\theta_0) \cdot V_0^2 \tag{3.27}$$

Table 3.5: *Calculation of power consumption of a modulator array consisting of tilting flaps. Only the power required for switching of the flaps is taken into account. The calculations are based on the simulation model 1 of section 3.2.2.*

number of flaps per area (100dpi resolution, 4 flaps per pixel)	N_{flaps}	6400 flaps/cm^2
energy required for switching flap OFF-ON ($\theta_{ON} = 60°$)	E_{switch}	100pJ
electrode-flap distance	d	65μm
switching frequency	f_{switch}	100Hz
power consumption	$P_{el.static}$	**64**$\mu W/cm^2$

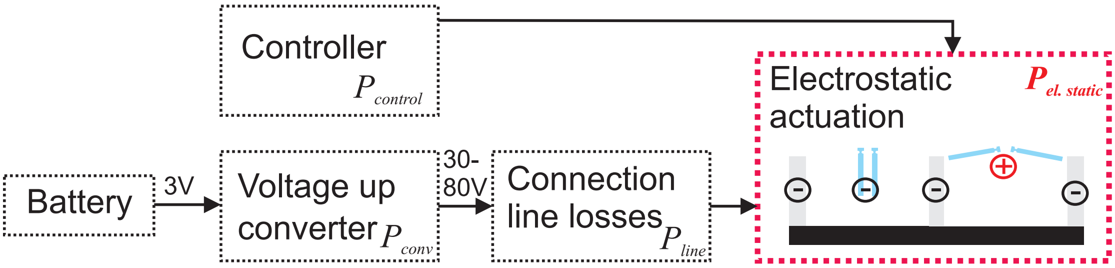

Figure 3.11: *Entities dissipating power in the system of a modulator array. The battery voltage has to be converted up using the power P_{conv}, there are losses in the connection lines (P_{lines}) and also a controller uses power ($P_{controll}$). The actuation of the modulators itself dissipates a power $P_{el.static}$*

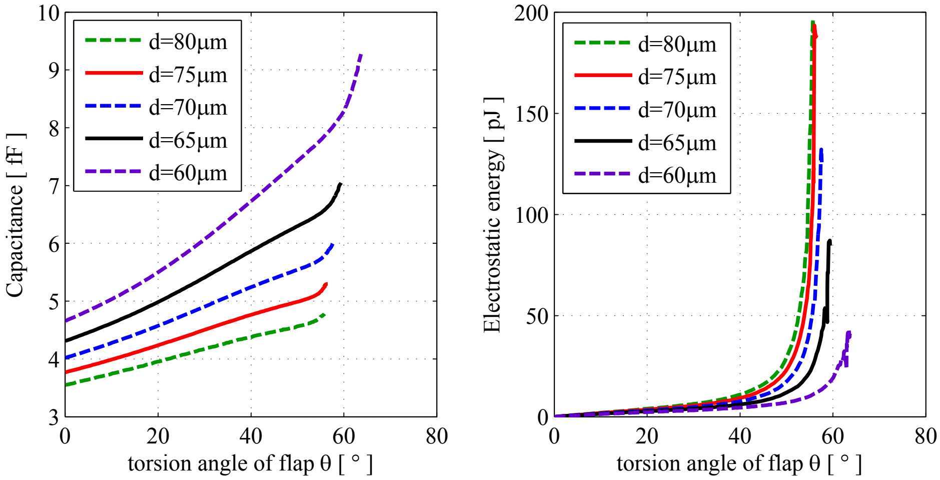

Figure 3.12: *The electrostatic energy required to switch a flap to a tilt angle of θ is shown. The calculations were done using the capacitance and actuation voltage values as obtained in the simulation model 1 of section 3.2.2 (figure 3.8). The model consists of one flap of 50x250μm^2 with a counter electrode.*

3.2.4 Power consumption

We analyse now the power consumption of the tilting flaps optical modulators. The different power dissipating entities of a whole system comprising a modulator array, controller and interconnection lines are shown in figure 3.11. If the system is battery driven, the voltage requires to be up-converted, since 30-80V are required for actuation of the flaps and a battery usually only delivers around 3V. We have also losses in the connection lines and energy dissipated by the controller. We will only consider the power consumption of the electrostatic actuators themselves. Each entity consisting of a tilting flap with electrode requires an electrostatic energy E_{switch} when it is actuated from OFF- to ON-position as defined in equation (2.1)

$$E_{switch} = \frac{1}{2} C \cdot V^2 \tag{3.28}$$

C denotes here the capacitance between the electrode and flap. It changes depending on the tilt angle of the flap as shown in figure 3.12 (left) and is in the range of 3 to 10fF. The capacitance values were calculated in the simulations model 1 (section 3.2.2) consisting of a single flap of 50x250μm^2 with a counter electrode. Inserting in equation (3.28) the voltage V required for reaching every tilt angle θ, as obtained in the same simulation model, E_{switch} can be computed for all θ. The results of the calculations are plotted in figure 3.12. We obtain values in the range of E_{switch} =100pJ per switching to maximal tilt angle of one flap.

The power consumption is calculated from the energy per switching-cycle of one flap by multiplying with the switching frequency f_{switch} and the number of flaps in a modulator array N_{flap}:

$$P_{el.static} = E_{switch} \cdot f_{switch} \cdot N_{flaps} \tag{3.29}$$

With equation (3.29) the power consumption of the switching of the flaps is estimated for the values shown in table 3.5. A modulator array requires about $64\mu W/cm^2$ for switching all flaps ON and OFF at a frequency of 100Hz. As stated above, the connection line losses are not taken into account. Since the parasitic capacitance of a connection line may be much higher than the capacitance between flap and electrode, the power dissipated on the connection lines may also have larger values. Therefore, for obtaining a low-power device it is important to minimize the parasitic capacitance of the connection lines.

3.3 Design of tilting flaps using electromechanical model

An analytical model and reduced order simulations have been presented in this chapter. We will now combine the results of the models with the requirements for a reflective display and transmissive shutters as stated in section 3.1.1.1. With this approach the systems dimensions will be designed. Let's first summarize the most important requirements:

- Low actuation voltage V.
- The maximal obtainable tilt angle θ should be as large as possible.
- The flap should not touch the electrode when actuated.
- Highest resonance frequencies possible.
- The fill-factor of the active optically modulating area has to be maximized.
- Maximize the pixel size.

The main equation used for designing a tilting flap system is 3.12. We will rewrite it again:

$$V(\theta) = \sqrt{\frac{4 \cdot d \cdot t_{beam}^3 \cdot w_{beam} \cdot G \cdot \theta}{3 \cdot \epsilon_r \epsilon_0 \cdot h_{flap} \cdot \frac{de(\theta)}{d\theta}(\theta) \cdot w_{flap} \cdot l_{beam}}} \tag{3.30}$$

Using the above equation and the trajectory in function of tilt angle θ, displacement Δx and actuation voltage V as obtained from reduced order simulations in section 3.2.2 we can give design rules for each parameter.

- w_{flap}: V scales with a factor $s^{-\frac{1}{2}}$ in dependence of the flap width. When taking into account that the beam length l_{beam} is proportional to w_{flap}, the scaling of V is even at a factor $\frac{1}{s}$. But, w_{flap} should not be too large since it defines the pixel size. We choose a value of $250\mu m$ giving a still reasonable pixel resolution of 100dpi.
- h_{flap}: The actuation voltage is invariant to scaling of the flap height, as long as d is scaled accordingly. The larger h_{flap} is the higher will be the fill-factor, at the same time the resonance frequencies will decrease. We will choose the length of h_{flap} depending on the fabrication technology employed.
- t_{flap}: The flap thickness has only an influence on the resonance frequency. The thicker it is the lower will be f. We will choose the thickness accordingly with the fabrication technology employed.
- l_{beam}: The voltage scales with $s^{-\frac{1}{2}}$ in dependence of the beam length. But the length of l_{beam} is also proportional to w_{flap}. It will therefore be chosen accordingly with the length of w_{flap} and the fabrication technology employed.

- w_{beam}: The voltage scales with $s^{\frac{1}{2}}$ in dependence of the beam width. We will choose the width according to the smallest dimension which can be achieved practicably by lithography of about $3.5\mu m$.
- t_{beam}: V scales with $s^{\frac{3}{2}}$ in dependence of the beam thickness. So t_{beam} is the parameter having the largest influence on the actuation voltage. We will choose the thickness of t_{beam} depending on the fabrication technology employed.
- $E_{modulus}$: The more compliant the material employed is the lower is the actuation voltage.
- d: As obtained from the simulations for $h_{flap} = 50\mu m$, d requires to be larger than $55\mu m$ since otherwise we risk that the flap touches the electrode.

In the next chapters two different concepts of tilting flaps will be presented. They both rely on different fabrication technologies and thus require different dimensions of the above parameters.

The first concept is based on flaps which are horizontal at rest state and tilted to vertical position when actuated. It will be presented in chapter 4.

The second concept uses flaps which are in vertical state after fabrication and at rest-position. These can be electrostatically actuated to horizontal position. This concept will be presented in chapter 5.

4 Design study with horizontal flaps

In the beginning of the project a first design study was performed for fabrication of optical modulators exhibiting a high visual contrast. The system should work with flaps having large angular rotation, which are actuated at low power. The main application is a reflective display having contrast and brightness close to printed paper and much higher than nowadays available liquid crystal based systems.

4.1 Concept

The system consists of flaps which are horizontal at rest state. The flaps are suspended by a torsion beam on top of a substrate. They are fabricated by surface micromachining of poly-silicon with a SiO_2 sacrificial layer. Directly above the flap, at a certain spacing, is placed a transparent electrode. When a voltage is applied between flap and electrode the electrostatic torque tilts the flap to be vertical to the substrate. Due to the rotation of the flap a mechanical opposing-torque is build up which tilts the flap back into horizontal position after setting back the electrode to same potential as the flap. It is important that the flap does not touch any surface when it rotates, since otherwise this can result in sticking.

4.1.1 Working principle as reflective display

As described in section 3.1.1 the main feature to use tilting flaps as a reflective display is to place a light absorbtive layer below the modulators. We choose therefore to fabricated the horizontal flaps on top of a black substrate.

A flap array as reflective display system is depicted in figure 4.1 on the left side. Light is reflected on the areas where the flaps are in horizontal state, giving bright, white pixels. When a flap is tilted into vertical position due to application of a voltage difference to an opposing electrode, incoming irradiation is absorbed on an underlying light absorptive layer, so the pixel is black. When the voltage difference between flap and electrode is set to zero again, the flap turns back into horizontal position due to the restoring torque of the rotated torsion

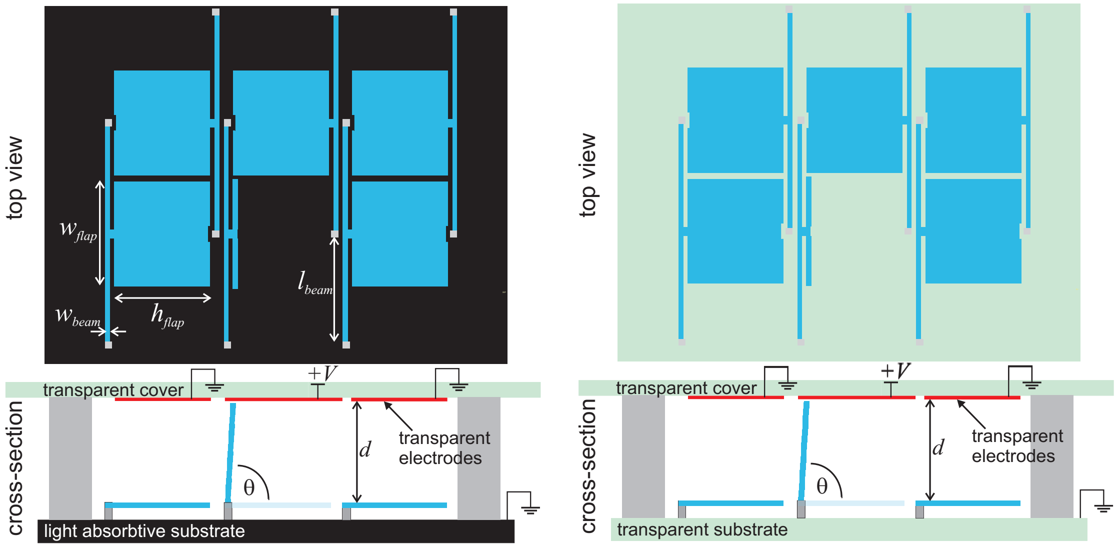

Figure 4.1: *Schematic of array of horizontal flaps suspended by torsion bars. All flaps are grounded. On the transparent electrode above the central flap a voltage V is applied, forcing this flap to tilt into vertical position. On the left side are show a flap array in the configuration as reflective display. The flaps are fabricated on top of a light absorptive substrate. On the right side is shown the flap array as transmissive shutters fabricated on top of a transparent substrate.*

beam and we obtain a white pixel again.

4.1.2 Working principle as transmissive shutter array

The system can also be used as transmissive shutter array with a slightly different arrangement. Here the electrode and also the substrate on which the flaps are placed have to be transparent. Light is blocked from transmission when the flaps are in horizontal rest-state. A schematic of such a system is depicted in figure 4.1 on the right side. At the position of a flap which is tilted into vertical position the light can pass through.

4.2 Design

4.2.1 Arrangement of flaps in an array

It is important to have a maximal fill-factor of the flaps for increasing the overall reflectivity in the case of a reflective display and the total transmissivity in the case of a transmissive shutter array. For this purpose the so called dead areas have to be minimized. These areas consist of the areas of the device which do not modulate the light, such as the torsion beam, the spacing between the flaps and the anchor points. With the flaps suspended by torsion beams the arrangement can look as depicted in figure 4.2. The torsion beam consists of two sub-beams with the length corresponding to the width of a flap.

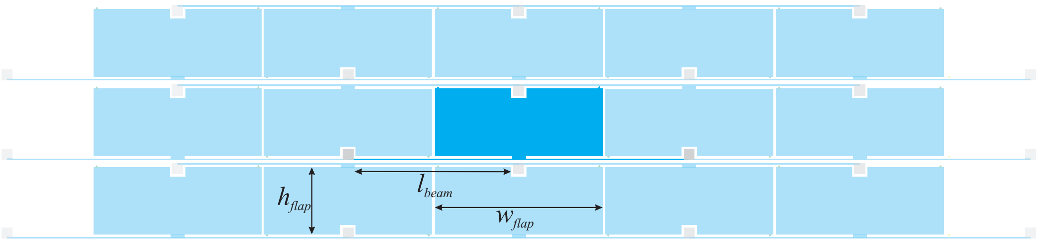

Figure 4.2: *Arrangement of flaps with torsion beams in an array optimizing the fill factor. A single flap is highlighted in darker color.*

Table 4.1: *Dimensions of a flap and torsion beam as used for fabrication. As flap and beam material poly-silicon is used, whose material parameter is given in table 3.3*

Description	Parameter	Value
Flap height	h_{flap}	100 μm
Flap width	w_{flap}	250 μm
Beam length	l_{beam}	235 μm
Beam width	w_{beam}	4 μm
Thickness of poly-Si	$t_{beam} = t_{flap}$	100 nm
Spacer thickness	d	120 μm

4.2.2 Design of geometrical dimensions

In section 3.3 most of the parameters have already been dimensioned. We will set the dimensions depending on the fabrication technology.

- d: The electrode-flaps distance was chosen according of the spacer thickness available. It requires also to be as large as possible for obtaining large fill-factor. We take $d = 120\mu m$.
- h_{flap}: The flap length is defined by the electrode-flap distance d. It has to be a bit shorter for the flap not to touch the electrode. We set h_{flap} to $100\mu m$.
- l_{beam}: The length of the beam is chosen accordingly with the arrangement of the flaps in an array as shown in figure 4.2 as $l_{beam} = 235\mu m$.
- $t_{beam} = t_{flap}$: The flap and beam have the same thickness since they are both patterned in the same poly-silicon layer. The thickness should be as small as possible for obtaining a low actuation voltage. We choose a still practicable thickness of poly-silicon of 100nm.

Table 4.1 summarizes the optimal dimensions for a flap and torsion beam. We obtain analytical values employing equations (3.18) and (3.19) for the resonance frequencies of a bending mode at 1.6kHz and a tilt-mode at 4.7kHz.

4.3 Fabrication Process

Test structures were fabricated for the above presented concept as reflective display. These test structures consist of single flaps placed beside each-other. The high fill-factor configuration as presented in section 4.2.1 was not employed yet. It was also chosen to fabricate only the reflective display concept with silicon as substrate for the flaps with a transparent electrode on top. The reason is the ease of fabrication. Silicon as substrate is a very commonly used material and most microfabrication processes are optimized for it.

The system consists of three components: The flaps on one substrate, the electrodes on another substrate and a spacer in-between.

The absorbing substrate can consist of a silicon wafer, which can be additionally coated or treated to be light absorbing. The transparent substrate can be made of Borofloat, Quartz or any other transparent material. A thin layer of about 100nm Indium-tin-oxide(ITO) is used as transparent electrode material.

For the material of the flaps the requirement is that it is reflective and conductive. We can use poly-silicon, a metal or also a polymer coated with a thin metal film. The thickness of the spacer has to be about 120 μm. It can consist of a bonded silicon-wafer, some thick polymer layer (Polyimide, SU-8) or also of an optical fibre.

In the following chapters the fabrication method for the flaps, electrodes and spacer are shown, as they were used for a first prototype.

4.3.1 Flap chip

Here the process is described for fabricating poly-Si flaps on top of a silicon wafer.

The process is depicted in figure 4.3. It starts with a standard p-doped silicon 100mm diameter wafer of about 500 μm thickness. In a) the wafer is oxidized. An about 2 μm thick layer of silicon dioxide (SiO_2) is grown onto the substrate. Subsequently in b) about 10 μm wide holes are patterned into the oxide by buffered hydrofluoric acid (BHF 1:7) etching. These holes will serve as anchor-points of the flaps. An about 100nm thick poly-Si layer is deposited by low-pressure chemical vapour deposition (LPCVD) in c). The poly-Si is then doped by coating with an additional phosphorous-doped oxide in chemical vapour deposition (CVD). An annealing at 1100$°C$ diffuses the dopant into the poly-Si and should in addition lower its intrinsic stress. The doped oxide is removed in a BHF 1:7 solution. As next step d) the poly-Si is structured by dry-etching to get the shape of the flaps. The wafer is then diced into chips in step e) and finally the flaps are released. For the release, the thermal oxide is etched in hydrofluoric acid (HF) vapour.

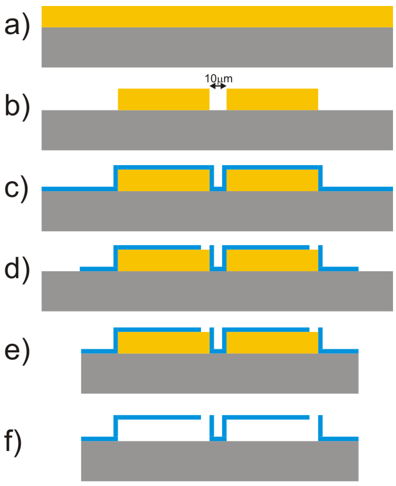

Figure 4.3: *Fabrication process for flap chip on Si substrate. Poly-Si (blue) as flap material is deposited onto patterned* SiO_2 *(yellow) sacrificial layer. Holes in oxide serve as anchors for the flaps. The flaps are released in HF-vapour.*

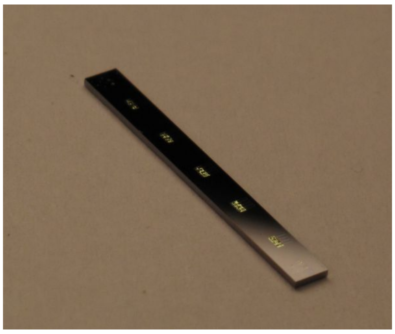

Figure 4.4: *Fabricated flap chip of 2.5mm by 24mm in size. Poly-silicon flaps on silicon substrate. The five flap-arrays look shiny on top of the substrate.*

4.3.2 Electrode chip

The electrodes are fabricated onto a transparent substrate. They require being transparent themselves, therefore a thin layer of 100nm ITO is used. Since ITO has a low conductivity, the interconnection lines and connection pads are made in metal (gold). The fabrication process is depicted in figure 4.5. A 100mm diameter, 500 μm thick Borofloat wafer is used as substrate. 100nm ITO is deposited by sputtering using a lift-off process (a)). The ITO layer is annealed at 200°C to enhance its conductivity and transparency. Next a gold (Au) layer for the interconnects is processed by lift-off in b). As final step c) the wafer is diced into chip size.

4.3.3 Spacer and assembly

Different processes can be used for fabrication of the spacer between the electrode and flap chip. For the prototype, a process using eutectic bonding of a silicon-on-insulator (SOI) wafer

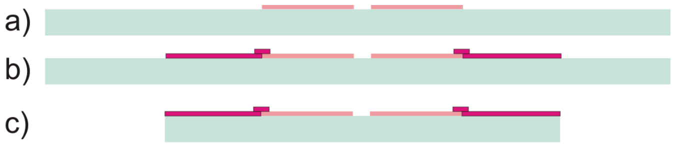

Figure 4.5: Cross-section of fabrication process for electrode chip. ITO electrodes are deposited onto Borofloat substrate (a). Gold is used for the interconnection lines and connection pads (b). The wafer is diced into chips (c).

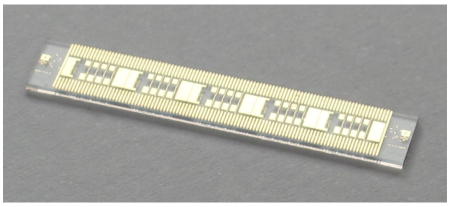

Figure 4.6: Fabricated electrode chip of 5 by 24mm in size. ITO electrodes with gold interconnection lines on Borofloat substrate. Along the side are placed the connection pads. On both ends are located alignment marks for assembly with the flap chip.

onto the flap chip was foreseen. As alternative for assembly of the chips, a standard optical fibre with a diameter of $125\mu m$ was used as spacer.

The two spacer processes directly assemble the flap and electrode chips. The chips have alignment marks at two ends. This way the chips can be optically aligned using a micropositioning system under a microscope.

4.3.3.1 Eutectic bonding of SOI-device layer

A SOI-device layer of 120 μm thickness is bonded onto the flap wafer. Eutectic bonding is used consisting of gold-silicon bonding at the eutectic temperature of $390°C$. After removing the handle layer of the SOI wafer the device layer serves as spacer. The process is shown in figure 4.7:

In a) the flap wafer is coated with a gold layer of about 500nm thickness at the areas where it will bonded to the SOI wafer. The flap wafer as processed in step d) of figure 4.3 is used. The $120\mu m$ thick device layer of a 100mm diameter SOI wafer is structured by deep reactive ion etching (DRIE) to form the spacers in c). On the backside of the SOI wafer about 100 μm wide holes are etched by DRIE. These holes serve for the release process. The device layer of the SOI-wafer is then bonded onto the wafer with the flaps in d). By heating above the eutectic temperature of 390° a silicon-gold alloy forms at the interface. The backside of the flap wafer is etched next in e). By DRIE the wafer is structured to obtain single chips. In f) the two bonded and structured wafers are placed in to a HF-vapour system. The device layer is now released from the handle layer. In the same step the flaps are released as well. As result are obtained single chips with released flaps and a silicon spacer layer of $120\mu m$ thickness (g).

The electrode chip can now be assembled (f) using a silver or UV-glue. The chips have to be optically aligned using a micropositioning system.

Through the silicon pillar spacers we achieve, an electrical connection between flap and electrode chip. This way all the electrical connections of the flaps can be carried to the electrode chip, where all connection pads are placed.

As reported in literature eutectic bonding is hermetic [67]. Using this process hermetic encapsulation of the flaps can be achieved.

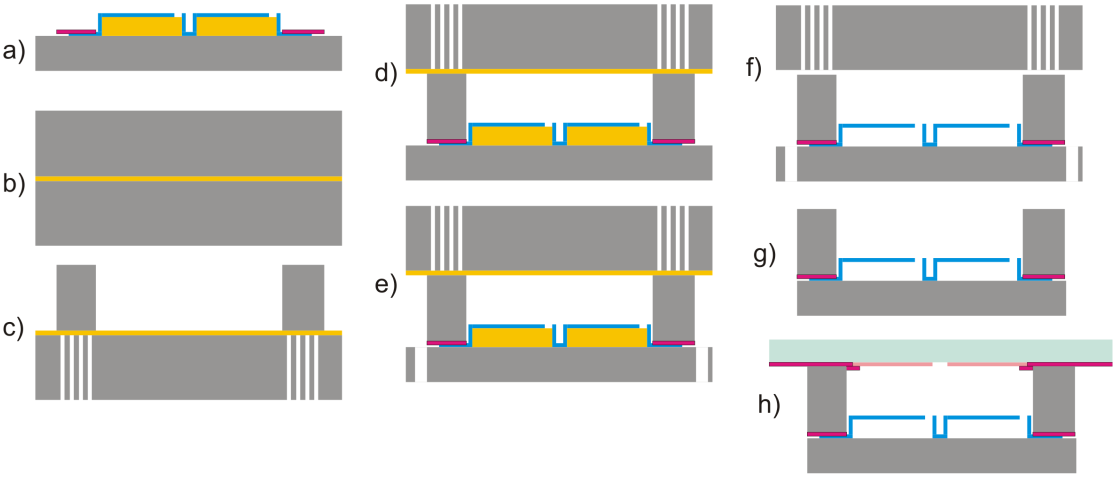

Figure 4.7: *Fabrication process of spacer using eutectic bonding of a silicon-on-insulator (SOI)-wafer to the flap wafer. The 120μm thick patterned device layer serves as spacer. The handle layer is released from the device layer in HF-vapor. The electrode chip is assembled with a UV-glue.*

4.3.3.2 Optical fiber

Single mode optical fibres have a very exact thickness of 125 μm +/- 1 μm and are therefore appropriate as spacer. Since the eutectic bonding process was not available, the first prototype chips were assembled using fibers as spacer. Ultra violet (UV) curing glue Norland Optical adhesive 78 was used for fixing the two chips and the fibers together.

In figure 4.9 the assembled chips and in figure 4.8 a cross-section of the schematic can be seen. For assembly first two fibres are placed at the edges of the flap chip. At the same location, a drop of UV-adhesive is applied. The electrode chip is then positioned onto the flap chip using a vacuum gripper on a micrometer gauge. Alignment marks on the side of the chips serve for accurate (+/- 10 μm) positioning via a binocular microscope. While applying pressure onto the two chips the UV-adhesive is cured using an UV spot source Bluepoint 3 of Dr. Hönle.

When using the optical fibre with UV-adhesive for assembly there is no electrical connection of the flap chip to the connection pads on the electrode chip. Therefore the flap substrate

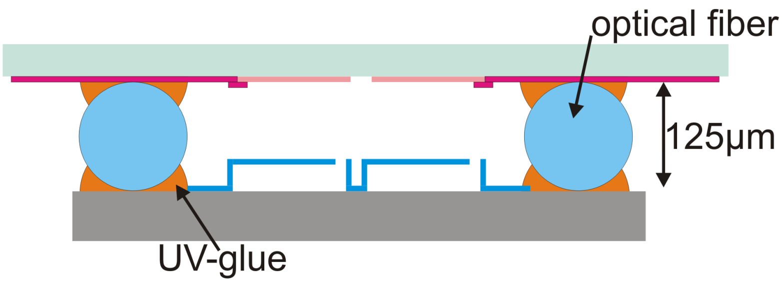

__Figure 4.8:__ Cross section of assembly of chips using as spacer a standard optical fibre of 125µm diameter. The flap chip, the electrode chips and the fibre are fixed together with an UV-glue. The electrode chip is wider than the flap chip since the electrical connection pads are placed here.

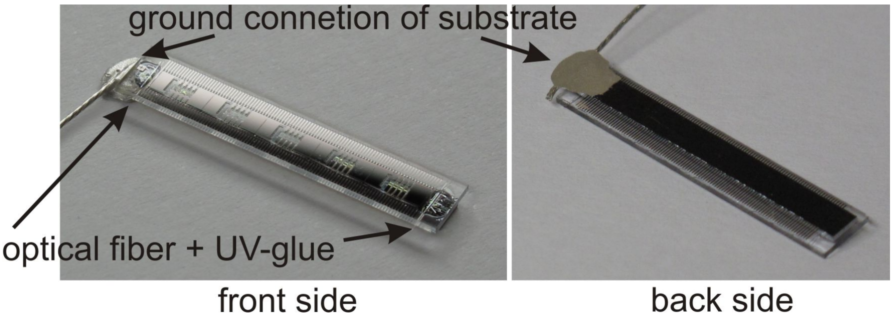

__Figure 4.9:__ Assembled chip with optical fibre as spacer. UV-adhesive was used to fix the two chips and the fibre together. For electrical connection of the flap chip a wire was glued with silver glue to the substrate. On the front side the flaps can be seen through the glass substrate.

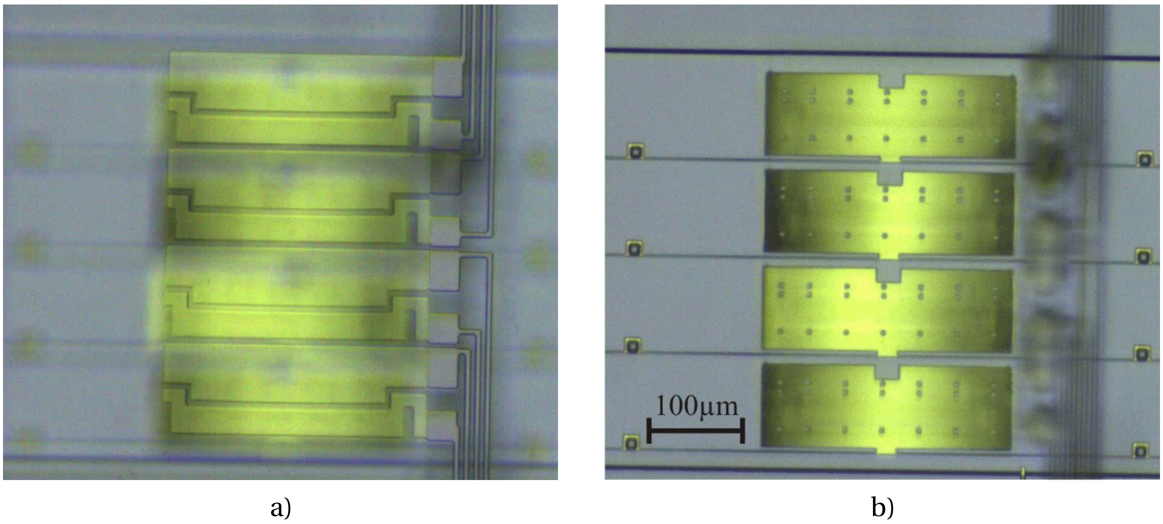

a) b)

__Figure 4.10:__ Top view of assembled devices seen though a microscope: a) focused on the electrode-layer, b) focused on the flaps. Four torsion beam flaps with segmented electrodes are shown. The flaps are slightly curved due to intrinsic stress. An array of holes on the flaps facilitate the release when etching the underlying SiO_2 sacrificial layer in fabrication.

requires to be electrically connected. This is made by gluing a wire to the substrate using silver adhesive, as can be seen in figure 4.9.

A microscope picture of an assembled chip is shown in figure 4.10. The microscope is once focused onto the electrode level and once onto the flap level. It can be seen that the electrode and flap are well aligned.

4.3.4 Connection of the chip to a PCB

The assembled chips have to be connected to a printed circuit board (PCB), for being able to be controlled with a driving circuitry. The connection pads for electrodes and flaps are all on the backside of the electrode chip, when we look from the top trough the transparent electrode substrate onto the flaps. Therefore it was chosen to use Zebra connectors for making the electrical assembly to the PCB. The Zebra connectors used have a conductor line pitch of 0.05mm, which is 4 times higher than the pitch of the connection pads on the chip and PCB. The assembly is shown in figure 4.11. The Zebra connectors require a certain contact pressure to make a good electrical connection. For this reason chip and the Zebra connectors are pressed onto the PCB by means of a metal plate fixed with screw and nuts. The metal plate on top of the chip has a opening as optical access to the flaps.

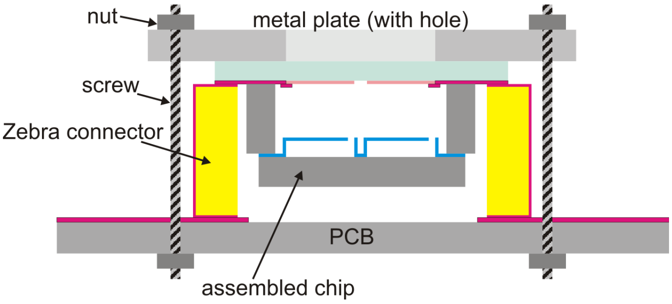

Figure 4.11: *Assembled chip connected to a printed circuit board (PCB) using zebra connectors. A metal plate screwed to the PCB presses the chip onto the Zebra connectors. The metal plate has a hole, so the flaps can be observed from the top.*

4.4 Characterization

4.4.1 Fabrication results

Many flaps are deformed most probably doe to a stress-gradient in the poly-silicon layer. In fact the annealing of poly-silicon during the doping process at 1000° should lead to a low stress in the layer [65]. But already a small stress gradient provokes a deformation over the whole flap width, which is larger than the spacing to the substrate. An image of fabricated flaps can be seen in figure 4.13, where the curved deformation of the flaps can be observed.

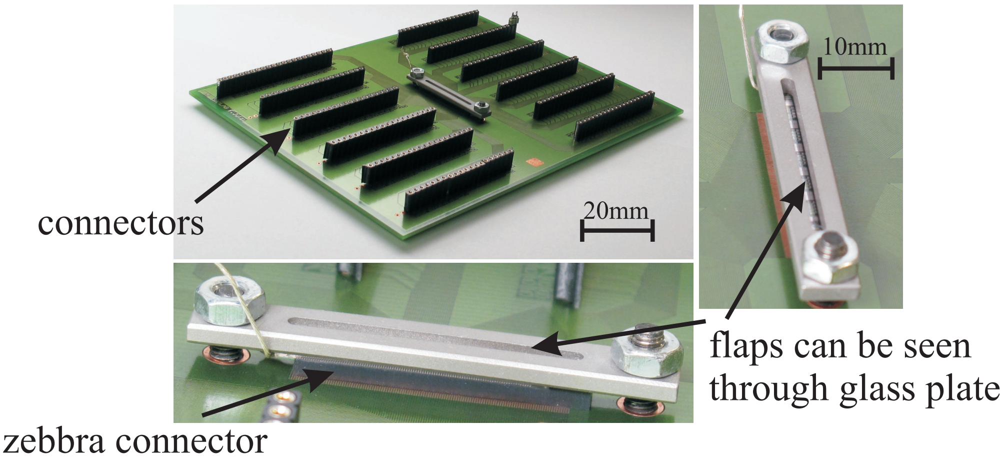

Figure 4.12: *Top left: PCB board with sockets for addressing every single electrode. The assembled chip is placed at the centre and connected to the board with Zebra connectors. Bottom and right picture show a close-up of the mounted chip. The metal plate pressing the chip onto the connectors has a hole for observation of the flaps.*

4.4.2 Actuation of flaps

An assembled chip was tested with an optical fibre as spacer and mounted onto a PCB, as described in section 4.3.4. The flaps are all connected to the substrate and set to ground and a voltage is applied to an electrode above. The other electrodes are at floating potential. A Keithley 2400 source meter was used as voltage source.

In figure 4.13 it can be seen a flap which is actuated with 35V. When tilted, the flap gets into a position almost vertical to the substrate. It is almost not visible any more when looking from the top.

As described above, the poly-silicon of the flaps is curved due to the intrinsic stress gradient. The flaps touch therefore the substrate. Since the contact forces between substrate and flap are considerably high, a higher force is required to pull the flaps up to vertical position. This higher force translates into a higher actuation voltage. On many other flaps not shown here, the contact forces to the substrate are too high and even at high voltage the flaps do not tilt.

4.5 Discussion and next steps

Poly-Si flaps have been fabricated by surface micromachining with a layer thickness of 100nm. The flaps are deformed probably due to intrinsic stress-gradient in the material. The deformation leads to the flap touching the substrate. Contact forces lead thus to higher actuation voltage or even to malfunction of the device.

The next step consist of optimizing the poly-Si process for obtaining a lower overall stress and specially a lower stress gradient. The following solutions can be employed:

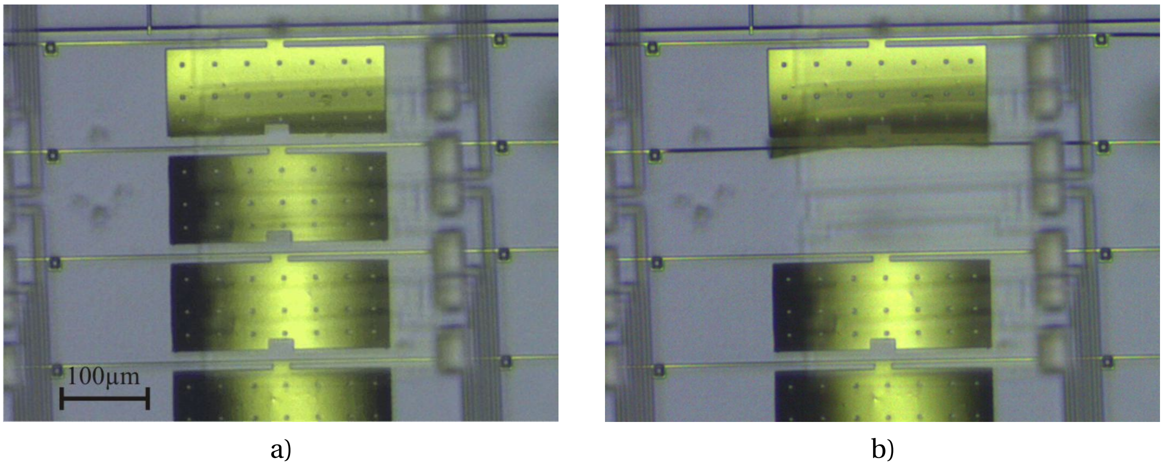

Figure 4.13: *Poly-Si torsion beam flaps assembled to electrode chip: a) no voltage applied b) 35V applied between flaps and the electrode on the second line. The flap turns to vertical position and is almost no longer visible from the top. The flaps are curved due to intrinsic stress gradient and touch probably the substrate, which leads to a higher actuation voltage.*

- Different groups report that the stress gradient and overall stress depends strongly on the deposition condition of the poly-Si [65, 68–71]. An optimization of the deposition process could lead to much lower stress values.

- It can be expected that a stress gradient arises due to the mismatch of the thermal expansion coefficient between the underlying SiO_2 sacrificial layer and the poly-Si. Using a sacrificial material with a more similar thermal expansion coefficient (for example silicon nitride) could be a solution to lower the stress gradient.

- Bombarding a poly-Si layer with argon ions is reported for flattening of stressed thin-films [72].

- Using a stacked layer of films with different stresses (one compressive, the other one tensile) can control the stress. A process using multiple poly-Si layers is reported in [71].

- Thicker layers are expected to have a lower stress gradient, since the difference in stress between the top and bottom layer will be distributed over a larger distance. In addition a thicker structure is stiffer and does deform less. The stresses in thin poly-Si are reported to be higher than for thick ones [70].

- The stress gradient may be caused by the doping-profile, since a the process uses diffusion from the top. Another doping technique of the poly-silicon layer may give lower stress-gradient values.

- Employ other flap- and beam material as for example Parylene. It is expected to have less stress problems, since thicker layers can be used, due to the 40 times lower Young modulus. Thicker layer are expected to deform less due to stress.

- For aluminium as flap material also different methods exist to get a stress-free layer. Deposition temperature, pressure, method (sputtering, evaporation, etc.) and annealing are parameters which can be adapted. Different groups report the fabrication of stress free metal layers used in free-standing structures, like micromirrors [73–75].
- Another approach is to have a thicker sacrificial layer. For SiO_2 the deposition thickness is limited to about 3-5μm (by using a combination of wet and CVD deposition). In addition such thick layer may lead to large stress in the whole substrate. A better solution is to employ Parylene or other organic material, such as thick photoresist or dry-foils as sacrificial layers as reported in [76, 77]. In this case an adapted flap material would need to be used such as amorphous silicon or aluminium.

We decided not to proceed with process optimization but to try a totally different approach for the fabrication of tilting flaps as optical modulators. The new approach will have flaps with a geometrical arrangement such that no surface is contacted by actuation or stress-induced deformation. The fabrication process will be also directly lead to a stress compensation. The concept will be presented in the next chapter 5.

5 Design and fabrication of vertical flaps

After the study of horizontal flaps fabricated by surface micromachining as presented in the preceding chapter a new concept was investigated. The system should be less prone to stress-induced deformation of the flaps. Any contact to any surface should be avoided to prevent stiction. The new concept is based on flaps which are vertical at their rest state and when actuated tilt electrostatically to horizontal position. The flaps are far apart of the substrate, so even if there is some deformation they cannot touch any surface. In addition due to the fabrication technology employed the stress on the flap is compensated. The system was designed for flat tilting flaps suspended by a torsion beam. But using the same fabrication process also a variety of shapes can be obtained.

5.1 Working principle of vertical flaps as optical modulator

The system consists of flaps which are vertical at their rest state, e.g. after fabrication. Therefore the concept is named further on vertical flaps. The flaps are suspended by a torsion beam and can be electrostatically tilted to almost horizontal position by applying a voltage between the flap and a electrode. The details of the design will be first explained by a basic flat flap with a fixed opposing electrode. More advanced designs with flaps of different shapes and other electrodes will be treated further on.

A schematic of the system is shown in figure 5.1. The flap is in rest state parallel to the fixed electrode. It is suspended by a torsion beam which is attached to the substrate at both ends. When a voltage is applied between flap and electrode an electrostatic force acts onto the flap tilting it around the torsion beam. It gets close to horizontal position.

When the voltage is switched off the flap returns back to vertical rest state by the restoring force of the deformed torsion beam. The actuation follows the same concept presented in chapter 3. As discussed the flap requires to be placed at a large enough distance from the electrode to avoid contact at actuation.

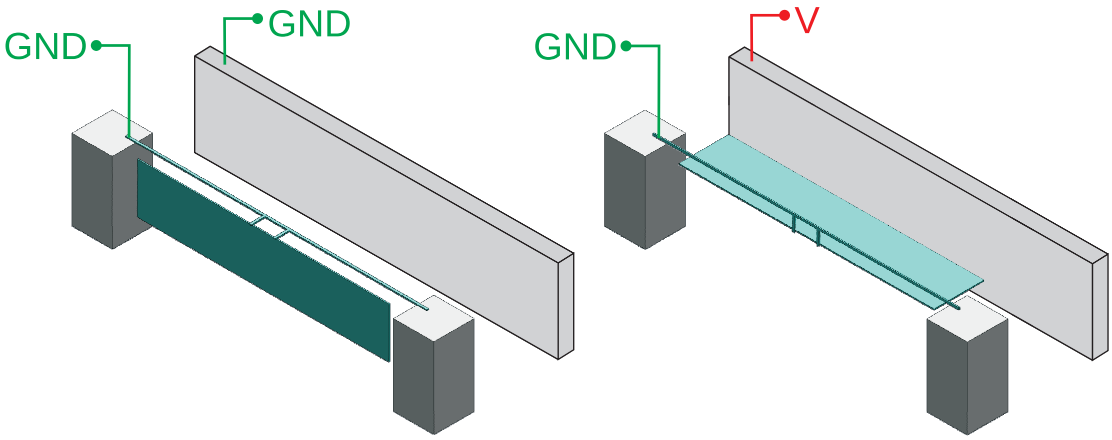

Figure 5.1: *Concept of optical modulator with vertical flaps suspended by a torsion beam. On the left the flap is in rest state perpendicular to the substrate. Parallel to it is placed a electrode, which is vertical as well. When a voltage difference is applied between flap and the electrode the flap turns due to the electrostatic torque to horizontal position. Light coming from above will be blocked or reflected, since the flap lays perpendicular to the light path.*

5.2 Concept of fabrication process of vertical flaps

A novel process was developed for fabrication of vertical flaps. It is based on a process employed previously for fabrication of inertial devices in poly-silicon [78–80] and other application partially employing Parylene [81–83]. A micromirror device has also been fabricated with a similar process [84]. A patent describing the fabrication scheme for reflective displays exists as well [38].

The concept of the process is shown in figure 5.2. It consists of micromoulding into thin high aspect ratio trenches. The trenches are etched by deep reactive ion etching into a silicon substrate. The walls of the trenches are subsequently covered with a layer of SiO_2. Next, the trenches are filled with a material, which can be deposited in a conformal process. The material will constitute the flap-material. It should therefore have the following properties:

- Conductive such, that the flap can be actuated by an electrostatic field.
- Intransparent to the wavelength at which the device will operate.
- Reflecting at those wavelengths at which the flap will be used.
- Good mechanical properties.

Possible materials comprise low pressure vapour deposited (LPCVD) poly silicon, metal deposited by atomic layer deposition (ALD) and Parylene when it is combined with a conductive material. A list and comparison of the different materials is shown in table 5.1.

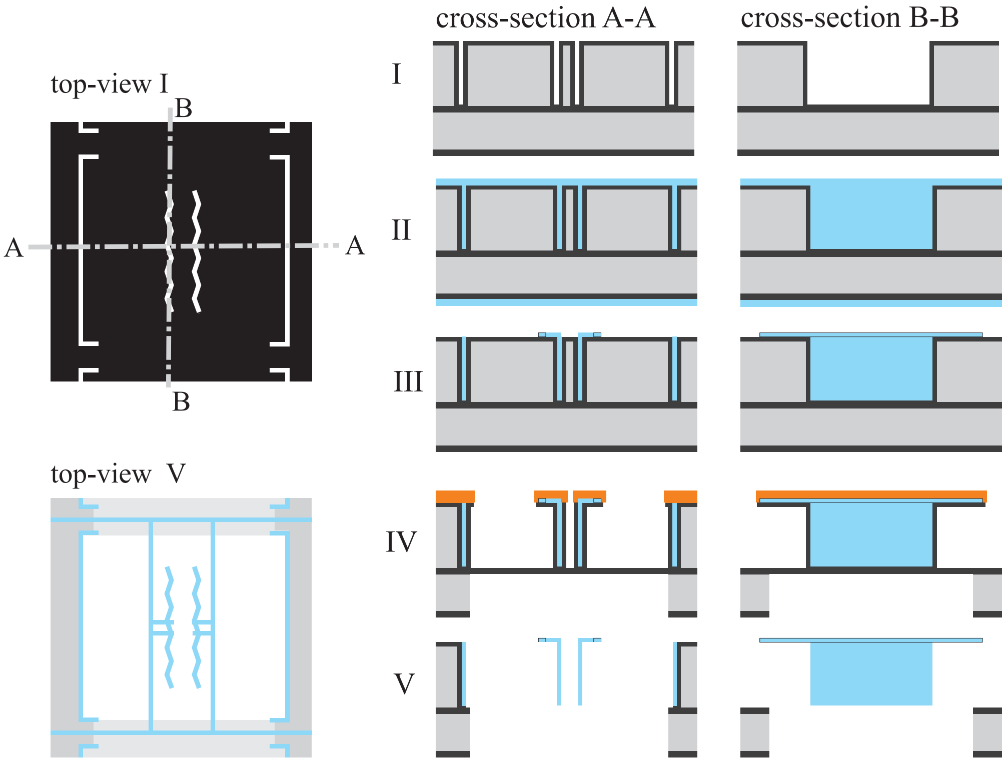

Figure 5.2: *Schematic explaining the concept of the fabrication process employed for obtaining the optical modulators based on vertical flaps. A micromoulding approach is used by filling thin high-aspect ratio trenches (I-II), patterning the top to the form as torsion beam (III) and releasing the vertical flaps by Si-etching of the material between the flaps and electrodes (IV-V).*

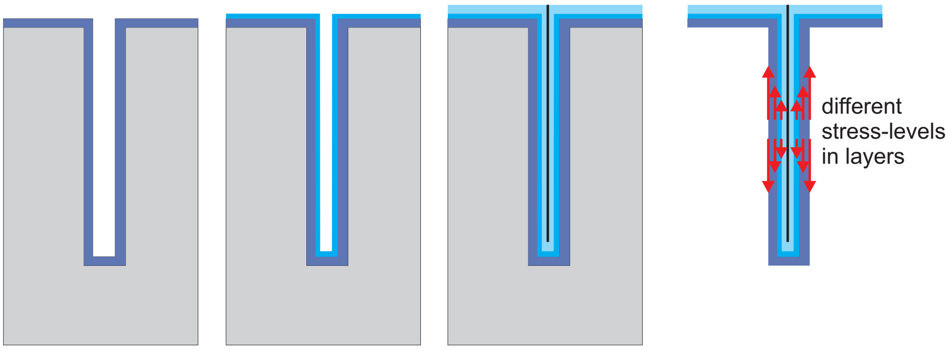

Figure 5.3: *Concept of auto stress-compensation: In the refill process of the trench defining the flap, the material is deposited in a conformal process. We see how layer on layer is formed inside the trench along the walls. Each layer can have a different stress level as depicted on the right image of the released flap. But, we find the same stress levels on both sides of the flap. The stress levels on the opposing sides compensates each other and we have no stress induced deformation of the flap.*

Table 5.1: *Materials for trench refill, having conformal deposition process*

Material	Deposition process	conductivity	possible thickness
Poly-silicon	LPCVD	doping by diffusion process required	500nm
Parylene-C	PVD	not conductive	$5\mu m$
TiN	ALD	conductive	100nm
Pt	ALD	conductive	100nm
Ru	ALD	conductive	100nm
silicon-nitride	LPCVD	not conductive	500nm

The location of the trenches define the position of the flaps and also the delimiting walls of the electrodes. This way the electrode-flap distance is directly defined by the first mask giving a good alignment tolerance. In the release step the substrate material between flap and electrode is etched away. In this step the filling of trenches is protected by the SiO_2 on its walls. A more detailed description of the process will be given in section 5.5.

The released flaps are supposed to be free of stress induced deformation. The reason is that the trenches are filled by a conformal process. Here the material is deposited on both walls of the trench simultaneously up to the point at which the layers on both walls touch and the trench is filed. So, even if there is a stress in the deposited layer, the same stress can also be found on the opposite side of the flap. We have no stress-induced deformation of the flap since the stress on both sides cancel out. We call this concept auto stress-compensation it is schematically depicted in figure 5.3.

The shape of the trench directly defines the shape of the flap and electrode. This way flaps of arbitrary shape can be fabricated, such as grating shape, grid-shape or comb-shape as shown in figure 5.4.

5.3 Concept of applications of vertical flaps

5.3.1 Concept as reflective display

In the application as reflective display each flap (or several flaps together) forms a pixel. A schematic of a 4 by 4 array of double-flaps in application as reflective display is shown in figure 5.5 on the left. An optically absorptive layer is placed at the backside of the chip. When a flap is at rest state incoming light arrives on the black layer, where it is absorbed. The area is perceived as black. When the flap is tilted to close to horizontal position light is reflected back up, we have a white pixel. In an array the flaps are electrically connected together along the rows and the electrodes along the columns. Line-column addressing can be used for addressing each single pixel as described in section 3.1.4. For this purpose the voltage required to hold

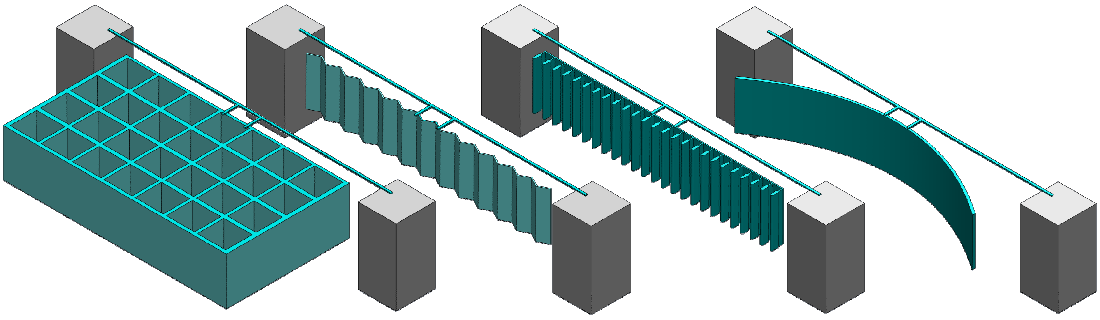

__Figure 5.4:__ With the fabrication employed for producing vertical flaps also devices with different other shapes can be made. We have from left to right a grid shaped structure, a zigzag shaped flap which can serve as blazed grating, a flap with combs and a lens-shaped structure. All devices are suspended by a torsion beam.

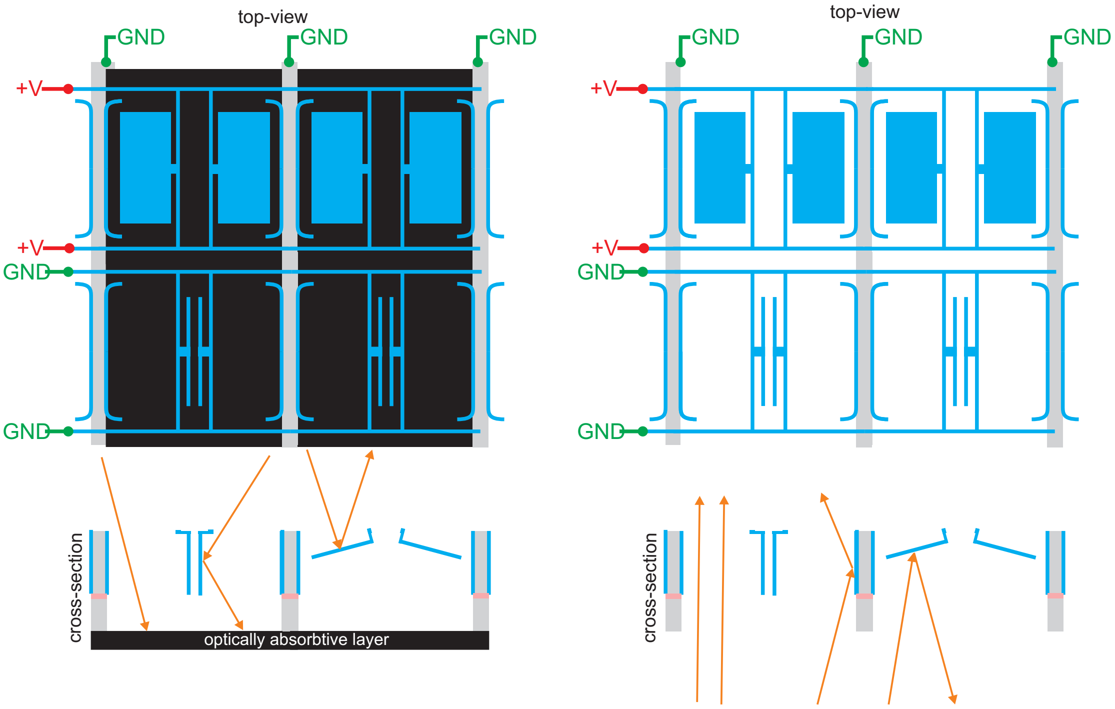

__Figure 5.5:__ This concept drawing shows a 2 by 2 array of vertical double-flaps. The flaps are connected in the rows and the electrodes along the columns. When a voltage is applied to a row of flaps these turn to horizontal position. On the left side the devices in application of reflective display is shown. Light gets absorbed on an underlying optically absorptive layer at the areas where the flap are in rest (vertical) state. At the locations where the flaps are in horizontal state we have back-reflection. In the application as transmissive shutter array, as shown on the right side, light gets either blocked or passes through the device.

the flap at horizontal position should be lower than for switching from ON- to OFF-state. For geometries where this is not the case an active matrix with a TFT back-plane is required.

5.3.1.1 Fill-factor and contrast

The system has an active modulating area corresponding to the fill factor F_{fill} as:

$$F_{fill}(\theta) = \frac{A_{flap-max} \cdot \sin(\theta)}{A_{pixel}} \tag{5.1}$$

Where $A_{flap-max}$ denotes the surface area of the flap (as seen perpendicularly), A_{pixel} the area of a whole pixel and θ the tilt angle of the flap.

Light arriving onto the torsion beam or the area surrounding the cavity, is reflected independently of the tilt angle of the flap. Therefore these surfaces require to be covered by a black matrix or coated with a light absorbing layer. We suppose that such a shielding layer has a reflectivity of $R_{shielding}$ and a fill factor corresponding to the non-active area at maximal tilt angle of the flap $1 - F_{fill}(\theta_{max})$. In this case the overall reflectivity of the display in all-white (ON-)state can be written as:

$$R_{all}(\theta_{max}) = F_{fill}(\theta_{max}) \cdot R_{flap} + (1 - F_{fill}(\theta_{max})) \cdot R_{shielding} \tag{5.2}$$

, with R_{flap} the reflectivity of the active modulating area, which corresponds in the ON-state to the reflectivity of the flap surface. In the all-black (OFF-)state the overall reflectivity is accordingly given by:

$$R_{all}(\theta = 0^\circ) = F_{fill}(\theta_{max}) \cdot R_{OFF} + (1 - F_{fill}(\theta_{max})) \cdot R_{shielding} \tag{5.3}$$

Here R_{OFF} is the reflectivity of the active modulating area as the flap is in vertical rest-state.

The overall contrast ratio of the display system can now be written using equation 2.17:

$$CR = \frac{R_{white}}{R_{black}} = \frac{R_{all}(\theta_{max})}{R_{all}(\theta = 0^\circ)} \tag{5.4}$$

A packaged device requires to have a protective transparent cover on top of the flap-array. Such a cover will have a reflectivity of R_{cover} and thus change equations (5.2) and (5.3) to:

$$R_{all,cover}(\theta_{max}) = F_{fill}(\theta_{max}) \cdot (R_{flap} + R_{cover}) + (1 - F_{fill}(\theta_{max})) \cdot (R_{shielding} + R_{cover}) \tag{5.5}$$

$$R_{all,cover}(\theta = 0^\circ) = F_{fill}(\theta_{max}) \cdot (R_{OFF} + R_{cover}) + (1 - F_{fill}(\theta_{max})) \cdot (R_{shielding} + R_{cover}) \tag{5.6}$$

5.3.1.2 Angular perception

An observer looking at the reflecting pixel sees on it the reflection of an object in the corresponding light path. If this object is dark the perceived brightness of the pixel will be quite low. Solutions to this problem were discussed in section 3.1.1.2 and figure 3.2 and can include to have a flap surface with roughness, wave-shaped flaps or an additional transparent diffuser in the light path. With the fabrication process of vertical flaps wave-shaped devices can be fabricated as shown in figure 5.4. A rough flap surface is more difficult to implement, since the flap surface is given by the shape of the deep trench. To include a transparent diffuser is easily feasible by placing one across the whole display surface at some distance above the flaps.

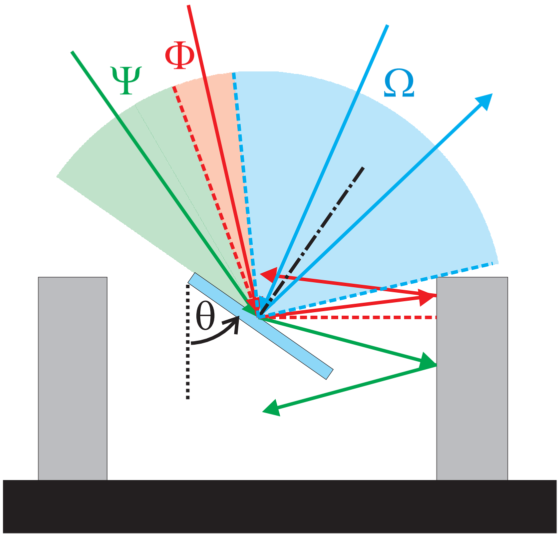

Figure 5.6: *A mirror-like flap at a tilt angle θ is observed from different incidence angles will be perceived with varying brightness due to the change in path of light arriving at the observers eye. When supposing a illumination of the mirror with constant intensity from all incidence angles the flap will be perceived in angular region Ω as bright. In Φ it will be less bright due to additional reflection at the electrode surface and in Ψ the flap will perceived as dark.*

Lets now analyse how a flat surface will be perceived when observed from different directions. A schematic with ray tracing for a flap at a tilt angle of θ is shown in figure 5.6. We take the case of uniform hemispherical illumination, where the light intensity arriving onto the device is constant from all incident angles. Here we perceive the flap as bright at all incident angles in the region Ω. At angular region Φ the perceived intensity will be lower since these rays will have reflected additionally on the electrode surface. For an observer looking from all angles inside Ψ the flap will look dark, since all rays arriving to these angles originate from the cavity below the flap, where the absorbing layer is placed. Numerically we can write these dark region Ψ as incident angles from normal incidence γ:

$$\gamma \in \Psi \Leftrightarrow 90^\circ - \theta < \gamma < 2\theta - 90^\circ \tag{5.7}$$

The above calculations of the angular regions Ω , Φ and Ψ are also useful to know for the case that a transparent diffuser is placed in the light path. The ratio of angular distance Ω to the angular rage of the diffuser (in optimal case 180°) gives the mean light intensity which is reflected for a certain tilt angle θ.

5.3.2 Concept as transmissive shutter array

An array of flaps can be used also as transmissive shutters. A schematic of a 4 by 4 array of double-flaps is shown in figure 5.5 on the right side. On the areas of the array where the flaps are in vertical rest position light passes through the device without any interaction. At the locations where the flaps are tilted to horizontal position the incoming light is blocked of transmission. The passive areas comprising electrode and beams are always blocking the beam path, lowering maximal possible transmittance as shown in figure 3.4. Therefore a maximal fill-factor of active modulating area is required as given by equation (5.1). At horizontal state still some light can pass through the device at the gap between flap and electrode and also next to the torsion beams. This issue can be solved by placing a lens in the beam path as discussed in section 3.1.2.2. An additional black-matrix covering the passive areas can additionally increase the contrast ratio.

5.4 Design of different structures

As next step we will fix the geometrical dimensions and material used. Most of the dimensions have already been set in section 3.3 and are common with the concept of horizontal flaps of chapter 4. Some properties are depended on the fabrication process these are:

- t_{flap}: The thickness of the flap requires to be thin for obtaining a high resonance frequency. But, also thick enough for blocking light in transmission. In the deposition-process of poly-silicon we are limited to about 500nm thickness. Therefore the trench width has to be limited to $1\mu m$ for obtaining a complete refill. The thickness of the flap is defined by the width of the deep trench. We choose t_{el} to be about $1\mu m$.
- h_{flap}: The height of the flap is defined by the depth of the deep trench. Since this trench requires to be as thin as possible the depth is defined be the maximal achievable aspect-ratio. We were able to fabricate $50\mu m$ deep trenches, which gives h_{el} of same size.
- l_{beam}: For having a maximal fill-ratio the beam should not be much longer than the flap is wide. We take l_{beam} as $145\mu m$.
- t_{beam}: We will take t_{beam} as the smallest feasible layer thickness of about 150nm.
- Material: We will fabricate flaps with poly-silicon as material.

The chosen dimensions correspond to the ones given in table 3.3 and for which the actuation voltage versus angle relationship was already calculated in section 3.2.2 and plotted in figure

3.8.

The resonance frequency and modes have been calculated in section 3.2.3.1 in table 3.4.

Different architectures of flap arrays are designed and fabricated. A first one is similar to the one shown in the schematic of figure 5.5 as an array of double-flaps with the beam placed at a certain offset from the flap. The second one is based on the first architecture, but employing only single flaps . In the third architecture the beam is attached in line with the flap at both ends.

5.4.1 Arrays of double flaps

An array of double flaps with the torsion beams placed at some offset beside the flaps is shown in the schematic of figure 5.7. If not marked on the schematic the dimensions are the same as given in table 3.3. The flap is attached to the torsion beam at its centre. Two flaps are placed in parallel with each having an opposing electrode, such that they tilt in butterfly-wings manner. The torsion beam is connected via a T-shaped structure to the substrate. In this configuration the stress in axial direction of the beam can be lowered by deformation of the perpendicularly laying T-structure.

Line-column addressing can be employed here. All the flaps are connected along the columns, the electrodes along the rows. At the crossing point of flap-connection beam and electrode-rows both layers are electrically insulated by an SiO_2-layer. The trenches delimiting the electrode are curved at both ends. The reason is the under-etching of the substrate at the release step, which requires the electrode to be larger at this locations.

5.4.2 Arrays of single flaps

In this architecture each unit consists of one single flap. It is based on the above described architecture of double-flaps, where the flaps are suspended by a torsion beam at a certain offset. An alternative architecture consists of placing the beam opposite on the side of the flap facing the electrode. The trench at the backside of the flap is electrically connected to the same potential as the flap, such that there is only an electrostatic force attracting the flap towards the electrode.

A similar stress-relief structure is placed on the torsion beam as for the double flap. In this configuration line-column addressing can be used as well, since the flaps are connected in the columns and the electrodes along the lines. A drawing of this architecture with geometrical dimensions is given in figure 5.8. Additional geometrical parameter are listed in table 3.3.

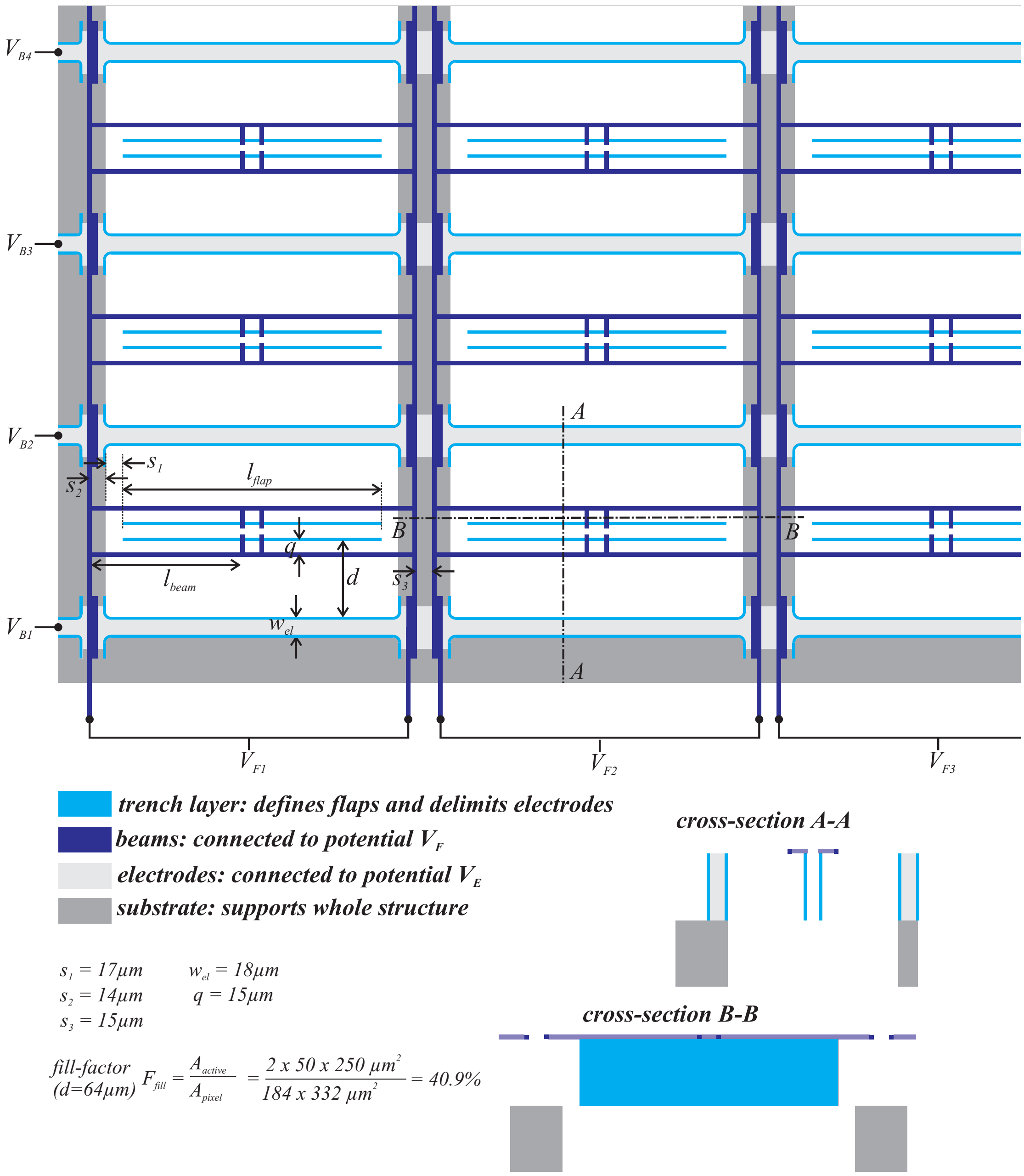

Figure 5.7: *Array of double-flaps with beam fixed at a certain offset.*

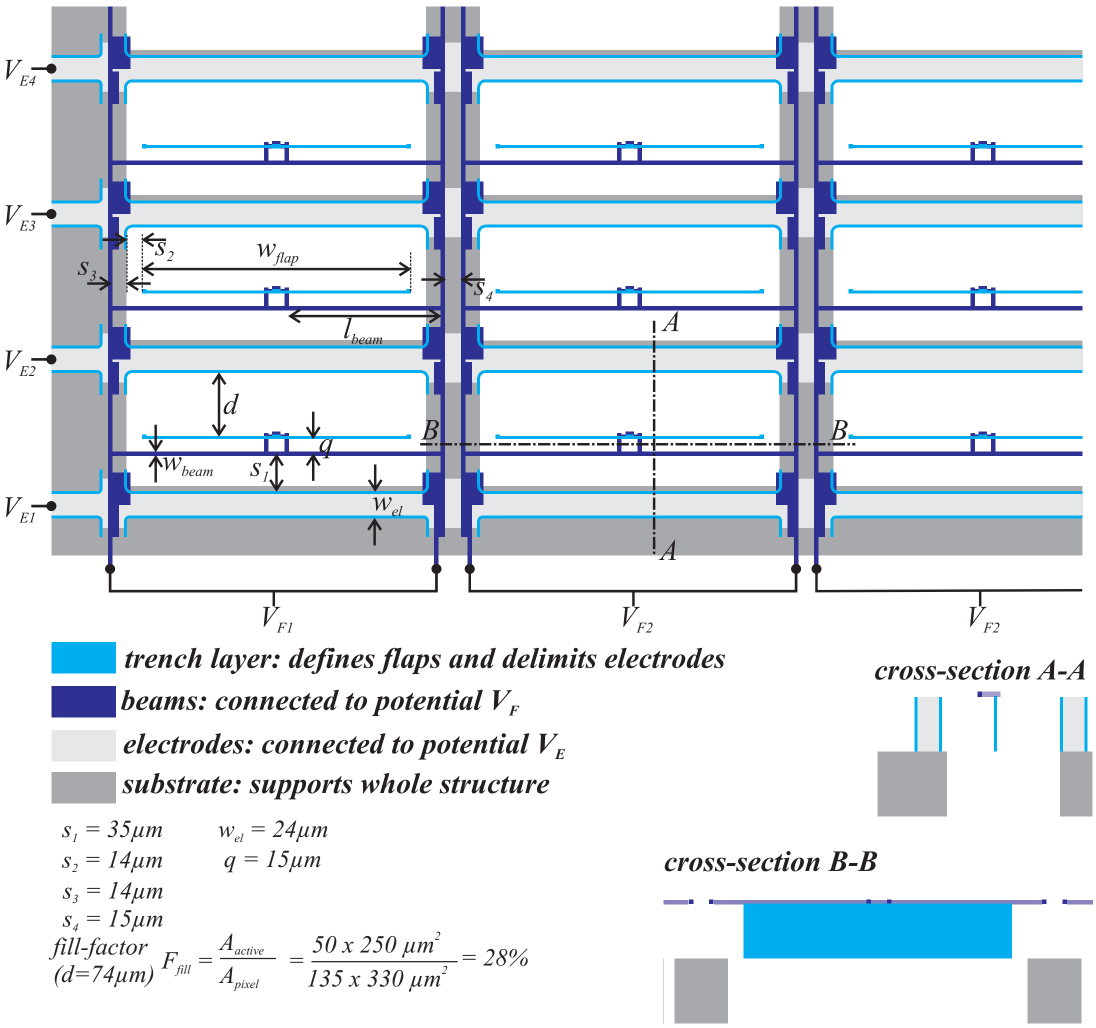

Figure 5.8: *Array of single-flaps with beam fixed at a certain offset.*

5.4.3 Arrays of double flaps with lateral beams

A drawing of an array of double flaps with the torsion beam fixed in line at both lateral ends is shown in figure 5.9. If not indicated otherwise, the geometrical dimensions are noted in table 3.3. Each unit consists of two flaps placed in parallel actuated towards the opposing electrodes in butterfly-wings manner.

Two variants, depending on the fabrication procedure can exist: In one the torsion beam is only connected to the central point of the flap, for which is employed the fabrication procedure as described in section 5.5.3. In the other way two torsion beams are connected to the two lateral ends, as it is the case when fabricating with the processes described in section 5.5.1 and 5.5.2. Each row of flaps is shifted by half the width of an unit. This way the torsion beams have about the same length as the flap is wide. The backside opening is placed below the double-flap region in between the two electrodes.

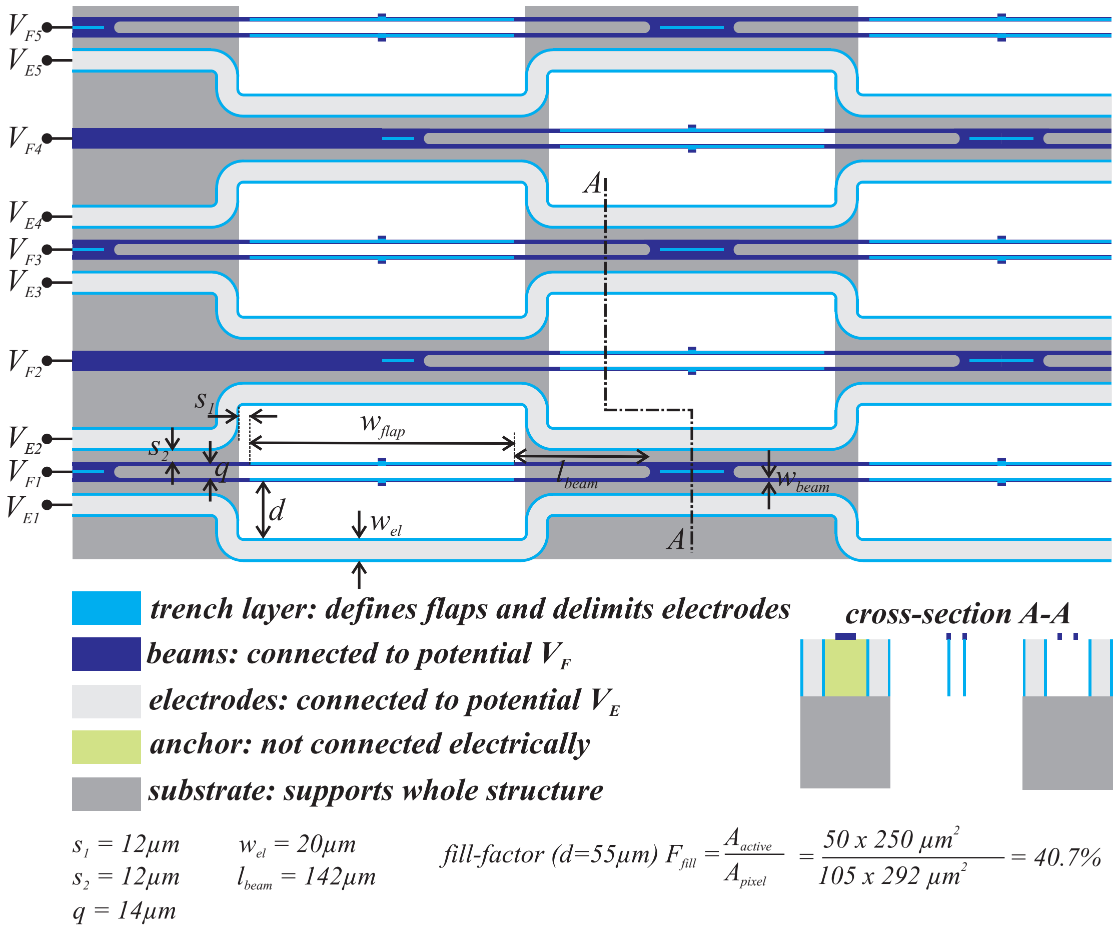

Figure 5.9: *Array of double-flaps with beam directly on top.*

In this design the addressing of each flap-unit is not implemented. One whole row is actuated at once. For having an addressing of each single flap a connection of the flaps along the columns would be required. This could be realized with an additional layer on top or below.

5.4.4 Different shapes of flaps

As already shown in figure 5.4 different shapes of flaps can be fabricated with the vertical flaps fabrication process. We go here into more detail of the architecture of three different ones.

Two comb-shaped flaps suspended each by a torsion beam are placed facing each other. The architecture is schematically shown in figure 5.10 on the left. When a voltage is applied between the two flaps, they tilt towards each-other. We obtain a optical modulation since the gap in-between the flap is closed. Thanks to the comb-shape we expect to have a larger capacitance and thus a lower actuation voltage. The dimensions of the torsion beams and of the flaps (width and height) are the same as given in table 3.3.

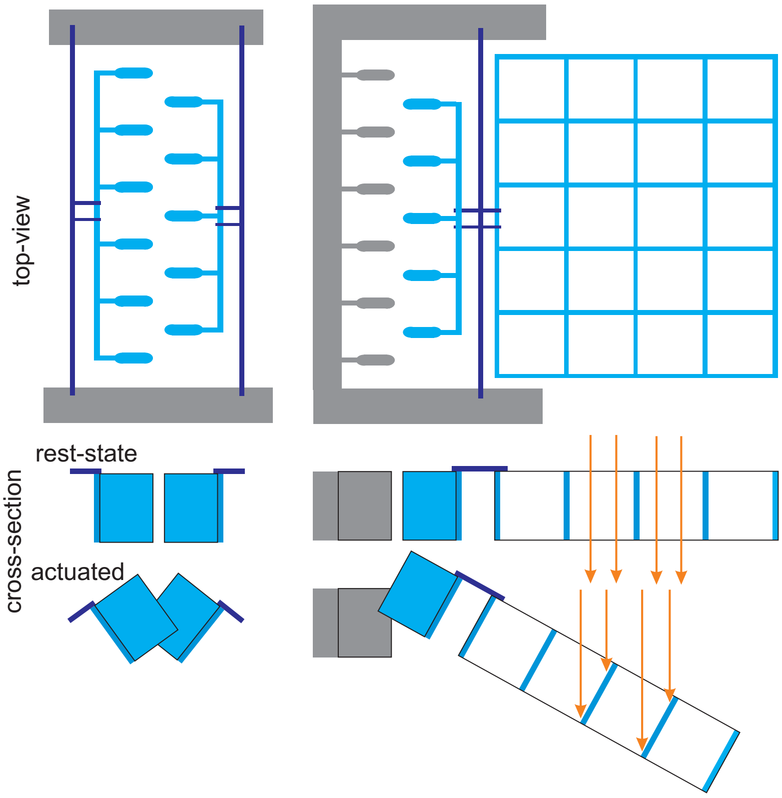

Figure 5.10: *On the left: Two comb-shaped flaps are actuated by applying a voltage difference between them. The two flaps tilt towards each-other closing the gap in-between. On the right: To a comb-shaped flap a grid-shaped structure is attached. The electrode opposing the comb-shaped flap has also the shape of a comb. In rest state light with normal incidence can pass through the grid. By application of a voltage the comb-flap is tilted towards the comb-electrode. The grid is tilted accordingly and light is blocked of transmission.*

A grid-shaped structure to which a comb-shaped flap is attached is shown in figure 5.10. Both structures are connected together and suspended by a torsion beam. An opposing comb-shaped structure fabricated into the substrate serves as electrode. In the rest state incoming light of normal incidence can pass through the grid. As a voltage is applied between flap and electrode, it tilts upwards. Since the grid is attached to the flap it tilts simultaneously by the same angle, but down-wards. In the tilted position light is blocked of transmission.

Figure 5.11: *A zigzag shaped flap can be fabricated. This zigzag shape can be interpreted as blazed grating with a grating period a and blaze angle φ. The blue areas indicate the trench and the green areas the torsion beam.*

A grating-shaped flap is fabricated in the architecture of the torsion beams connected laterally, as presented in section 5.4.3. The shape of the flap is shown in figure 5.11.

5.5 Fabrication process

The concept of the fabrication process was already presented in section 5.2. Two different substrates are used to fabricate the vertical flaps. On a silicon on insulator (SOI) wafer flaps were obtained with a through opening. These devices can be used as transmissive shutters or when placing a light absorbing layer below as reflective display. This fabrication process is presented in section 5.5.1.

In a simpler process the devices can also be made on a bulk substrate. In this case the flaps lay in a cavity, which does not permit transmission of light. This fabrication process was employed for evaluation of the feasibility of fabrication and for characterising the electromechanical properties of the flaps. It is described in section 5.5.2.

A fabrication process with some additional steps for obtaining a torsion beam directly on top of the flap, but only connected at the centre is presented in section 5.5.3.

Due to the technology limitation in the fabrication facility 100mm diameter wafer were used as substrate. A release concept was developed to obtain chips directly by dry etching.

5.5.1 Fabrication process on SOI wafer

In this section is described the fabrication process using a silicon on insulator wafer. It is schematically depicted in figure 5.12 and 5.13 and a list describing each step can be found in table 5.2.

As substrate a SOI wafer with a device-layer thickness of 50 μm is used. The typical thickness of the buried silicon dioxide (BOx) is $2\mu m$ and $350\mu m$ for the handle layer. As first step 3 μm wide trenches are etched into the device-layer until reaching the BOx. Deep reactive ion etching (DRIE) is used with a $5\mu m$ thick photoresist mask. The wafers are subsequently oxidized with a 1 to $2\mu m$ thick layer of wet SiO_2. The silicon dioxide covers the wall of the trenches and also the surface of the substrate. For this step the oxide thickness has to be carefully chosen, such to obtain a precise trench thickness and most important to avoid closing the trench.

The now obtained even thinner trenches of less than $1\mu m$ width are filled using a conformal deposition process. LPCVD poly-silicon is used. Typically used poly-silicon thicknesses were 400 to 500nm. Since the desired poly-silicon thickness on the substrate surface is only 150nm for obtaining compliant enough torsion beams the deposition is done in two steps. The first step fills the trench and in the second step we deposit the desired thickness for the torsion beam. The poly-silicon of the first deposition step is removed from the surface by chemical mechanical polishing (CMP). The second poly-Si layer of 150nm is doped by deposition of a phosphorous-doped SiO_2 by chemical vapour deposition(CVD) followed by a diffusion process at 1100°C. The diffusion process anneals the poly-silicon layer simultaneously, lowering its stress to very low values [65].

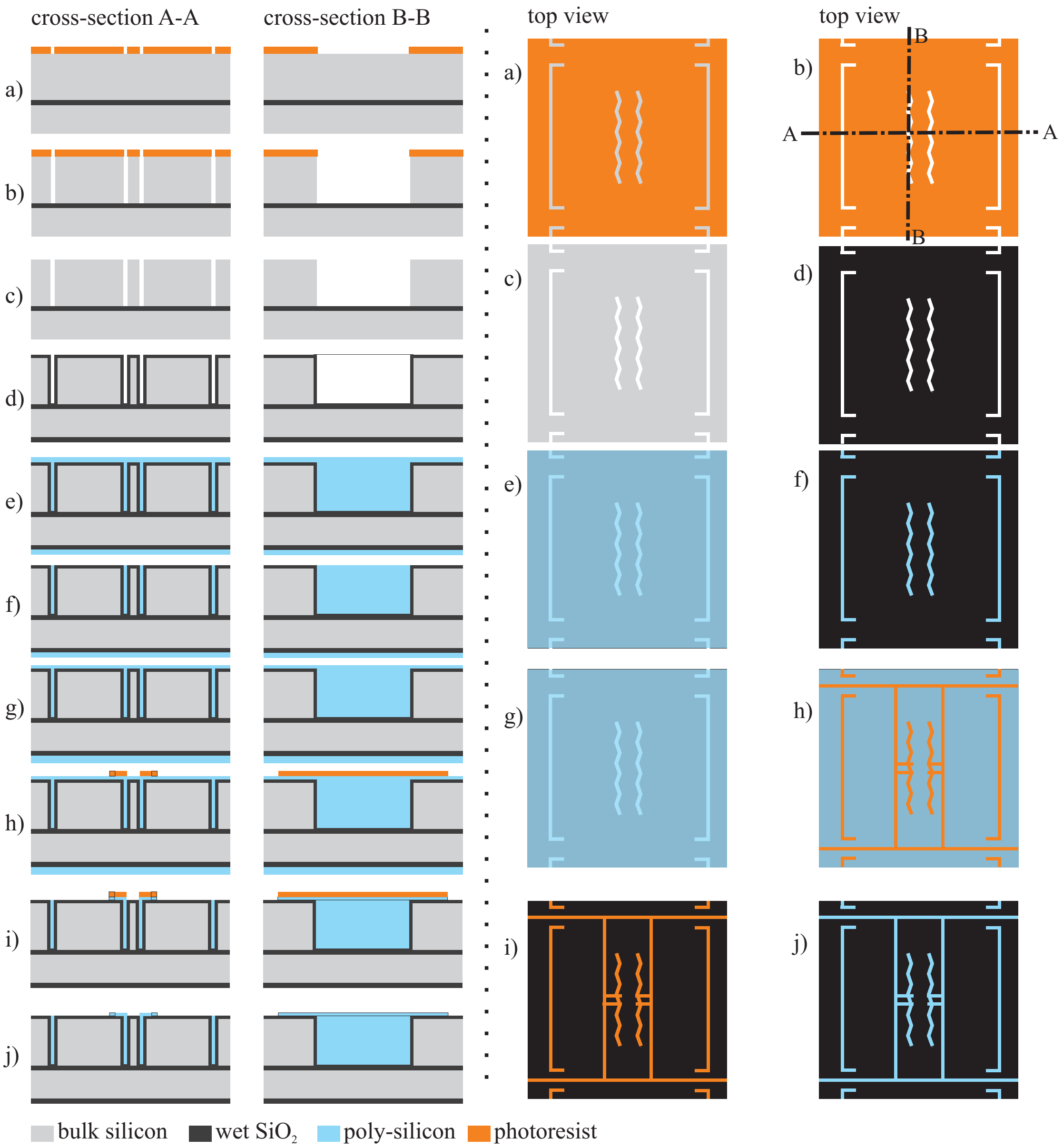

__Figure 5.12:__ First part of process schematic for fabrication of vertical flaps on a SOI wafer substrate. The fabrication starts by DRIE of thin trenches in (a-c), subsequently wet SiO_2 *is grown (d), the trenches filled with poly-silicon (e), the top poly-Si polished in CMP (f) and a thinner 150nm thick poly-Si redeposited (g). The top poly-Si layer is next patterned to shape of torsion beams (h-j).*

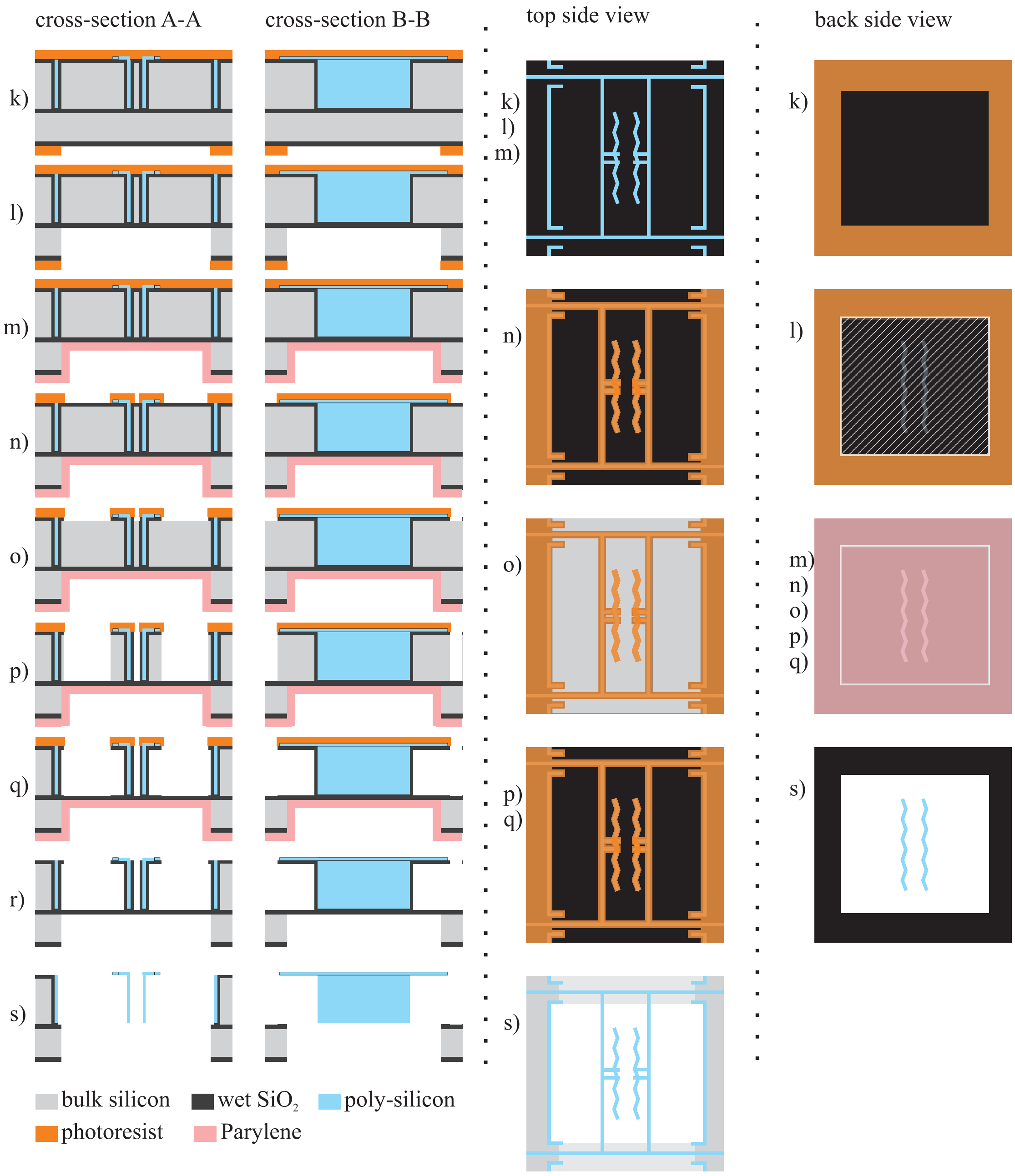

***Figure 5.13:** Second part of process schematic for fabrication of vertical flaps on a SOI wafer substrate, continued from figure 5.12. A backside opening is etched (k-l) and protected with Parylene (m). On the front-side subsequently the material between flap and electrode is etched by DRIE (n-p), followed by isotropic Si etching (q). The flaps are finally released by oxygen plasma ashing (r) and HF-vapour etching of* SiO_2 *(s).*

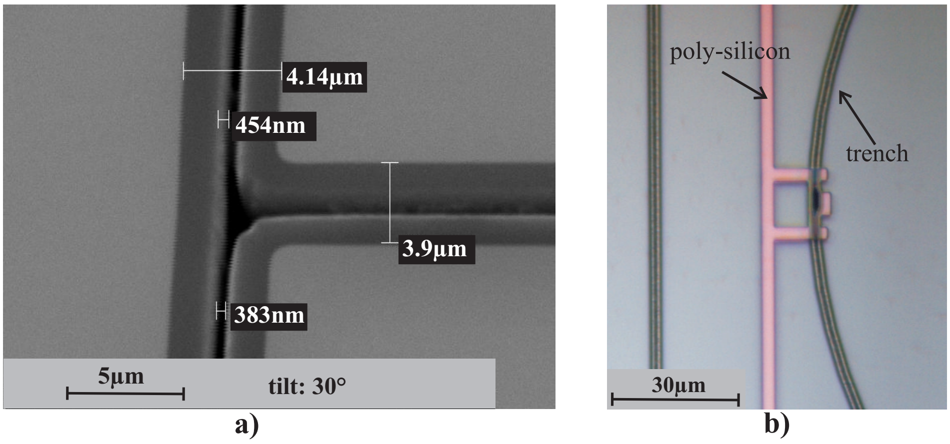

Figure 5.14: *a) shows a trenches filled with a first layer of poly-silicon after CMP. There is still a gap of 380nm inside the trench which will be filled by the second poly-silicon layer. This second layer will be patterned to the form of torsion beam as shown in b). Here is depicted the attachment point of the torsion beam to a curved flap-trench.*

Next the poly-silicon is patterned to the form of the torsion beams. Dry etching is used with a photoresist mask of $1.5\mu m$ thickness. We proceed by processing the backside. The front side is protected with a photoresist layer for this purpose. Using a $8\mu m$ thick photoresist layer as mask the backside is opened by etching a deep trench through the handle layer until reaching the BOx. A 2 to $5\mu m$ thick layer of Parylene is deposited for covering the backside hole and secure the BOx membrane of breaking during the subsequent front etching. The front side is protected of Parylene deposition by means of a blue-tape.

As next step the processing on the front side is continued by etching the material between the flaps and electrodes. The poly-silicon torsion bars and the regions serving as electrodes are protected with a thick photoresist layer of $8\mu m$. The top SiO_2 layer is etched, followed of DRIE through the device layer until the BOx is reached. Next the silicon at the side walls is removed by isotropic etching until reaching the SiO_2 walls of the refilled trenches. In this step the material below the torsion beams is removed as well. The remaining photoresist and protecting Parylene on the backside is removed in an oxygen plasma. As last step the devices are released in hydrofluoric (HF) vapour. In this last step single chips are obtained.

Table 5.2: *Steps of fabrication process. A SOI wafer is used as substrate with a device layer of* $50 \mu m$ *and handle layer of* $350 \mu m$*.*
**: Only done in process with torsion beam directly on top of flap described in section 5.5.3.*

Step	Description	Parameters	Comments
a)	Photolithography for defining thin trenches (Mask 1)	$6 \mu m$ positive tone photoresist	The photoresist will serve as mask in the subsequent etching process.
b)	DRIE etching of thin trenches	50 μm depth	For SOI process: stop on BOx, For bulk process: depth requires to be well controlled.
c)	Stripping of photoresist, cleaning of wafer	Photoresist is removed in oxygen plasma, standard cleaning for subsequent wet oxidation step	
d)	wet SiO_2 growth	0.5 to 2 μm thickness of SiO_2	Thickness has to be adapted depending on desired trench width.
d*)	CVD-oxide deposition	0.5 to 1 μm thickness of CVD-SiO_2	Required thickness for closing top of trenches has to be evaluated experimentally.
e)	poly-silicon deposition	500nm thickness	other materials can comprise ALD-metal, silicon nitride or Parylene.
f)	chemical mechanical polishing (CMP)	remove poly-silicon at top surface until reaching SiO_2	this step is only done when a different thickness for the torsion beams is desired, than deposited in the preceding step.
g)	poly-silicon deposition & doping	150nm poly silicon + 100nm p-doped CVD-SiO_2 + 300nm undoped CVD-SiO_2 + diffusion at 1100° C, subsequently CVD-SiO_2 is removed in BHF	doping diffuses also into poly-silicon in trench
h)	Photolithography for defining torsion beams (Mask 2)	1.2 μ positive tone photo resist	The photo resist will serve as mask in the subsequent etching step.
i)	poly-silicon etching	150nm poly-silicon by DRIE	defines the shape of the torsion beams

Continued on next page

Table 5.2 – continued from previous page

Step	Description	Parameters	Comments
j)	remove photoresist	strip photoresist in oxygen plasma	
k)	Photolithography for backside patterning (Mask 3)	8μm positive tone photo resist	The front-side is protected with photo resist, for the subsequent processing steps l) and m)
l)	Back side etching	SiO_2 etching in RIE followed by DIRE through whole handle layer of SOI wafer (about 350 μm) for defining the backside openings of the flap cavities.	The photo resist mask may be totally etched and the underlying SiO_2 serves as additional mask.
m)	Parylene deposition	2 to 5 μm thickness for protecting the BOx-membrane of braking in step p) and 1)	Parylene deposition is conformal. The front side is protected with blue tape.
n)	Photolithography on front side as protection layer (Mask 4)	5 μm positive tone photoresist	The resist protects the torsion beams, top of flaps and electrodes in the subsequent steps o) to q)
o)	SiO_2 etching	0.5 to 2μm of SiO_2 require being etched depending on thickness deposited in step d) and d*)	Considerable under etch of photoresist mask of up to 1μm
p)	DRIE etching of Si	Etch through whole handle layer to remove material between flap and electrode	For case of bulk substrate, the etch depth will be about 4 times the flap-height
q)	isotropic Si etching	Remove remaining Si below torsion beams and next to flap	The SiO_2 layer on the trenches serve as etch stop.
r)	remove photoresist and Parylene	dry etching of photoresist and Parylene in oxygen plasma	
s)	release structures	HF-vapour etching of remaining SiO_2 at 45°C	SiO_2 on flap, electrodes and below the beams is removed

5.5.2 Fabrication process on bulk wafer

The same process as described in section 5.5.1 can also be fabricated on a bulk silicon wafer. The fabrication process is a simplified version of the one used on SOI wafers. It processes the wafer only on the front-side and the fabricated devices have no backside opening. Therefore no transmissive shutters and reflective displays can be obtained with this process. It was mainly used to verify the feasibility of fabrication of vertical flaps and to be able to measure the electromechanical properties of the flaps.

The process starts by etching thin high aspect ratio trenches in to the substrate. In difference to the SOI-process the trench is not defined by reaching the BOx layer, but the desired etch depth is obtained by regulating the etch time.

The process flow is shown in figure 5.15, with a detailed description in table 5.2. The steps of SiO_2-oxidation followed of trench refilling and pattering of the top poly-silicon layer to the form of torsion beams is identical to the SOI process above. In difference to the SOI process the Si between flap and electrode is etched to much deeper depth. A similar process as presented in [81] is used. The DRIE step etches an up to four times deeper hole than the one of the thin trench ($200\mu m$ instead of $50\mu m$). A longer isotropic silicon etch follows which should not only release the the flaps by removing the Si up to the SiO_2 wall of the trench, but also a large part of Si material below the trench. It is important to have a large gap between the bottom edge of the flap and the lower surface of the cavity to avoid electrical attraction by the substrate.

As last step the devices are released by etching the remaining SiO_2 in HF-vapour.

5.5.3 Flaps with torsion beams on top

Here a variety of the vertical flaps process is presented with the torsion beams being placed directly above the flap, but only connected to the flap at its centre point.

The process flow is shown in figure 5.16 with a description of each step in table 5.2. The first steps of trench etching and SiO_2 oxidation are identical to the above processes. The width of the trench should be less than $1\mu m$ or even close to 500nm. By deposition of a CVD SiO_2 of about $1\mu m$ thickness the top of the trench is closed. This is achieved thanks to the non-conformal CVD process. At a certain location the trench is wider, such that the top is not closed by the CVD SiO_2. We obtain now a cavity with one opening hole at its centre. The next steps are all identical to the ones presented in the bulk process. By a conformal deposition process the trench-cavity is filled though the access hole. The poly-silicon is patterned to the form the torsion beam just above the flap. The SiO_2 serves as sacrificial separation layer between flap and trench.

The following steps of DRIE, isotropic Si etching and HF-vapour release are identical to the SOI-process.

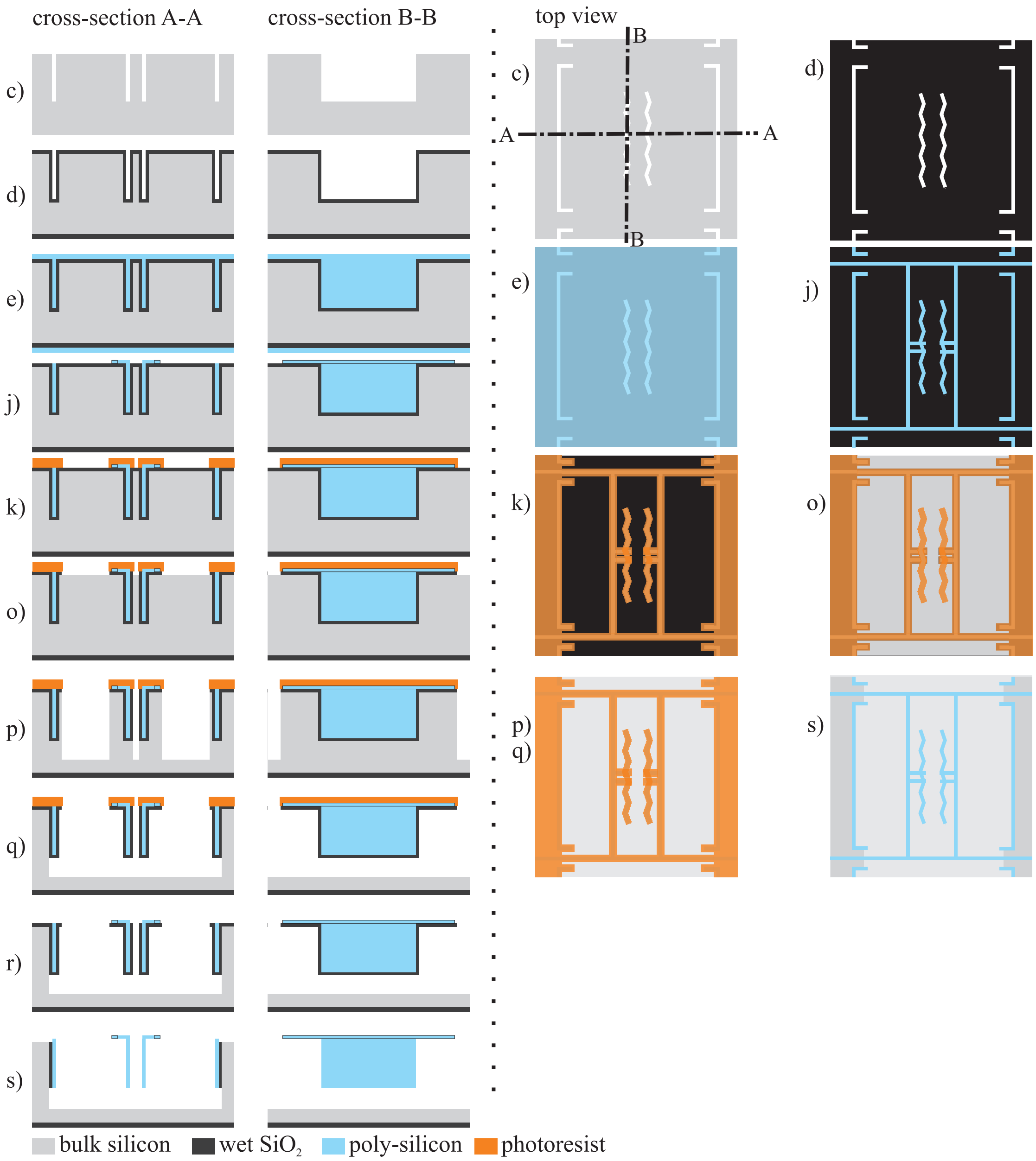

Figure 5.15: *Process schematic for fabrication of vertical flaps on bulk wafer. Only steps different of the SOI-process are shown. Thin high aspect-ratio trenches are etched (c), the walls covered with* SiO_2 *(d), the trenches filled with poly-silicon (e), the top layer patterned to form of torsion beams (j). The top torsion beam layers protected with photoresist(k). The flaps are released by DRIE of 200µm depth followed by isotropic Si etching (q), oxygen plasma etching (r) and* SiO_2 *etching by HF-vapour in (s).*

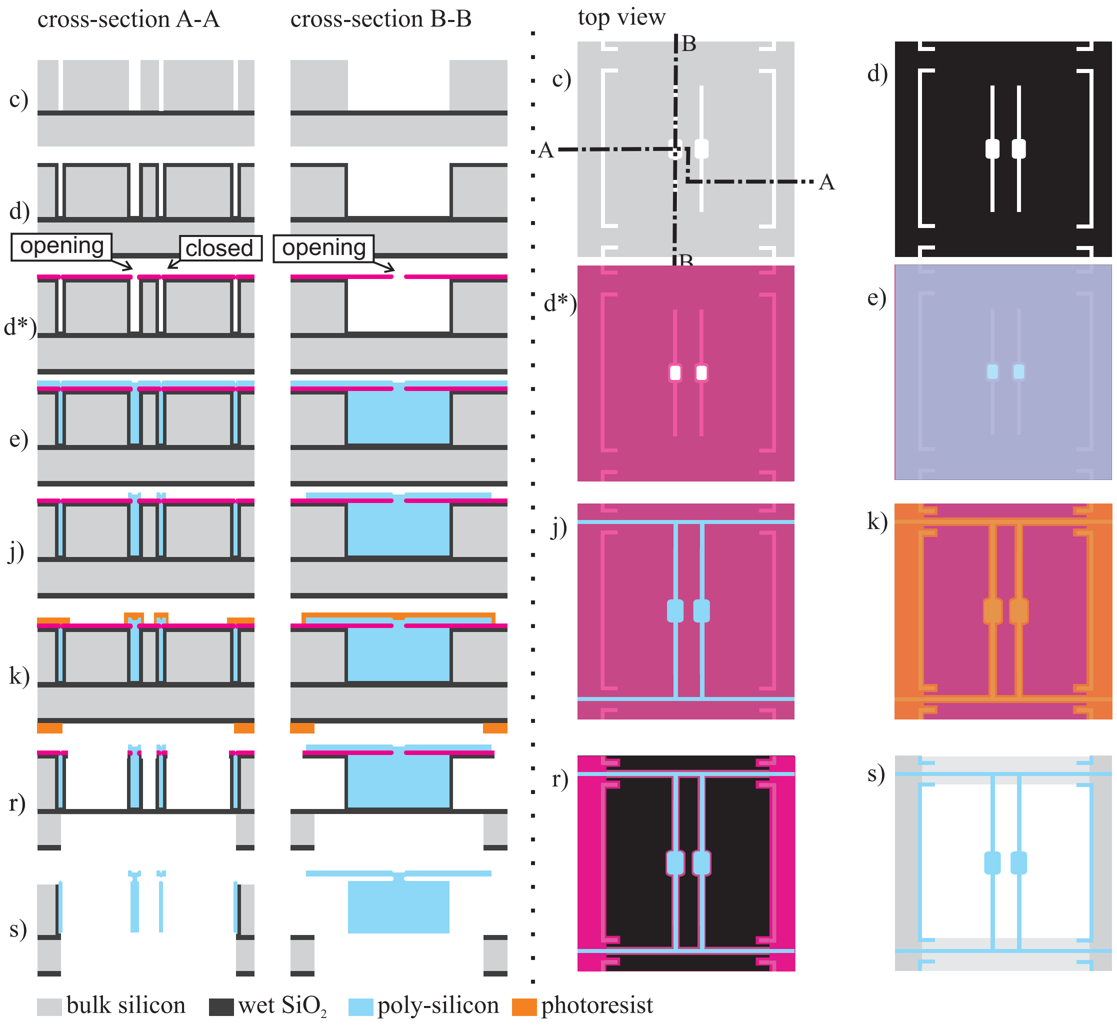

Figure 5.16: *Process schematic for fabrication of vertical flaps with torsion beam placed directly on top of flap using intermediate sacrificial layer. Only the steps different of the SOI-process are shown. The process starts by etching thin high-aspect ratio trenches by DRIE (c). The trenches defining the flap are wider at the centre. Wet-*SiO_2 *is grown (d) and the top of the trenches closed with CVD-*SiO_2 *(d*). Here a opening remains at the region where the flap is wider. The trenches are then filled through the access hole (e), the top poly-silicon layer patterned to form of torsion beams (j), the back-side and front side openings etched (k-r) and the flap released (s).*

5.6 Details of fabrication process

In this section will be treated in more detail some critical process steps.

5.6.1 Fabrication and refill of trenches

Here the fabrication and refill process of the thin high-aspect ratio trenches will be analysed in more detail. SEM images of the cross-section of a trench at different fabrication steps are shown in figure 5.17. We first etch high aspect ratio trenches of up to $50\mu m$ depth by DRIE into the crystalline silicon. Subsequently the width of the trench is narrowed by oxidation of the walls. We require a maximal trench width which is the double of the possible deposition thickness of the refill material. Otherwise the layers on the walls of the trench (see figure 5.3) will not touch each other giving a flap consisting of two individual layers. The typical maximal poly-silicon deposition-thickness at the clean-room where the fabrication was done is 500nm. Therefore, the trench should be less than $1\mu m$ wide. When using Parylene for trench refill a thickness of up to $5\mu m$ is possible. ALD metals need to be combined with another deposition process, since their thicknesses are limited to less than 100nm due to economical reasons.

5.6.1.1 Thin high aspect ratio trenches

To obtain a trench with a width of less than $1\mu m$ and a depth of $50\mu m$ only by a DRIE-step is very challenging. Therefore, the small trench width is obtained in two steps of DRIE followed by wet-SiO_2 for thinning the trench width. After DRIE a test wafer is clipped and the trench cross-section is measured as shown in figure 5.17 a). The thickness of the subsequent wet oxidation is chosen accordingly such that the required final trench width is obtained. Technically feasible are maximally 2 to $3\mu m$ of wet SiO_2. Since a too thick SiO_2 layer induces stress, thus bow of the wafer, the initial trench should have a width of less than $3\mu m$. For $50\mu m$ deep trenches this was obtained by using a $6\mu m$ thick photoresist mask exposed with $1.5\mu m$ wide features on the mask.

5.6.1.2 Closing top of the trenches

As described in the fabrication process of section 5.5.3, the top of the trenches can be closed by additional deposition of CVD SiO_2. For this purpose the trench width should not exceed $1\mu m$. It is even preferable to have a width of only 500nm after wet-SiO_2. The reason is the limit in CVD SiO_2 thickness which can be deposited. Too large CVD SiO_2 layers may cause high stress levels leading to breaking of the torsion beams during the release. In figure 5.17 c) a cross-section of the top of a trench is shown with the CVD SiO_2 closing the top. The initial trench width was 500nm as measured before CVD SiO_2 deposition in figure 5.17 b). The employed CVD SiO_2 thickness was $1\mu m$.

As can be seen in the top view of figure 5.18 the trenches are closed at the top, only leaving an

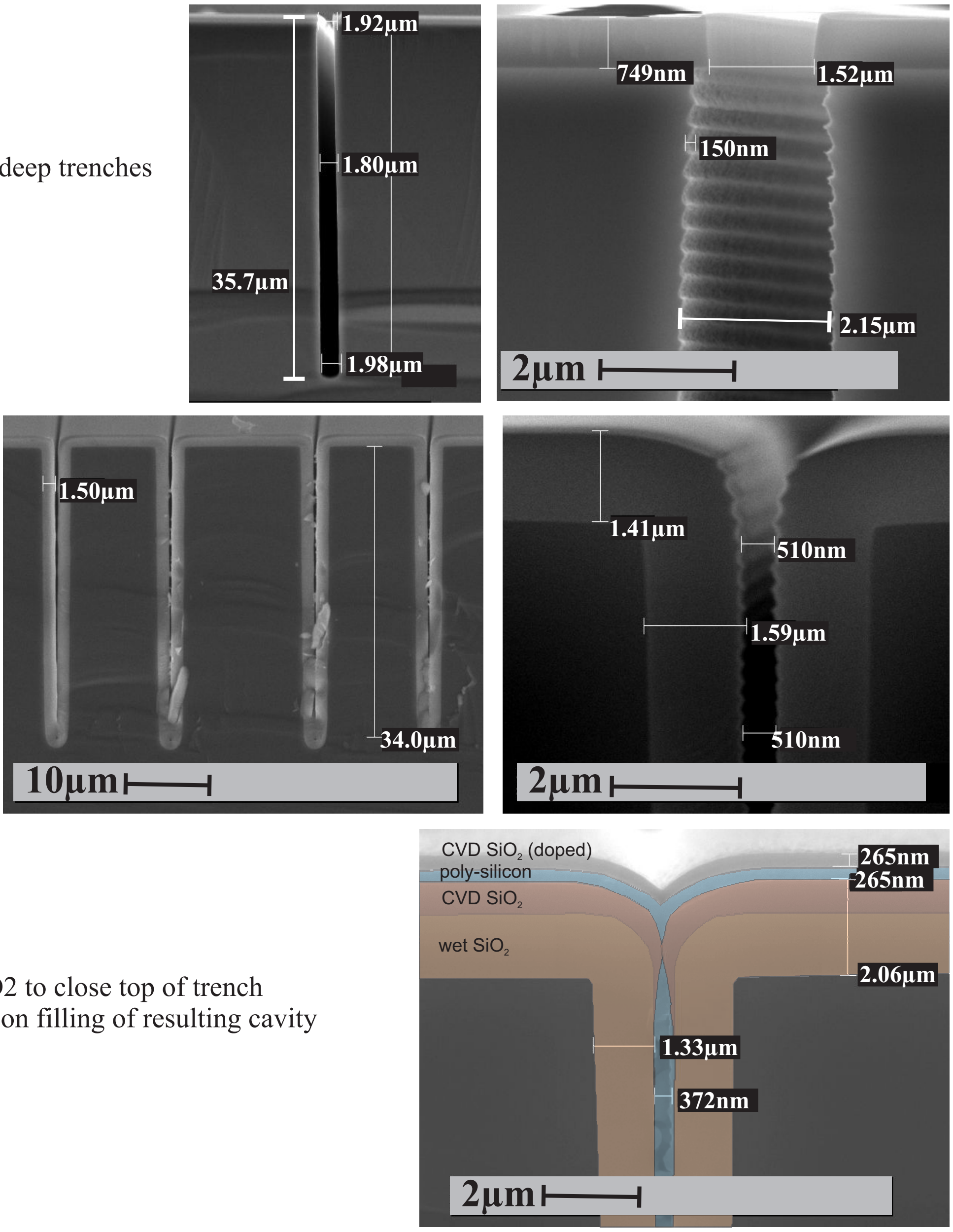

a) DRIE of deep trenches

b) wet SiO_2

c) CVD SiO2 to close top of trench
+ poly-silicon filling of resulting cavity

Figure 5.17: *Cross-section of deep etched trenches taken in SEM. In a) is shown a 35µm deep and about 1.8µm wide trench with a detail of the top part. The remaining photoresist can be seen and also the typical scalloping of the walls due to the etch process. In b) a wet oxidation gives a 1.5µm thick layer of* SiO_2*. The trench becomes narrower and is now only about 500nm wide, while scalloping is still remaining. In c) the different layers are emphasized in colour. A 1.2µm thick CVD* SiO_2 *closes the top of the trench. Subsequently the resulting cavity is filed with poly-silicon through the access hole shown in figure 5.18 (CVD* SiO_2 *is added for doping on top).*

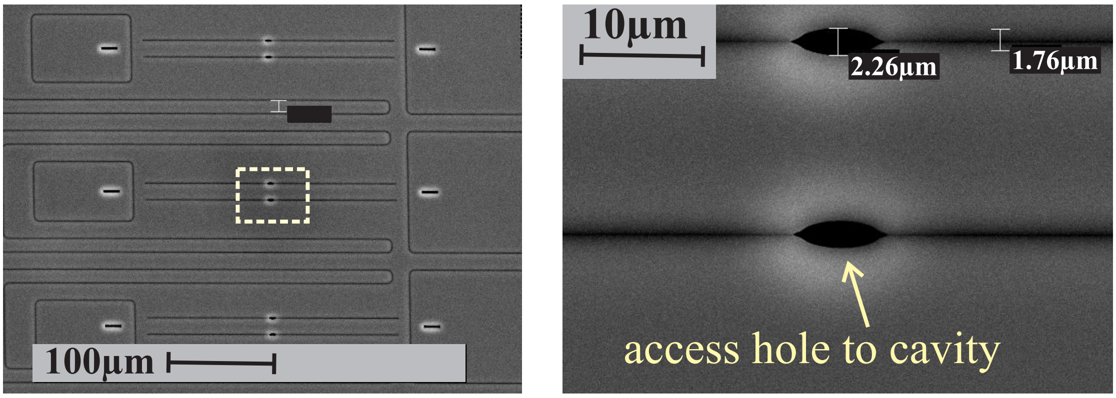

Figure 5.18: *Top view of trenches after closing the top with $1.2\,\mu m$ of CVD SiO_2. On the right detail image the access hole to the underlying cavity can be seen. At this location the trench is larger such that the CVD SiO_2 thickness deposited is not enough for closing the top. Through this opening the cavity is filled subsequently with poly-silicon.*

opening at a certain location where the trench have a larger width. This opening will be used to fill the trenches.

5.6.1.3 Filling of the trenches

A conformal process is required for filling the trenches of high aspect ratio. In the case at which the trenches are closed at the top and the deposition has to be done through a single opening, the conformity requires to be even higher. A list of possible materials for use in the refill process and which will constitute the material of the flap are given in table 5.1.

In figure 5.19 a wave-shaped flap is shown whose trench was closed at the top and which was filled with poly-silicon through an access hole as depicted in figure 5.18. It can be seen that poly-silicon was deposited up to $80\mu m$ along the cavity. Here we attain the limits of conformal poly-silicon deposition.

5.6.2 Release process

In the release first the material between flap and electrode is etched away by DRIE followed by isotropic silicon etching. Next remaining photoresist is stripped in oxygen plasma and the SiO_2 etched in HF-vapour. In figure 5.20 the different states of the release process are shown, for devices fabricated on a bulk substrate. In a) the Si was etched in DRIE up to the double flap depth. Subsequent isotropic etching removes the Si up to the SiO_2 layer on the flap. The material below the beams and the flap was not removed yet. More isotropic etching is required.

In b) the device is totally released from the Si. The material below the beam and the flap is etched. It can be seen that on the bottom of the substrate a elevation remains, which is due to

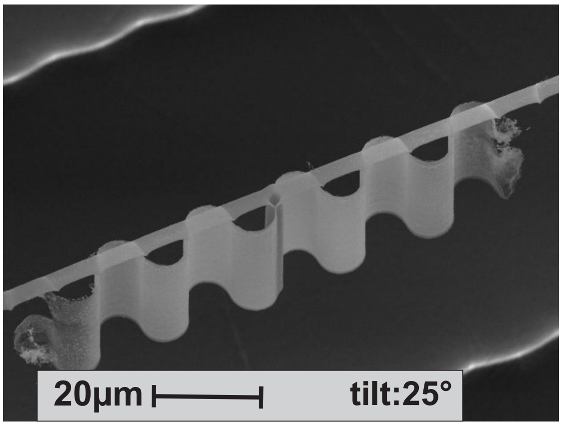

Figure 5.19: *Wave-shaped flap with beam on top connected only at its centre. The flap cavity with the wave shape was filled only through the access hole at the centre. It can be seen how far poly-silicon was deposited in the cavity. Poly-silicon was deposited up to a distance of about 80 μm from the access hole.*

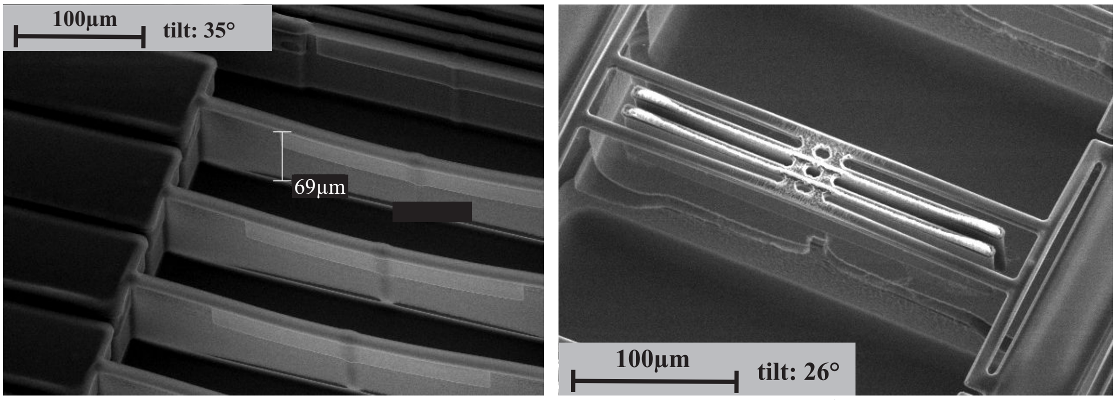

[redacted]

a) **b)**

Figure 5.20: *The two images show the release of the flaps by DRIE followed by isotropic etching of the substrate between flap and electrode in a bulk process. In a) there is still some Si remaining below the flaps and the beams. The isotropic etch was not enough, yet. In b) after some additional etching time the flaps are released from the substrate, there is also no Si remaining below the beams. Nevertheless directly below the flaps an elevation at the bottom of the cavity remains.*

the etch-profile. On this device there is still the photoresist mask and the SiO_2 remaining.

In figure 5.21 a lens-shaped flap is depicted at the different states in the release process. In a) the Si below the beams is not completely removed yet. In b) the structure after complete Si-release is shown with photoresist remaining. c) shows the final released structure after photoresist stripping and HF-vapour etching of SiO_2.

During the isotropic etching step the electrodes are protected by the trenches defining its shape. The SiO_2 on the walls of the trenches serves as etch-stop. At the crossing point of electrodes connected along the rows and the flaps connected on the beam-layer along the

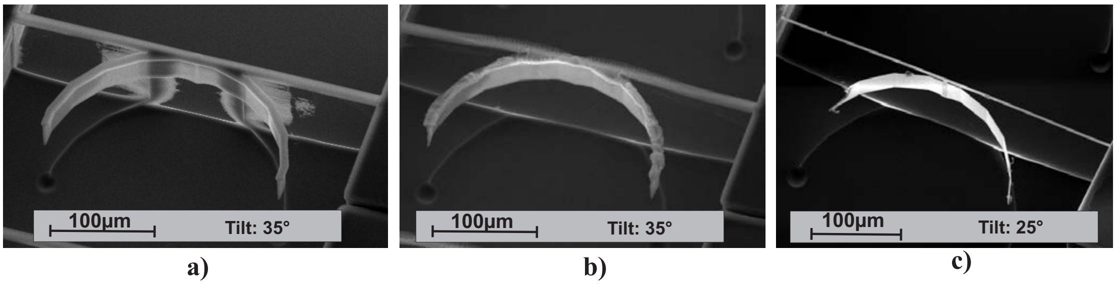

Figure 5.21: *The release process of a lens-shaped structure suspended by a torsion beam is shown as SEM images. In a) still some Si is remaining below the beam after DRIE and isotropic etching. In b), after some additional isotropic etching, the structure is completely released from the bottom substrate. There is still the photoresist mask and* SiO_2 *remaining. Picture c) shows the structure after photoresist strip in oxygen plasma and* SiO_2 *etch in HF-vapor.*

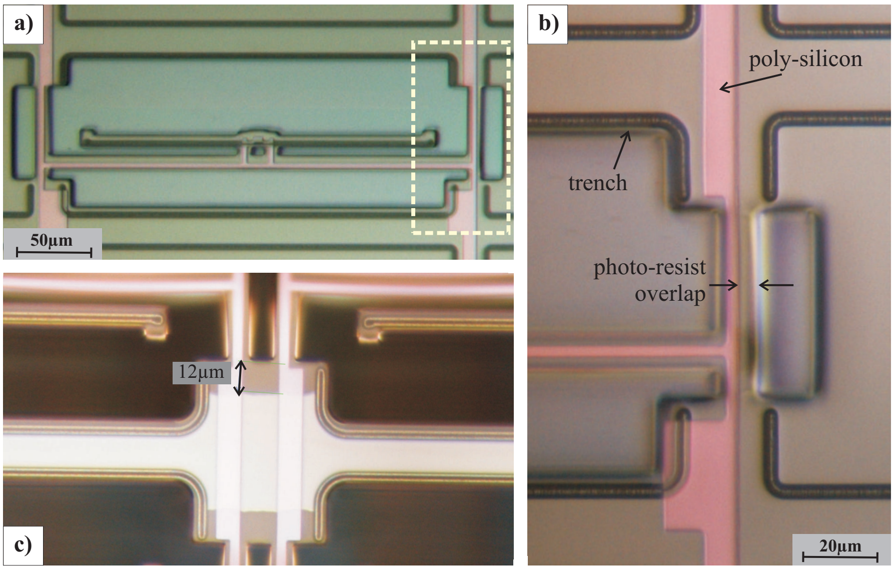

Figure 5.22: *In a) and corresponding detail b) the resist mask of the release step is shown. The resist overlaps the poly-silicon beams and trenches by* $3\mu m$*. Between flap-trench and beam there is an etch-opening as well. Image c) shows the structures after the Si-etch release with remaining photoresist. At the location not protected by the trenches the Si-substrate was under-etched by* $12\mu m$*.*

columns the electrode is not protected. At this location the electrode material will be attacked in the isotropic etching. For this reason the trench defining the electrode is curved thickening the material at this area. In figure 5.22 the close up of such a crossing point is shown with the under-etch of the electrode due to the isotropic Si-etching step.

The poly-silicon beams require to be protected during the Si-etch release as well. This is done by having a photoresist mask overlap of about $3\mu m$. At the bottom surface the poly-silicon beams are protected from the etching plasma by a SiO_2 layer. The shape of the mask used for the Si-etching release is shown in figure 5.22.

5.6.3 Packaging

Chips of 4 by 13 mm^2 size are obtained after the release step in HF-vapour. The chips are directly defined in the backside and front side dry-etching steps of the release. A similar approach is used as described in [85]. The obtained chips are subsequently glued onto a printed circuit board (PCB) and wires are bonded for connectivity. The wirebonds are made directly onto the poly-silicon layer for connecting the flaps and on the crystalline silicon of the device layer for connecting the electrodes. An image of the packaged device is shown in figure 5.23. The PCB has an opening on the backside, so the modulator can be used in transmission mode. For the application as reflective display a light absorbing foil is placed directly below the chip inside the opening of the PCB. The foil is a *Metal Velvet* of *Acktar Advanced coatings* [86] exhibiting 99.9% specular absorbance and less than 1% hemispherical reflectivity in the visual spectrum.

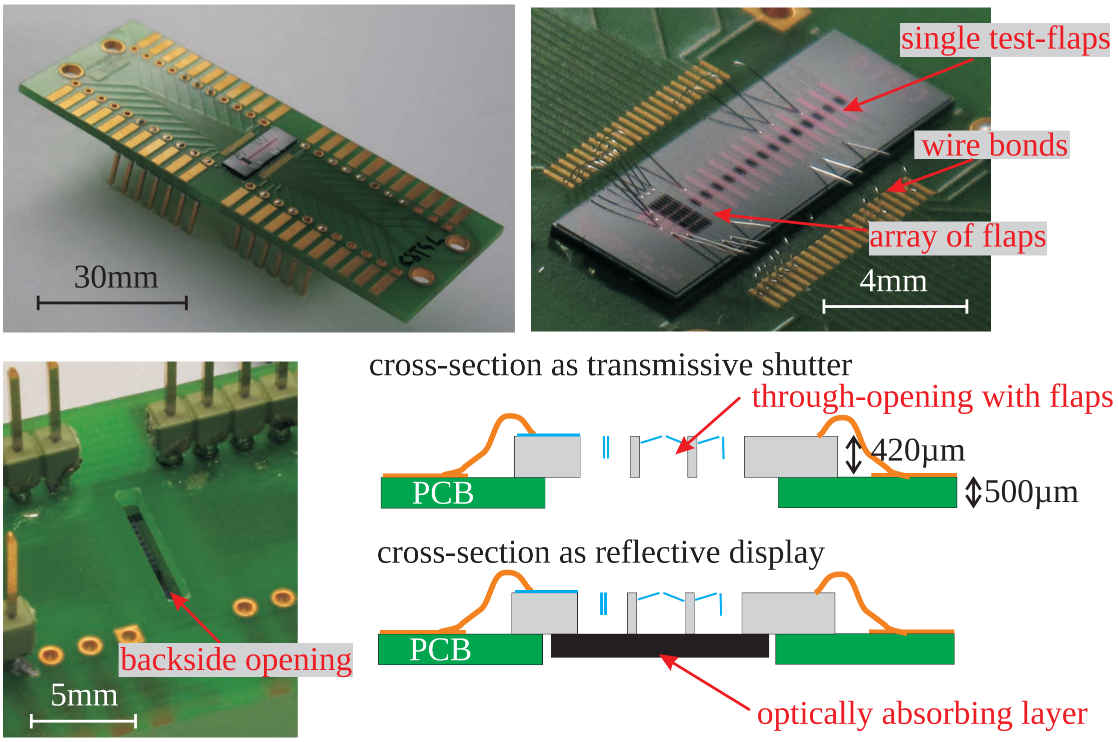

Figure 5.23: *The 4mm by 13mm large chip is glued on top of a PCB. The chip is electrically connected to the PCB by wirebonds. On the chip are located different single flaps and an array of 5 by 5 flaps. The PCB has an opening, so the optical modulators can be employed in transmission mode and as reflective display.*

6 Characterization of vertical flaps

In this chapter the fabricated vertical flaps will be characterized. We will first analyse how the fabrication succeeded, by observing released structures in a SEM. Next different working fabricated devices will be characterized electromechanically for obtaining the voltage to tilt angle trajectory. The dynamic behaviour will be tested as well. We will also analyse two devices in more detail on their optical properties of reflectivity, contrast ratio and transmissivity.

6.1 Fabrication results

The fabricated devices were characterized in a scanning electron microscope (SEM). In figure 6.1 the same structure is shown for which the fabrication process was depicted in figures 5.12 and 5.15. It consists of a device whose architecture was presented in section 5.4.1, with the zigzag shaped flap of figure 5.11. A flap with such a profile could also serve as blazed grating. It has been fabricated in a SOI-process and also in a bulk-process. On the detail image of figure 6.1 c) can be noticed the remaining elevation below the flap in the bulk substrate. The distance between the lower edge of the flap and the elevation on the substrate is about $25\mu m$. We have to make sure that this distance is large enough otherwise the flap may be pushed down at actuation or the actuation voltage may increase.

Again the architecture of section 5.4.1 can be seen in figure 6.2. This time with arrays of flat flaps. In a detail image is shown the intersection point of an electrode-row and the beams connecting the flaps along columns. SiO_2 insulates the conductive poly-silicon beam layer from the conductive bulk Si of the electrode. The SiO_2 was under-etched by about 1 to 2 μm in the HF-vapour release. On the same image we can see that the electrode was etched in the Si isotropic-etch release step. At this region the electrode's side walls are not protected by the trenches. But, up to $20\mu m$ of underetch is permitted since the electrode is wider at this area due to the trenches being curved towards the flaps.

An array of the architecture presented in section 5.4.2 is depicted in figure 6.3. It consists of single flaps which are connected to a torsion beam at an offset. In the array some beams of

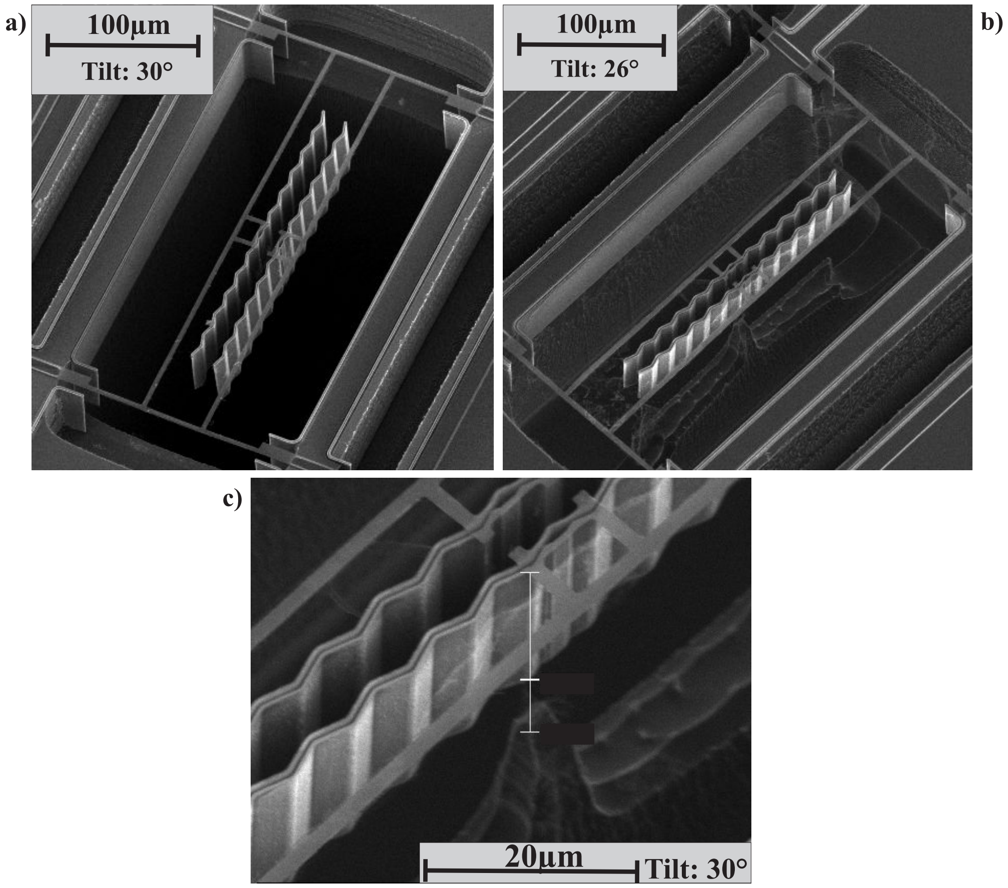

Figure 6.1: *SEM image of blazed-grating shaped flaps for which the fabrication process was presented in section 5.5. a) shows the device fabricated using the SOI-process and b)the same structure fabricated using the bulk process. c) is a detail of b) depicting the substrate below the flap in the bulk process. Below the centre of the flap there is an elevation which lays at a distance of about 25µm. On the rest of the cavity the ground lays at about 150µm below the lower rim of the flap.*

the flaps are broken. This happened either during the dry-etch release due to stress or in the wire-bonding step, which induces strong vibrations. Figure 6.3b) shows a close up of an unit consisting of a single flap with the opposing electrode. The trench at the back-side of the flap (delimiting the electrode of the unit behind) is connected to the same potential as the flap and beams. This way the there is an electrostatic shielding to the back-electrode and the flap is only attracted by electrostatic force to the front.

In figure 6.4 an image was taken of an array of double-flaps with the torsion beam connected at both lateral ends as described in section 5.4.3. The picture was made just before the final release in HF-vapour. In this device the electrode and flaps are connected along the rows. For line-column addressing an additional connection layer is required.

An example of different flap structures which have been fabricated is shown in figure 6.5. We

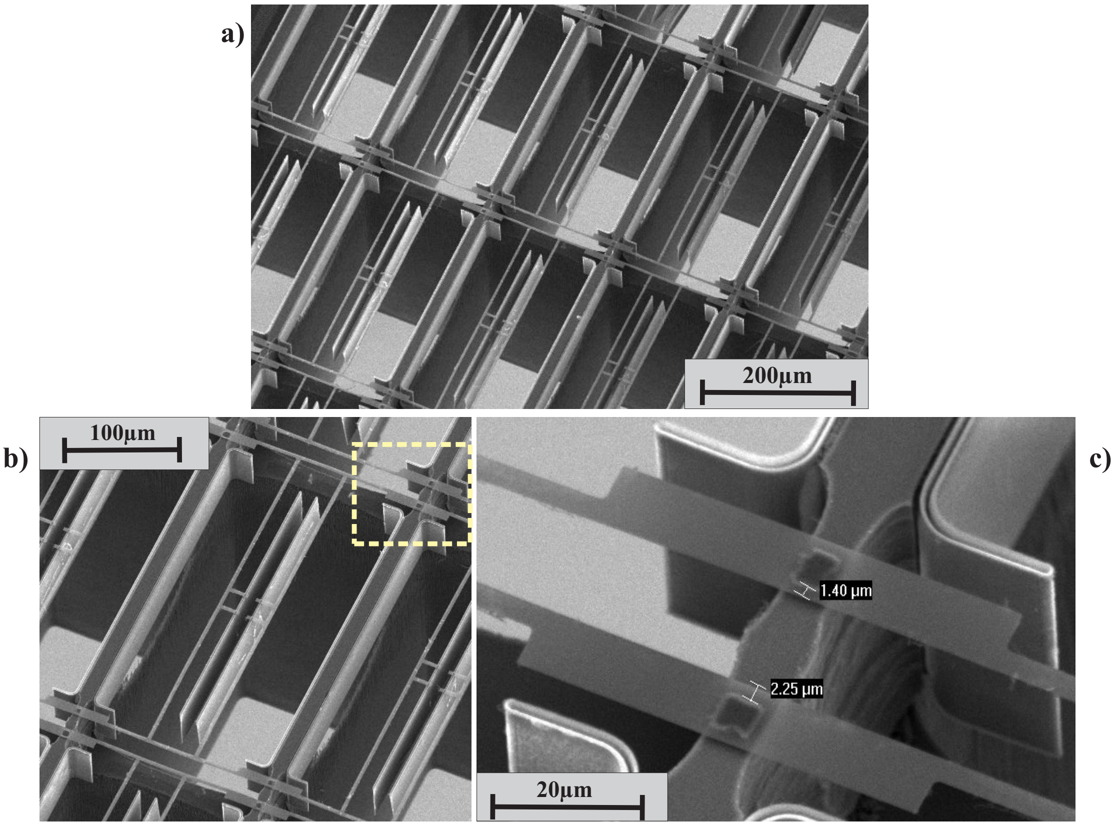

Figure 6.2: *SEM image of an array of double flaps which are suspended by beams at a certain offset. The systems architecture was presented in section 5.4.1. In the detail image c) is shown an intersection point of the electrode connected in the rows and the beams connecting the flaps along the columns. A* SiO_2 *layer which is under-etched in the HF-vapour release insulates both conductors. The under-etch of the electrode bulk-Si material can be noticed. The trench delimiting the electrode at this location is now partially free-standing.*

have in a) two comb-shaped flaps each suspended by a torsion beam at a certain offset, whose concept was presented in section 5.4.4. When a voltage difference is applied to both flaps they are supposed to tilt towards each-other. A wave-shaped flap is displayed in b) similar to the single flap shown in figure 6.3b). This shape of flap increases the viewing angle for the application as reflective display, since it reflects incoming light into all directions as described in figure 3.2. Lens shaped flaps with a corresponding curved electrode have been fabricated as well (c). In d) a grid-like structure is suspended by a torsion beam at one side as presented in figure 5.10. At the other side of the torsion beam is attached a comb-drive structure. By applying a voltage difference between the combs on the grid-structure and the combs on the bulk-substrate the structure tilts.

All of above discussed structures are made in poly-silicon. As shown in table 5.1 also other materials can be used for fabricating a flap. These materials require a conformal deposition process. Parylene combined with ALD-TiN was used in a test-run. One fabricated flap consist-

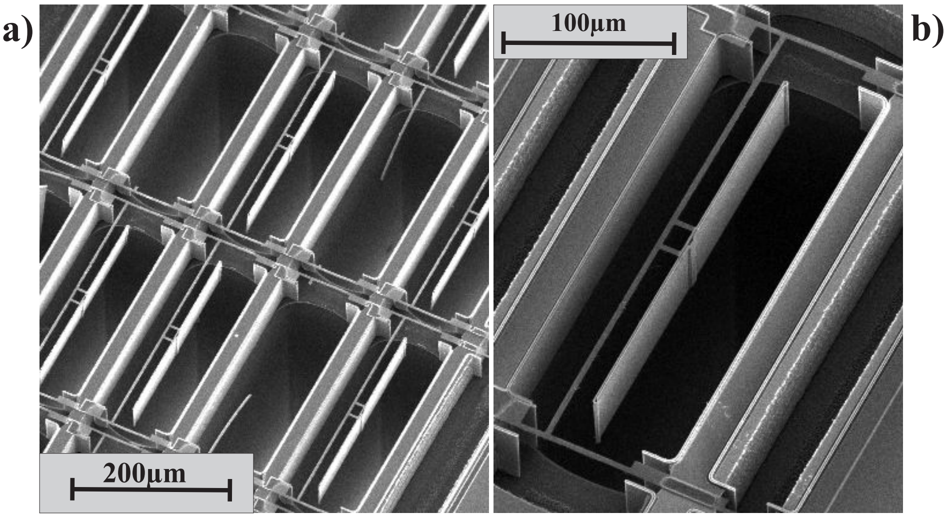

Figure 6.3: *SEM image of array of flap architecture presented in section 5.4.2. b) shows a close-up of an unit with a single flap suspended by a torsion beam at an offset. The trench at the back of the flap is set to the same potential as the flap and the beams for electrostatic shielding. In c) is depicted the same device, but with a wave-shaped flap, which should improve the reflection performance in the application as reflective display.*

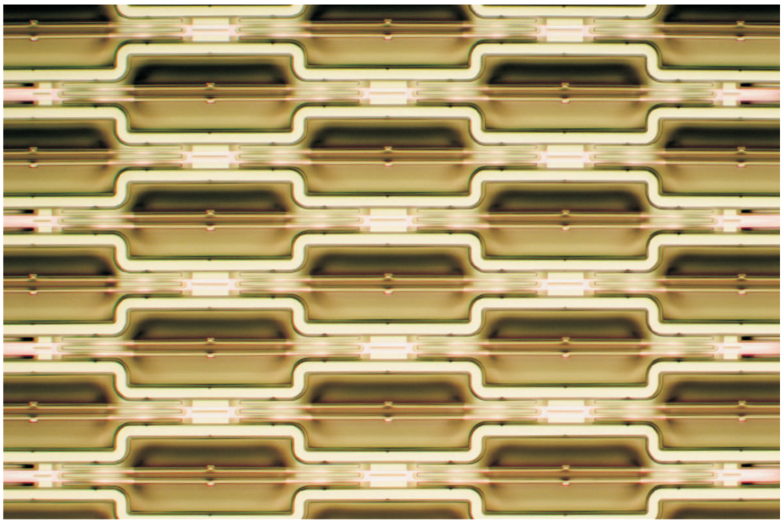

Figure 6.4: *Fabricated array of chip B type flaps as described in section 5.4.3. The array is shown just after the final release step in HF-vapour. The flaps and electrodes are connected along the rows.*

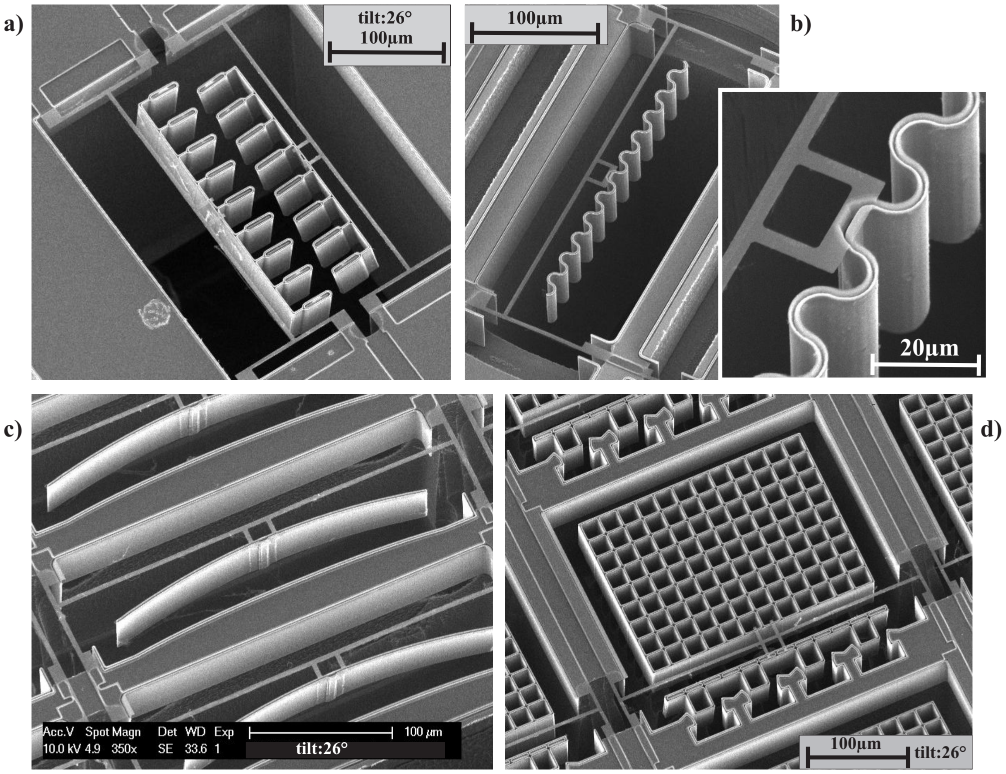

Figure 6.5: *SEM image of different flap structures whose fabrication have been demonstrated. In a) are shown two combs suspended each by a torsion bar at some offset. In b) a lens structure has an accordingly curved electrode. The grid-shaped structure in c) is suspended by a torsion beam and has a comb-drive actuator at one side.*

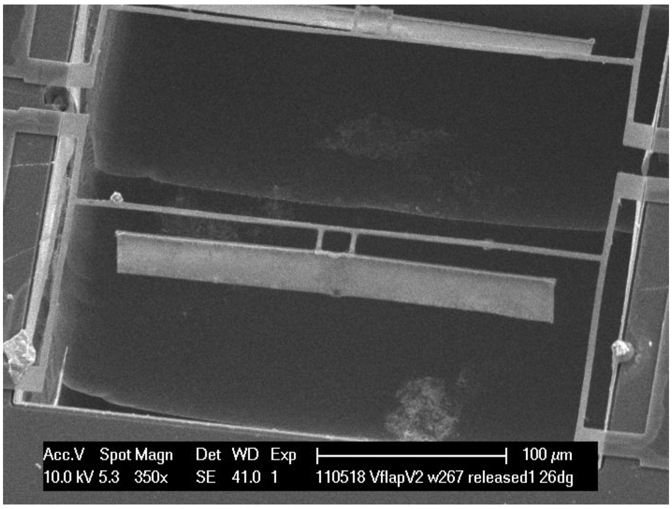

Figure 6.6: *The material of the flap shown in this SEM image is a combination of Parylene and ALD-TiN. TiN was used as conductive and reflective layer. Due to the limited deposition thickness in ALD Parylene was added as structural material with a low Young modulus.*

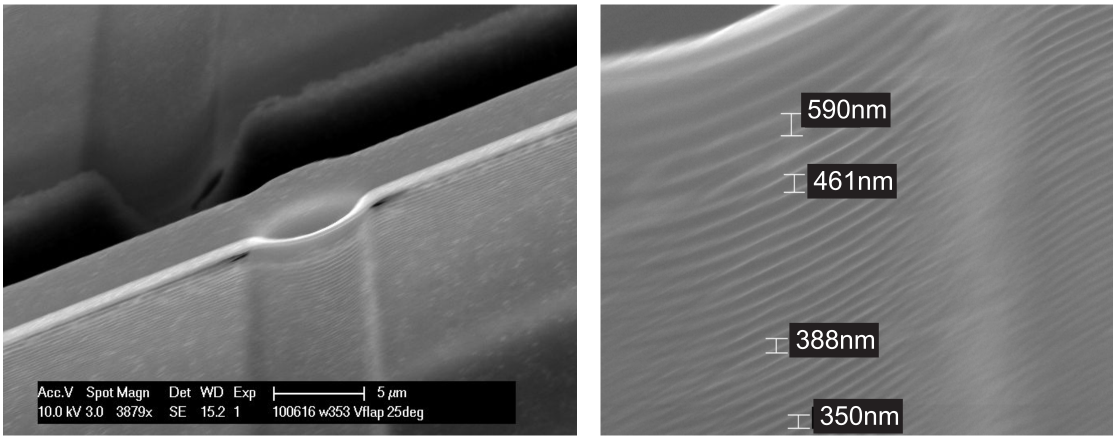

Figure 6.7: *SEM image of a flap having the beam directly on top with an interconnection only at the centre fabricated with the process described in section5.5.3. The detail image on the right shows the surface quality of the flap. It has a remaining scalloping from the trench deep etch with 500nm grid spacing. A more detailed analysis of the surface quality can be found in figure 6.32*

ing of Parylene as structural material and TiN as reflective and conductive layer is depicted in figure 6.6. Parylene was used because of its low Young Modulus [87, 88] leading to a low actuation voltage. Since Parylene is neither conductive nor has a high reflectivity a metal was added. Short circuits between the flap and the electrode were observed in the single processed wafer with Parylene as flap-material. The reason is probably that the insulating SiO_2 between the ALD-metal on the flap and beam and the conductive Si-substrate was partially etched away. This is due to the Parylene absorbing some HF in the release process using HF-vapour. The liquid HF in the Parylene etched at some location the insulating SiO_2. This issue could be addressed with a slightly different fabrication process, but was not perused further on because of lack of time.

An example of a device fabricated with the process closing the top of the trench with a CVD SiO_2 layer leading to long torsion beams, connected only at the centre of the flap is shown in figure 6.7. At the same image a SEM close-up of the surface quality of the flap is displayed. A regular scalloping can be observed with a grid spacing of about 500nm. This scalloping is due to to the DRIE process of deep-etching of the thin trenches as described in section 2.1.4. The surface quality of a flap was further analysed in section 6.3.5.

6.2 Electromechanical characterization

Different devices with typical properties representing the performance of all tilting flaps fabricated by the vertical-flap technology were characterized electromechanically. The main four chips which were tested (Chip A, B, C and D) are presented in table 6.1.

The actuation voltage to tilt-angle relationship is evaluated first in section 6.2.1. Next the

Table 6.1: *Description of chips characterized electromechanically and optically in more details. The device architecture and its geometrical dimensions are indicated. These chips were chosen for closer evaluation because they represent a typical behaviour.*
* *was estimated by fitting frequency response model to measured values in section 6.2.3.*
** *was estimated by fitting displacement vs. voltage model to measured values in section 6.2.1.*

Property	**Chip A**	**Chip B**	**Chip C**	**Chip D**
Architecture	 Single-flap with beam at offset (sect. 5.4.2)	 Double-flap with beams at side (sect. 5.4.3)	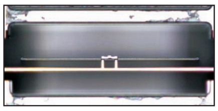 Single-flap with beam at offset (sect. 5.4.2)	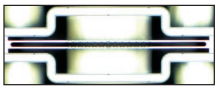 Double-flap with beams at side (sect. 5.4.3)
Process type	SOI-process	SOI-process	bulk-process	bulk-process
Flap material	poly-silicon	poly-silicon	poly-silicon	poly-silicon
Electrical connection	wire-bonded PCB	wire-bonded PCB	prober needles	prober needles
w_{flap}	$250\mu m$	217 μm	250 μm	217 μm
h_{flap}	$50\mu m$	$50\mu m$	$50\mu m$	$50\mu m$
t_{flap}	$1\mu m^{*}$	$1\mu m^{*}$	$1\mu m^{*}$	$1\mu m^{*}$
l_{beam}	$145\mu m$	$142\mu m$	$145\mu m$	$142\mu m$
w_{beam}	$3.5\mu m$	$3.5\mu m$	$3.5\mu m$	$3.5\mu m$
t_{beam}	$130\mu m^{**}$	$145\mu m^{**}$	$120\mu m^{**}$	$140\mu m^{**}$
E_{mod}	$160\mu m$	$160\mu m$	$160\mu m$	$160\mu m$
d	$75\mu m$	$65\mu m$	$66\mu m$	$64\mu m$ / $66\mu m$
q	$15\mu m$	$0\mu m$	$15\mu m$	$0\mu m$

transient and frequency response of a device is characterized in section 6.2.3.

6.2.1 Tilt-angle measurements

The difficulty when measuring the tilt angle is the steepness of the flap at rest state and at low voltages. At tilt angles of less than 45° there is no upwards light reflection and measuring the tilt angle with the classical method of looking at the displacement of a reflected laser beam is not a solution.

Two different methods were used for measuring the tilt angles:

- The length of the flap-profile is measured from the top. By taking the flap height as a known value the angle can be calculated by trigonometry.

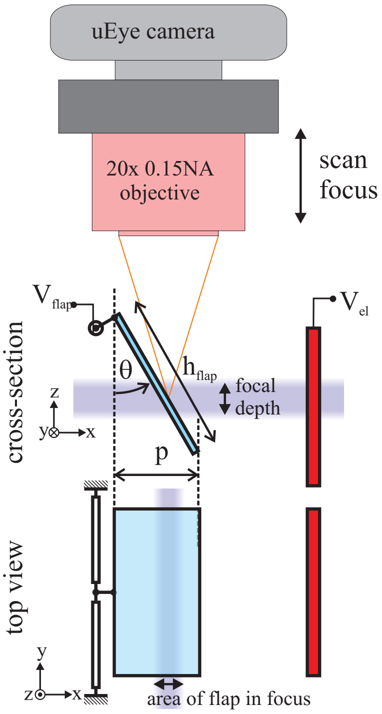

Figure 6.8: *Setup for measuring tilt angle θ of a flap in function of the actuation voltage. The device is observed from the top with a microscope, such that we can measure the length p. Since the focal depth of the microscope is only about 6μm, pictures had to be taken at different focal distances. The images were combined in a focal stacking program Combine ZP.*

- The tilt angle is measured using an optical profiler which uses white light vertical scanning interferometry .

6.2.1.1 Flap profile length measurement method

For measuring the tilt angle of the flap the length of its profile as seen from the top was metered as depicted in figure 6.8. It was supposed that the flap height is known, since the device was fabricated on an SOI-wafer, though h_{flap} being defined by the thickness of the device layer. The tilt angle θ can be obtained from the profile length p with the following relation:

$$\theta = \arcsin(\frac{p}{h_{flap}}) \qquad (6.1)$$

The measurement was done in a microscope with an objective having a field of view covering the maximal value of p. A 20x magnification objective was used having a focus depth of $6.1\mu m$. Since the focus depth is smaller than the total flap height, several images at different focal distances were recorded. The pictures were subsequently combined to an image with a high focal depth. For combining the pictures was used the freeware program CombineZP [89].

Table 6.2: *Estimated errors in variables for calculation of* $\theta_{profile}$ *using the flap profile measurement method*

Error variable	**Error**	**Comments**
ΔN_{pixels}	2 pixels	Pixel error due to wrong estimation of flap-rim location, because of low contrast in the image.
ΔS	2%	Relative error in the pixel to μm conversion scale.
Δh_{flap} (SOI-wafer)	$1\mu m$	For the device fabricated on a SOI-wafer the flap height is defined by the device layer thickness, but there might be process variations.
Δh_{flap} (bulk-wafer)	$2\mu m$	For the device fabricated on a bulk-wafer the flap height is controlled in fabrication by the etch depth, which gives a larger uncertainty in h_{flap} than in the SOI-wafer case.

Error evaluation of profile measurement method The profile length p is obtained by measuring in the focus-stacked image the number of pixels N_{pixels} between the upper and lower rim of the flap and multiplying it with the image-scale S. We have thus $p = N_{pixels} \cdot S$. S was previously measured with a known dimension on a calibration image.

The equation for obtaining the angle of the flap $\theta_{profile}$ can be written as:

$$\theta_{profile} = \arcsin\left(\frac{N_{pixels} \cdot S}{h_{flap}}\right) \tag{6.2}$$

There are three possible error contributors in the tilt angle measurement.

- ΔN_{pixels}: The profile length of the flap as numbers of pixel in the image can be measured wrong. In low contrast images the location of the top and bottom rim of a flap are difficult to evaluate.
- ΔS: The error in the scale used to convert the flap profile length in number of pixels into micrometers.
- Δh_{flap}: The error in flap height. For a flap fabricated in the SOI-process h_{flap} is directly given by the device layer thickness, but there might still be some variations in fabrication. In the bulk-process h_{flap} can only be estimated or requires to have been previously measured.

The absolute error in tilt angle $\Delta\theta_{profile}$ due to the error in the above given variables can be written with the total derivative of $\theta_{profile}$:

$$\Delta\theta^2_{profile} = \left|\frac{d\theta_{profile}}{dN_{pixels}}\right|^2 \cdot \Delta N^2_{pixels} + \left|\frac{d\theta_{profile}}{dS}\right|^2 \cdot \Delta S^2 + \left|\frac{d\theta_{profile}}{dh_{flap}}\right|^2 \cdot \Delta h^2_{flap} \tag{6.3}$$

When equation (6.3) is computed using (6.2) we obtain:

$$\Delta\theta^2_{profile} = \frac{1}{1-\left(\frac{N_{pixels}S}{h_{flap}}\right)^2}\left\{\left(\frac{S}{h_{flap}}\right)^2 \cdot \Delta N^2_{pixels} + \left(\frac{N_{pixels}}{h_{flap}}\right)^2 \cdot \Delta S^2 + \left(\frac{N_{pixels}S}{h^2_{flap}}\right)^2 \cdot \Delta h^2_{flap}\right\} \tag{6.4}$$

The absolute error of the tilt angle in the flap-profile measurement method $\Delta\theta_{profile}$ is finally expressed as:

$$\Delta\theta_{profile} = \sqrt{\frac{1}{h^2_{flap} - N^2_{pixels}S^2}\left(S^2 \cdot \Delta N^2_{pixels} + N^2_{pixels} \cdot \Delta S^2 + \left(\frac{N_{pixels}S}{h_{flap}}\right)^2 \cdot \Delta h^2_{flap}\right)} \tag{6.5}$$

The estimated errors of the different variables for calculating $\theta_{profile}$ are given in table 6.2.

6.2.1.2 Optical profiler measurement method (white light interferometer)

Another method to measure the tilt angle is to use an optical profiler. A Wyko NT1100 optical profiling system from Veeco [90] was utilized which employs white light vertical scanning interferometry as measurement principle.

The challenge of a white light interferometer measurement is given by the maximal measurable tilt towards the optical axis of the instrument, due to the limited acceptance angle of the employed objective. Tilt angles from the horizontal larger than 15° are very difficult to measure. To be able to measure higher tilt angles the chip was positioned with a certain pre-tilt $\alpha_{pre-tilt}$ below the equipment. Thanks to roughness at the edge of the flaps also at steeper angles there was some back reflection, such that the contour of the flap could be measured. A schematic of the measurement setup is shown in figure 6.9. Two different measurement methods were used. For larger tilt angles θ_{wyko} the tilt was measured on the flap surface with the profile $x1_{wyko}$ and the corresponding height data $z1_{wyko}$. θ_{wyko} was obtained in this case with the following equation:

$$\theta_{wyko} = \arctan\left(\frac{x1_{wyko}}{z1_{wyko}}\right) - \alpha_{pre-tilt} \tag{6.6}$$

For small θ_{wyko} there is not enough back reflection from the flap surface. The measurement is done with a objective of high magnification (50x) on top of the torsion-beam and flap.

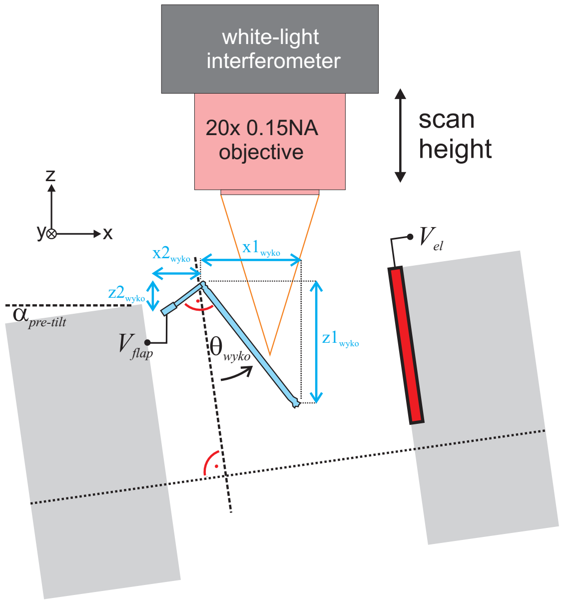

Figure 6.9: *Schematic of white light interferometer measurement setup for measuring tilt angle of a flap in function of the actuation voltage. The device is placed at a certain pre-tilt of* $\alpha_{pre-tilt}$ *for the purpose to be able to measure steeper angles, since the maximal possible observation angle is limited by the numerical aperture of the objective. Due to roughness on the flap surface also small* θ_{wyko} *could be measured employing* $x1_{wyko}$ *and* $z1_{wyko}$ *in equation (6.6). A second method consists of measuring the tilt-angle on top of the beam using* $x2_{wyko}$ *and* $z2_{wyko}$ *with equation (6.7)*

The profile $x2_{wyko}$ and height difference $z2_{wyko}$ are used to calculate the tilt-angle with the following equation:

$$\theta_{wyko} = \arctan\left(\frac{z2_{wyko}}{x2_{wyko}}\right) - \alpha_{pre-tilt} \tag{6.7}$$

A sample white light interferometer height profile demonstrating the tilt angle measurement method on the flap surface is shown in figure 6.10 on the left. This profiler measurement was done with the flap actuated at 42V with a 20x objective and 1x additional magnification. It can be noticed that only the top and lower edge of the flap is visible. Even though of $\alpha_{pre-tilt} = 4.9°$, the tilt-angle of the flap surface is higher than the maximal measurable angle with the instrument. Due to some roughness on the edges of the flap surface some height data is obtained on these locations. In the cross-sectional data A-A the values $x1_{wyko}$ and $z1_{wyko}$ are measured to calculate θ_{wyko} using equation (6.6).

With a 50x objective and 1x additional magnification the height profile on top of the torsion beam is obtained as shown in figure 6.10 on the right. It corresponds to the detail II with the torsion beam and top edge of the flap. A pre-tilt of 2.56° keeps the tilt angle of the top beam surface inside the acceptance angle of the instrument. The height $z2_{wyko}$ and profile $x2_{wyko}$ are measured in the cross-section B-B. θ_{wyko} can be calculated using equation (6.7).

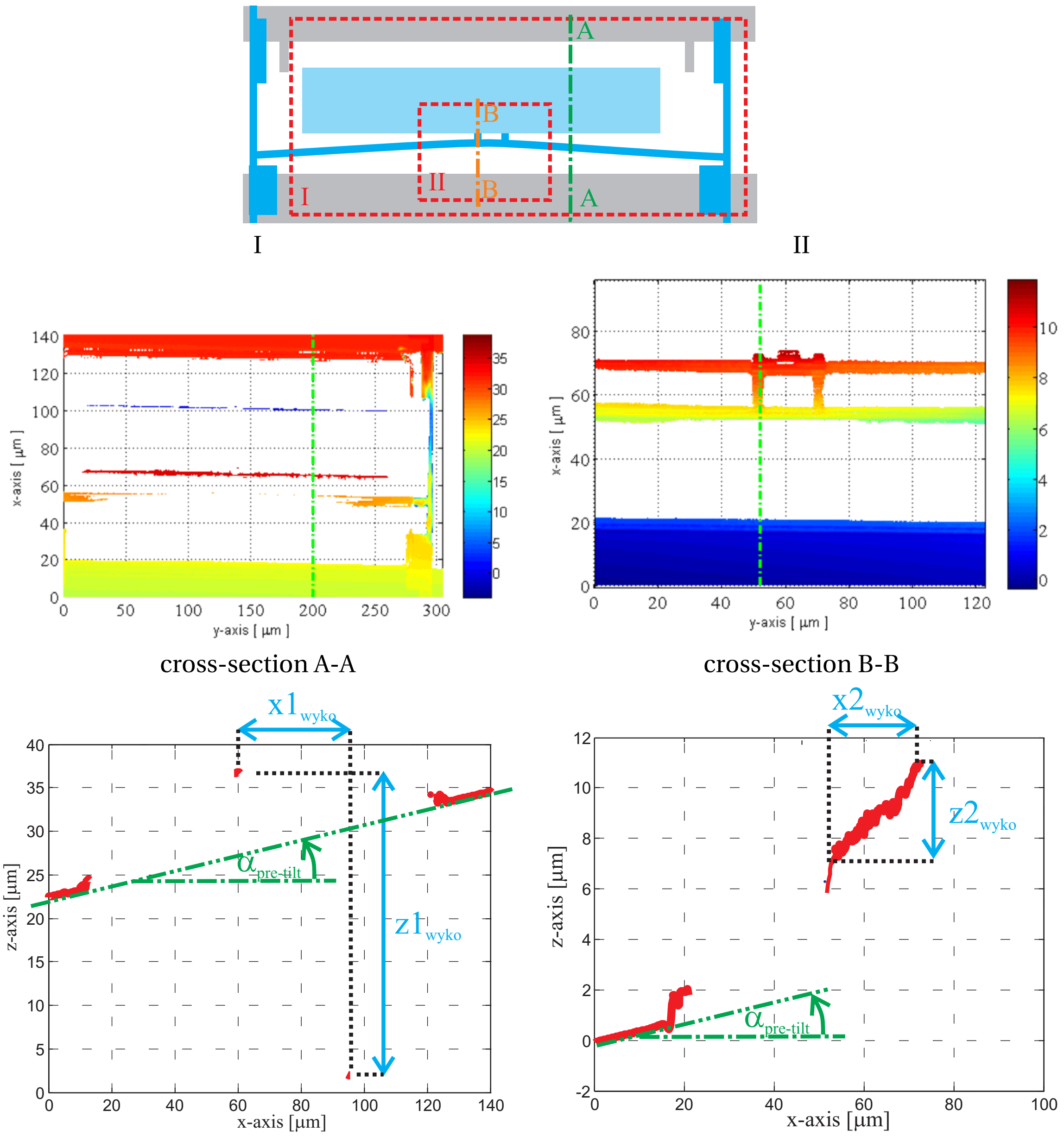

Figure 6.10: *Here is illustrated the concept used for the tilt angle measurement on the optical profiler. We see on the top a schematic of the tilted flap with the marked areas I and II.*
In area I the height profile was obtained using a 20x objective with chip A actuated at 42V and placed at a $\alpha_{pre-tilt} = 4.9°$ *below the instrument. Due to some roughness height data is obtained for the edges of the flap surface, despite its steepness. The tilt angle* θ_{wyko} *is obtained inserting the measured distances* $x1_{wyko}$ *and* $z1_{wyko}$ *in equation (6.7).*
In area II the height profile was obtained using a 50x objective with chip A actuated at 35V and $\alpha_{pre-tilt} = 2.56°$*. The tilt angle* θ_{wyko} *is obtained here by measuring the distances* $x2_{wyko}$ *and* $z2_{wyko}$ *on top of the torsion beam and top edge of the flap and by employed the values in equation (6.7). This method is utilized for* $\theta_{wyko} < 35°$*, where no height-data is obtained for the edges of the flap surface.*

Table 6.3: *Estimated error in variables for calculation of θ_{wyko} using optical profiler measurement method (white light interferometer)*

Error variable	Error	Comments
x_{wyko}	2%	Relative error in profile length measurement due to inaccuracy of scale.
z_{wyko}	2%	Relative error in height measurement due inaccuracy of scale and surface roughness.
$\alpha_{pre-tilt}$	2%	Relative error in pre-tilt measurement due to unevenness of the chip surface where the tilt is measured.

Error evaluation of optical profiler measurement method Similar to equation 6.3 the absolute error of the tilt angle $\Delta\theta_{wyko}$ can be calculated by the total derivative. The errors Δx_{wyko} and Δy_{wyko} of the variables x_{wyko} and y_{wyko} are taken in to account.

$$\Delta\theta^2_{wyko} = \left|\frac{d\theta_{wyko}}{dx_{wyko}}\right|^2 \cdot \Delta x^2_{wyko} + \left|\frac{d\theta_{wyko}}{dz_{wyko}}\right|^2 \cdot \Delta z^2_{wyko} + \left|\frac{d\theta_{wyko}}{d\alpha_{pre-tilt}}\right|^2 \cdot \Delta\alpha^2_{pre-tilt} \tag{6.8}$$

For the case of measuring θ_{wyko} on the flap surface equation (6.6) is employed in equation (6.8) such that the absolute error in tilt angle can be expressed as:

$$\Delta\theta^2_{wyko1} = \left(\frac{1}{1+\left(\frac{x1_{wyko}}{z1_{wyko}}\right)^2}\right)^2 \left\{\left(\frac{1}{z1_{wyko}}\right)^2 \cdot \Delta x1^2_{wyko} + \left(\frac{x1_{wyko}}{z1^2_{wyko}}\right)^2 \cdot \Delta z1^2_{wyko}\right\} + \Delta\alpha^2_{pre-tilt} \tag{6.9}$$

$$\Delta\theta_{wyko1} = \sqrt{\left(\frac{z1_{wyko}}{z1^2_{wyko}+x1^2_{wyko}}\right)^2 \left\{\Delta x1^2_{wyko} + \left(\frac{x1_{wyko}}{z1_{wyko}}\right)^2 \cdot \Delta z1^2_{wyko}\right\} + \Delta\alpha^2_{pre-tilt}} \tag{6.10}$$

For the case of measuring θ_{wyko} on the top of the torsion beam equation (6.7) is employed in equation (6.8) such that the absolute error in tilt angle can be expressed as:

$$\Delta\theta^2_{wyko2} = \left(\frac{1}{1+\left(\frac{z2_{wyko}}{x2_{wyko}}\right)^2}\right)^2 \left\{\left(\frac{1}{x2_{wyko}}\right)^2 \cdot \Delta z2^2_{wyko} + \left(\frac{z2_{wyko}}{x2^2_{wyko}}\right)^2 \cdot \Delta x2^2_{wyko}\right\} + \Delta\alpha^2_{pre-tilt} \tag{6.11}$$

$$\Delta\theta_{wyko2} = \sqrt{\left(\frac{x2_{wyko}}{x2^2_{wyko}+z2^2_{wyko}}\right)^2 \left\{\Delta z2^2_{wyko} + \left(\frac{z2_{wyko}}{x2_{wyko}}\right)^2 \cdot \Delta x2^2_{wyko}\right\} + \Delta\alpha^2_{pre-tilt}} \tag{6.12}$$

The estimated errors for the different variables for calculating θ_{wyko} are given in table 6.3.

6.2.1.3 Results and discussion

In figures 6.11 and 6.12 is given the tilt angle θ in function of the actuation voltage as measured using both methods presented above on chip A, B, C and D. The dimensions and properties of the different chips are indicated in table 6.1. For each chip is fitted a trajectory curve of the reduced-order model of section 3.2.2. The parameters employed for the fit of the simulation are noted in table 6.4. We will now discuss the trajectory curves of the four chips measured which represent typical actuation behaviours.

Chip A The flap could be actuated to a maximal tilt angle of 55° at an actuation voltage of about 60V. All angles could be reached, since there was no pull-in on the trajectory. The same trajectory was obtained with increasing as with decreasing voltages. At actuation voltages above 65V could be observed a pull-in towards the electrode and sticking of the flap. The largest change in tilt angle was found between 35 and 40V. The flap-profile measurement method and the optical profiler (Wyko) gave similar results. Nevertheless they differed at actuation voltages below 35V. The difference may originate in a systematic error of the Wyko measurement method on top of the torsion beam. The error of this method may not have been estimated well in table 6.3.

Two simulations models were fitted to the measured data, one with only one electrode (model 1 of figure 3.8) and another taking into account the bulk-substrate acting as electrode as well (model 3 of figure 3.9). Model 1 fits better to the data for large tilt angles, whereas model 3 fits better at small angles. In model 3 the flap is also attracted electrostatically by the underlying silicon substrate and not only by the electrode as in model 1. Therefore it might be deduced that there was an attraction force from the substrate at low torsion angles which is overwhelmed by the attraction of the electrode at larger tilt angles. Since the substrate was kept at a floating potential some charges in this layer may lead to electrostatic forces, which are particularly important at low attraction forces from the electrode (i.e. at small tilt angles). At larger tilt angles the flap is further away from the charged substrate such that the model with only one electrode (model 1) fits better the data.

For both simulation-fits was used a smaller electrode-beam distance d as the chip actually has ($d = 66\mu m$ instead of $d = 75\mu m$). The actual d of the fabricated device may be smaller due to some misalignment of flap and beam . This may account to maximal $3\mu m$ difference in d. Another error may come from the inaccuracy of the model, where the force in z-direction and also the fringing field at both lateral ends of the flap have not been taken into account, for example.

Chip B The flap could be actuated to a tilt angle of up to 65° at an actuation voltage of about 60V. The trajectory curve was different for increasing and decreasing voltages. At increasing voltages we had a pull-in at about 50V from θ =18 to 55°. As the voltage were decreased again the flap remained at tilt angles above 50° down to 47V. When lowering the actuation voltage

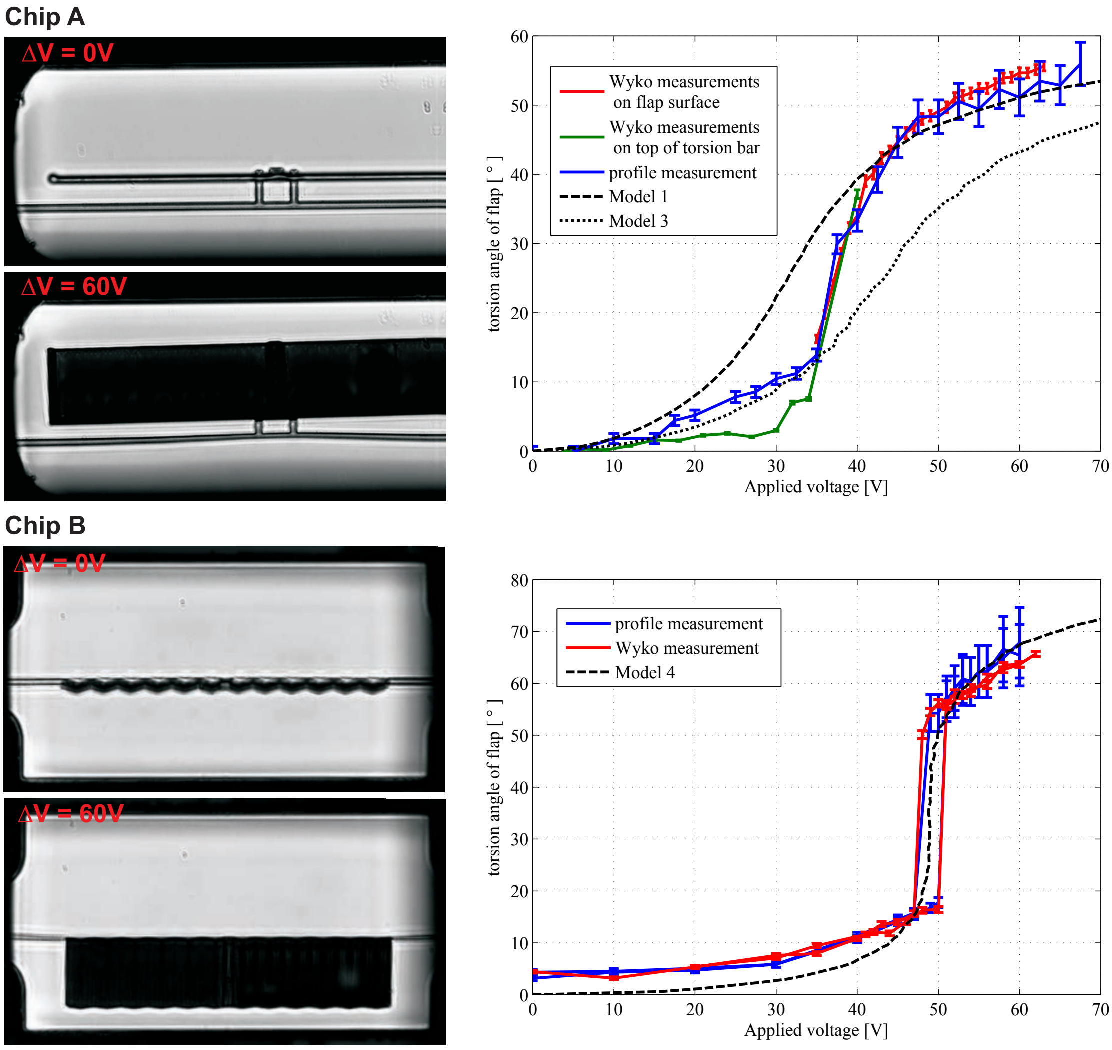

Figure 6.11: *Measurement of tilt angle θ in function of actuation voltage V with the corresponding fit to the reduced order model of section 3.2.2. Chip A could be tilted to $\theta = 55°$ with an actuation voltage of about 60V. All tilt angles could be reached, since there was no pull-in in the actuation curve. Tilt angles of 65° could be reached with chip B at an actuation voltage of 60V. The curve shows different trajectories at increasing and at decreasing voltages. This chip had a pull-in from $\theta = 18°$ to 55° at 50V. The angles in-between could not be reached. When lowering the voltage the pull-out was at a lower voltage of 47V.*

further we had a pull-down directly to $\theta = 18°$. At higher actuation voltages than 60V the flap was not tested, since a pull-in towards the electrode could occur and break the device. The measurements done with the methods of profile length measurement and optical profiler (Wyko) agreed quite well along the whole trajectory.

In this device one of the double-flaps was non-existent since it had broken before. So, the flap was attracted by both electrodes at the front- and back-side. Therefore we chose model 4

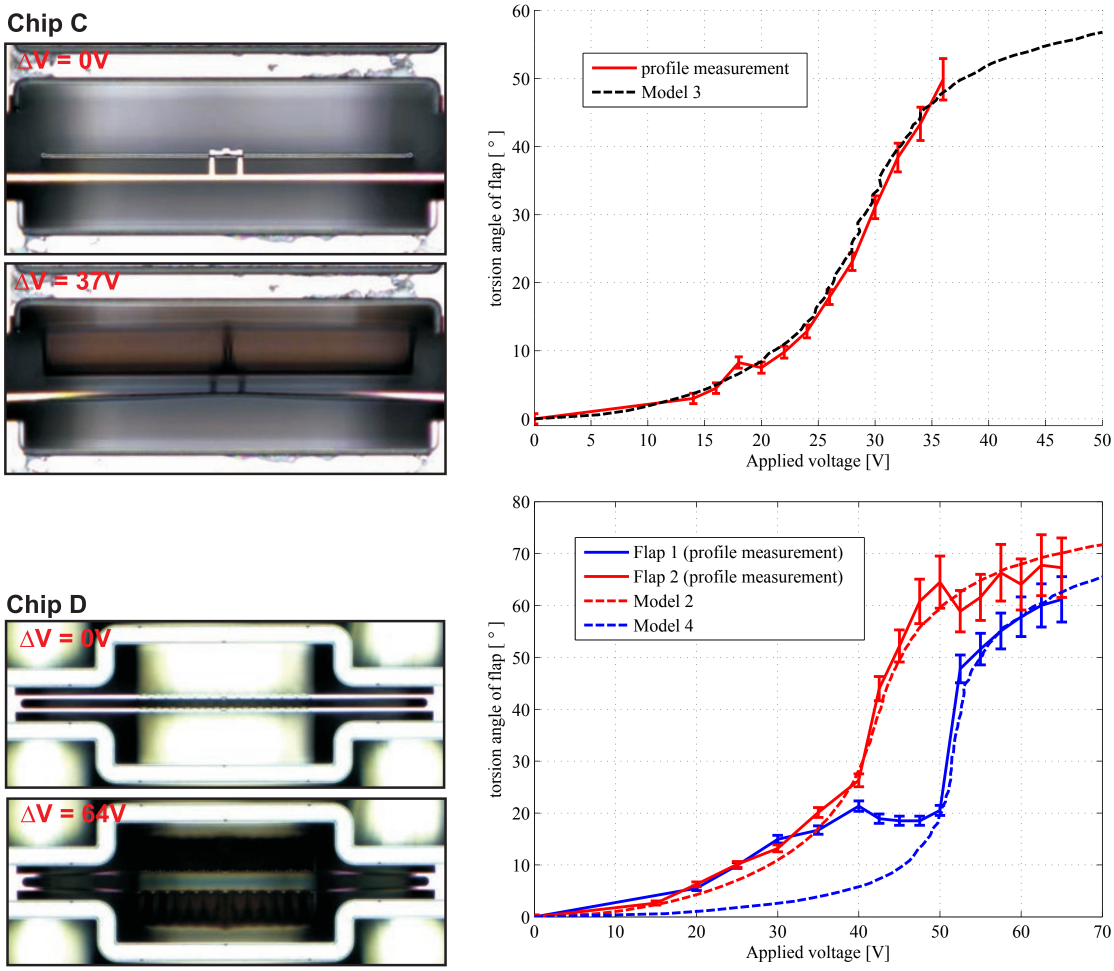

Figure 6.12: *Measurement of tilt angle* θ *in function of actuation voltage* V *with the corresponding fit to the reduced order model of section 3.2.2. Chip C could be actuated at very low voltage of 35V to a tilt angle of 50°, since the electrode-beam distance* d *was lower than for chip A. In chip D the trajectory curve of each of the double flaps is shown separately. Flap 2 tilted at lower voltage than flap 1. The flaps were actuated at 65V to* $\theta = 65°$.

of section 3.9 to be fitted to the measured values. With an electrode-beam distance d $5\mu m$ smaller than the device actually has ($d = 60\mu m$ instead of $d = 65\mu m$) the model fits well to the measurements. The reason for the difference in d may be due by the form of the flap. It has a zigzag shape and model 4 was calculated for a flat flap.

Chip C This flap could be actuated at a very low voltage of 35V to a tilt angle of 50°. All tilt angles could be reached and from 10 to 50° the voltage to tilt angle relation was almost linear. The chip was only measured with the flap-profile measurement method. Since the device was fabricated on a bulk substrate, the whole substrate acted as electrode. The best model corresponding to this case is model 4 given in figure 3.9. This model fitted with a d of $60\mu m$

Table 6.4: *Employed models and parameters for fitting to measured data of tilt angle in function of actuation voltage. The model types are described in section 3.2.2. As beam material polysilicon is employed with the parameters as given in table 3.3.*

Chip Type	Model Type	electrode - beam distance d	t_{beam}	l_{beam}	w_{beam}
A	1	$66\mu m$	135nm	$145\mu m$	$250\mu m$
A	3	$66\mu m$	135nm	$145\mu m$	$250\mu m$
B	4	$60\mu m$	145nm	$142\mu m$	$217\mu m$
C	3	$60\mu m$	120nm	$145\mu m$	$250\mu m$
D (flap 1)	4	$64\mu m$	140nm	$142\mu m$	$217\mu m$
D (flap 2)	2	$62\mu m$	140nm	$142\mu m$	$217\mu m$

instead of the real $66\mu m$ agrees well with the measured data.

Chip D The double flaps could be actuated at voltages of 65V to tilt angles of about 65°. Both flaps had a different trajectory. Model 2 with only one electrode fits better to flap 2. Model 4 with two electrodes fits better to flap 1. For both a $2\mu m$ smaller d is employed in the model than the devices actually had because of the zigzag shape of the flap. At small angles both flaps followed the same trajectory and agreed to model 2 with one electrode. Here flap 1 served as electrostatic shielding of its electrode towards flap 2 and vice versa. At 40V flap 2 tilted to larger angles. The reason was that it had a $2\mu m$ smaller d than flap 1 (because of an error in the mask). From this point onwards flap 1 followed the model 4 with two electrodes, since flap 2 did not shield any more the opposite electrode.

Various flap shapes and configurations As described above different other flap configurations and profiles could be fabricated with the vertical flaps process. Flaps with the profile shape of a comb, wave, lens and gird were obtained as depicted in figure 6.5. These more particular flap-shapes were not characterised on the whole voltage to tilt-angle trajectory, but just the ON-OFF switching was tested. The measurement results are summarized in table 6.5. The tilt angle measurement was done with the profile length measurement method of section 6.2.1.1. The following behaviour can be observed for the different configurations:

- **Double flap with off-centred beam:** This architecture was presented in section 5.4.1. It consists of two flaps, each suspended by a torsion beam which located at a distance $q = 15\mu m$ closer to the electrode. In this configuration the electrode-flap distance is higher than in case of chips A, B, C and D, leading to higher actuation voltage. But the flap can be tilted to larger tilt angles close to 90° due to the favourable geometry. One test device fabricated on a bulk wafer was actuated at 57V to a tilt angle of about 90°. These flaps were touching the electrodes, what led to sticking in some cases.
- **Wave-shaped single-flap with off-centred beam:** In this device the beam is as well placed closer to the electrode as in the double flap above. This geometry permits the flap

Table 6.5: *A variety of devices types actuated at a voltage difference ΔV between flap and electrode (or opposite second flap) and measured tilt angle θ evaluated by profile-length measurement method. The dimensions of the devices are as given in table 3.3, if not otherwise stated.*

	Rest-state no voltage applied	**Actuated with ΔV**		
Double flap with off-centered beam	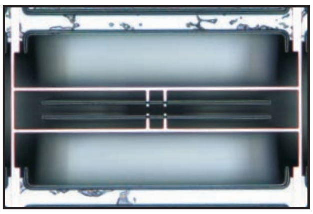	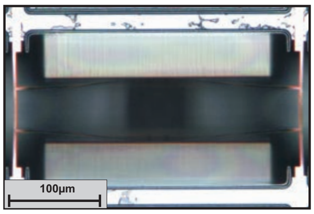	$\Delta V = 57$V $\theta \approx 90°$	$d = 62\mu m$ $q = 15\mu m$ $w_{flap} = 250\mu m$ bulk-process
Wave-shaped single-flap with off-centered beam	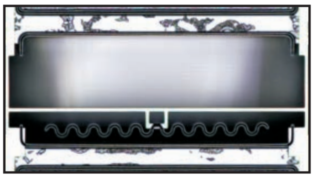	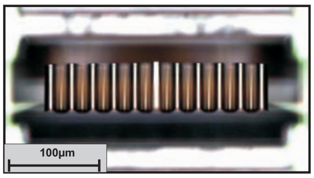	$\Delta V = 85$V $\theta \approx 90°$	$d = 74\mu m$ $q = 15\mu m$ $w_{flap} = 250\mu m$ bulk-process
Two flaps actuated against each other beam off-centered	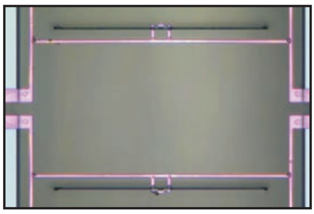	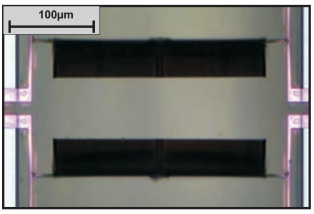	$\Delta V = 85$V $\theta \approx 70°$	$d_{beam\text{-}beam} = 158\mu m$ $q = 15\mu m$ $w_{flap} = 250\mu m$ SOI-process
Two comb-shaped flaps actuated against each other beam off-centered	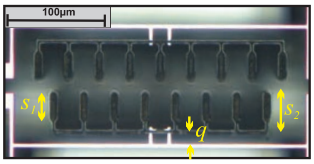	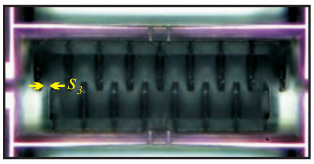	$\Delta V = 7.5$V $\theta_{top} = 14.5°$ $\theta_{bottom} = 11°$	$d_{beam\text{-}beam} = 123\mu m$ $q = 15\mu m$ $s_1 = 30\mu m$ $s_2 = 40\mu m$ $s_3 = 9.5\mu m$ bulk-process
Grid actuated by comb-fingers	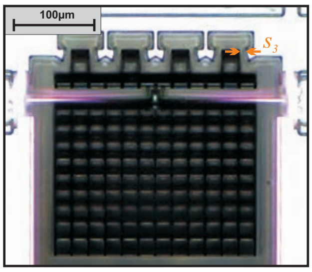	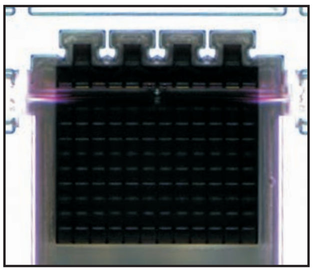	$\Delta V = 7$V $\theta_{\Delta V=0V} = 17°$ $\theta_{\Delta V=7V} = 28°$	$w_{grid} = 250\mu m$ $s_3 = 6\mu m$ SOI-process
Lens-shaped flap with off-centered beam	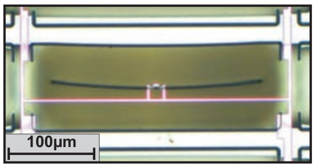	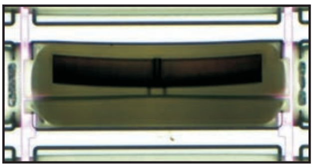	$\Delta V = 32$V $\theta = 42°$	$d = 68\mu m$ $q = 15\mu m$ $f_{focus} = 500\mu m$ SOI-process
	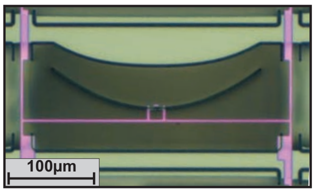	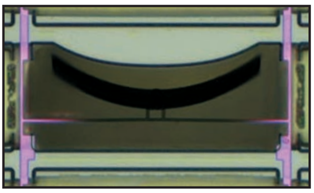	$\Delta V = 30$V $\theta = 29°$	$d = 92\mu m$ $q = 15\mu m$ $f_{focus} = 83\mu m$ SOI-process

to tilt to angles close to θ =90°. A measured device required an actuation voltage of 85V. The flap has a wave-shape. Such as shape can be useful in the application as reflective display for reflecting light form all direction such to have a large angular viewing range (as depicted in figure 3.2). The periodic wave-shape can also be interpreted as diffraction grating structure. We have here an example of a switchable grating.

- **Two flaps actuated against each other:** The two flaps are suspended by a torsion beam at some offset as on the two devices above, permitting to attain large tilt angles. The distance between the two torsion beams is $d = 158\mu m$. As a voltage difference of 85V is applied between the two flaps they tilt towards each-other reached each a tilt angle of 70°. This demonstrates the working principle of two flaps being actuated towards each-other. At higher actuation voltage the flaps pulled-in towards each-other leading to sticking. Also on devices with smaller beam-beam distance d a pull-in leading to sticking could be observed.

- **Two comb-shaped flaps:** The architecture of two comb-shaped flaps suspended by a torsion beam were presented in section 5.4.4 and schematically depicted in figure 5.10. When applying a voltage between the two flaps they tilt towards each-other. Because of the comb-shape we have a larger surface leading to a larger electrostatic force giving much lower actuation voltages. The combs are thicker at the outer front part, such to limit the displacement in torsion before the two flaps touch. The characterised device could be tilted to angles of θ = 14.5° and 11° at an actuation voltage of 7.5V. At higher voltages there is an instability in twist-direction and the two sides of the combs touch, leading to stiction.

- **Grid shaped flap:** The architecture of a grid shaped flap was discussed in section 5.4.4 with a schematic in figure 5.10. The device consists of a grid-shaped structure suspended by a torsion beam on one side. On the opposite side of the torsion beam is placed a comb-shaped structure with comb-shaped electrodes in the device layer of the SOI-wafer. The material of the handle layer below the whole structure is etched away. By applying a voltage between the suspended comb-structure and the electrode the structure tilts. The comb-structure is tilted upwards, whereas the gird-structure is tilted downwards accordingly. The characterised device had a pre-tilt after fabrication of 17°. When applying a voltage of 7V between the suspended structure and the comb-shaped electrode a tilt of 28° is measured, what corresponds to a net-tilt of 11°. This small tilt can already be used for optical modulation in transmission.

- **Lens shaped flap:** Flaps with parabolic shape have been fabricated with various focal distances. One flap has a focal distance $f_{focus} = 500\mu m$ and the other $f_{focus} = 83\mu m$. The opposing electrode is curved accordingly, such that the flap can not touch the electrode as it tilts. The flap with the larger f_{focus} was actuated to a tilt angle of 42° at 32V actuation voltage. The flap with short f_{focus} (with a larger curvature) was actuated at 30V to a tilt angle of 29°. At higher actuation voltages was observed a pull-in towards the electrode leading to stiction. The characterised flaps were fabricated with the SOI-process. Such tilting lens-shaped flaps could be used when arranged in an array as switchable lens or adaptive lens device.

6.2.2 Actuation in an array

The actuation of different flaps in a 3 by 2 array identical to chip A was demonstrated. In this chip the electrodes are connected together along the rows and the flaps along the columns. A voltage of 0 V was applied to the corresponding column on which the flaps should be actuated. On the corresponding electrode row was applied a voltage of 50V. The other rows and columns were set to floating potential. In table 6.6 the actuation of different flaps is shown.

Table 6.6: *Single flaps actuated separately in a 3 by 2 array of chip A type. 0V and 50V were applied to the corresponding electrode row and flap column. The other connections were at floating potential.*

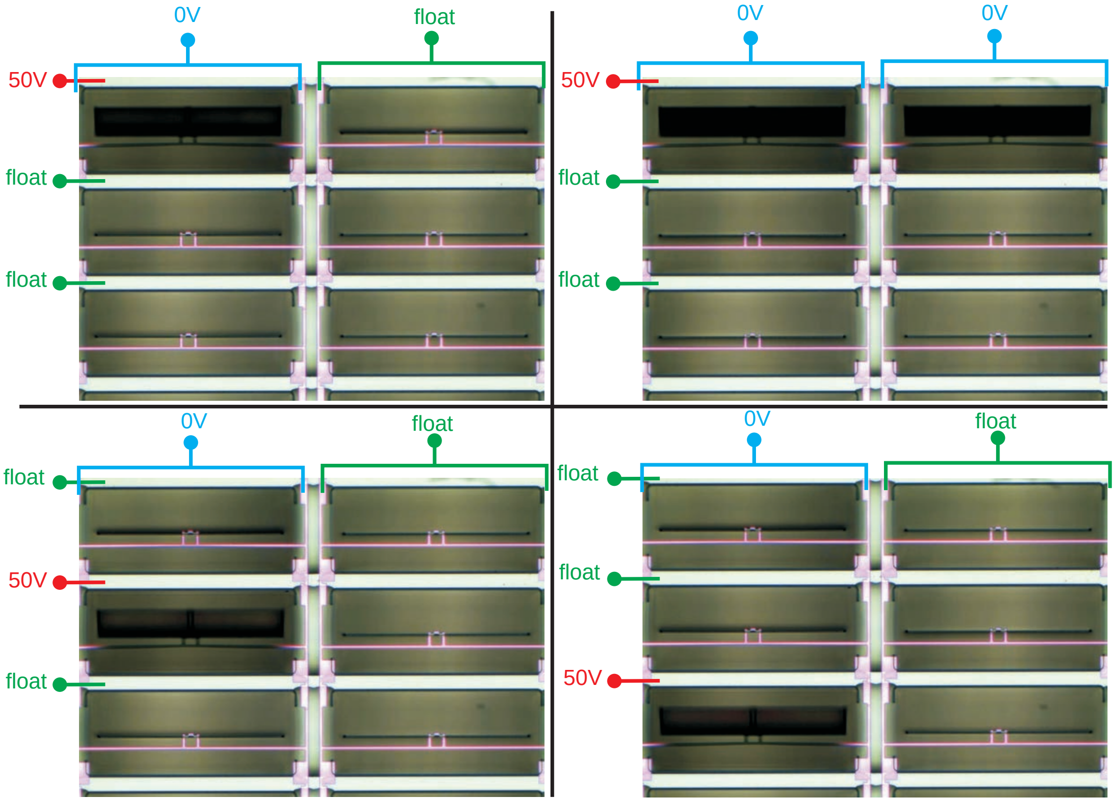

6.2.3 Frequency response / transient

In this section is characterized the dynamic behaviour of the tilting flaps. The switching time, step response and resonance frequency of the different modes were measured. The measurements were all done in air on chip A because of its typical behaviour. It was used a Laser-Doppler vibrometer (LDV) MSA400 of Polytech [91] mounted onto a microscope employing a 50x objective with a NA of 0.45. With the system can be obtained a signal up to tilt angles of $\beta_{aceptance} = 26°$ towards the optical axis. Two different approaches were employed. In the first the step response of the system was measured. In the second one the frequency response was obtained with a chip signal and the change of resonance frequency in function of the DC-actuation voltage was evaluated.

6.2.3.1 Step response measurement

Setup The step response of the system was measured by placing chip A at a pre-tilt angle of $\alpha_{pre-tilt} = 30°$ below the microscope (similar to figure 6.9). This way in the ON-state the flap reflected the laser back into the instrument. The laser spot was focused on the point of the flap surface shown in figure 6.13. When the flap was at OFF-state there was no signal on the LDV. As it was switched ON a signal was obtained as soon as the flap had a tilt angle θ larger than $\theta = 90° - \beta_{aceptance} - \alpha_{pre-tilt} = 34°$.

The step signal consisted of a low frequency square wave of 5Hz (far below the resonance frequency) with a 56V peak-to-peak amplitude (46V in another case). The velocity signal of the LDV was monitored using an oscilloscope with a trigger on the square-wave signal. The LDV was set to a sensitivity of $50mm/s/V$. From the measured velocity signal the corresponding displacement can be obtained by integrating the velocity in time. The measured data is shown in figure 6.14.

From the obtained step response in velocity the frequency response can be calculated by taking the Fourier transform as will be explained here. The frequency response can be expressed as impulse response in the Fourier domain $H(s)$. The step response in displacement $s(t)$ can be written as the convolution of step-function $u(t)$ and impulse response $h(t)$, what corresponds in the Fourier domain to the multiplication of the corresponding Fourier transforms $U(s) = \frac{1}{s}$ and $H(s)$ [92].

$$s(t) = u(t) * h(t) \Rightarrow FFT \Rightarrow S(s) = \frac{1}{s} \cdot H(s) \tag{6.13}$$

The following calculation shows that the step response in velocity $s'(t)$, corresponding to the derivative of $s(t)$, is in the Fourier domain equal to the Fourier-transform of the impulse response $H(t)$, thus the frequency response:

$$s'(t) = \frac{d}{dt} u(t) * h(t) \Rightarrow FFT \Rightarrow s \cdot S(s) = s \cdot \frac{1}{s} \cdot H(s) = H(s) \tag{6.14}$$

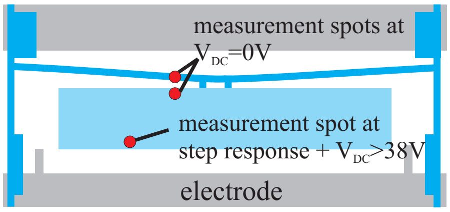

Figure 6.13: *Locations on which the laser was focused for the measurements with the LDV. For the step response and $V_{DC} > 38V$ the spot was at the tip of the flap. At $V_{DC} = 0V$ spots on the beam and on top of the flap were chosen.*

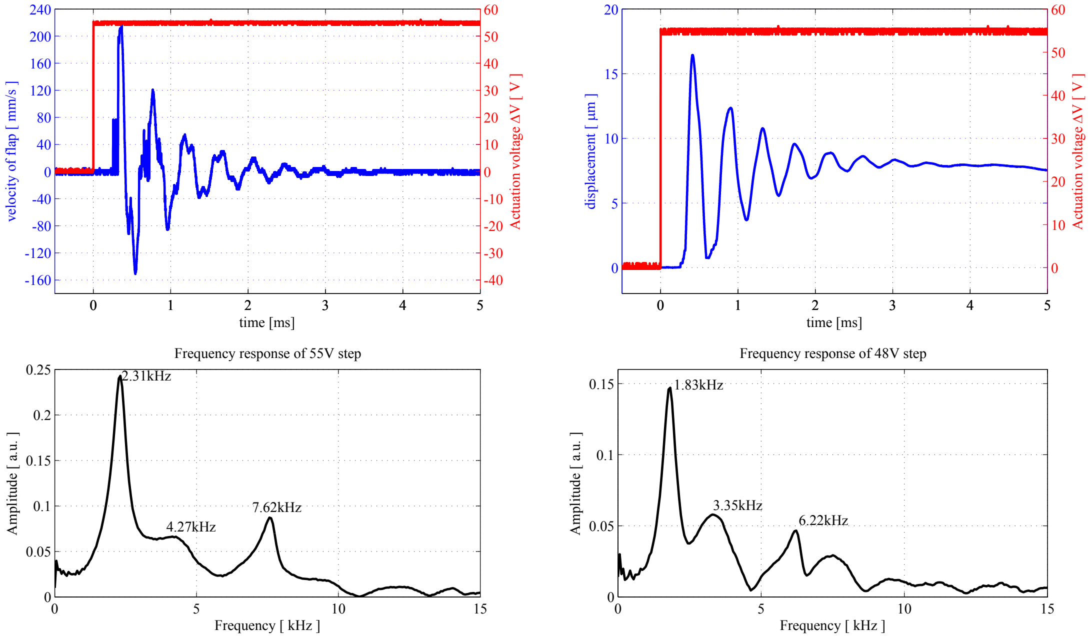

Figure 6.14: *The response to a step of ΔV of 55V as measured on a LDV-setup is shown in the two graphs on the top. The velocity measured is depicted on the left side and the corresponding displacement can be found on the right side. The flap switched within less than 0.5 ms from OFF to ON-state. The ringing with amplitudes above $0.5\mu m$ lasted for less than 3 ms. The Fourier-transform of the velocity step-response is shown in the two graphs below, once for a step of 55V and the other for a step of 48V. The peaks indicate the resonance frequencies of different modes.*

The frequency response calculated from the obtained velocity data for a step signal of 56V and 48V is given in figure 6.14.

Discussion of results From the step response measurements results of figure 6.14 could be obtained different properties of the dynamic behaviour of the system. We saw that a first velocity signal was measured after 0.25ms. This is the the time the flap required to tilt from OFF-position to the angle $\theta = 90° - \beta_{acceptance} - \alpha_{pre-tilt}$ which lays in the acceptance-cone of the microscope objective. The rise time of the flap to the first displacement peak was 0.41ms. Afterwards there was some ringing with a peak-to-peak amplitude of $16\mu m$. The settling time for which the ringing goes to an amplitude below 500nm was about 3ms.

In the frequency response three resonating peaks could be observed in the bandwidth up to 10kHz. Their frequencies were different when changing the actuation voltage. At 55V we had resonance peaks at 2.31kHz, 4.27kHz and 7.62kHz, whereas at 48V they laid at 1.83kHz, 3.35kHz and 6.22kHz. The mode with the highest amplitude was the one with the lowest frequency. The quality factor Q of this mode can be calculated by the ratio of resonance frequency f_{res} over frequency bandwidth Δf at half peak-value:

$$Q = \frac{f_{res}}{\Delta f} \tag{6.15}$$

From above equation is obtained a Q factor of 3, what corresponds to a damping $\zeta = \frac{1}{2Q}$ of 0.16. The device was operated in air and had thus a large damping due to the large flap area.

6.2.3.2 Resonance frequency at different actuation voltages

Setup The change in resonance frequency depending on the actuation voltage was further evaluated by measuring the frequency response at different voltages with a chirp signal.

A voltage composed of a DC component V_{DC} and an oscillating component V_{AC} was applied to the flap. V_{AC} was a chirp signal changing the frequency f from about 100Hz to 1kHz:

$$V(f, V_{DC}, V_{AC}) = V_{DC} + V_{AC} \cdot \sin(2\pi f \cdot t) \tag{6.16}$$

The electrostatic force and torque as given in equation (2.2) and (2.3) is proportional to the actuation voltage squared:

$$F_{el} \propto V(f, V_{DC}, V_{AC})^2 = 2 \cdot V_{DC} \cdot V_{AC} \cdot \sin(2\pi f \cdot t) - \frac{1}{2} V_{AC}^2 \cdot \cos(2 \cdot (\pi f \cdot t) + V_{DC}^2 + \frac{1}{2} V_{AC}^2 \tag{6.17}$$

We have thus a force with three different frequencies, one at DC-voltage another at frequency

f and a third at the double frequency $2f$:

$$F_{el}(0Hz) \propto V_{DC}^2 + \frac{1}{2}V_{AC}^2 \tag{6.18}$$

$$F_{el}(f) \propto 2 \cdot V_{DC} \cdot V_{AC} \cdot \sin(2\pi f \cdot t) \tag{6.19}$$

$$F_{el}(2 \cdot f) \propto \frac{1}{2}V_{AC}^2 \cdot \cos(2 \cdot 2\pi f \cdot t) \tag{6.20}$$

The oscillating voltage component V_{AC} had a peak-to-peak amplitude of 1V. For large V_{DC} the $2f$ force component was much smaller than the f component. A force was exerted onto the flap with the same oscillation frequency of V_{AC}. At low V_{DC}, specially at $V_{DC} = 0V$ the $2f$ force component was larger than the f component. Here the device was vibrating at the double of the V_{AC}-frequency. Therefore in the measurements results shown in figure 6.15 the amplitude for the measurements done at $V_{DC} = 0V$ are shown for the double of the actuation voltage frequency f.

The measurement was done at the same location on the flap surface and the same pre-tilt of the chip as for the step response measurement for actuation voltages above 38V. At the 0V DC-actuation voltage the velocity data was obtained on the beam surface and at the top edge of the flap as shown in figure 6.13.

Discussion of result In figure 6.15 we can see the resonance peaks at different applied DC-voltages. For measurements at high V_{DC} two resonance modes can be found, whose frequencies decrease with decreasing V_{DC}. At $V_{DC} = 0V$ three main resonance modes can be identified at 1.58kHz, 2.8kHz and 9.2kHz. A fourth one at a low frequency of about 700Hz can be estimated, but is mostly hidden in the low-frequency noise.

In figure 6.16 the different measured resonance modes are shown in function of the applied DC-voltage V_{DC}. The resonance frequency correspond to the peaks in figure 6.15. The resonance frequencies were measured with a chip signal superposed by a DC-voltage ranging from 38 to 56V and also at $V_{DC} = 0V$. Two different modes were observed at high V_{DC}, which are marked as mode A and B. The four resonance modes measured at $V_{DC} = 0V$ are marked separately. In the same figure the resonance frequencies are added which were obtained with the step response method. Here a third mode can be identified at high V_{DC}, which lays at frequencies between mode A and B.

The measured data is compared to the electrostatic stiffening model developed in section 3.2.3.2. The stiffening model was combined with the fit of simulation model 1 to chip A (see figure 6.11 for model-configuration, the fitting parameters are indicated in table 6.4). The electrostatic stiffening spring constant k_{el} given in equation (3.27) is calculated from the second derivative of the capacitance $\frac{d^2C}{d\theta}$ of simulation model 1. Since the $\frac{d^2C}{d\theta}$-data from

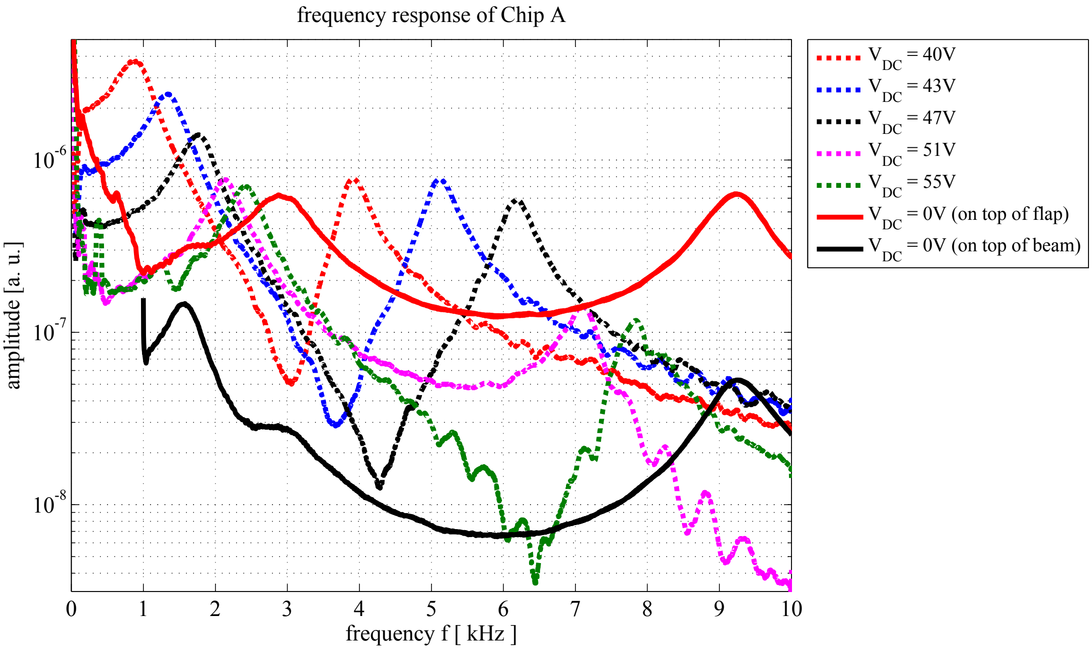

Figure 6.15: *Laser Doppler Vibrometer measurement on flap surface of chip A actuated with DC-voltage* V_{DC} *superimposed by a chirp* V_{AC} *scanning frequencies* f *from 0.1 to 10kHz.* V_{AC} *had an amplitude of 0.6 to 1V peak-to-peak. As shown in equation 6.17 the electrostatic force had a component in* f *and* $2f$*. At high* V_{DC} *the component in* f *was higher than the one in* $2f$*, as given in equation (6.19). For low frequencies the force in* $2f$ *overwhelmed the one in* f *as given in equation (6.20), therefore for* $V_{DC} = 0$ *the results are shown at the double of the actuation frequency.*

simulations is noisy due to numerical errors, a polynomial fit of $\frac{d^2C}{d\theta}$ is used for calculations of k_{el}, as shown in figure 6.17. The change in resonance frequency for a torsional mode taking into account k_{el} is plotted in figure 6.16 using equation (3.26).

The model of the torsional resonance frequency with electrostatic stiffening does agree quite well with the measured data. At $V_{DC} = 0V$ the resonance mode at 1.58kHz seems to correspond to the torsional mode. At high V_{DC} the mode found only in the step response measurement method, lying between mode A and B, might correspond to the torsional one.

With equation (3.19) the resonance frequency f_z of the bending mode is calculated analytically using the dimensions of Chip A as given in table 6.1. A resonance frequency $f_z = 892Hz$ is obtained, which is close to the lowest measured mode at $V_{DC} = 0V$ of 700Hz. Therefore we suppose that this lowest measured mode corresponds to the bending mode of the flap. The mode A measured at high voltage might also be a bending mode. The other identified modes (e.g. mode B) may correspond to higher order modes.

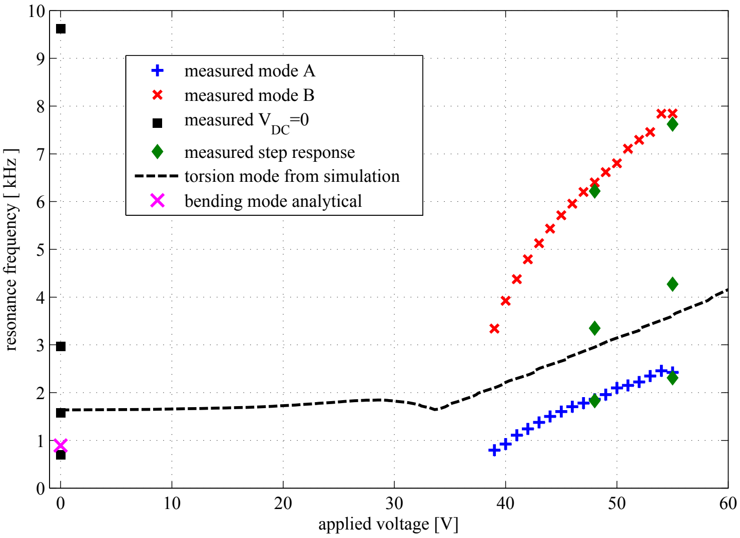

Figure 6.16: *Resonance frequencies of different modes in function of DC actuation voltage V_{DC} as measured on chip A, taken from frequency sweep of figure 6.15 and step response of figure 6.14. The model of torsional resonance with electrostatic stiffening of section 3.2.3.2 agrees well with the measurement results. The lowest frequency mode A and 700Hz at $V_{DC} = 0V$ correspond probably to a bending mode. At 1.58kHz ($V_{DC} = 0V$) we have a torsional mode.*

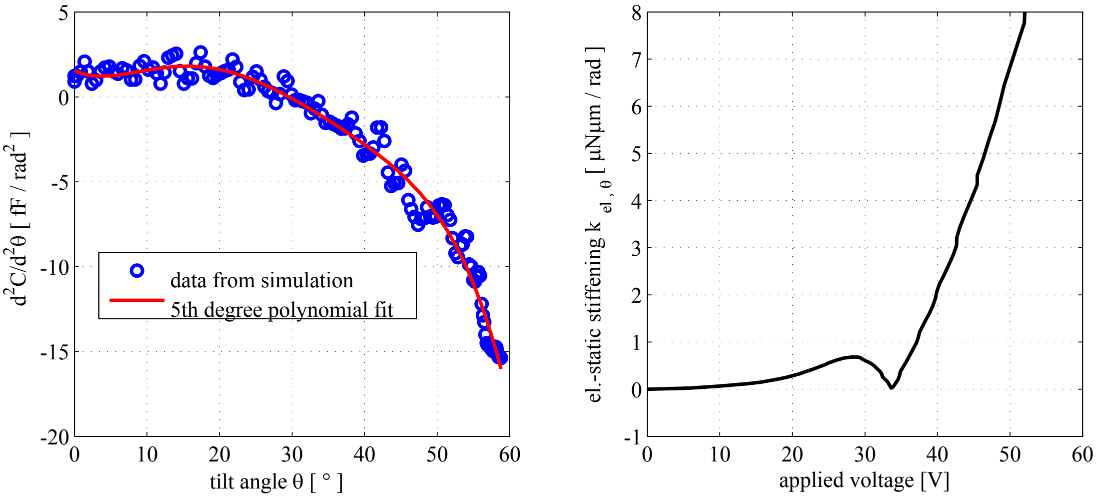

Figure 6.17: *Left side: Second derivative of capacitance $\frac{d^2C}{d\theta}$ taken from fit of simulation model 1 on chip A of figure 6.11. Since the data is noisy due to numerical calculation errors because of low mesh quality in capacitance simulation, a 5th-order polynomial function was fitted to it in Matlab. On the right side: The electrostatic stiffening k_{el} is calculated as given with equation (3.27), with the polynomial fit of $\frac{d^2C}{d\theta}$.*

6.3 Optical properties characterization

The optical performance of the modulator device will be evaluated in this section. The following optical parameters will be characterised:

- The reflectivity of the device.
- The contrast ratio between the ON- and OFF-state in the application as reflexive display, as defined in section 2.2.4.
- The contrast ratio between the ON- and OFF-state in the application of a transmissive shutter.
- The surface quality / roughness of a flap.
- For grating shaped flaps the performance of a blazed grating should be tested.

6.3.1 High dynamic range irradiation measurement using digital camera

For measuring a high contrast ratio a high dynamic range of intensity values require to be measured. This range can not be obtained with a single image of a low bit-depth digital camera, since it may be saturating in some regions. Here will be presented a method for measuring high contrast ratios using a digital camera having 8-bit of pixel values.

A schematic of the conversion procedure from irradiation I to digital pixel value on the camera image file is given in figure 6.18. The incoming irradiation I passes first an optical transfer function L due to the lens, aperture and optical configuration. L is supposed to be linear in relation to I giving the output $I' = L \cdot I$. The camera sensor receives an exposure E corresponding to the integration over time of I' by the shutter. For an exposure time of Δt we get $E = \Delta t \cdot I'$. The pixel value Z on the image of the digital camera is finally obtained by the transfer function $f(E)$ of the camera sensor and its electronics. The pixel value Z can now be represented in the following manner [93–95]:

$$Z = f(L \cdot I \cdot \Delta t) \tag{6.21}$$

For contrast and brightness measurements the irradiation I corresponding to the measured pixel value Z is wanted:

$$I = \frac{f^{-1}(Z)}{L \cdot \Delta t} \tag{6.22}$$

When supposing that the sensors transfer function is linear as $Z = f(E) = \eta \cdot E$ the contrast ratio as defined in equation (2.17) can be obtained as:

$$CR = \frac{I_1}{I_2} = \frac{f^{-1}(Z_1)/L\Delta t_1}{f^{-1}(Z_2)/L\Delta t_2} = \frac{Z_1/\eta L\Delta t_1}{Z_2/\eta L\Delta t_2} = \frac{Z_1/\Delta t_1}{Z_2/\Delta t_2} \tag{6.23}$$

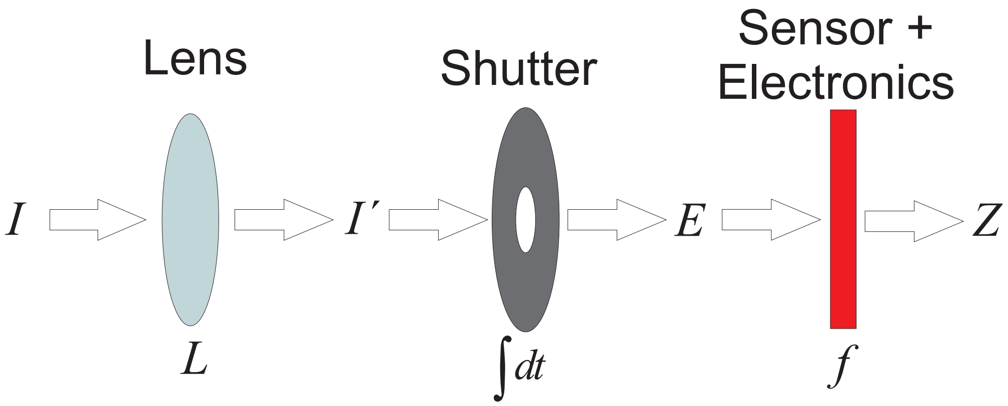

Figure 6.18: *Concept of image acquisition with a digital camera. The incoming irradiation I gets first through a optical transfer function L due to the optical system (lenses, aperture). The exposure E arrives onto the sensor by integration in time of I'. The digital pixel value Z on the image is obtained by the response function f of the sensor and the cameras electronics.*

It has to be taken into account that pixel value Z is an integer number between 1 and $2^{R_{bit}}$ for a camera with a R_{bit} resolution. For a camera with a 8-bit pixel resolution depth this implies Z-values between 1 and 256. Below a certain threshold exposure value E_0 the sensors output is 1 and above the saturation limit of the sensor E_{sat} the maximal pixel value corresponding to the bit-resolution is obtained.

$$Z = \begin{cases} 1 & \text{if } E < E_0 \\ N_Z & \text{if } E_0 < E < E_{sat},\ N_Z = [1, 2, ..., 2^{R_{bit}}] \\ 2^{R_{bit}} & \text{if } E > E_{sat} \end{cases} \tag{6.24}$$

We see that pixel values above saturation and below threshold exposure do not correctly represent the irradiation. For this reason the exposure has to be adapted for each pixel in the image such to lay within the saturation and threshold limits. This can be done by adapting the exposure time Δt, since the exposure is directly proportional to irradiation I by $E = I \cdot \Delta t$.

In equation 6.23 the camera response function is supposed to be linear over its whole range. For many cameras the response function is only linear for a certain span of pixel values Z. To take this fact into account a more extensive method is required. Therefore the irradiation I_n of each pixel n of a image is calculated with the following procedure similar as described in [93–95]:

1. A series of images i with different exposure times Δt_i will be taken. The range of exposure time will be chosen such that for each pixel n there is at least one image with the corresponding exposure on the pixel $E_{n,i}$ within the saturation and threshold limits (and inside the linear range of the camera). The images are all taken with the same optical configuration as zoom, focus and aperture, such to have an identical L. The identical sensor settings are used as well, in order to have the same $f(Z)$.

2. The irradiation I_n at each pixel n is computed by combining the pixel values $Z_{n,i}$ of the different images i with exposure time Δt_i using a weight function $w(Z)$. The weight function takes into account only the pixel values laying in the linear region of the cameras response function. It has also a higher weight for pixel values at the centre of the span, since we make the assumption that the response function of the camera has a higher linearity at the centre of the Z-values span.

The following equation is used to calculate the corresponding irradiation I_n at each pixel n using a series of images i with each having a different exposure time Δt_i.

$$I_n = L\eta \frac{\sum_i w(Z_{i,n}) \cdot {}^{Z_{i,n}}/_{\Delta t_i}}{\sum_i w(Z_{i,n})} \tag{6.25}$$

The optical transfer function L (which is supposed to be linear) and camera response function proportionality η are unknowns. But, as shown in equation (6.23), these constants cancel out when calculating the contrast ratio.

6.3.1.1 Characterization of camera used for irradiation measurements

The camera used was a IDS uEye UI-1465LE-C-HQ [96] with a CMOS sensor, 3.1 Megapixels and 8-bit pixel resolution depth. The cameras gain was set to a maximal value, the gamma factor to 1, frame-rate to 0.57Hz and the pixel clock to 5MHz. Images were saved as *.bmp* in 8-bit grey-scale. The cameras spectral sensitivity for the different color channels and for grey-scale images is given in figure 6.20.

A method for obtaining the response function f of any digital camera for converting each pixel value Z to a corresponding exposure E as $E = f(Z)$ is described in [93]. For this purpose a series of images with different exposure times Δt requires to be taken of a static scene with different intensities. The whole series has to be taken with the same optical configuration and viewing frame. By building an equation system with different pixels of the image the response function is obtained using singular value decomposition method. For more details on the method please refer to [93].

Using the series of images of different exposure times of table 6.7 at 0V, $\gamma = -25°$ and $\phi = 0°$ we evaluated the response function of the camera. The pixel values of 40 points on the image were taken and the calculation done with the Matlab-function *gsolve.m* given in [93]. The obtained response function $E = f(Z)$ is shown in figure 6.19. It can be seen that the camera has a good linearity up to pixel values of $Z = 200$.

We set now the weight function for obtaining the irradiation value I according to equation (6.25) as triangular function with maximum at the central pixel value of the span ($Z = 128$). In addition the function is 0 for the pixel values between 0 and 20 to avoid exposure values below

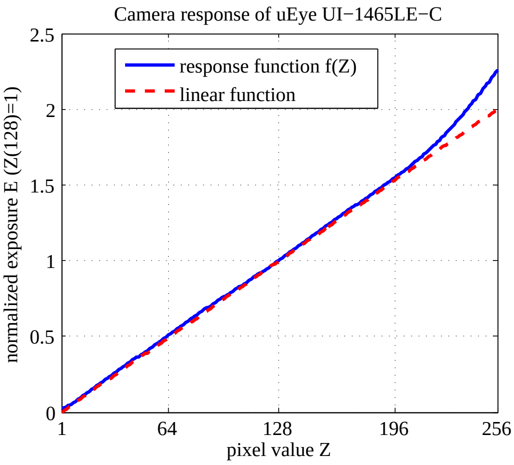

Figure 6.19: *Response function of uEye UI-1465LE-C calculated with Matlab function gsolve.m of [93]. It can be seen that up to Z=200 the cameras response is linear.*

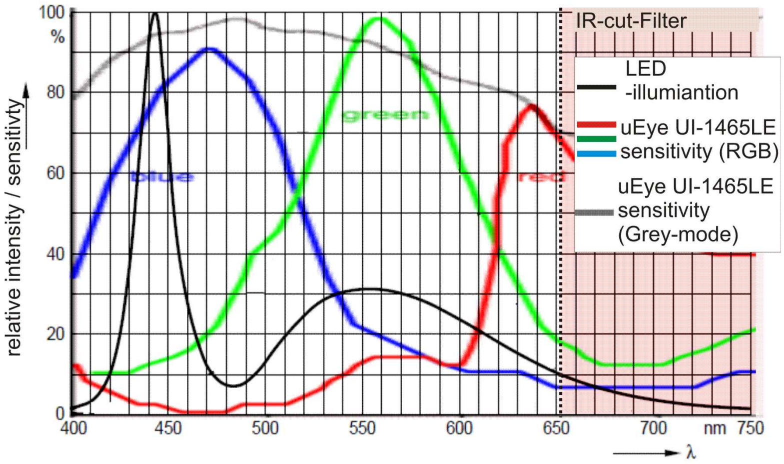

Figure 6.20: *The sensitivity of the different colour channels of a uEye UI-1465LE-C digital camera is shown as given by the manufacturer [96]. The camera has an infra-red cut-off filter at* $\lambda = 650nm$*. In the same image is superimposed the spectral density function of a LED-illumination MCWHL2-C1 (Thorlabs) employed for the reflectivity and transmission measurements of section 6.3.2 and 6.3.4. The data is given by the LED-manufacturer [97, 98]*

threshold and above 200 for staying in the linear region and avoid saturated pixels. The weight function $w(Z)$ can be written as:

$$w(Z) = \begin{cases} 0 & \text{if } Z < 20 \\ |128 - Z| & \text{if } 0 < Z < 200 \\ 0 & \text{if } Z > 200 \end{cases} \tag{6.26}$$

6.3.2 Reflectivity of flap

6.3.2.1 Setup

The reflectivity of the flap surface was characterised by comparing its irradiation with the one of a reference mirror both having the same illumination setup. The measurement setup is illustrated in figure 6.21. The flap surface was illuminated coaxially by the microscope objective which is also employed for observation. The microscope had a LED-illumination MCWHL2-C1 from Thorlabs [97] and a 10x objective with 0.15NA. The reflectivity was measured for the flap placed perpendicular to the optical axis. Since the maximal tilt angle of the measured chip A was only 55° the chip was placed below the microscope at a pre-tilt $\alpha_{pre-tilt}$ of about 35°. The irradiation of the flap was measured with a digital camera employing the concept of high dynamic range of intensities as described in section 6.3.1. From the resulting image the intensity on a small area on the flap surface was integrated giving I_{flap}. The same measurement was done as reference with a Ag-mirror having a known reflectivity of 98% giving I_{mirror}. Since the reflection intensity changes a lot in function of the incidence angle of observation and it is difficult to place the chip and mirror exactly at the same angle towards the microscope objective, the reflection measurements were done at different incidence angles. The tilt angle of the flap and of the mirror were both scanned by $+/-\beta_{scan}$. Subsequently the intensities $I_{flap}(\beta_{scan})$ and $I_{mirror}(\beta_{scan})$ were calculated for all β_{scan}. The flap and mirror were supposed to be exactly perpendicular to the microscope objective at the angle β_{scan} at which was measured the maximal value of intensity. In figure 6.22 the measured intensities for flap and mirror are plotted, in function of β_{scan}. The reflectivity is then calculated as:

$$R_{flap} = \frac{max(I_{flap}(\beta_{scan}))}{max(I_{mirror}(\beta_{scan}))} = \frac{I_{flap}(0°)}{I_{mirror}(0°)} \tag{6.27}$$

The area on the flap surface on which the reflection intensity I_{flap} was measured corresponds to A_{small} depicted in figure 6.27.

6.3.2.2 Results & Discussion

The measurement results for the surface of chip A is shown in figure 6.22. It consists of a $1\mu m$ thick poly-silicon layer. Calculating with equation 6.27 is obtained a reflectance of 0.371. Theoretical calculations in appendix A of the reflectance of a poly-silicon thin-film of $1\mu m$ thickness give a value of 0.417 as presented in figure A.3b). For this calculation were taken into account the intensity distribution of the LED-source employed and the sensitivity of the camera in gray-image mode as depicted in figure 6.20. The theoretical reflectance value is thus higher than the measured one. The difference may be due to measurement error but it may also be given by the roughness of the flap surface. The flap has actually a roughness of more than 100nm peak-to-peak as shown in figure 6.32 of section 6.3.5. Incoming light might be scattered due to this roughness, such that we measure a lower intensity.

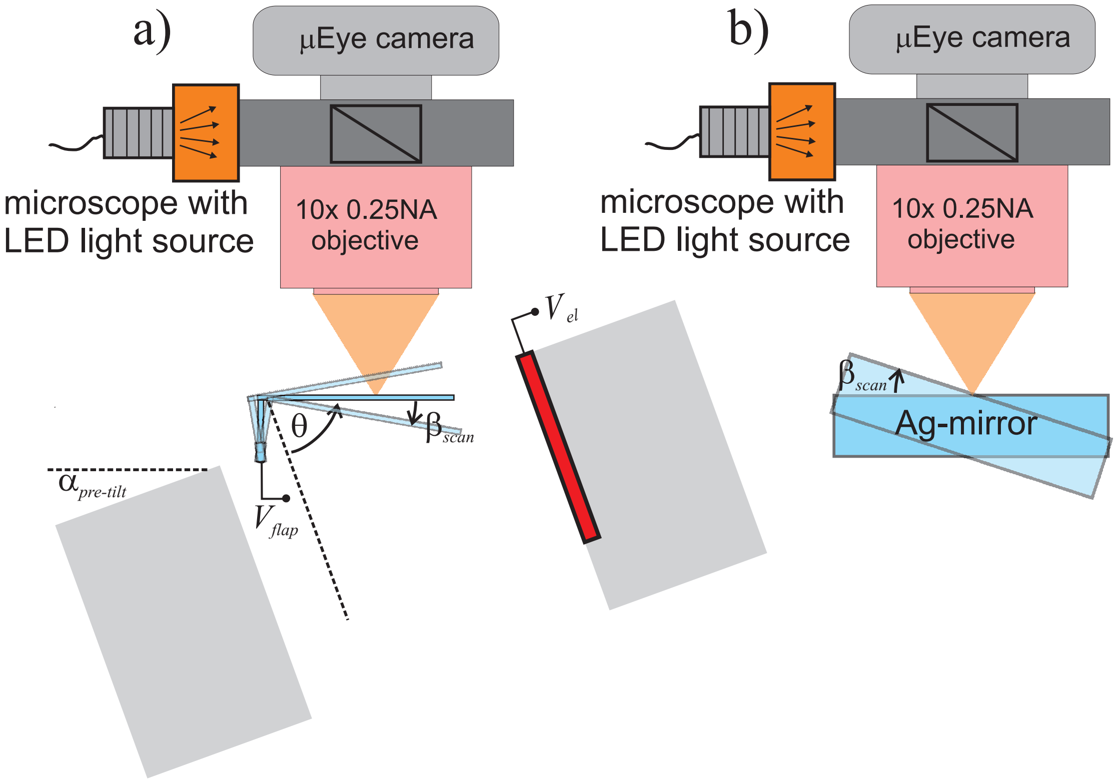

Figure 6.21: *Setup for measuring the reflectivity of the flap surface. A microscope with a coaxial LED illumination is used. The light intensity on the flap is measured with a digital camera employing the method described in section 6.3.1. In a) the irradiation of the flap is measured. The chip is placed at a pre-tilt* $\alpha_{pre-tilt}$ *below the microscope such that the flap is perpendicular to the optical axis when actuated to maximal tilt angle. In b) as reference the irradiation is measured of a Ag-mirror having a reflectivity of about 98%. The tilt angle of flap and mirror is scanned by* $+/-\beta_{scan}$ *for finding the horizontal position.*

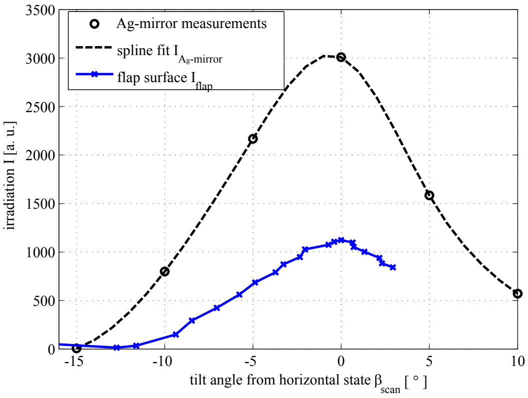

Figure 6.22: *Irradiation of flap surface and Ag-mirror measured for different angles* β_{scan} *around the horizontal position. The horizontal position was determined as the point of the curves with the maximum intensity. A reflectivity* $R_{flap} = I_{flap}/I_{Ag-mirror}$ *of 0.372 is obtained at horizontal position for the flap area* A_{small} *as depicted in figure 6.27.*

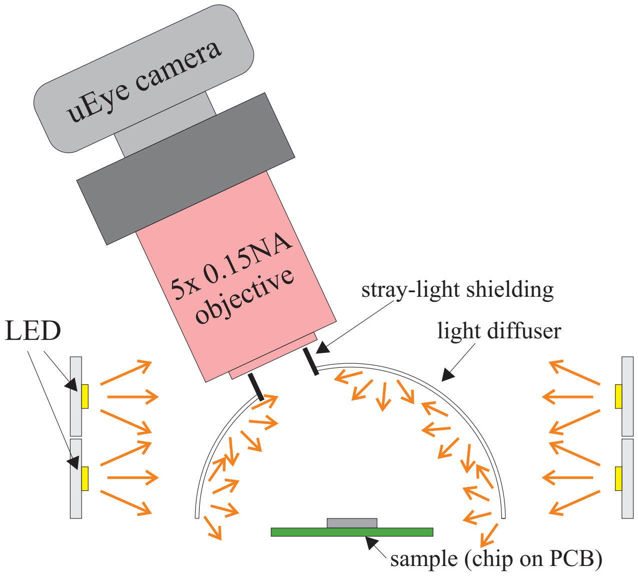

Figure 6.23: *Schematic of setup approaching uniform hemispherical illumination. The sample is placed at the centre of a diffusive hemisphere, which is illuminated from outside by several LEDs. A hole in the diffuser serves for observation through a microscope-objective on which the images is acquired with a digital camera.*

6.3.3 Contrast in application of reflective display

There is no widely used standard for measuring the contrast of a reflective display system. The illumination setting was therefore chosen to be an illumination approaching a real world case of a reflective display. We suppose that there is light arriving from all inclination angles equally onto the display. Just from the observers location there is no illumination onto the device, since the head of the person looking at the display will shadow it. A similar illumination approach was also presented in [99, 100].

6.3.3.1 Illumination configuration

A special setup was conceived for obtaining an illumination which has equal intensities from all incident angles in azimuth and inclination. We call it uniform hemispherical illumination. At the centre of a hemisphere was placed the device being measured. The hemisphere is diffusive in transmission and illuminated from outside. A schematic is shown in figure 6.23. Since the sample was observed with a microscope objective having a working distance of 22.5mm, the available space for the illumination system was rather small. As sphere a table tennis ball (40mm diameter) was used, since it had the optimal dimensions to serve as diffuser. The ball was cut in to half and a hole was drilled into it for observation with the microscope. Around the hemisphere at a distance of 15mm two rows of white LEDs strips were placed (each row consisted of 12LEDs of Paulmann yourLED neutral white, with total 168lm). The optical path between microscope objective and observation hole in the diffuser was shielded

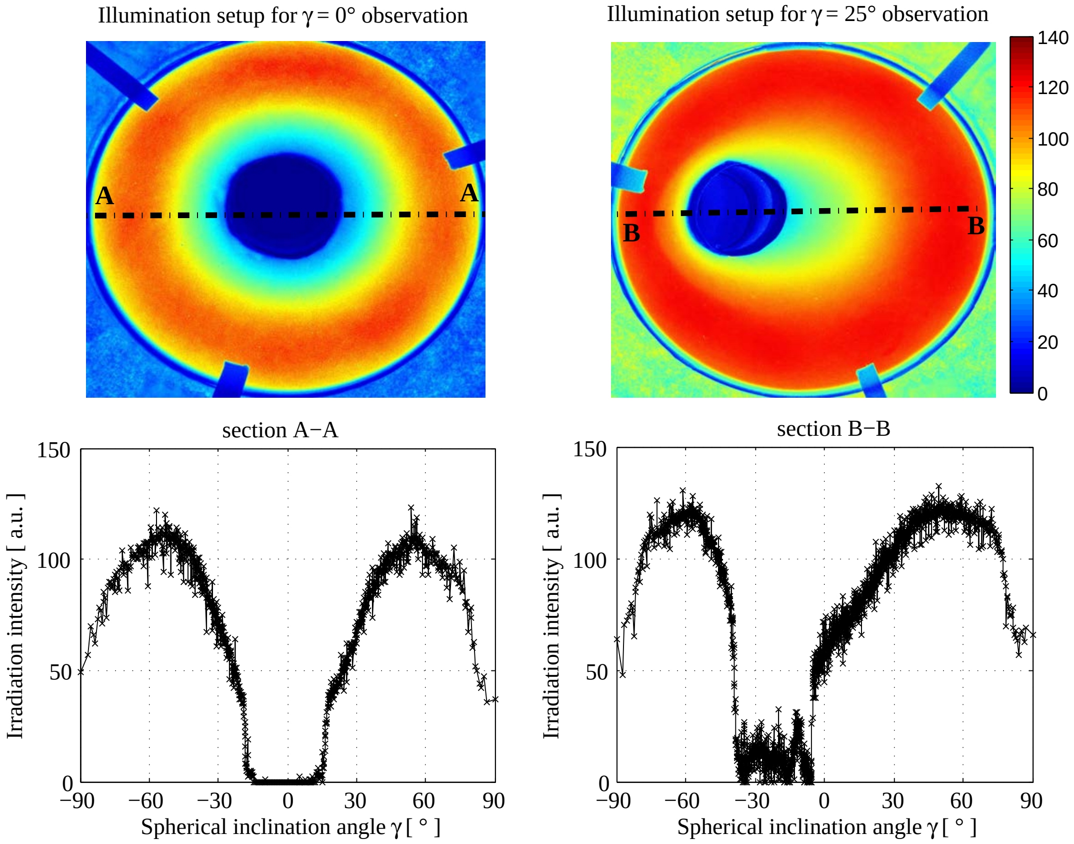

Figure 6.24: *Spacial distribution of illumination intensity for setup approaching uniform hemispherical illumination. On the left side is shown the setup for observations at 0° inclination and on the right side the one for observation at -25° inclination. It can be noticed that the intensity in all azimuthal angles is very uniform. Along the inclination angles there is a minimum around the location of the observation hole. This is due to shadowing of the microscope objective. A maximum can be found around 50° inclination, since these areas of the diffusing sphere lays between the two rows of light source and is therefore irradiated with a higher intensity.*

with an optically absorbing material, such that no stray light could couple into the microscope. For every incidence angle of observation a different diffuser hemisphere was used with an opening hole at corresponding location.

The intensity distribution of the illumination configuration was characterized. For this purpose a digital camera picture was taken from below at a distance of about 10cm. The image was taken with a linear pixel value to intensity response curve. We supposed that every point on the hemisphere diffuses incoming irradiation in all angular directions equally. Therefore the pixel values of an image taken from below, are proportional to the intensities at the corresponding point of the hemisphere. For a cross-section A-A and B-B through the image of the hemisphere the corresponding incidence angle was calculated. By this means we obtained an intensity-profile of the hemisphere surface in function of the inclination angle. The results for two different illumination configurations is displayed in figure 6.24. On has an observation hole at incidence angle $\gamma = 0°$, the other at $\gamma = -25°$.

When analysing the results it can be noticed that the intensity is very uniform for all azimuthal angles. Along the incidence angle there is a variation of the intensity. It is the lowest close to the observation hole, due to shadowing of the microscope objective. The highest intensities are at around $\gamma = 50°$. The reason is that at these areas the hemisphere gets the highest irradiation from the two rows of LED-stripes. Towards the edge of the hemisphere the intensity decreases again, since here the irradiation comes mainly from one of the two rows of LED-stripes.

We can conclude that the illumination has a close to uniform intensity profile along the different azimuthal angles. It varies by $+/-15\%$ between 40° and 80° incidence angle. Even if the illumination is not totally hemispherically uniform, it simulates quite well ambient light of a real environment.

6.3.3.2 Measurement procedure

The measurement setup is shown schematically in figure 6.23. The chip being measured is placed under a microscope, illuminated by the uniform hemispherical illumination configuration presented above. Images of the device in focus, actuated at different voltages, are taken through a 5x magnification microscope objective with a NA of 0.13. This microscope objective with a NA giving a acceptance angle of $2 \cdot 7.4°$ was chosen because the angle of the light cone is similar to the one of the human eyes. When taking a distance between the two human eyes of 10cm a NA of 0.13 would correspond to looking at an object from 38cm distance.

A high dynamic range of irradiation values are required to be measured between OFF-state, where light is absorbed on a black layer, and the ON-state where light is reflected by the flap. The method and camera employed for the measurements are described in section 6.3.1 and 6.3.1.1.

The measurements were done on two different chips A and B at various angles of observation. The chips were tested for an inclination of $\gamma = 0°$ and 25° and all azimuthal directions with increments of 45°. The chip placement in function of the azimuthal angle as seen from the top is sketched in figure 6.26.

Figure 6.25 shows chip A observed with the measurement setup at an incidence angle of $\gamma = -25°$ and azimuth of $\phi = 315°$. The electrode-row is set to 0V and the two flap columns are first set to 0V, such that we have a black area at the location of the flap. When the voltage on the flaps is set to 60V they tilt to horizontal position and can be seen as bright spot. The contrast-ratio between the black-state and the bright state is calculated as in equation (2.17):

$$CR_{Area}(\theta) = \frac{I_{Area}(\theta)}{I_{Area}(\theta = 0°)} \tag{6.28}$$

On three different areas A the contrast ratio was calculated. These areas are shown in figure

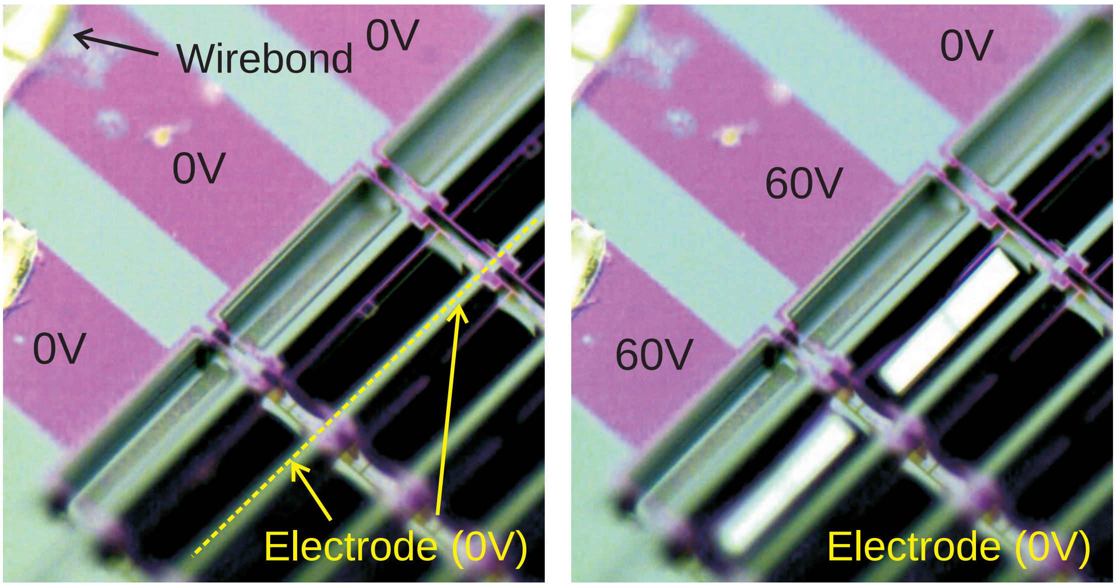

Figure 6.25: *Microscope picture showing detail of an array of chip A type flaps observed with the setup of figure 6.23. The flaps are once in OFF- and once in ON-position. The electrode marked with a line is kept at both cases at 0V. Two flap columns with rose-coloured poly-silicon lines and torsion beams are set in the ON-state to 60V, leading the flap to become a bright spot.*

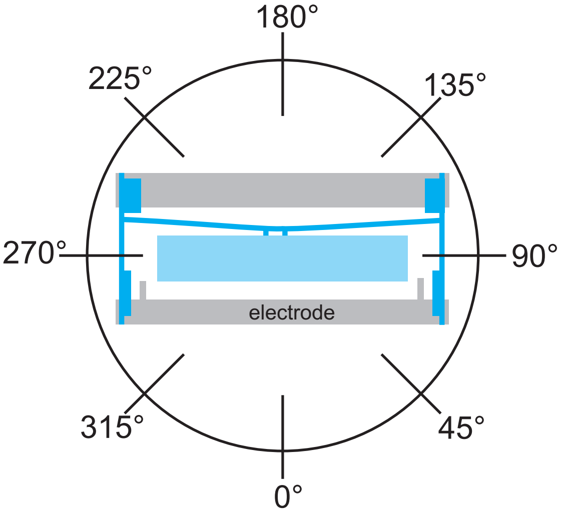

Figure 6.26: *Azimuthal observation angles ϕ employed in the contrast ratio measurement with uniform hemispherical illumination. The top view of the flap actuated to a certain tilt angle is shown in the centre with the measured azimuthal viewing directions around.*

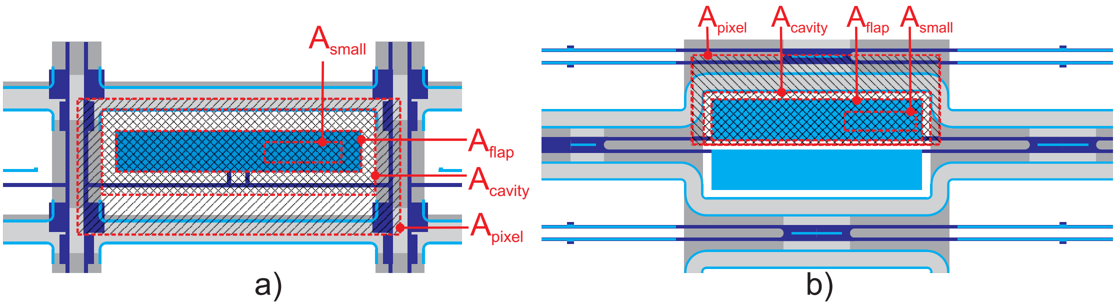

Figure 6.27: *The integration areas A_{cavity}, A_{flap} and A_{small} were used for calculating the contrast ratio on a) chip A and b) chip B.*

6.27 and are:

- A_{cavity}: Is defined by the cavity in which the flap is placed. The area is delimited by the electrode on one side by the torsion beam on the other side and laterally by the interconnection-beams. This area does correspond to the equivalent area of a pixel, without the reflecting surfaces of electrode and interconnection beams.
- A_{flap}: Is defined by the flap when actuated to maximal tilt angle θ.
- A_{small}: A small area on the flap is chosen for measuring the highest achievable contrast.

6.3.3.3 Discussion of results

The contrast ratio CR as given in equation 6.28 evaluated on the three areas A_{cavity}, A_{flap} and A_{small} of the two chips A and B is plotted in figure 6.28. The values are given for various inclinations γ and azimuths ϕ. The corresponding intensity image for the ON- and OFF-state can be found in table 6.7. We can make the following observations from the measurement results:

- The highest contrast ratio with a value of $CR_{small} = 145$ is obtained in chip B at maximal tilt angle for A_{small} observed at $\gamma = 0°$.
- The lowest contrast ratio of all measurements is obtained at $\gamma = -25°$ and $\phi = 180°$. We are here in angular region Ψ as described in figure 5.6 of section 5.3.1 where all rays originate from the underlying absorbing layer, leading the flap surface to be perceived as dark.
- At $\gamma = -25°$ high contrast ratio are obtained for $\phi = 270°$ to 90°. At these angles we are in the angular region Ω as on figure 5.6.
- Larger contrast ratios are obtained for $\gamma = 0°$ than for $\gamma = -25°$. The reason is the illumination configuration. At $\gamma = 0°$ the flap surface reflect light coming from $\gamma_0 = 2 \cdot$

Table 6.7: *Grey scale images with high range of intensities obtained by combination of images with different exposure times as described in section 6.3.1. The measurements were made at different inclination angles γ and azimuthal angles ϕ of observation on two different chips. Uniform hemispherical illumination was used as defined in section 6.3.3.1. It can be seen that the highest contrast is obtained at $\phi = 0^\circ$. The corresponding contrast ratio is plotted in figure 6.28*

	Chip type A Act. voltage: 0V	Chip type A Act. voltage: 60V	Chip type B Act. voltage: 0V	Chip type B Act. voltage: 60V
γ=0° φ=0°		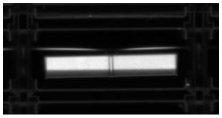		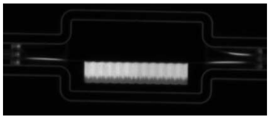
γ=25° φ=0°	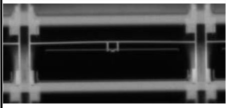	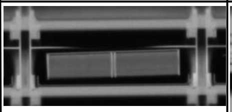	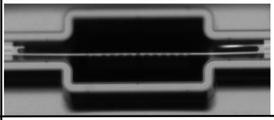	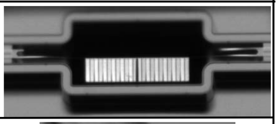
γ=25° φ=45°	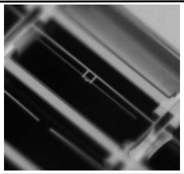	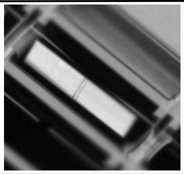	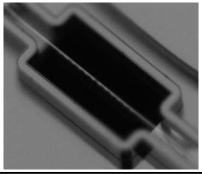	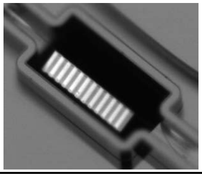
γ=25° φ=90°			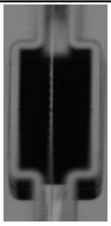	
γ=25° φ=135°	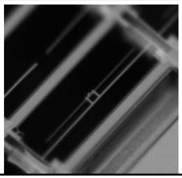	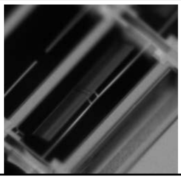	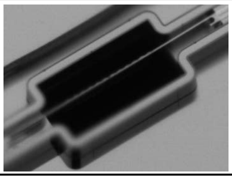	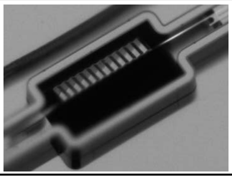
γ=25° φ=180°	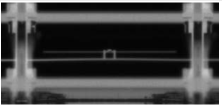	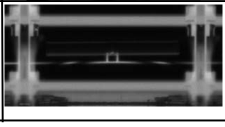	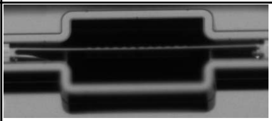	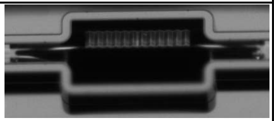

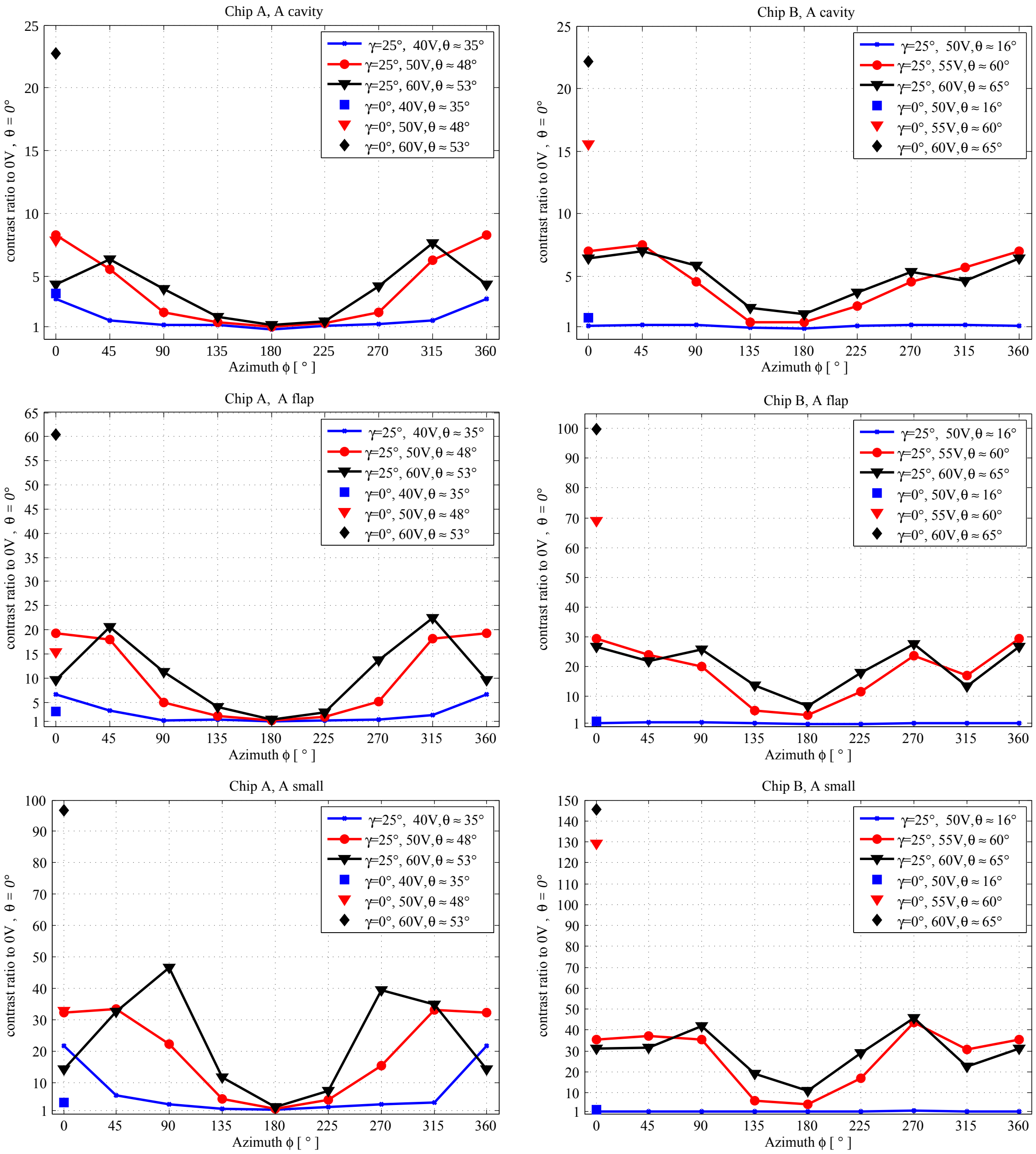

__Figure 6.28:__ Contrast ratio at uniform hemispherical illumination for different inclination γ and azimuthal angles ϕ. The measurement were done on two different chips A and B actuated at various voltages to the corresponding tilt angle θ. The contrast ratio was evaluated towards the non actuated state ($\Delta V = 0V, \theta = 0°$) on the three different areas on the modulator. The areas A_{cavity}, A_{flap} and A_{small} are given in figure 6.27. It can be observed that the contrast ratio is the highest at 0° inclination. The lowest contrast ratio is obtained for observation angles of $\gamma = -25°$ and $\phi = 180°$.

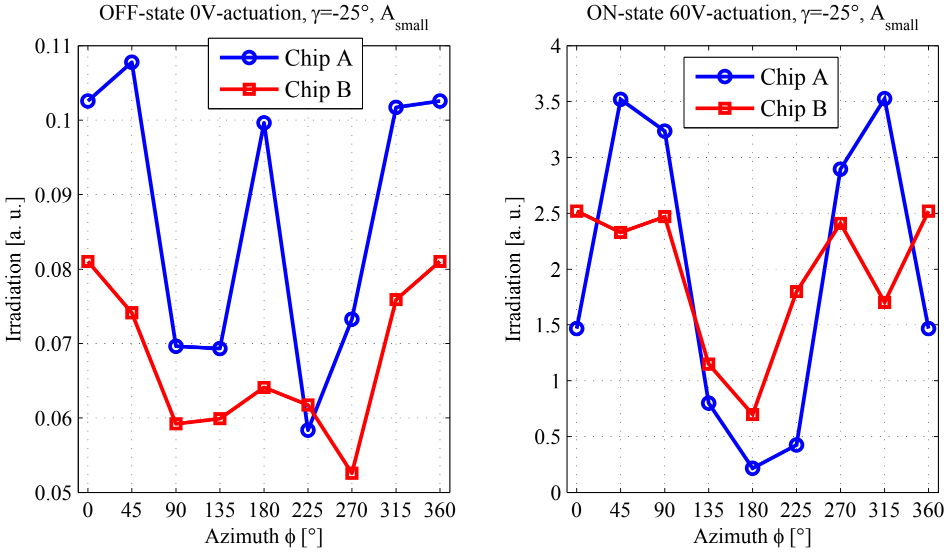

Figure 6.29: *Irradiation intensity as measured on area A_{small} for chips A and B in OFF- and ON-state. The irradiation intensity in the ON-state is comparable for both chips. In the OFF-state we measure higher intensities on chip A than on chip B.*

$(90° - \theta)$. This corresponds at maximal tilt angle of $\theta = 53°$ for chip A and $\gamma = 65°$ for chip B to $\gamma_0 = -74°$ and $\gamma_0 = -50°$ for which the illumination setup has high intensities as can be seen in figure 6.24. At the OFF-state the black-layer below the chips is perpendicular to the observation direction. Specular reflections on this layer originate directly from $\gamma_0 = 0$, where there is very low illumination intensity as shown in figure 6.24. An ON-position illuminated at high irradiation intensity and an OFF-position illuminated at very low irradiation intensity leads thus to a very high contrast ratio.

- At $\gamma = -25°$ specular reflections on the black layer originate from $\gamma_0 = 25°$, where there is a high illumination intensity. This lowers thus for all $\gamma = -25°$-measurements the contrast ratio. For the same reason the surrounding substrate is also perceived as bright.

- Chip B has generally a higher contrast ratio than chip A. There are different reasons for this: First the fill-factor A_{flap}/A_{cavity} is larger for chip B than chip A. Secondly, when looking at the irradiation values measured for mask A_{small} in figure 6.29 we observe at ON-state comparable irradiation values on both chips, whereas at the OFF-state chip A has higher values than chip B. The black-layer in chip A is thus brighter than the one in chip B. The reason could be that on chip A the black layer was placed below the PCB, at some distance from the silicon substrate. However, in chip B it was placed directly below the silicon substrate. Therefore in chip A some light may couple-in from below the chip through the PCB, giving higher irradiation values.

- At $\gamma = -25°$ and $\phi = 270 - 90°$ we have a constant contrast ratio on chip B, whereas for chip A we have a large drop for $\phi = 0°$. It is due to the drop in intensity at ON-state for chip A which can be observed in figure 6.29. The reason is that the irradiation is originating at this state from $\gamma_0 = 2 \cdot (\theta(60V) - 90) + \gamma = -49°$ where we have a rather low illumination intensity. Chip B on the other side has a zigzag shaped flap surface so we see reflection of light from other brighter spots. This observation demonstrates the utility of having a non-flat flap shape.

- The measured contrast ratio on A_{cavity} is about 2-5 times smaller than the one measured on A_{flap}. The fill-factor A_{flap}/A_{cavity} cannot explain this difference. In fact we have at the OFF-state in A_{cavity} highly reflecting surfaces of the torsion beam and top edge of the flap. We notice, thus that these surfaces would need to be covered by a shielding for improving the contrast ratio in a real reflective display device.

6.3.4 Contrast in transmission mode

6.3.4.1 Setup

The flap is characterized here as optical modulator in transmission. Light from below the substrate passes through the backside opening arriving onto the flap. When the flap is tilted it blocks light, at vertical rest state the incoming light passes through. Chip A which is packaged onto a PCB with a back-side opening was measured with a microscope employing a LED-illumination placed below (MCWHL2-C1 from Thorlabs [97], spectral density indicated in figure 6.20). A schematic of the measurement setup is drawn in figure 6.30. The intensity was acquired using a digital camera (see section 6.3.1.1) and combining a series of images taken at different exposure times for getting a high dynamic range of intensity values (section 6.3.1). The measurement was done using colour images in the RGB-mode. This way the response is obtained separately in the red, green and blue part of the spectrum. The sensitivity of the three colour channels and the illumination spectrum are presented in figure 6.20. Intensity maps of the ON- and OFF-state of chip A are shown in figure 6.31. For a marked area is calculated the intensity I and the corresponding contrast ratio as $CR = \frac{I(0°)}{I(\theta)}$. We get separate values for the red, green and blue pixel-response of the camera.

Table 6.8: *Blocking of light transmitted through flap of* $1\mu m$ *thick poly-silicon. The measured contrast ratio values indicated in figure 6.31 were calculated to absorbance* $A = 1 - 1/CR$ *according to equation (A.3). Theoretical values as calculated with method of appendix A are shown as comparison.*

Colour	**Measured contrast ratio** CR	**Measured absorbance** A	**Theoretical absorbance** A
Blue	20	95%	97.5%
Green	10	90%	88.4%
Red	7	85%	82.9%

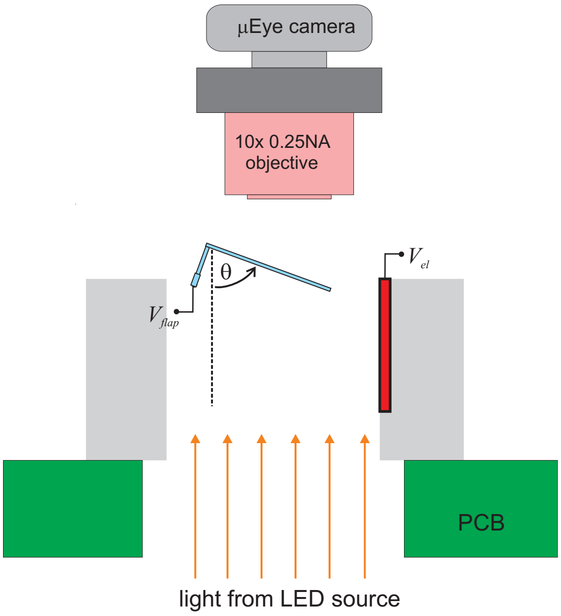

Figure 6.30: *Schematic of the setup for measuring the contrast of a flap-modulator in transmission mode. The flap placed on a PCB with an opening hole is illuminated from the back side with a LED-lamp. The irradiation intensity is observed with a microscope and measured using a digital camera with the procedure described in section 6.3.1.*

6.3.4.2 Discussion of results

The measurement results of chip A are presented in figure 6.31. The highest contrast ratio is obtained at the blue channel of the camera. It has a value of $CR = 20$ for the maximal tilt angle of $\theta = 53°$. The contrast ratio for the green channel is at about $CR = 10$ and for the red channel at $CR = 7$. Knowing the contrast ratio also the fraction of light blocked when passing through the flap can be calculated as $A = 1 - \frac{1}{CR}$ (A as defined in equation (A.3)). The contrast ratio and absorption values are summarized in table 6.8.

We have thus a higher absorption for shorter wavelengths, than for longer ones. This agrees with the poly-silicon material properties as discussed in appendix A. There the theoretical A values through a $1\mu m$ thin poly-silicon layer were calculated. For the calculations were also taken into account the sensitivity of the red, green and blue channel of the camera (which is shown in figure 6.20). The theoretical values computed are indicated in table 6.8. The theoretical and measured values agree well.

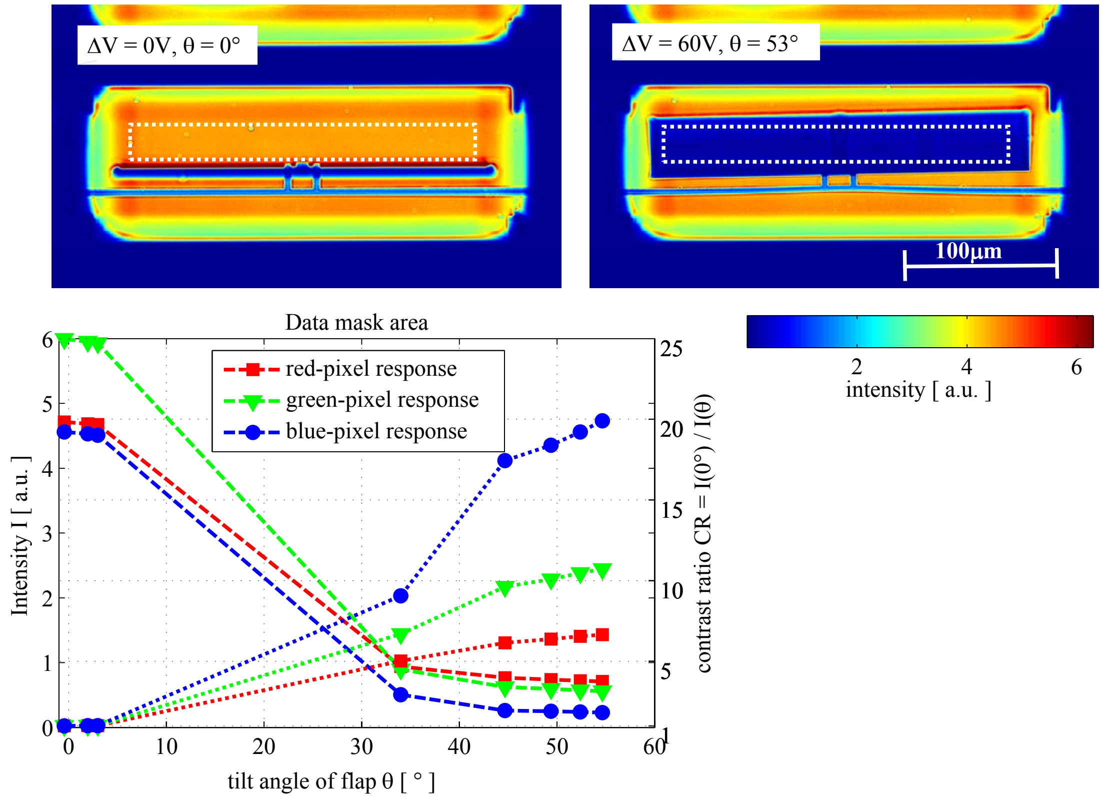

Figure 6.31: *Back-illuminated chip A: On the top the intensity map is displayed of the flap at rest state (left) and actuated with 60V to a tilt angle of 55° (right). For the indicated area the intensity $I(\theta)$ and corresponding contrast ratio $CR(\theta) = I(0°)/I(\theta)$ is plotted in function of the tilt angles θ. The measurement was done using the red, green and blue-pixels channel of a digital image. It can be seen that blue light is absorbed more by the flap than red light.*

6.3.5 Flatness of flaps

The flatness of a surface is an important indicator of usefulness for different optical applications. Height differences give rise to phase shifts as light is reflected. When the employed light is coherent the phase shifts lead to interferences, which can be undesired depending on the application. Roughness of a surface leads also to more scattering. In the application as reflective display such diffusion is very desired as described in section 3.1.1.1.

6.3.5.1 Setup

The roughness was measured on chip A using a optical profiling system (Veeko Wyko NT1100). As described in section 6.2.1.2 the maximal measurable inclination angle with this instrument is only about 15°, but the maximal tilt angle of the flap was only about 53°, giving a tilt angle towards the horizontal of 37°. Therefore the device was placed at a pre-tilt $\alpha_{pre-tilt}$ below the instrument. Similar as in section 6.3.2 and in figure 6.21 a pre-tilt of about 35° was employed,

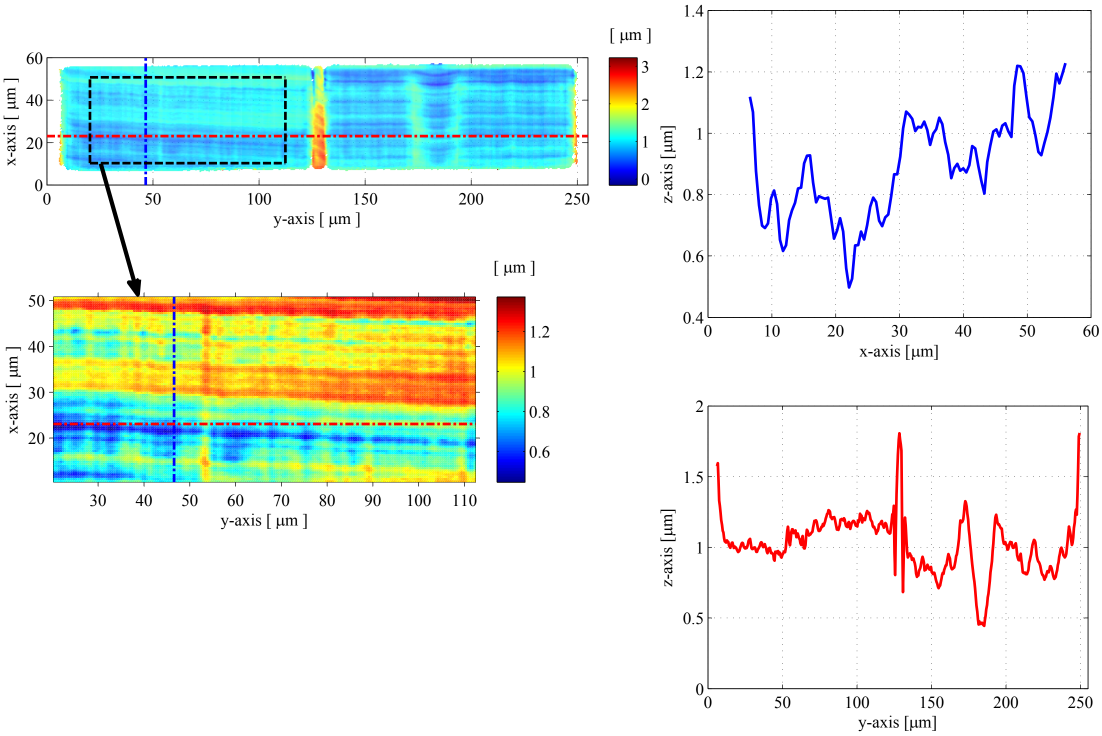

Figure 6.32: *White light interferometer measurements of flap surface on chip A. An unevenness of 500nm over the flap surface can be seen superposed by a roughness of high spacial frequency 100nm. The large unevenness may be due to stress-related deformation of the flap, due to remaining* SiO_2*. The roughness is due to the fabrication process using DRIE. At the edges and in the centre elevations of up to 1*μm *can be found. These are defined by the form of the mask having a wider trench width at these locations.*

such that the flap was perpendicular to the optical axis of the instrument when being actuated to maximal tilt angle. Because of the size of the chip was used a long working distance 10x objective. The measurement results for the flap surface of chip A are shown in figure 6.32.

6.3.5.2 Discussion of results

Looking at the results for the measured flap surface of chip A in figure 6.32 we notice a flatter part and two elevations of up to $1\mu m$ height at the centre and at the right and left edges. The elevation at the centre and at the both edges are originate of the form of the trench-mask, being wider at these locations. On the rest of the surface a peak to peak unevenness of up to 500nm can be found. A small amplitude superimposed by a large amplitude roughness can be found in x-direction. The small amplitude roughness has a period of about $2\mu m$ and a peak to valley height of 100nm. It is due to the deep dry-etch process as described in 2.1.4. For the larger amplitude unevenness there may be two different reasons. First it may be induced by the deep-etch process giving also rise to larger width differences due to variations of the etch-chamber conditions over time. And second, some remaining SiO_2, which may not have been etched totally in the release-step can induce stress leading to deformation and additionally lead to measurement errors in the white light interferometer due to its transparency and different refractive index. In y-direction a low and a high amplitude roughness can be observed as well. The high amplitude roughness has 500nm peak-to-peak values which may be due to remaining SiO_2, but also originate in non-uniformities in the lithography-mask defining the flap-trench. A low amplitude roughness with 50nm peak-to-peak values and a period of about $5\mu m$ is probably due to the etch process.

6.3.6 Grating shaped flaps: Switchable grating

Chip B has a flap with the shape of a blazed grating as shown in figure 5.11. It has a grating periodicity of a=17.85μm and a blaze angle of $\varphi = 17.7°$. The application of the flap as blazed grating was demonstrated in a simple experiment. The measurement setup is described in figure 6.33. A red diode-laser of wavelength around 670nm is focused onto the tilted flap in Littrow-condition (incidence angle and blaze-angle φ are equal). The reflected light arrives upon a screen, on which a diffraction pattern can be observed as shown in figure 6.33. When changing the tilt-angle of the flap the whole diffraction pattern can be scanned up-and down. We can observed a displacement of the pattern as the flap was actuated once at 54V and once at 57V. As expected of a blazed-grating in a Littrow-condition, the diffraction order with the largest intensities laid at a diffraction angle corresponding to φ.

The diffraction angles β_N for every diffraction order N can be theoretically calculated using the grating-equation with an incidence angle of φ.

$$\beta = \arcsin(\frac{\lambda}{a}N - \sin\varphi) \tag{6.29}$$

We measured the diffraction angles of the different orders on the pattern on the screen. This measured angles is plotted together with the theoretically expected diffraction angles of the different orders in figure 6.34. A wavelength of 670nm was employed for the theoretical calculations. It can be seen that the theoretical and measured data agree well. Therefore we can say that the measured flap has the properties of a blazed grating.

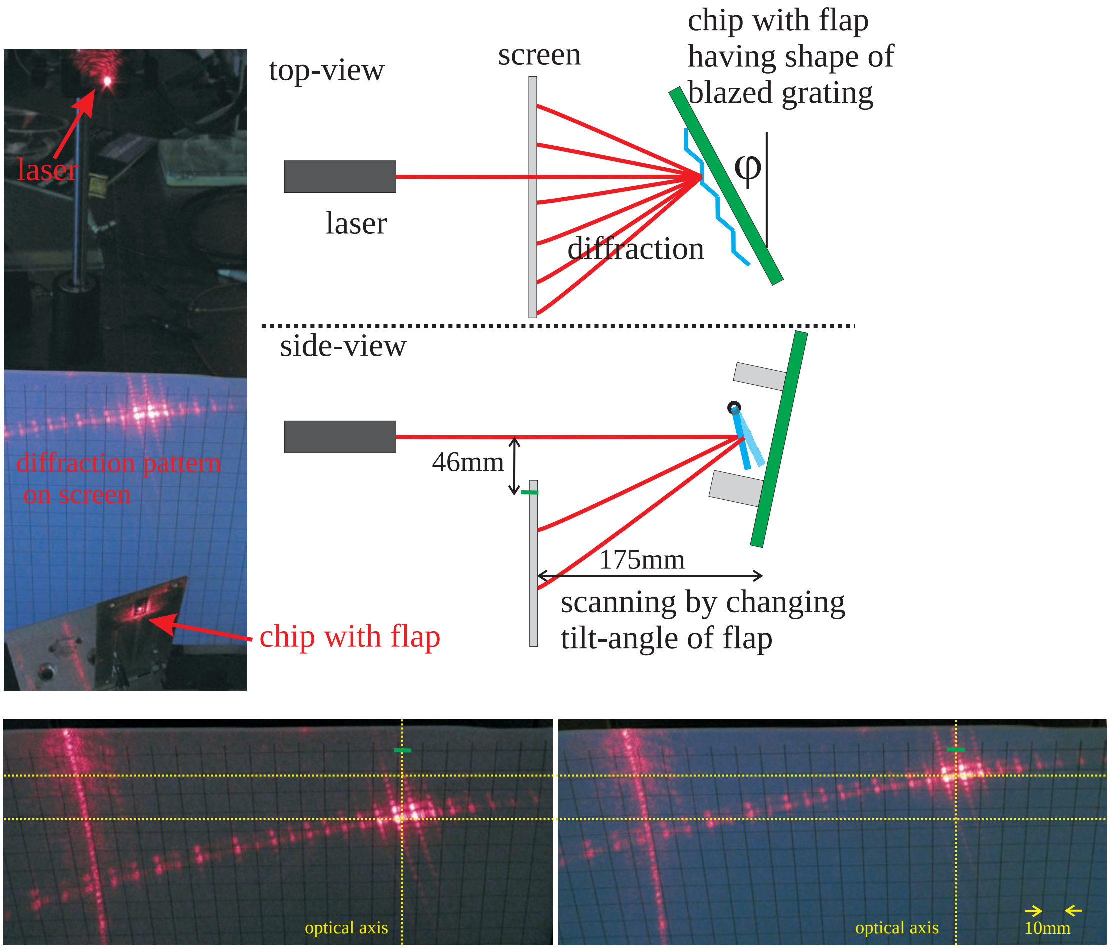

flap actuated at 54V

flap actuated at 57V

Figure 6.33: *A laser is focused onto the flap of grating-shape with a blaze angle φ placed at Littrow-condition. The laser beam gets diffracted on the flap surface and reflected onto a screen. By changing the tilt angle of the flap the diffraction-pattern on the screen is scanned up and down. As expected of a blazed grating in the Littrow-condition the diffraction orders with the largest intensities laid near the optical axis.*

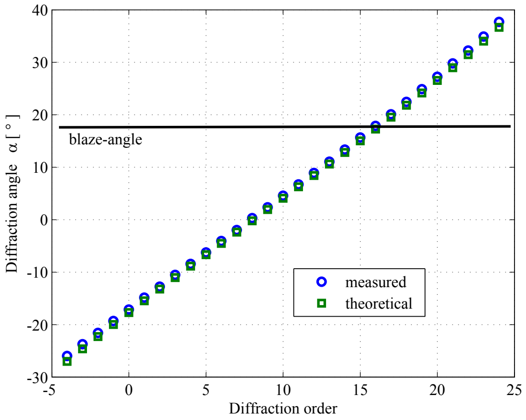

Figure 6.34: *We can see the measured diffraction angles of the different diffraction orders and the theoretical values calculated with the grating equation (6.29) for a wavelength of 670nm. Theory and measured data agree and we can say that the flap has the properties of a blazed grating.*

7 Discussion & Outlook

In this chapter will be discussed the results of the vertical flap concept and the horizontal flap concept. The suitability for using the vertical flaps in different applications will be analysed and an outlook given on further work to be done.

7.1 Discussion of characteristics of vertical flaps

We summarize here the electromechanical and optical properties as measured in chapter 6. An overview is given in table 7.1. We want to briefly discuss the different properties.

Actuation Actuation voltage and maximal achievable angle depend a lot on the geometry of the device. The stiffness of the torsion beam (i.e. the spring constant in rotation) influences the actuation voltage in a square-root relation as shown in equation (3.12) what we could also observe in the measurements. Since the thickness of the torsion beam has the largest impact on the stiffness, it is also the parameter changing the strongest the actuation voltage. The measured chip C of section 6.2.1 had the lowest actuation voltage with a value of 35V, since it had a thinner beam than the other chips. In a the typical actuation behaviour about 60V were required for reaching a maximal tilt angle, which laid between 55 and 70°.

The form of the trajectory depends on the electrode-beam distance and the position of the beam, which is attached to the flap either at a certain offset or directly connected laterally. In the measured chips A, C and D we had a continuous trajectory-curve, where all tilt angles could be reached by applying a proper voltage. On one chip (chip B) a pull-in behaviour was obtained, combined with a hysteresis leading to 3V difference between pull-in- and hold-voltage. Such a hysteresis is required for line-column addressing as discussed in section 3.1.4. In general the simulation model for the form of the trajectory gives a good agreement with the measured devices with two flaws. First the electrode-beam distance for the fitted model and the measured data have a difference of up to $5\mu m$, what might be due to charging effects of the underlying substrate which was kept in the measured devices at a floating potential.

Secondly, it does not take into account a pull-in of the flap due to instability in twist direction at high actuation voltages.

Frequency response The lowest resonance frequency measured at rest state was at about 700Hz. When actuated to maximal tilt angle the same device had the lowest resonance frequency at 2.31kHz. This shows that we have a strong electrostatic stiffening as modelled in section 3.2.3.

Switching time A switching time of less than 0.5ms was measured. The device had a high damping since it was operated in air, therefore the ringing after actuation had a settling time of less than 3ms.

Fill-factor A fill factor F_{fill} of the active modulating area of 28 to 40% was calculated in section 5.4 depending on the configuration. This value corresponds to the case of the flap tilted by 90° to horizontal position. For lower tilt angles equation (5.1) has to be employed, which is proportional to $\sin\theta$. For tilt angles of 60° we have $0.87 \cdot F_{fill}$ and for 70° we have $0.94 \cdot F_{fill}$. From this result can be deduced that tilt angles of 60 to 70° are large enough to keep the fill-factor at high value.

Reflectivity We measured a reflectivity of 37% on a flap surface consisting of a $1\mu m$ thick poly-silicon layer. The measured value agreed well with the theoretical one, obtained by thin-film-reflection theory of annex A.

Contrast ratio The contrast ratio was very dependent on the viewing angle and the illumination condition, since the measured flaps had a flat surface on which there is specular reflection of the incoming light. Depending on the position of observation the reflection of a light source is seen or not. Solutions would be to have scattering on the flap surface or a wave-shaped flap, as discussed in section 3.1.1.2. The highest contrast ratio measured was 145. For this measurement the illumination conditions were favourably. Typical contrast ratios were between 30 and 40 as measured on the flap surface.

Absorbance The absorbance was measured on a $1\mu m$ thick poly-silicon flap. Values of 85 to 95% were obtained, which agreed well with thin-film theory of annex A.

Power consumption The power consumption of the electrostatic actuation of a flap has been estimated to $64\mu W/cm^2$. But in this value the parasitic capacitance of the interconnection lines are not included.

Table 7.1: *Overview of electromechanical and optical characteristics of vertical flaps*

Parameter	**Value**	**Comments**
Actuation voltage	35-80V	depends on the geometry of the device
Tilt angle θ	55 - 85°	the smaller d the larger is θ
Typical actuation behaviour	60° at 60 V	pull-in for small d, all angles can be addressed with large d
Resonance frequency at rest state	700Hz	first mode, measured on chip A
Resonance frequency at actuated state	2.31kHz	first mode, measured on chip A
Switching time	<0.5 ms	measured on chip A by applying step of 55V
Settling time t_s	<3 ms	after t_s amplitudes are smaller than 500nm
Fill-factor $\frac{A_{active}}{A_{total}}$	30-40%	larger fill-factor for double-flaps than for single-flaps
Reflectivity o flap surface	37%	measured on $1\mu m$ thick flap surface.
Absorbance of flaps	85-95%	measured on $1\mu m$ thick flap surface. Depending on wavelength (higher for short wavelengths)
Contrast-ratio (maximal value)	145	measured Chip B at normal incidence on flap surface (active modulating area)
Contrast-ratio (average value)	30 - 40	on flap surface (active modulating area)
Surface roughness of flaps	100-200nm	on flap surface
Power consumption	$64\mu W/cm^2$	only electrostatic actuation of flaps (from model data)

7.2 Discussion of characteristics of horizontal flaps

We want to summarize electromechanical and optical properties of the horizontal flap concept presented in chapter 4. Since only few devices could be actuated, because of sticking to the substrate caused by a stress-gradient in the poly-silicon layer, many values are only estimated theoretically. An overview is given in table 7.2.

Actuation voltages of 35V were measured with a flap tilting to about 85°. This is a lower voltage and a higher tilt angle compared to the vertical flaps. It has to be pointed out that the device had a torsion beam of only 100nm, compared to 130-150nm on the vertical flaps, what explains the difference in voltage. Compared to the vertical flaps concept we had also a higher resonance frequency and higher fill-factor. But, unfortunately the fabrication process was not mature enough for obtaining arrays of reliably working devices. This concept of horizontal flaps has a good potential. Developing further the fabrication process, solving the sticking problems would give a device with excellent properties as reflective display.

Table 7.2: *Overview of electromechanical and optical characteristics of horizontal flap of chapter 4. Because the devices could not be characterized in detail of problems in the fabrication process, many values are only estimated theoretically.*

Parameter	**Value**	**Comments**
Actuation voltage	35V	measured
Tilt angle θ	85°	estimated from figure 4.13
Resonance frequency	1.6kHz	first mode, theoretical estimation
Fill-factor $\frac{A_{active}}{A_{total}}$	80%	when using flap arrangement of figure 4.2.
Reflectivity of flap surface	30%	estimated, since same material as vertical flaps.
Contrast-ratio	NA	similar values as in vertical flaps can be estimated

7.3 Applications

Here we will evaluate the ability of the vertical flaps concept of being used in different applications. The horizontal flaps concept will not be included in this analysis, since it was not fully functional.

7.3.1 Reflective MEMS display

For evaluation of the suitability of using arrays of vertical flaps as as reflective display device we will look at the requirements as stated in section 3.1.1.1.

- **Overall reflectivity:** The overall reflectivity depends on the fill-factor. For the active modulating area is obtained a fill-factor A_{flap}/A_{pixel} of about 40%. Supposing that the passive area is covered by a light-shielding of reflectance $R_{shielding}$ =1% the overall reflectivity can be calculated with equation (5.2) giving a value of 15%. With an optimised vertical flap configuration having a reflectivity of 90% on the flap surface and a fill-factor of 50% an overall reflectance of 45% can be achieved.

- **Contrast ratio:** The overall contrast ratio can be calculated utilizing equation (5.4). The reflectivity of the active modulating area in the OFF-state R_{OFF} was not directly measured, but can be estimated from the measured contrast ratio as $R_{OFF} = \frac{CR}{R_{flap}}$. Taking an average contrast ratio of the active modulating area of 40 (as given in table 7.1) and R_{flap} =37% we obtain a value of R_{OFF} =0.92%. Using again $R_{shielding}$ =1%, the overall contrast ratio is 15 for a fill-factor of 40%. On an optimised device with a flap-reflectivity of R_{flap} =95% and a fill-factor of 50% an overall contrast ratio around 50 could be possible. When taking into account a transparent cover with a reflectivity of R_{cover} =1%, employing equations (5.5) and (5.6) in (5.4), the overall contrast ratio of an optimised device is about 25.

- **Angular response:** The measured contrast ratio depended a lot on the position of observation in incidence and azimuthal angle. But the measurement were only done on one single flap. When having a double-flap configuration the variation in azimuthal observation direction cancels out. At every angle one flap will exhibit a large contrast ratio and the other a low one. On flat flaps the angular region where the flap is perceived as dark depends on the tilt angle of the flap, as illustrated in figure 5.6 of section 5.3.1. The more the flap is tilted the smaller is the dark angular region. Flaps tilting by more than 70° may give the best results. In general the angular response will also depend on the diffusivity of each pixel. The requirement of a viewing angle of 45° is most probably met.

- **Diffusivity:** One measured device had a zigzag-shaped flap, which should reflect light from different directions than a flat-shape, leading it to be perceived brighter. In the measurement with uniform illumination profile this effect could only be observed at one single direction of observation. A measurement with different light sources would be required for testing the influence of the flap-shape on the contrast ratio. A flap-shape leading to the highest light scattering is probably the wave-shaped flap as shown in figure 6.3c). To place a transparent diffusive material on top of the flap array is another possibility.

- **Resolution:** In the requirements a 100 dpi resolution was desired. With a unit size of about 70 by 300μm this value can almost be satisfied with 4 units forming one pixel. The unit size could be decreased by optimizing the configuration to dimension around 60 by 280μm. Smaller pixel sizes will require to have smaller flap widths w_{flap}, what leads to an increase in actuation voltage with a scaling of $V \propto w_{flap}^{-1/2}$.

- **Grey levels:** Depending on the flap configuration all tilt angles can be attained by actuating at a proper actuation voltage. With the tilt angle changes also the perceived brightness of a pixel. So, by adapting the actuation voltage we can obtain different grey-levels. Because of the flaps fast switching response also another solution is to use pulse-width modulations.

- **Actuation voltage:** Values as low as 40V have been demonstrated on a fabricated device. By decreasing further the thickness of the torsion beam an actuation voltage close to 20V should be achievable. Torsion beams thinner than 100nm may be in the limit of feasibility.

- **Insensitivity to environmental vibrations:** The measured resonance frequency at rest state of about 700Hz does not meet the requirement of having values above 1kHz. It has to be added here that the resonance frequency at actuated state is up to three times higher.

We compare now the vertical flap reflective display in table 7.3 with different existing technologies introduced in section 2.1.1:

- Reflectivity: Most of the technologies have a reflectivity in the range of 40%, which is half as much as on white paper. With a highly reflecting flap surface a value could be attained which is comparable to the other technologies.

- Contrast ratio: The values range for the different technologies (including paper) from 7 to 25. The fabricated vertical flaps lay in this range as well. But, with an optimized structure could be achieved the highest contrast ratio of all technologies with a value of 48.

- Switching time: The values differ a lot between the different technologies. The vertical flaps concept has the fastest response time, enabling it to be driven with a high refresh rate.

Table 7.3: *Comparison of reflective display technologies*
[1]*: flap-reflectivity 37% , fill-factor: 40%*
[2]*: contrast-ratio on flap 40 , fill-factor: 40%*
[3]*: flap-reflectivity 95%, fill-factor: 50%*
[4]*: transparent cover with* R_{cover} *=1%, flap-reflectivity 95%, fill-factor: 50%*
[5]*: for LCoS device [10]*
[6]*: 25 for normal incidence, 11 for large incidence angles of observation*
[7]*: temperature dependent, 1s at 50° C, 7s at 0° C*
[8]*:* $+/-15V$
[9]*: reflectivity Al-surface = 90%, fill-factor ≈ 50%.*

Technology	**Overall reflectivity**	**Contrast-ratio**	**Switching time**	**Pixel size**	**Actuation voltage**
Vertical flaps as fabricated	15%[1]	16[2]	<0.5 ms	70x $300\mu m^2$	40V
Vertical flaps with high reflectivity & optimized fill-factor	45%[3]	50[3], (25[4])	<0.5 ms	60x $280\mu m^2$	40V
reflective LCD (TN-cell with 2 polarisers) [8]	30%	15	1ms [101]	10x10μm^2 [5]	5V
cholesteric LCD [18]	30%	25 - 11 [6]	1-7s[7]	215x $215\mu m$	45V[17]
Electrophoretic (E-ink) [23]	40%	10	250ms	125x $125\mu m^2$	30V[8]
Interference (Qualcomm) [25, 26]	45% (green)	7	10ms	200x $200\mu m^2$	5V
Electrowetting (Liquavista) [30]	40%	15	10ms	240x $240\mu m^2$	22V
Shutter based [6]	45%[9]	20	2ms	80x $480\mu m^2$	10V
White Paper (laser printer)	80%	12	static	80x $80\mu m^2$	-

- Pixel size: Sizes vary in the various technologies. The vertical flaps have with a 70 by 300 μm large unit size a value in the centre of the span.

- Actuation voltage: The different technologies work with actuation voltages from 5 to 45V. Here the vertical flaps concept has a rather high value. The electrostatic actuation with a small capacitance per flap in the 10fF range gives nevertheless a low power consumption.

Concluding it can be said that the vertical flaps concept in an optimized configuration having a highly reflective flap surface and maximized fill-factor will be a very competitive technology in the application as reflective display. It would have the largest reflectivity, contrast ratio and switching time of all technologies compared.

7.3.2 Transmissive shutter array

To evaluate if the fabricated vertical flaps optical modulators are suitable for the application as transmissive shutter array lets look at the requirements stated in section 3.1.2.1. Most of the points as the actuation voltage, power consumption and fill-factor have already been treated analysing the system as reflective display. We have only to look at the ability of the modulator of blocking light. An absorbance of the flap surface was measured in the range of 85 to 95% in the visible spectrum. In an optimized device with a flap surface covered by a metal layer the absorbance of the flap surface could be 100%.

At the actuated state of the fabricated devices there is still light passing at the gap between flap and electrode and also at the sides. A shielding layer would be required for covering these areas. A solution similar as the one implemented in [51] could be used. Another solution would consist of using a micro-lens array as already discussed in figure 3.4 of section 3.1.2, what also would lead to an increase in fill-factor.

On table 7.4 the vertical flaps device is compared to existing technologies of shutter based transmissive modulators. We can notice the following: The Pixtronix device has a rather low fill-factor. The shutter of the University of Tokyo is actuated at very high voltages and has 1mm large shutters. The JWST-shutter array has a very high fill-factor, but is actuated with an external magnet leading to long switching times. The shutter based reflective display has a comparable fill-factor and lower actuation voltage, but the size of the shutter is the double of the vertical flaps device.

Concluding it can be said that the vertical flaps device has the best overall properties as transmissive shutter array when regarding fill-factor, actuation voltage, switching time and unit-size together.

Table 7.4: *Comparison of transmissive shutter array technologies*

Technology	**Fill-factor**	**Actuation voltage**	**Switching time**	**Pixel size**
Vertical flaps with poly-silicon (as fabricated)	40%	40V	<0.5 ms	70x 300μm^2
Vertical flaps with optimized dimensions	50%	40V	<0.5 ms	60x 280μm^2
Pixtronix [43, 44]	11.5%	>15V	<0.1ms	80x 80μm^2
University of Tokyo [3, 51]	40% (estimated)	200V	1-10 ms (estimated)	100x 1000μm^2
NASA JWST [2, 52]	80% (estimated)	magnetic (20V)	long (magnet sweep)	100x 200μm^2
Shutter based reflective display [6, 32]	50%	10V	2ms	80x 480μm^2

7.3.3 Other applications

Beside the above described applications as reflective display and transmissive shutter array the vertical flaps device could also be used in other applications. Because of the small thickness of the flaps only applications with low irradiations power can be considered:

- The switching of a blazed grating shaped flap was demonstrated in section 6.3.6. Arrays of gratings of any desired shape are easily feasible. With an array of switching or scanning gratings the overall diffracted light power could be increased. An application could be a light switch as demonstrated in the GEMS-device [55] or commercialised by Silicon Light Machines [56, 58]. These devices employ the 1st or 2nd diffraction order for modulation. By means of blazed gratings the light power could be bundled in higher diffraction orders.

- Having an array of different types of grating, an adaptive diffractive device could be designed for which at any time the desired grating shape can be switched to ON-state. Application of such a device could be in projectors, spectroscopy or spectral imaging.

- A switchable lens or scanning lens could be an application as well. The actuation of a lens-shaped flap was demonstrated in table 6.5. When the lens-flap is in actuated tilted position incoming light will reflect on its surface and be bundled in its focal point. An array of such flaps could give a high reflective power. Another possibility could be to fabricate an array of lenses with different focal lengths. By switching ON the lens with the desired focal length we would have an adaptive lens device.

- An array of flat flaps at which each row is tilted to a different angle could be used as adaptive reflective Fresnel lens.

7.4 Further developments

There is a lot of room for improvements of the optical modulators based on on tilting flaps. For the horizontal surface micromachined flaps of chapter 4 further work has to be done for obtaining a more reliable fabrication process. The main points have already been discussed in the corresponding chapter.

For the vertical flaps optical modulators the following points can be further developed:

- In the frame of the development of a reflective display larger arrays would need to be fabricated.
- Increase of fill-factor: This can be done by decreasing the passive area consisting of the electrodes and interconnection lines. By fabricating electrodes of smaller width (values down to $w_{el} = 5\mu m$ should probably be feasible), optimizing the distances between the interconnection lines and in-between the double flaps it can be reached a fill-factor of up to 50%. The flap height h_{flap} could also be increased. The limit here lays on the feasible depth of the thin trenches defining the flaps. Flap heights up to $80\mu m$ should be possible and would give fill factors around 60%. For a transmissive shutter array and also on a reflective display the fill factor could also be increased by means of a micro-lens array.
- Increase reflectivity of the flap surface: The evaporation of an around 20nm thin Al layer on the fabricated poly-silicon flaps is one solution. A problem could be here the deformation of the flap due to induced stress. Higher reflectivity could also be obtained by fabricating flaps consisting of thin film-stacks giving a Bragg-reflector. The combination of silicon-nitride and poly-silicon layers in the trench refill could be an example. An other possibility is to use metals deposited by ALD in combination with Parylene.
- Fabricate light shielding: The passive areas not modulating light are required to be shielded for different applications. In the case of a reflective display these areas have to be covered by a light absorbing layer. On a transmissive shutter light has to be blocked. An additional layer on top of the flap array would be required to be fabricated for this purpose.
- Decrease actuation voltage: A thinner torsion beam would decrease the actuation voltage. The limit is here the feasibility and reliability of fabrication of thin layers. It is difficult to obtain LPCVD poly-silicon layer lower than 100nm of exact thickness. In [6] were fabricated 50nm thin Al beams, what should be feasible to do in the vertical flaps process as well. An actuation voltage below 20V could be obtained this way.

- Obtain hysteresis in actuation: When a lower voltage is required to keep a flap at large tilt angle than to actuated it, line-column addressing can be used. On some of the fabricated devices this hysteresis phenomena could be demonstrated. By further optimizing the electrode-beam distance and the offset between flap and beam we can obtain a larger hysteresis.

- Optimize flap shape for light scattering: In the application of reflective display the scattering properties of a flap surface can be obtained for example with a wave-shaped flap. The optimal flap profile for maximized scattering has to be found.

- Process optimization: The fabrication reliability could be increased by slightly changing the fabrication process. Specially during the release process many torsion beams break, probably due to stress induced by the SiO_2 membrane of the BOx below the flaps. By first etching the front side, protecting it with a thick Parylene layer and only subsequently opening the backside a better result is expected.

- Colour reflective display: A reflective display exhibiting different colours could be fabricated in different ways. One possibility is to have a flap surface reflecting only one wavelength by means of a Bragg-reflector composed of a thin-film stack. This way a red, a blue and a green flap would form one pixel. For example by switching ON the red flap and switching OFF the other two a red pixel would be obtained. The same could be done with the other colours and combination thereof. Another possibility for obtaining a colour-display could be to have wavelength selective reflector instead of the black absorbing layer placed below the flap-array.

In addition to the above list of points to be optimized the various applications as switchable grating arrays would need to be tested out. Also could be explored the applications of the various other demonstrated flap-shapes such as a grating, lens or a comb.

8 Conclusion

In this thesis the design, modelling, fabrication process and characterization of novel optical modulators were presented. The modulators were based on flaps tilting by large angles using electrostatic actuation. The main applications were a reflective display and a transmissive shutter array.

Flaps suspended by a torsion beam which are vertical at their rest state and after fabrication were tilted towards an opposing electrode with low actuation voltage compared to other electrostatic shutters reported in literature. When used as a reflective display, light was absorbed by an underlying black layer when the flaps were in their vertical rest state. As the flaps were tilted to a nearly horizontal position, the light was back reflected. For use as a transmissive shutter, light passed through the device in the vertical state and was blocked in the horizontal state.

An electromechanical model was made of the electrostatically tilting flaps describing the scaling laws and the voltage to tilt-angle trajectory. With this model, different configurations of the modulator were designed and fabricated by means of a novel developed process. The fabrication process used micro-moulding of poly-silicon in narrow high-aspect ratio trenches. The structures were released by a sequence of dry-etching steps. This process also permitted to the fabrication of various flap shapes including a blazed grating, a grid or a lens.

The fabricated devices were characterized electromechanically using specifically designed measurement setups. Typically, the flaps could reach a tilt angle of 60° at an actuation voltage of 60V. Other devices worked at voltages ranging between 35 and 85V and some exhibited hysteresis in the actuation trajectory. Actuation voltages below 10V for up to 15° tilt have been demonstrated on comb-shaped flaps. Switching times were below 0.5ms with a 700Hz resonance frequency in the rest state and values above 2kHz in the actuated state.

A special methodology and illumination setup was developed for optical characterization. On the flap surface, the measured reflectivity was 37%, while the measured absorbance of the transmission mode was 85-95%. When used as reflective display, a contrast ratio on the active modulating area of up to 145 was obtained (with an average value of 30-40). Taking into account the minimum fill-factor of 40%, the reflective display would have an overall reflectivity of 15%, a contrast ratio of 16 and a 85dpi resolution. Optimizing the modulators by having a highly reflective flap surface and increasing slightly the fill-factor would give an overall reflectivity of 45% and a contrast ratio of 50. These values are very competitive when compared to other reflective display technologies reported in the literature.

The application of a vertical flap with a blazed grating profile as a switchable diffraction grating has also been demonstrated. The diffraction pattern of an incident laser beam was observed on a screen and could be scanned up-and-down by changing the tilt angle of the flap.

Besides the vertical flaps, an additional concept was presented for flaps in the horizontal position at rest. The devices were fabricated using surface micromachining. The poly-silicon flaps were tilted from the horizontal to the vertical position with an actuation voltage of 35V. The reliability of the fabrication process was low due to stress-related sticking of the flaps. By solving the challenges in the fabrication process, this concept could present a competitive reflective display technology as well.

There are several aspects on which further research should be done on the vertical flaps concept: The fill-factor could be increased by optimization of the non-active areas of a flap array or fabrication of flaps of larger height. A higher reflectivity of the flap surface could be obtained by deposition of a thin aluminium layer or by fabricating flaps composed of a thin-film stack forming a Bragg reflector. Larger arrays would be required to be fabricated for demonstrating the application as reflective display or transmissive shutter array. These arrays should be combined with proper addressing circuitry and have light shielding to cover the non-active modulating areas. In addition, a large variety of applications could be explored with the various flap shapes which can be fabricated with the vertical flaps process, such as arrays of switchable gratings or switchable lenses.

A Calculation of thin film reflectance

The reflectance R and transmittance T of a thin film can be calculated out of the optical material properties of refractive index n and absorption coefficient α. The Abeles Matrix method as described in [102, 103] can be used for this purpose.

The thin-film system is given in figure A.1. It consists of a layer of thickness t, which is surrounded by air. Incoming light has an intensity I_0. The light is reflected with an intensity I_R and transmitted through the layer with an intensity I_T. The reflectance R, transmittance T and absorbance A are here defined as:

$$R = \frac{I_R}{I_0} \tag{A.1}$$

$$T = \frac{I_T}{I_0} \tag{A.2}$$

$$A = 1 - T \tag{A.3}$$

We calculate the reflectance for a poly-silicon film of $1\mu m$ thickness and a bulk silicon substrate

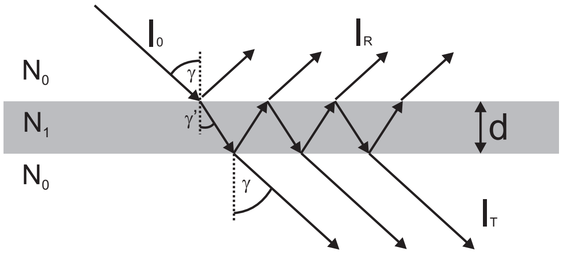

Figure A.1: *Schematic of thin-film system with incoming irradiation of intensity I_0 at an incidence angle γ, reflected intensity I_R and transmitted intensity I_T. The film has a complex index of refraction $N_1 = n + i\frac{\lambda}{4\pi}\alpha$ and is surrounded by air of refractive index $N_0 = 1$.*

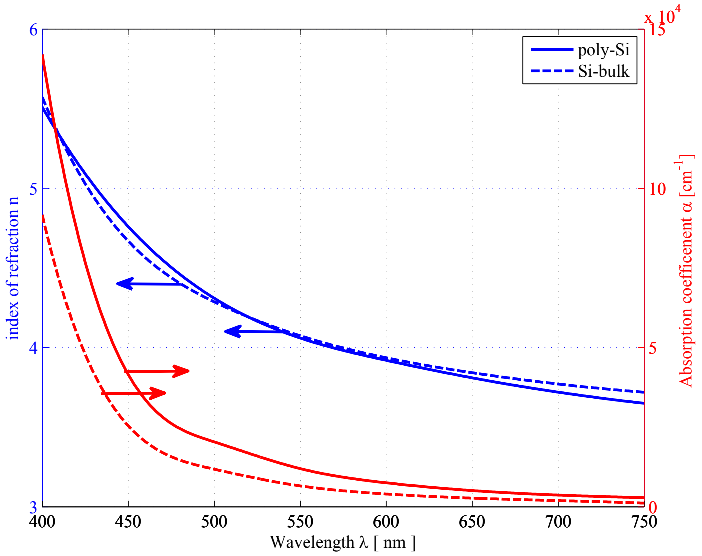

Figure A.2: *Optical properties of poly-silicon [103] and crystalline silicon [104]. Both materials have comparable values. Note that the absorption coefficients drop above 450nm wavelength.*

(of infinite thickness) with the Ables Matrix method using the optical properties of poly-silicon as given in [103] and plotted in figure A.2.

The reflectance R and absorbance A of a poly-silicon layer of $1\mu m$ thickness compared to a crystalline silicon substrate is shown in figure A.3a). The reflectance of the poly-silicon layer changes a lot in function of the wavelength due to interference. The reflectance of the silicon substrate follows the curve of poly-silicon, but without the amplitude oscillations from 0.48 at $\lambda = 400nm$ to 0.33 at $\lambda = 750nm$. The absorbance of the poly-silicon thin-film decreases from almost full absorbance at $\lambda = 400nm$ to 0.6 at $\lambda = 750nm$. Also the reflectance and transmittance of the poly-silicon thin-film in function of the incidence angle γ was evaluated. The results are shown in figure A.3b) with values given for the optical system for measuring the reflectance of section 6.3.2. The intensity distribution of the illumination and the sensitivity of the camera in grey-mode as given in figure 6.20 were taken into account in the calculations. It can be seen that the reflectivity R stays quite constant at 0.417 up to a $\gamma = 75°$. Also A has a constant value around 0.94 up to the same γ.

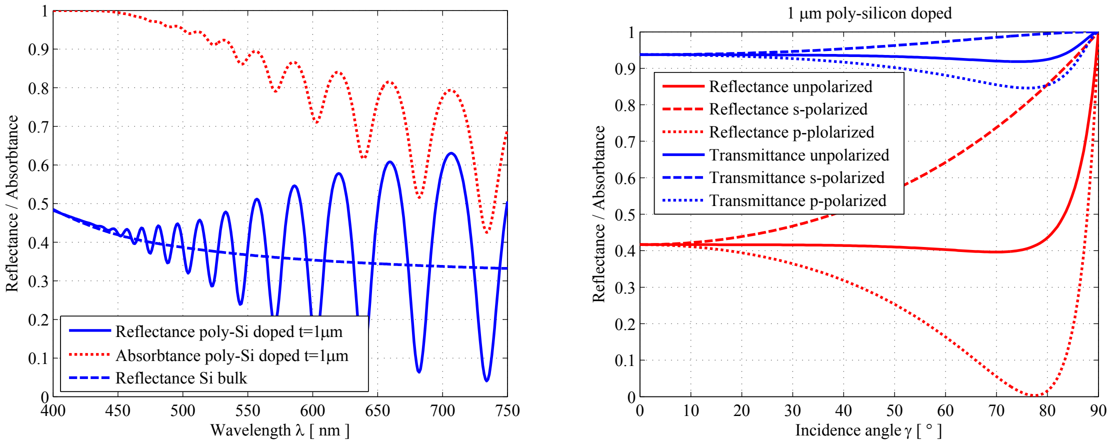

a) b)

Figure A.3: *a) The reflectance R and absorbance A of $1\mu m$ thick poly-silicon layer in air as shown in figure A.1 and of thick crystalline Si substrate at normal incidence. The absorbance decreases for larger wavelengths. b)The reflectivity and absorbance of a $1\mu m$ thick poly-silicon layer in air calculated for the optical system for reflectivity measurements of section 6.3.2. The reflectivity stays constant at 0.417 up to $\gamma = 75°$.*

Bibliography

[1] A. K. Bhowmik, Z. Li, and P. J. Bos, *Mobile displays: technology and applications.* John Wiley & Sons, 2008.

[2] M. Li, N. Acuna, E. Amatucci, M. Beamesderfer, R. Boucarut, S. Babu, S. Bajikar, A. Ewin, R. Fettig, and D. e. a. Franz, "Microshutter array development for the James Webb space telescope," in *Proc. SPIE*, vol. 5650, p. 9, 2005.

[3] K. Motohara, T. Takahashi, H. Toshiyoshi, M. Mita, N. Kobayashi, and N. Kashikawa, "Development of microshutter arrays for ground-based instruments," in *Proc. Instrumentation of Extremely large Telescopes*, pp. 3–7, 2005.

[4] Y. Yoon, K. Bae, J. Kim, H. Choi, and B. Koh, "A low voltage actuated micromirror with an extra vertical electrode for 90° rotation," *J. Micromech. Microeng.*, vol. 13, p. 922, 2003.

[5] M. Zickar, *MEMS based Optical Cross Connects for Fiber Optical Communication.* PhD thesis, University of Neuchâtel, 2006.

[6] R. Vuilleumier, A. Perret, F. Porret, and P. Weiss, "Novel electromechanical microshutter display device," in *Proc. SID Eurodisplay'84*, vol. 3, pp. 41–44, Sept. 1984.

[7] M. Schadt, "Voltage-Dependent Optical Activity of a Twisted Nematic Liquid Crystal," *Applied Physics Letters*, vol. 18, no. 4, p. 127, 1971.

[8] S. Wu and D. Yang, *Reflective liquid crystal displays.* John Wiley & Sons, 2001.

[9] D. Armitage, I. Underwood, and S.-T. Wu, *Introduction to Microdisplays.* John Wiley & Sons, 2006.

[10] Sony, "SXRD 4K Projection Introduction," *http://www.sony.com*, 2008.

[11] D.-K. Yang, L.-C. Chien, and J. W. Doane, "Cholesteric liquid crystal/polymer dispersion for haze-free light shutters," *Applied Physics Letters*, vol. 60, no. 25, p. 3102, 1992.

[12] T. Schneider, D. J. Davis, S. Franklin, N. Venkataraman, D. McDaniel, F. Nicholson, E. Montbach, A. Khan, and J. W. Doane, "New developments in flexible cholesteric liquid crystal displays," in *Proc. SPIE*, vol. 6487, p. 64870J, 2007.

[13] J. Doane, D. Davis, A. Khan, E. Montbach, T. Schneider, and I. Shiyanovskaya, “Cholesteric reflective displays: thin and flexible,” in *Proc. IDRC 2006*, pp. 9–12, 2006.

[14] A. Green, E. Montbach, N. Miller, D. Davis, A. Khan, T. Schneider, and J. Doance, “Energy efficient flexible reflex displays,” in *Proc. Int. Display Research Conf*, pp. 55–58, 2008.

[15] E. Montbach, N. Venkataraman, A. Khan, I. Shiyanovskaya, T. Schneider, J. Doane, L. Green, and Q. Li, “Novel Optically Addressable Photochiral Displays,” in *SID Symposium Digest of Technical Papers*, vol. 39, p. 919, 2008.

[16] D. Marhefka, N. Venkataraman, A. Khan, S. Barua, F. Nicholson, T. Ernst, and J. Doane, “Novel Pulsed Drive Scheme for Improved Gray-Level Uniformity of Large-Area Cholesteric Displays,” in *SID Symposium Digest of Technical Papers*, pp. 810–813, 2008.

[17] A. Khan, I. Shiyanovskaya, T. Schneider, and J. W. Doane, “Recent Progress in Flexible and Drapable Reflective Cholesteric Displays,” in *SID Symposium Digest of Technical Papers*, pp. 1728–1731, 2006.

[18] Kent Display, “Reflex Graphic Display Module 128x32,” *http://www.kentdisplays.com*, 2009.

[19] B. Comiskey, J. Albert, H. Yoshizawa, and J. Jacobson, “An electrophoretic ink for all-printed reflective electronic displays,” *Nature*, vol. 394, no. 6690, pp. 253–255, 1998.

[20] Y. Chen, J. Au, P. Kazlas, A. Ritenour, H. Gates, and M. McCreary, “Flexible active-matrix electronic ink display,” *Nature*, vol. 423, no. 6936, p. 136, 2003.

[21] S. Inoue, H. Kawai, S. Kanbe, T. Saeki, and T. Shimoda, “High-resolution microencapsulated electrophoretic display (EPD) driven by poly-si TFTs with four-level grayscale,” *IEEE Trans. on Electron Dev.*, vol. 49, pp. 1532–1539, Sept. 2002.

[22] R. Zehner, “Electronic Paper Displays,” in *Mobile Displays: Technology and Applications*, ch. 15, pp. 427–442, John Wiley & Sons, 2008.

[23] E-Ink Coorporation, “E Ink Pearl Imaging Film Active Matrix Monochrome Electronic Paper,” tech. rep., 2011.

[24] Qualcomm MEMS Technologies, “White Paper: Operating Principles of the IMOD Drive,” *http://www.mirasoldisplays.com*, 2009.

[25] Qualcomm MEMS Technologies, “White Paper: Technology Overview,” *http://www.mirasoldisplays.com*, 2009.

[26] Qualcomm MEMS Technologies, “Data Sheet: Qualcomm Bichrome 1.2" Display,” *http://www.mirasoldisplays.com*, 2007.

[27] C. Lo, O. Huttunen, J. Hiitola-Keinanen, J. Petaja, H. Fujita, and H. Toshiyoshi, "MEMS-controlled paper-like transmissive flexible display," *J. Microelectromech. Sys.*, vol. 19, no. 2, pp. 410–418, 2010.

[28] R. Hayes, B. Feenstra, and Others, "Video-speed electronic paper based on electrowetting," *Nature*, vol. 425, pp. 383–385, Mar. 2003.

[29] T. Roques-Carmes, R. Hayes, B. Feenstra, and L. Schlangen, "Liquid behavior inside a reflective display pixel based on electrowetting," *J. Appl. Phys.*, vol. 95, no. 8, p. 4389, 2004.

[30] B. Feenstra, R. Hayes, I. Camps, L. Hage, M. Johnson, T. Roquest-Carmes, and L. Schlangen, "A reflective display based on electrowetting: principle and properties," in *Proc. Society for Information IDRC Display Symposium*, vol. 23, pp. 322–324, 2003.

[31] A. Giraldo, J. Aubert, N. Bergeron, F. Li, A. Slack, and M. V. D. Weijer, "Transmissive Electrowetting-Based Displays for Portable Multi-Media Devices Color architectures," in *SID Symposium Digest of Technical Papers*, pp. 479–482, 2009.

[32] M. Cadman, A. Perret, F. Porret, R. Vuilleumier, and P. Weiss, "New micromechanical display using thin metallic films," *IEEE Electron Device Letters*, vol. 4, no. 1, pp. 3–4, 1983.

[33] A. Perret and R. Vuilleumier, "Method of manufacturing a device with micro-shutters and application of such a method to obtain a light modulating device," *US Patent 4,584,056*, Apr. 1986.

[34] R. Vuilleumier, "Light modulation device with matrix addressing," *US Patent 5,078,479*, Jan. 1992.

[35] P. Grandjean, M. Cadman, R. Vuilleumier, and R. Guye, "Miniature display device," *US Patent 4'383'255*, May 1983.

[36] R. Vuilleumier and P. Weiss, "Miniature shutter type display device with multiplexing capability," *US Patent 4,564,836*, Jan. 1986.

[37] P. Weiss, "MEMS & MOEMS Reliability : Wafer- Level Packaging and Low-Temperature Processing Issues," in *IEEE/LEOS Workshop on Fibres and Optical Passive Components*, pp. 75 – 86, 2005.

[38] J. Teijido, W. Noell, M. Zickar, and N. De Rooij, "Shutter Device For Pixel Element and Pixel Arrangement," *US Patent 2008/0303781 A1*, Feb. 2008.

[39] M. Pizzi, V. Koniachkine, M. Nieri, S. Sinesi, and P. Perlo, "Electrostatically driven film light modulators for display applications," *Microsystem Technologies*, vol. 10, pp. 17–21, Dec. 2003.

[40] K. Wang and M. Sinclair, "An electrostatic zigzag transmissive microoptical switch for MEMS displays," *J. Microelectromech. Sys.*, vol. 16, no. 1, pp. 140–154, 2007.

[41] G. Perregaux, P. Weiss, B. Kloeck, I. Vuilliomenet, and J. Thiébaud, “High-speed micro-electromechanical light modulation arrays,” in *Int. Conf. Solid State Sensors and Actuators (Tranducers 97)*, vol. 1, pp. 71–74, 1997.

[42] G. Perregaux, S. Gonseth, and P. Debergh, “Arrays of addressable high-speed optical microshutters,” in *IEEE 14th Int. Conf. Micro Electro Mechanical Systems (MEMS 2001)*, no. January, pp. 232–235, 2001.

[43] J. Steyn, T. Brosnihan, J. Fijol, J. Gandhi, N. Hagood, M. Halfman, S. Lewis, R. Payne, and J. Wu, “A MEMS Digital Microshutter (DMS) for Low-Power high brightness displays,” in *Int. Conf. Opt. MEMS and Nanophotonics*, pp. 73–74, 2010.

[44] N. Hagood, R. Payne, L. Steyn, J. Fijol, J. Gandhi, S. Lewis, G. Fike, R. Barton, and M. Halfman, “Pixtronix DMS Display Technology : Ultra-Low Power Consumption and Exceptional Video Image Quality,” *WhitePaper Pixtronics*, pp. 1–3, 2008.

[45] N. Binh-Khiem and K. Matsumoto, “Reflective display using ionic liquid,” in *IEEE 22nd Int. Conf. Micro Electro Mechanical Systems (MEMS 2009)*, pp. 168–171, 2009.

[46] A. C. Arsenault, D. P. Puzzo, I. Manners, and G. a. Ozin, “Photonic-crystal full-colour displays,” *Nature Photonics*, vol. 1, pp. 468–472, Aug. 2007.

[47] A. L. Pyayt, G. K. Starkweather, and M. J. Sinclair, “A high-efficiency display based on a telescopic pixel design,” *Nature Photonics*, vol. 2, pp. 492–495, July 2008.

[48] P. V. Kessel, L. Hornbeck, and R. Meier, “A MEMS-based projection display,” in *Proc. IEEE*, vol. 86, pp. 1687–1704, 1998.

[49] H. Toshiyoshi and H. Fujita, “Electrostatic micro torsion mirrors for an optical switch matrix,” *J. Microelectromech. Sys.*, vol. 5, no. 4, pp. 231–237, 1996.

[50] G. Zhu, M. Packirisamy, M. Hosseini, and Y.-A. Peter, “Modelling and control of an electrostatically actuated torsional micromirror,” *J. Micromech. Microeng.*, vol. 16, pp. 2044–2052, Oct. 2006.

[51] T. Takahashi, M. Mita, K. Motohara, N. Kobayashi, H. Fujita, H. Toshiyoshi, and N. Kashikawa, “Electrostatically addressable visored shutter array by electroplating for astronomical spectrography,” in *Int. Conf. Opt. MEMS and Nanophotonics*, pp. 79–80, 2011.

[52] M. Li, T. Adachi, C. Allen, S. Babu, S. Bajikar, M. Beamesderfer, R. Bradley, N. Costen, K. Denis, and A. e. a. Ewin, “Microshutter array system for James Webb Space Telescope,” in *Proc. SPIE*, vol. 6687, p. 668709, 2007.

[53] M. Kowarz, J. Brazas Jr, and J. Phalen, “Conformal grating electromechanical system (GEMS) for high-speed digital light modulation,” in *IEEE 15th Int. Conf. Micro Electro Mechanical Systems (MEMS 2002)*, pp. 568–573, 2002.

[54] J. Agostinelli, M. Kowarz, D. Stauffer, T. Madden, and J. Phalen, "Gems: A simple light modulator for high-performance laser projection display," in *IDW 06*, pp. 1579–1582, 2006.

[55] J. Brazas and M. Kowarz, "High-resolution laser-projection display system using a grating electromechanical system (GEMS)," in *Proc. SPIE*, vol. 5348, pp. 1579–1582, 2004.

[56] D. Bloom, "The grating light valve: revolutionizing display technology," in *Proc. SPIE*, vol. 3013, pp. 165–171, 1997.

[57] D. Amm and R. Corrigan, "Optical performance of the grating light valve technology," in *Proc. SPIE*, vol. 3634, pp. 71–78, 1999.

[58] Silicion Light Machine Inc. *http://www.siliconlight.com*, 2011.

[59] M. Madou, *Fundamentals of microfabrication.* CRC Press New York, 1997.

[60] J. Bhardwaj and H. Ashraf, "Advanced silicon etching using high-density plasmas," in *Proc. SPIE*, vol. 2639, p. 224, 1995.

[61] S. Aachboun, P. Ranson, C. Hilbert, and M. Boufnichel, "Cryogenic etching of deep narrow trenches in silicon," *J. Vacuum Science & Technology A: Vacuum, Surfaces, and Films*, vol. 18, no. 4, p. 1848, 2000.

[62] W. C. Young, *Roark's Formulas for Stress & strain.* McGraw-Hill, 6th ed., 1989.

[63] R. A. Serway, *Physics for Scientists and Engineers.* Publishing, Saunders College, 1986.

[64] H. Goldstein, *Classical Mechanics.* Addison-Wesley, 2nd ed., 1980.

[65] P. J. French, "Polysilicon: a versatile material for microsystems," *Sensors and Actuators A: Physical*, vol. 99, no. 1-2, pp. 3–12, 2002.

[66] W. Tang, M. Lim, and R. Howe, "Electrostatic comb drive levitation and control method," *J. Microelectromech. Sys.*, vol. 1, no. 4, pp. 170–178, 1992.

[67] J. Mitchell, G. R. Lahiji, and K. Najafi, "Long-term reliability, burn-in and analysis of outgassing in AuSi eutectic wafer-level vacuum packages," in *Solid state sensors and actuators workshop*, pp. 376–379, 2006.

[68] Y. Yee, M. Park, and K. Chun, "A sticking model of suspended polysilicon microstructure including residual stress gradient and postrelease temperature," *J. Microelectromech. Sys.*, vol. 7, no. 3, pp. 339–344, 1998.

[69] S. Greek, F. Ericson, S. Johansson, M. Fürtsch, and A. Rump, "Mechanical characterization of thick polysilicon films: Young's modulus and fracture strength evaluated with microstructures," *J. Micromech. Microeng.*, vol. 9, pp. 245–251, 1999.

[70] D. Maier-Schneider, A. Koprululu, S. Ballhausen Holm, and E. Obermeier, "Elastic properties and microstructure of LPCVD polysilicon films," *J. Micromech. Microeng.*, vol. 6, no. 4, pp. 436–446, 1996.

[71] J. Yang, H. Kahn, A. Q. He, S. M. Phillips, and A. H. Heuer, "A new technique for producing large-area as-deposited zero-stress LPCVD polysilicon films: the MultiPoly process," *J. Microelectromech. Sys.*, vol. 9, no. 4, 2000.

[72] T. G. Bifano, H. T. Johnson, P. Bierden, and R. K. Mali, "Elimination of stress-induced curvature in thin-film structures," *J. Microelectromech. Sys.*, vol. 11, no. 5, pp. 592–597, 2002.

[73] M. Yang, A. Gatto, and N. Kaiser, "Optical thin films with high reflectance, low thickness and low stress for the spectral range from vacuum UV to near IR," *J. Opt. A: Pure Appl. Opt.*, vol. 8, no. 3, p. 327, 2006.

[74] D. S. Gardner and P. A. Flinn, "Mechanical stress as a function of temperature in aluminum films," *IEEE Trans. on Electron Dev.*, vol. 35, no. 12, pp. 2160–2169, 1988.

[75] M. A. Helmbrecht and M. He, "Advanced optical coatings of a segmented MEMS DM," in *Proc. SPIE*, vol. 7209, p. 72090M, 2009.

[76] K. Walsh, J. Norville, and Y. Tai, "Photoresist as a sacrificial layer by dissolution in acetone," in *IEEE 14th Int. Conf. Micro Electro Mechanical Systems (MEMS 2001)*, pp. 114–117, 2001.

[77] A. Bagolini, L. Pakula, T. Scholtes, H. Pham, P. French, and P. Sarro, "Polyimide sacrificial layer and novel materials for post-processing surface micromachining," *J. Micromech. Microeng.*, vol. 12, p. 385, 2002.

[78] F. Ayazi and K. Najafi, "High aspect-ratio polysilicon micromachining technology," *Sensors and Actuators A: Physical*, pp. 46–51, 2000.

[79] F. Ayazi and K. Najafi, "High aspect-ratio dry-release poly-silicon MEMS technology for inertial-grade microgyroscopes," in *IEEE Position Location and Navigation Symposium*, pp. 304–308, 2000.

[80] F. Ayazi and K. Najafi, "High aspect-ratio combined poly and single-crystal silicon (HARPSS) MEMS technology," *J. Microelectromech. Sys.*, vol. 9, no. 3, pp. 288–294, 2000.

[81] K. a. Shaw, Z. Zhang, and N. C. MacDonald, "SCREAM I: A single mask, single-crystal silicon, reactive ion etching process for microelectromechanical structures," *Sensors and Actuators A: Physical*, vol. 40, pp. 63–70, Jan. 1994.

[82] Y.-J. Yang and W.-C. Kuo, "A novel fabrication method for suspended high-aspect-ratio microstructures," *J. Micromech. Microeng.*, vol. 15, pp. 2184–2193, Nov. 2005.

[83] Y. Suzuki and Y. Tai, “Micromachined high-aspect-ratio parylene spring and its application to low-frequency accelerometers,” *J. Microelectromech. Sys.*, vol. 15, no. 5, pp. 1364–1370, 2006.

[84] M. Wu and W. Fang, “A molded surface-micromachining and bulk etching release (MOSBE) fabrication platform on (1 1 1) Si for MOEMS,” *J. Micromech. Microeng.*, vol. 16, pp. 260–265, Feb. 2006.

[85] T. Overstolz, P. Clerc, W. Noell, M. Zickar, and N. de Rooij, “A clean wafer-scale chip-release process without dicing based on vapor phase etching,” in *IEEE 17th Int. Conf. Micro Electro Mechanical Systems (MEMS 2004)*, pp. 717–720, 2004.

[86] Acktar Advanced Coatings Ltd *http://www.acktar.com*, Dec 2011.

[87] S. Dabral, J. Van Etten, X. Zhang, C. Apblett, G. R. Yang, P. Ficalora, and J. F. McDonald, “Stress in thermally annealed parylene films,” *J. Electronic Materials*, vol. 21, no. 10, pp. 989–994, 1992.

[88] T. Harder, T. Yao, Q. He, C. Shih, and Y. Tai, “Residual stress in thin-film parylene-C,” in *IEEE 15th Int. Conf. Micro Electro Mechanical Systems (MEMS 2002)*, pp. 435–438, 2002.

[89] Combine ZP *http://www.hadleyweb.pwp.blueyonder.co.uk* , Dec 2011.

[90] Veeco Wyko NT1100 *http://www.veeco.com*, Dec 2011.

[91] Polytec MAS-400 *http://www.polytec.de*, Dec 2011.

[92] A. V. Oppenheim and A. S. Willsky, *Signal and Systems.* Prentice Hall, 2nd ed., 1996.

[93] P. Debevec and J. Malik, “Recovering high dynamic range radiance maps from photographs,” in *ACM SIGGRAPH 2008 classes*, p. 31, 2008.

[94] M. Robertson, S. Borman, and R. Stevenson, “Dynamic range improvement through multiple exposures,” in *Int. Conf. Image Processing ICIP 99*, vol. 3, pp. 159–163, 1999.

[95] M. a. Robertson, S. Borman, and R. L. Stevenson, “Estimation-theoretic approach to dynamic range enhancement using multiple exposures,” *J. Electronic Imaging*, vol. 12, no. 2, p. 219, 2003.

[96] IDS Imaging Development Systems GmbH *http://www.ids-imaging.de*, Dec 2011.

[97] Thorlabs MCWHL2-C1 *http://www.thorlabs.de/Thorcat/20900/20900-D02.pdf*, Dec 2011.

[98] OSRAM Opto Semiconductors GmbH, “Diamond DRAGON LUW W5AP,” tech. rep., 2009.

[99] G. Barna, “Apparatus for optical characterization of displays,” *Review of Scientific Instruments*, vol. 47, no. 10, pp. 1258–1260, 1976.

[100] M. Becker, "Standards and Metrology for Reflective LCDs," in *SID Symposium Digest of Technical Papers*, vol. 33, p. 136, 2002.

[101] S. Gauza, X. Zhu, W. Piecek, R. Dabrowski, and S. Wu, "Fast switching liquid crystals for color-sequential LCDs," *J. Display Technology*, vol. 3, no. 3, pp. 250–252, 2007.

[102] K. Ohta and H. Ishida, "Matrix formalism for calculation of electric field intensity of light in stratified multilayered films," *Appl. opt.*, vol. 29, pp. 1952–9, May 1990.

[103] G. Lubberts, "Optical properties of phosphorus-doped polycrystalline silicon layers," *J. Appl. Phys.*, vol. 52, no. 11, p. 6870, 1981.

[104] "Sopra 100," *http://refractiveindex.info*, Dec 2011.

Acknowledgements

First of all I would like to thank my thesis director Prof. Nico de Rooij for having given my the possibility of doing this thesis at the Sensors, Actuators and Microsystems Laboratory (SAMLAB) of EPFL, for having organized the financial frame and managing this laboratory to be a place with great infrastructure and working climate.

A thank-you also to my thesis co-director and supervisor Dr Wilfried Noell, for having set up and guided my through the project and managing the financial and administrative matters. His numerous ideas helped me a lot.

I would also like to thank the Swatch Group R&D, Division Asulab for financial funding in the first phase of the project. Thanks to its staff for the technical discussions and inputs.

It was also always a pleasure to work and have fruitful discussion with my colleagues of the optical MEMS group Roland Bitterli, Michael Canonica, Jonathan Masson, Yves Pétremand and the former members Caglar Ataman, Dara Bayat, Nicolas Golay, Sébastien Lani and Stefan Weber. The same with the other PhD students of SAMLAB David De Koninck, Rokhaya Gueye, Blaise Guélat, Pattanaphong Janphuang, Olivier Lässer, Frédéric Loizeau, Francisco Molina Lopez, Luca Ribetto, Rahel Strässle, Sara Talaei, Andres Vasquez Quintero, Yexian Wu and Philip Wägli. Equally with the other current and former members of the laboratory Teru Akiyama, Danick Briand, Jérome Courbat, Olivier Frey, Franz Friedrich, Sebastian Gautsch, Alexandra Homsy, Don Isarakorn, Robert Lockhart, Giorgio Mattana, Jason Ruan and Peter Van der Wal. Special thanks to Karine Frossard for taking care efficiently of all administrative matters and Claudio Novelli for IT-support. Thanks to everybody of you for all technical help you gave me. With all of you SAMLAB was always a enjoyable place to work with entertaining coffee breaks, unforgeable apéros and fun after-work activities.

Thanks also to my colleagues of LMTS-EPFL for the possibility of using their equipment, the technical help and contribution to the a nice working climate in the building: Prof Herbert Shea, Samin Akbari, Caglar Ataman (special thanks for the help with LDV-measurements), Subha Chakraborty, Simon Dandavino, Kaustav Ghose, Luc Maffli, Myriam Poliero, Samuel Rosset, Jun Shintake and Vinu Venkatraman.

A great thank-you goes also to the staff of the CSEM microtechnology division, Neuchâtel. Without their help, it would not have been possible to fabricate the devices developed in this thesis. They did all an excellent processing job and were always available for any technical question. Special thanks to Pierre-André Clerc for his extraordinary work of DRIE, Stéphane Ischer for the numerous thin-film depositions, Sébastien Lani for answering any imaginable processing-related question, Edith Milotte for her availability and Sylviane Pochon for the dicing, wirebonding and coffee-machine-managing. Thanks also to Giovanni Bergonzi, Jean-Daniel Cretin, Rémy Fournier, Laurent Guillot, Sylvain Jeanneret, Sabina Jenny, Jean-Paul Morel, Thomas Overstolz and José Vaquera. A thank-you goes also to Massoud Dadras and Mireille Leboeuf of the service of microscopy for permitting me to take nice pictures of my devices.

I would also to thank the staff of the center of microtechnology CMI of EPFL, Lausanne. Special thanks to Philippe Flückiger, Cyrille Hibert, Nareg Simonian, Didier Bouvet, Georges-André Racine for help in technological questions, introduction to the equipment, and thin-film depositions.

I want also to send my thanks to the semester and master students Benjamin Zhai and Steve Fahrni for their contributions in the project.

My gratitude goes also to the staff of the Institute des Microtechnologies Apliquées of HE-ARC, La Chaux-de-Fonds, in particular Prof Herbert Keppner and Jérome Charmet for their technical discussions and help in Parylene deposition.

I also would like thank various people who helped throughout the project with helpful discussion: Prof Gursel Alici, Joanna Bitterli, Friedrich Heitger and Frédéric Zamkotsian.

Last but not least I want to thank all the people not directly related to this work, but who supported my during these years and specially during the last laborious months: My friends, my parents and my girlfriend.

I would like to thank my parents for having supported my financially and morally during my whole studies, giving me the possibility of getting to the point of finishing this PhD thesis. Thanks to my mother for always looking after me, to my father for the valuable technical discussions and practical help. I like to thank my girlfriend Bruna for the patience and emotional help, specially during these last intensive months. The time spent with here was wonderful and permitted me to regain energy.

If ever I forgot anyone who helped me or contributed to this project I would like to send my thanks to him/her as well!

Publications list

Publications related to this thesis

F. Jutzi, W. Noell, N. de Rooij, "Low voltage vertical flaps arrays as optical modulating elements for reflective display and switchable gratings", in *SPIE Photonics West 2012*, San Francisco, USA (oral presentation, accepted).

F. Jutzi, W. Noell, N. de Rooij, "Vertical flaps of arbitrary shape for reflective MEMS displays and optical modulators", in *Int. Conf. Optical MEMS & Nanophotonics*, pp. 155-156, August 2011, Istanbul, Turkey (oral presentation).

F. Jutzi, W. Noell, N. de Rooij, "Electrostatic torsional vertical flaps for reflective MEMS display", in *16th Int. Conf. Solid-State Sensors, Actuators and Microsystems, (Transducers 11)*, pp. 2924-2927, June 2011, Beijing, China (oral presentation).

F. Jutzi, W. Noell, N. de Rooij, "Vertical, electrostatically 90° turning flaps for reflective MEMS display", in *Proc. SPIE* 7930, 79300H, January 2011 (oral presentation).

F. Jutzi, F. Gueissaz, W. Noell, N. de Rooij, "Low voltage electrostatic 90° turning flap for reflective MEMS display", in *Int. Conf. Optical MEMS & Nanophotonics*, pp. 77-78, August 2010, Sapporo, Japan (oral presentation).

Publications not related to this thesis

F. Jutzi, D.H.B. Wicaksono, G. Pandraud, N. de Rooij, P.J. French,"Far-infrared sensor with LPCVD-deposited low-stress Si-rich nitride absorber membrane - Part 1. Optical absorptivity - Part 2: Thermal property", *Sensors and Actuators A: Physical*, vol. 152 (2), pp. 119-138, June 2009.

C. Ataman, S. Lani, W. Noell, F. Jutzi, D. Bayat, N.de Rooij, "Fabrication and characterization of 3D integrated 2 DOF Micromirror Arrays for excessive thermal loads", in *IEEE 24th Int. Conf. on Micro Electro Mechanical Systems (MEMS)*, pp. 684 – 687, 2011.

S. M. Weber, L. Bonacina, W. Noell, D. Kiselev, J. Extermann, F. Jutzi, S. Lani, O. Nenadl, J.-P. Wolf, and N. de Rooij, "Design, simulation, fabrication, packaging, and characterization of a MEMS-based mirror array for femtosecond pulse-shaping in phase and amplitude", *Rev. Sci. Instrum.*, vol.82 (7), p. 075106, 2011.

J. Extermann, S. M. Weber, D. Kiselev, L. Bonacina, S. Lani, F. Jutzi, W. Noell, N. de Rooij, and J.-P. Wolf,"Spectral phase, amplitude, and spatial modulation from ultraviolet to infrared with a reflective MEMS pulse shaper", *Optics Express*, vol. 19 (8), pp. 7580-7586, 2011.

Curriculum Vitae

Fabio Jutzi
born 1983 in Bern, Switzerland
Swiss and Brazilian citizenships

Education

PhD student at Sensors, Actuators and Microsystems Laboratory (SAMLAB) of Ecole Polytechnique Fédérale de Lausanne (EPFL), Neuchâtel, Switzerland Advisors: Dr. W. Noell and Prof. N. de Rooij • Development of novel MEMS-based optical modulators for reflective display application. • Collaboration in different projects of development of micro-mirror arrays	2008 –2012
Master of Science MSc in Microengineering at EPFL Specialization Micro- and Nanosystems Minor in Management of Technology and Entrepreneurship	2002 –2007
Master project at TU Delft, the Netherlands: Topic: Radiation absorption and thermal proprieties of a novel infrared sensor Advisors: Prof. N. de Rooij and Prof. P. French	2007
Exchange year at University of Waterloo, Ontario, Canada (3rd study year)	2004 – 2005
Gymnasium in Bern with Matura diploma (Orientation: Maths and Physics)	1998 – 2002

Past positions

R&D engineer at Soil and Environmental Physics Laboratory (LASEP) of EPFL Implementation of wireless communication between soil water content sensors devices	Oct. 2007 – Feb. 2008
Internship at LASAG AG (Swatch Group) in Thun, Switzerland Elaboration of a production process for micro lens mounting.	Aug. 2005 – Oct. 2005

Technical knowledge

FEM simulation software:	Ansys, Comsol, Coventor
Mask / PCB design software:	Expert, Clewin, Altium Designer
Programming:	Matlab, LabView, Assembler
Microfabrication technology:	practical clean room experience, know-how of MEMS characterization

Languages

German & Portuguese:	Mother tongues
English & French:	Fluent
Spanish & Italian:	Good knowledge